

27 July 2012 | \$10

Science



EDITORIAL

- 390 Iceberg Alert for NIH
Henry R. Bourne and Mark O. Lively

NEWS OF THE WEEK

- 394 A roundup of the week's top stories

NEWS & ANALYSIS

- 397 Needed Antarctic Upgrades Would Trim Science Budget
- 398 Data Dispute Revives Exoplanet Claim
- 399 Panel Votes to End Prevention Fund, Cut Economics Studies, Freeze NIH
- 400 Using Radiocarbon to Go Beyond Good Faith in Measuring CO₂ Emissions
- 401 U.S.'s Best Science and Math Teachers to Get Bonuses

NEWS FOCUS

- 402 Planetary Science Is Busting Budgets
>> Science Podcast
- 405 For China and Kazakhstan, No Meeting of the Minds on Water
- 408 Evolution Ottawa Meeting
Insulin May Guarantee the Honesty of Beetle's Massive Horn
>> Science Express Report by D. J. Emlen et al.
Texas Wildflower's Red Keeps It a Species
By the Skin of Their Teeth

LETTERS

- 410 Pollution in the Yangtze
H. Yang et al.
- Reducing Red Tape for Research in Europe
M. Da Graça Carvalho and M. Geoghegan-Quinn
- Stemming the U.S. HIV Epidemic: Act Local
J. Justman and W. M. El-Sadr

BOOKS ET AL.

- 412 Golden Holocaust
R. N. Proctor, reviewed by T. H. Brandon
- 413 No Time to Lose
P. Piot, reviewed by J. C. H. Tam

POLICY FORUM

- 414 Challenges to India's Pharmaceutical Patent Laws
B. N. Sampat et al.

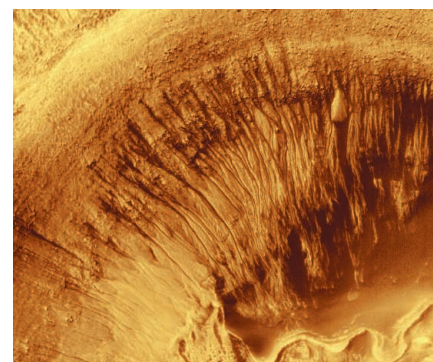
PERSPECTIVES

- 416 The Mind of a Male?
D. B. Chklovskii and C. I. Bargmann
>> Research Article p. 437
- 417 A Roadmap for the Assembly of Polyhedral Particles
J. de Graaf and L. Manna
>> Report p. 453
- 418 dSarm-ing Axon Degeneration
X. M. Yu and L. Luo
>> Report p. 481
- 420 HD6 Defensin Nanonets
A. J. Ouellette and M. E. Selsted
>> Report p. 477
- 421 Use and Abuse of RNAi to Study Mammalian Gene Function
W. G. Kaelin Jr.
- 423 Retrospective: Phillip V. Tobias (1925–2012)
T. D. White

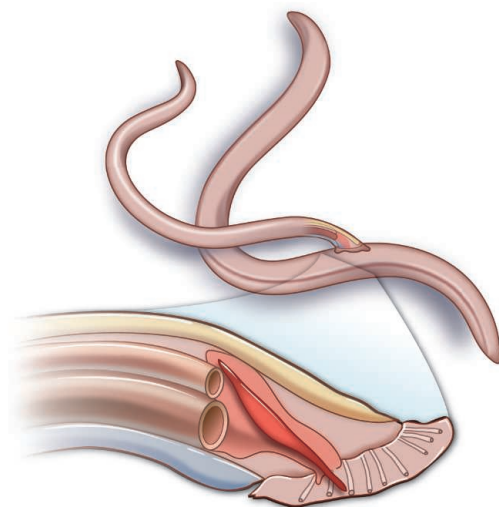
SCIENCE PRIZE ESSAYS

- 424 Aipotu: Simulation from Nucleotides to Populations and Back Again
B. T. White
- 426 Engaging Students in Molecular Biology via Case-Based Learning
M. Bergland et al.

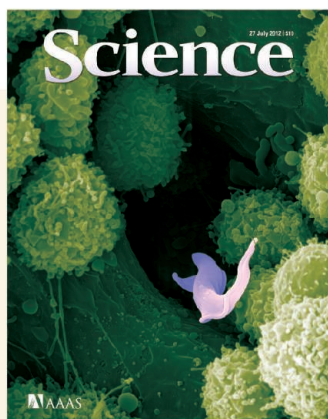
CONTENTS continued >>



page 402



pages 416 & 437



COVER

False-colored scanning electron microscopy image of innate immune cells and the parasite *Trypanosoma brucei* (purple; length: 15 micrometers) in an infected mouse liver. The parasite is transmitted between mammalian hosts, including humans, by the bite of infected tsetse flies and is responsible for human sleeping sickness, a lethal disease that is a serious problem in Africa. See page 463.

Image: Gilles Vanwalleghem, Daniel Monteyne, Etienne Pays, and David Pérez-Morga, Laboratory of Molecular Parasitology and Center for Microscopy and Molecular Imaging, Université Libre de Bruxelles, Gosselies, Belgium

DEPARTMENTS

- 388 This Week in *Science*
- 391 Editors' Choice
- 392 *Science* Staff
- 428 AAAS News & Notes
- 488 New Products
- 489 *Science* Careers

REVIEW

- 431** New Paradigms in Type 2 Immunity
B. Pulendran and D. Artis

BREVIA

- 436** Explosive Backpacks in Old Termite Workers
J. Šobotník et al.
As *Neocapritermes taracua* termites age, they develop a suicidal toxic apparatus that bursts during aggressive encounters.
>> *Science Podcast*

RESEARCH ARTICLE

- 437** The Connectome of a Decision-Making Neural Network
T. A. Jarrell et al.
The complete wiring structure of the synaptic network governing mating behavior of male nematodes is revealed.
>> *Perspective p. 416*

REPORTS

- 444** Binary Interaction Dominates the Evolution of Massive Stars
H. Sana et al.
Analysis of a sample of massive stars in our Galaxy implies that most will interact with a nearby companion.
- 446** Excitation of Orbital Angular Momentum Resonances in Helically Twisted Photonic Crystal Fiber
G. K. L. Wong et al.
Adding chirality to the structure of a photonic crystal fiber may provide another route to controlling light transmission.
- 450** Plasmonic Nanolaser Using Epitaxially Grown Silver Film
Y.-J. Lu et al.
An atomically smooth layer of silver enhances the performance of nanophotonic devices.
- 453** Predictive Self-Assembly of Polyhedra into Complex Structures
P. F. Damasceno et al.
Two parameters relating to particle shape and nearest neighbors reveal the preferred packing of complex structures.
>> *Perspective p. 417; Science Podcast*
- 457** The Tides of Titan
L. Iess et al.
Gravity measurements by the Cassini spacecraft suggest that Saturn's moon Titan hosts a subsurface ocean.

- 459** Isotropic Events Observed with a Borehole Array in the Chelungpu Fault Zone, Taiwan
K.-F. Ma et al.
High-pressure fluids induce fracturing along preexisting cracks near the site of a recent earthquake.

- 463** Adenylate Cyclases of *Trypanosoma brucei* Inhibit the Innate Immune Response of the Host
D. Salmon et al.
Parasites release cyclic adenosine monophosphate when swallowed up by myeloid cells, thereby turning off a host defense pathway.

- 467** GFAJ-1 Is an Arsenate-Resistant, Phosphate-Dependent Organism
T. J. Erb et al.

- 470** Absence of Detectable Arsenate in DNA from Arsenate-Grown GFAJ-1 Cells
M. L. Reaves et al.
Claims of arsenic substitution for phosphorus in the biomolecules of a Mono Lake bacterium are not independently reproduced.

- 473** The Structure and Catalytic Cycle of a Sodium-Pumping Pyrophosphatase
J. Kellosalo et al.
Structures of a *Thermotoga maritima* sodium ion-pumping, membrane-integral pyrophosphatase provide a model of the pumping mechanism.

- 477** Human α -Defensin 6 Promotes Mucosal Innate Immunity Through Self-Assembled Peptide Nanonets
H. Chu et al.
Rather than killing bacteria directly, a gut antimicrobial peptide forms netlike structures that ensnare invading bacteria.
>> *Perspective p. 420*

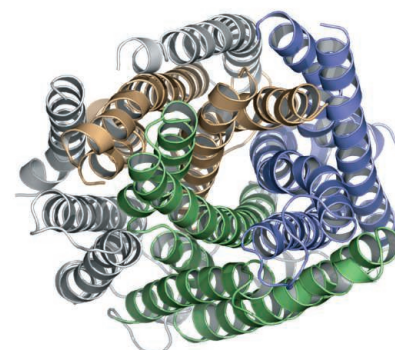
- 481** dSarm/Sarm1 Is Required for Activation of an Injury-Induced Axon Death Pathway
J. M. Osterloh et al.
Mutations in a scaffold protein block the Wallerian degeneration of axons in flies and mice.
>> *Perspective p. 418*

- 485** Memory's Penumbra: Episodic Memory Decisions Induce Lingering Mnemonic Biases
K. Duncan et al.
It takes time for the hippocampus to switch between laying down new memories and recalling old ones.

CONTENTS continued >>



page 450



page 473

SCIENCEONLINE

SCIENCEEXPRESS

www.scienceexpress.org

UV Dosage Levels in Summer: Increased Risk of Ozone Loss from Convectively Injected Water Vapor

J. G. Anderson et al.

Convective injection of water vapor into the stratosphere increases the rate of ozone destruction there.

10.1126/science.1222978

A Mechanism of Extreme Growth and Reliable Signaling in Sexually Selected Ornaments and Weapons

D. J. Emlen et al.

Rhinoceros beetle horns, a sexually selected weapon, are more sensitive to nutrition and reliably indicate male quality.

10.1126/science.1224286

>> *News story p. 408*

Identification of the Cdc48•20S Proteasome as an Ancient AAA+ Proteolytic Machine

D. Barthelme and R. T. Sauer

The AAA+ enzyme Cdc48 combines with the 20S peptidase to function as an alternative type of proteasome.

10.1126/science.1224352

Compartmentalized Control of Skin Immunity by Resident Commensals

S. Naik et al.

The skin microbiota plays a selective role in modulating immunity in the skin of mice.

10.1126/science.1225152

Transforming Fusions of *FGFR* and *TACC* Genes in Human Glioblastoma

D. Singh et al.

A fusion gene detected in a small subset of human brain tumors encodes a potentially druggable target.

10.1126/science.1220834

SCIENCENOW

www.sciencenow.org

Highlights From Our Daily News Coverage

Bats Catch Mating Flies in the Act

A study reveals that bats home in on noises made by copulating flies.

<http://scim.ag/Mating-Flies>

Selfish Sheep Seek the Center

GPS tracking provides evidence to back up biology's selfish herd theory.

<http://scim.ag/Selfish-Sheep>

Artificial Jellyfish Swims Like the Real Thing

Cell-silicone hybrid may inform the design of replacement hearts.

<http://scim.ag/Artificial-Jellyfish>

SCIENCE SIGNALING

www.sciencesignaling.org

The Signal Transduction Knowledge Environment

24 July issue: <http://scim.ag/ss072412>

RESEARCH ARTICLE: p53 Functions in Endothelial Cells to Prevent Radiation-Induced Myocardial Injury in Mice

C.-L. Lee et al.

PODCAST

D. G. Kirsch et al.

The transcription factor p53 protects the heart from radiation-induced damage.

RESEARCH ARTICLE: Distinct Spatial and Molecular Features of Notch Pathway Assembly in Regulatory T Cells

L. R. Perumalsamy et al.

PERSPECTIVE: Notch and the Survival of Regulatory T Cells—Location Is Everything!

L. M. Minter and B. A. Osborne

A cytosolic function of Notch helps regulatory T cells survive.

GLOSSARY

Find out what CTK, Rag, and Rheb mean in the world of cell signaling.

EVENTS

Plan to attend a signaling-relevant meeting, with more than 30 new meetings and conferences added in July.

SCIENCE TRANSLATIONAL MEDICINE

www.sciencetranslationalmedicine.org

Integrating Medicine and Science

25 July issue: <http://scim.ag/stm072512>

FOCUS: In the Public Interest?

L. C. Sayres et al.

Restrictive patenting and licensing for cell-free fetal DNA testing has serious consequences for technology advances and benefits to public health.

RESEARCH ARTICLE: MHC-Resident Variation Affects Risks After Unrelated Donor Hematopoietic Cell Transplantation

E. W. Petersdorf et al.

The success of HLA-matched unrelated donor hematopoietic cell transplantation depends on non-HLA MHC region genetic variation.

RESEARCH ARTICLE: Temsirolimus Activates Autophagy and Ameliorates Cardiomyopathy Caused by Lamin A/C Gene Mutation

J. C. Choi et al.

Cardiomyopathy arising from lamin A/C mutations in mice can be corrected by enhancing autophagy through blockade of mTOR with temsirolimus.

RESEARCH ARTICLE: Rapamycin Reverses Elevated mTORC1 Signaling in Lamin A/C–Deficient Mice, Rescues Cardiac and Skeletal Muscle Function, and Extends Survival

F. J. Ramos et al.

Rapamycin treatment of a mouse model for a human laminopathy improves cardiac and muscle function, suggesting a therapy for human patients.

SCIENCE CAREERS

www.sciencecareers.org/career_magazine

Free Career Resources for Scientists

Experimental Error: Help Not Wanted

A. Ruben

The United States faces a severe shortage of qualified scientists—so why are there so many unemployed scientists?

http://scim.ag/EE_NotWanted

Q&A: A Career on the Fence

E. Pain

A graduate school dean and former Olympic athlete reflects on science, fencing, and how the two activities have benefited each other.

<http://scim.ag/OntheFence>

SCIENCE PODCAST

www.sciencemag.org/multimedia/podcast

Free Weekly Show

On the 27 July *Science* Podcast: self-assembly at the nanoscale, suicide-bombing termites, what's next for NASA's planetary program, and more.

SCIENCE INSIDER

news.sciencemag.org/scienceinsider

Science Policy News and Analysis

SCIENCE (ISSN 0036-8075) is published weekly on Friday, except the last week in December, by the American Association for the Advancement of Science, 1200 New York Avenue, NW, Washington, DC 20005. Periodicals Mail postage (publication No. 484460) paid at Washington, DC, and additional mailing offices. Copyright © 2012 by the American Association for the Advancement of Science. The title SCIENCE is a registered trademark of the AAAS. Domestic individual membership and subscription (51 issues): \$149 (\$74 allocated to subscription). Domestic institutional subscription (51 issues): \$990; Foreign postage extra: Mexico, Caribbean (surface mail) \$55; other countries (air assist delivery) \$85. First class, airmail, student, and emeritus rates on request. Canadian rates with GST available upon request, GST #1254 88122. Publications Mail Agreement Number 1069624. Printed in the U.S.A.

Change of address: Allow 4 weeks, giving old and new addresses and 8-digit account number. **Postmaster:** Send change of address to AAAS, P.O. Box 96178, Washington, DC 20090-6178. **Single-copy sales:** \$10.00 current issue, \$15.00 back issue prepaid includes surface postage; bulk rates on request. **Authorization to photocopy** material for internal or personal use under circumstances not falling within the fair use provisions of the Copyright Act is granted by AAAS to libraries and other users registered with the Copyright Clearance Center (CCC) Transactional Reporting Service, provided that \$30.00 per article is paid directly to CCC, 222 Rosewood Drive, Danvers, MA 01923. The identification code for Science is 0036-8075. Science is indexed in the Reader's Guide to Periodical Literature and in several specialized indexes.



ADVANCING SCIENCE. SERVING SOCIETY

Insights into Type 2 Immunity

Different pathogens trigger characteristic immune responses. Although the immune responses against many bacteria, viruses, and fungi are relatively well understood, those against parasitic worms—termed type 2 responses—are much less so. Intriguingly, type 2 responses also mediate responses to allergens and allergic asthma. **Pulendran and Artis** (p. 431) review progress in understanding the signals that trigger type 2 immunity and the cellular responses that these responses initiate.

The Male Wiring Diagram

The function of the nervous system is thought to represent an emergent property of its network connectivity. However, there are few complete descriptions of all the physical connections between neurons within a real nervous system. Working in nematodes, **Jarrell et al.** (p. 437; see the Perspective by **Chklovskii and Bargmann**) identified the complete connectome—every single chemical and gap junction synapse—of the tail ganglia, which govern mating behavior.

Fiber with a Twist

Optic fibers provide the backbone of communication networks. Controlling light propagation through the fiber is key to maximizing the capacity of information flow. By introducing a literal twist on the photonic crystal fiber, **Wong et al.** (p. 446) show that adding chirality to the cladding surrounding the core may provide another route to manipulating the transmission of light. Coupling between the twisted cladding and the core results in dips in the transmission spectrum, which are dependent on the degree of twist introduced into the fiber. Such twisted microstructure fibers may offer opportunities for coupling, filtering and manipulating light.

Star Partners

Stars more massive than eight times the mass of the Sun are rare and short-lived, yet they are fundamentally important because they produce all the heavy elements in the universe, such as iron, silicon, and calcium. **Sana et al.** (p. 444) examined the properties of a sample of

Sarm-Assisted Suicide >>

Neurodegenerative disease or nerve lesions cause axons and synapses to disintegrate through a process known as Wallerian degeneration, which may involve an active “axon death program.” **Osterloh et al.** (p. 481, published online 7 June; see the Perspective by **Yu and Luo**) identify loss-of-function mutations in *Drosophila* dSarm that are capable of blocking the degeneration of severed axons for the fly life span. Deletion of mouse Sarm1 provides similar protection to severed axons for weeks after injury, which suggests that Sarm is part of an ancient axonal death signaling cascade.

~70 massive stars in six stellar clusters located nearby in our galaxy. Over half of the stars in the sample belong to a binary system and, during the course of their lifetimes, most of the stars in these binaries will interact with one another, either by merging or exchanging mass. Binary interaction may thus affect the evolution of the majority of massive stars.

Going Green with Nanophotonics

Plasmons are optically induced collective electronic excitations tightly confined to the surface of a metal, with silver being the metal of choice. The subwavelength confinement offers the opportunity to shrink optoelectronic circuits to the nanometer scale. However, scattering processes within the metal lead to losses. **Lu et al.** (p. 450) developed a process to produce atomically smooth layers of silver, epitaxially grown on silicon substrates. A cavity in the silver layer is capped with a SiO₂ insulating layer and an AlGaIn nanorod was used to produce a low-threshold emission at green wavelengths.

Getting Packed

If one neglects the role of specific interactions, the packing of similar-shaped objects will depend only on the particular shape of the object. **Damasceno et al.** (p. 453; see the Perspective by **de Graaf and Manna**) present computer simulations of the behavior of different types of polyhedra with simple and complex shapes that are packed under thermal equilibrium into various structures, from crystals to amorphous materials through liquid crystals. Despite the

wide variety of starting shapes, the packing behavior could be quantitatively described using just two criteria; one for the particle shape as a function of its volume and surface area, and one for the number of nearest neighbors.

Getting to Know Titan

Gravity-field measurements provide information on the interior structure of planets and their moons. **Iess et al.** (p. 457; published online 28 June) analyzed gravity data from six flybys of Saturn’s moon, Titan, by the Cassini spacecraft between 2006 and 2011. The data suggest that Titan’s interior is flexible on tidal time scales with the magnitude of the observed tidal deformations being consistent with the existence of a global subsurface water ocean.

Tricky Tryps

African trypanosomes, responsible for human sleeping sickness, are known for their powerful strategies of immune evasion, in particular antigenic variation. Adding another facet to this adaptive potential, **Salmon et al.** (p. 463, published online 14 June; see the cover) now show that early after infection, these parasites subvert the first line of innate host defense by inhibiting tumor necrosis factor—synthesis in myeloid cells. This occurs through the stress-induced synthesis and release of cyclic adenosine monophosphate by phagocytosed parasites. The findings provide a long-sought function for the abundant and diverse adenylate cyclases in salivarian trypanosomes. Furthermore, this altruistic host colonization strategy, in which a proportion of parasites are sacrificed so that others can thrive, also highlights the selective advantage of population behavior in infection.

Resisting Arsenic

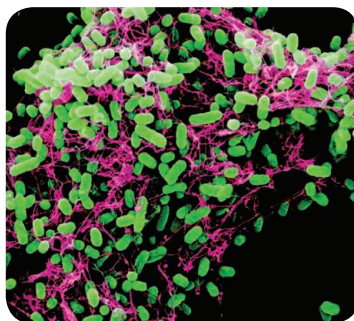
The discovery of a bacterium living in the extreme conditions of Mono Lake, California, created a major controversy because it was claimed to be able to grow solely on arsenic and could substitute arsenate for phosphate in its key macromolecules, including DNA. Working with the same *Halomonas* spp. bacterium, known as GFAJ-1, and ultrapure reagents, **Erb *et al.*** (p. 467) found that the bacterium needed a low level of phosphate (1.6 μM) to grow at all. Rather than significant specific arsenic incorporation, when the organism was grown in 40 mM arsenic, its nucleic acids acquired a trace of arsenic. Similarly, **Reaves *et al.*** (p. 470) found that GFAJ-1 could not grow in the absence of phosphate and, moreover, that its growth was not stimulated by the addition of arsenate, although a trace amount of arsenic was also detected in DNA. Thus, GFAJ-1 shows no particular facility to substitute arsenic for phosphate, when phosphate is limiting, but it can tolerate high concentrations of the poison while efficiently scavenging phosphate.

View of a Sodium Pump

Membrane-integral pyrophosphatases (M-PPases) found in plants, protozoans, bacteria, and archaea, link pyrophosphate hydrolysis or synthesis to sodium or proton pumping and contribute to generating an electrochemical potential across the membrane. **Kellosalo *et al.*** (p. 473) report the structure of the sodium pumping M-PPase from *Thermotoga maritima* in the resting state with product bound. The structures reveal the conformational changes that are likely to accompany pyrophosphate binding and provide insight into the ion-pumping mechanism.

Netting the Bad Guys

Antimicrobial peptides are an evolutionarily conserved component of innate immunity in the intestine. One family, α -defensins, typically exert their antimicrobial effects through microbicidal activity against bacteria. Humans express only two α -defensins, human defensin 5 (HD5) and HD6. HD5 exhibits bactericidal activity and plays a role in shaping the bacterial composition of the gut. HD6, on the other hand, does not show bactericidal activity and its function in the gut is unclear. Now, **Chu *et al.*** (p. 477, published online 21 June; see the Perspective by **Ouellette and Selsted**) show that HD6 protects against bacterial pathogens. Rather than killing them directly, HD6 binds to bacteria surface proteins and, through a process of self-assembly, forms fibrils and nanonets that ensnare invading bacterial pathogens.



New for Old?

When confronted with a visual stimulus, such as an object or a scene, the brain decides whether it is new, and thus deserves to be encoded as a new memory, or old, which triggers the retrieval of the previously encoded memory. When shown a series of stimuli, some of which are similar to, but not identical to, old memories, it becomes necessary to switch back and forth between encoding and retrieval processing. Using behavioral tasks performed by human test subjects, **Duncan *et al.*** (p. 485) took advantage of the fact that switching takes a second or two and found that a subsequent object, presented before switching has occurred, was more likely to be identified as new when the previous object was new, and identified as old when the previous object was old.

Cracking Up

Hydraulic fracturing by fluids at high pressure results in damage or breakage along cracks in deep rocks, a process that in some cases causes earthquakes. This process can occur naturally when the hydrologic setting is just right, or can be induced by human activity when fluids are pumped at high pressure into deep aquifers. By studying the fault along which the 1999 magnitude 7.6 Chi-Chi earthquake occurred in Taiwan, where there are currently low tectonic stresses following the large earthquake, **Ma *et al.*** (p. 459) observed an unusual type of earthquake-like event that they attribute to natural hydraulic fracturing.

CREDIT: HIUTUNG CHU

Iceberg Alert for NIH

A CENTURY AGO, THE UNSINKABLE *TITANIC* CHARGED INTO A MOONLESS NIGHT, FULL STEAM AHEAD. Today, unless it changes course to escape its own icebergs, the U.S. biomedical research enterprise hurtles toward a similar doom. The fiscal year 2012 budget of the U.S. National Institutes of Health (NIH) buys 18% less research than in 2004. On 2 January 2013, budget sequestration mandated by the Budget Control Act of 2011 could reduce NIH extramural funds still further, producing a staggering cumulative 41% decline in a single decade (in constant dollars, from 2004 to 2014), down to the level that NIH invested in 1997. In contrast, China's governmental support for biomedical research may double that of the United States, or even, in proportion to gross domestic product (GDP), quadruple it by 2017.*

In dollars, the contributions of NIH-supported research to human health, jobs, and national economic growth far surpass investments budgeted by Congress. The obvious inference: Investment in NIH should not shrink but steadily increase, at a rate proportional to GDP. Instead, as grant dollars shrink, institutions will be forced to curtail biomedical research drastically, mimicking the recent layoff of 150 research faculty and hundreds of other employees by the University of Miami's Miller School of Medicine. Established researchers at rich institutions may survive, but many in the rising generation of young investigators and in small research programs will drown. Institutions will further trim hard-money contributions to faculty salaries and find it even harder to pay for and populate research facilities they recently expanded. Competition for faculty positions, grants, and published papers will grow ever fiercer. And the postdoctoral holding tank will brim over, as myriad well-trained young scientists vainly seek research jobs.

Apparently unaware that the model for funding U.S. biomedical research is close to collapse, key stakeholders in the biomedical research community, like mythical *Titanic* passengers, busy themselves rearranging deck chairs. We urge those stakeholders—faculty, academic administrators, funding agency leaders, and (if it can) Congress itself—to unite to plot a dramatically different course. Radical actions are called for that distribute scarce resources more efficiently, with a focus on helping the best young and established scientists survive the present storm for as long as it lasts, even if it means a substantial decrease in the size of their research groups.

Research institutions must discard their present corporate business model, which is based on the assumption that federal funds to support research programs will increase every year. Those institutions must invest more in direct salary support for faculty scientists and less in bricks and mortar. NIH should require institutions to pay a larger share of principal investigators' salaries (in increments, spread over time), and indirect cost rules that currently encourage universities to build labs rather than nourish their own faculty must be changed.† Even more broadly, faculty, administrators, research institutions, and NIH must work together to tackle knotty problems of resource distribution, as we describe in the supplement.

Academic labs today depend on graduate students and postdocs to supply the workforce that keeps them humming. This dependence, which generates multiple potential competitors for soft-money positions and grants but does not always train young scientists effectively, must be reduced by implementing and further strengthening the recommendations of a just-released report from NIH's Biomedical Research Workforce Working Group.‡

To devise effective local and national responses to the impending crisis, new strategies must be implemented quickly. The status quo is untenable, and the alternatives are dire: Failure to adjust to the new reality means that stakeholders may be forced to scrounge seats in a lifeboat, or—like the majority of *Titanic* passengers—drown.

— Henry R. Bourne and Mark O. Lively

10.1126/science.1226460

*See supplementary materials at www.sciencemag.org/cgi/content/full/science.1226460/DC1 (text and figure).

†B. Alberts, *Science* **329**, 1257 (2010). ‡http://acd.od.nih.gov/bmw_report.pdf.



Henry R. Bourne is professor emeritus in the Department of Cellular and Molecular Pharmacology at the University of California at San Francisco. E-mail: bourne@cmp.ucsf.edu.



Mark O. Lively is a professor in the Department of Biochemistry at the Wake Forest School of Medicine, Winston-Salem, NC. E-mail: mlively@wakehealth.edu.



CELL SIGNALING

Toll-Like Receptor Tag Team

How many receptors does it take to initiate an antiviral response? Yamashita *et al.* say it's two, plus an additional tyrosine kinase. First, you need Toll-like Receptor 3 (TLR3), which has a well-characterized role in the detection of double-stranded RNA (dsRNA) and initiation of protective cellular responses. Earlier findings showed that TLR3 differs from other TLRs in requiring phosphorylation of two tyrosine residues in its cytoplasmic tail for activation. Here, another receptor is implicated in the activation of antiviral responses by TLR3—the epidermal growth factor receptor (EGFR), which is itself a tyrosine kinase. The EGFR was found to associate with dsRNA-activated TLR3 in endosomal membranes along with another tyrosine kinase, Src. Both EGFR and Src appeared to phosphorylate a particular tyrosine residue in TLR3, and inhibition of the kinases inhibited TLR3-dependent antiviral responses. Thus, antiviral responses may involve interactions between signaling systems controlling cell growth and those mediating innate immune responses. — LBR

Sci. Signal. **5**, ra50 (2012).

PSYCHOLOGY

A Wealth of Meaning

The United Nations recently reported that women spend anywhere from twice to four times the number of hours on family and domestic responsibilities as men, which has invigorated a discussion about the tradeoffs between career and family that women often face. Kushlev *et al.* examined the link between wealth—in the form of education and income—and subjective measures of the meaningfulness of life and happiness of residents of British Columbia. An inverse relation was observed between socioeconomic status and the meaningfulness of life for parents when taking care of their children, whereas during the rest of the day, there was no such correlation. In a follow-up field experiment, the concept of wealth was casually introduced while asking attendees at a children's festival about their happiness and sense of meaning. Once again, there was no link between wealth and happiness, but a negative relation between thoughts of wealth and a sense of meaningfulness. Thus, paradoxically, affluence may compromise one of the subjective benefits of parenting—a sense of meaning in life. — GJC

J. Exp. Soc. Psychol. **48**, 10.1016/j.jesp.2012.06.001 (2012).

OCEAN SCIENCE

Refuges for Corals

Global warming presents a real and present danger to coral reefs, owing to the increasing frequency of bleaching events as water temperatures rise. In the central Pacific, for instance, sea surface temperatures are projected to increase by nearly 3°C by the end of this century, a rise that could be devastating to many of the rich marine ecosystems that thrive there. However, the climate system is complex and heterogeneous in its response to global warming, particularly at smaller scales, and there should be regions in which surface ocean warming is less pronounced than others. Karnauskas and Cohen report that warming around some Pacific islands could be mitigated by enhanced upwelling caused by the strengthening of the equatorial undercurrent, which models predict will occur. Less warming should translate into less severe negative impacts on the coral reefs and rich ecosystems in those locations, potentially providing vital refuges in otherwise more hostile environmental conditions. Although few coral reefs may benefit from this island effect, because the equatorial undercurrent flows only around the Equator, knowing where refuges could exist might help planning efforts to protect them in ways that we can control. — HJS

Nat. Clim. Change **2**, 530 (2012).

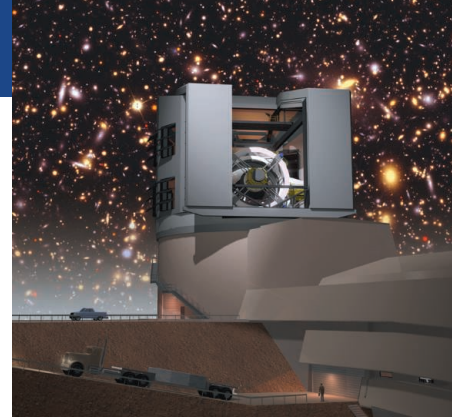


MICROBIOLOGY

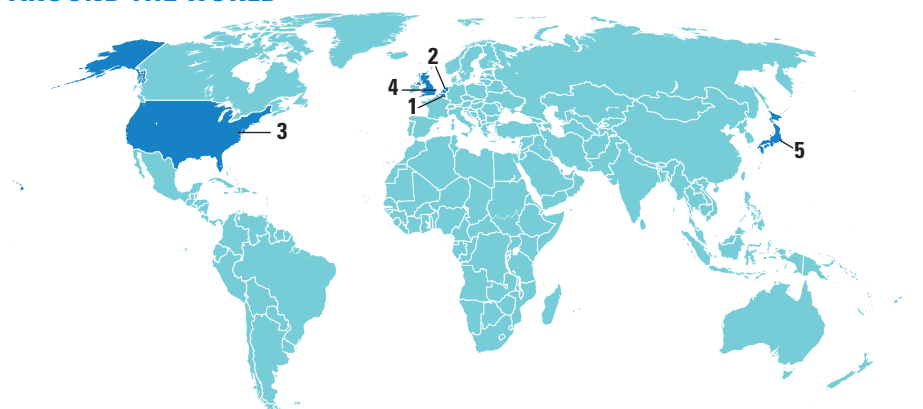
Cryptic N₂ Fixation

Lichen-covered buildings, rocks, and trees are a common sight. Indeed, if they remain static for long enough, or simply grow slowly, most objects on Earth's surface become coated by cyanobacteria, algae, fungi, lichens, and bryophytes. These coatings are called cryptogamic covers, and Elbert *et al.* estimate that these photoautotrophic communities make substantial contributions to carbon and nitrogen cycling. Carbon uptake by these communities was estimated to be highest in Europe (at about 10% of net primary production) and lowest in Africa (at about 4%) and in total to constitute about 1% of the carbon content of terrestrial vegetation. Far more striking is their relative contribution to total biological nitrogen fixation, ranging from 30% in Europe and South America to more than 80% in Asia and North America. This means that models of nitrogen cycling need to account for the activities of cryptogamic covers, or they may miss the majority of biological nitrogen fixation occurring in some regions. — CA

Nat. Geosci. **5**, 459 (2012).



AROUND THE WORLD



Brussels 1

European Commission Proposes Deep-Sea Protections

The European Commission wants to tighten its oversight of deep-sea habitat in the Northeast Atlantic, proposing last week to phase out deep-sea trawling and implement scientific quotas for fishing. “This action is a complete turning point in potential protection of deep-sea bottom communities,” says marine biologist Les Watling of the University of Hawaii, Manoa.

Only 1% of fish caught in the Northeast Atlantic come from the deep sea, but the

The Netherlands 2

Europe Poised to Approve Gene Therapy

For the first time, a gene therapy treatment appears to be headed for regulatory approval in a Western country. Last week, the European Medicines Agency (EMA) recommended that the European Commission approve Glybera, a drug for patients with a rare disorder that leads to a dangerous buildup of fat in the blood.

Glybera, which is injected into leg muscles, uses a virus to deliver a gene for an enzyme called lipoprotein lipase (LPL) that breaks down fats. EMA turned down a Glybera application three times in the past 13 months because data on 27 patients failed to convincingly show that the drug resulted in fewer pancreatitis attacks, but EMA experts changed their minds after reviewing data on patients with the most severe symptoms. Only such patients will be allowed to receive the drug. The Dutch company developing the drug, uniQure, must submit monitoring data on treated patients.

The European Commission usually follows the advice of EMA. Currently, only China and Russia have approved gene therapy treatments.

Washington, D.C. 3

U.S. Science Board Green-Lights Telescope

The U.S. National Science Board (NSB), the policymaking body of the National Science Foundation (NSF), has given the go-ahead to the foundation’s plan to construct the Large Synoptic Survey Telescope (LSST): an 8.36-meter-wide instrument to be built in

Chile. The endorsement marks a significant milestone for the proposal.

The telescope will survey the sky twice a week using a 3-billion-pixel camera, collecting images of billions of galaxies. The repeat observations will help astronomers detect changes in stars and galaxies in an unprecedented way, probe dark matter and dark energy, and discover transient phenomena such as stellar explosions.

NSB’s vote of approval allows NSF to include a line in its 2014 budget request to Congress for beginning construction. The estimated construction cost is \$665 million. The bulk of the cost—70%—will be borne by NSF, while the Department of Energy has agreed to pay 24%. The remaining 6% is coming from private donors. If Congress approves funding, the project is expected to be completed in 5 years. Officials hope that it will be ready to collect data starting in 2022.

Norwich, U.K. 4

Police Close Climategate Investigation

Police in the United Kingdom have ended their investigation into “Climategate,” the November 2009 theft of thousands of e-mails from the Climatic Research Unit at the University of East Anglia in Norwich. The public release of the e-mails, many of which were written by prominent climate scientists, came just prior to a major meeting in Copenhagen on an international agreement to curb climate change. The often blunt and sometimes unflattering messages were seized by those who doubt climate science and used to argue that some researchers had manipulated data and violated ethical standards. Several investigations, however, cleared the scientists of wrongdoing. The Norfolk Constabulary announced on 18 July that it was ending Operation Cabin, its investigation into what detectives called a “sophisticated and carefully orchestrated attack.” Britain’s Computer Misuse Act has a 3-year statute of limitations, noted Detective Chief Superintendent Julian Gregory, and “the complex nature of this investigation



methods used to catch them are particularly destructive of fragile habitats and can contain up to 20% “bycatch” of unwanted species, such as deepwater sharks. The proposal would phase out licenses for deep-sea trawling 2 years after the regulation is approved, require strict quotas for deep-sea species that lack solid scientific data on population size, and require impact assessments for opening new areas to deep-sea bottom fishing. The proposal will go to the European Parliament and Council of Ministers for review when they reconvene in early September. <http://scim.ag/deeptrawl>

means that we do not have a realistic prospect of ... launching criminal proceedings within the time constraints imposed by law.”

Tokyo 5

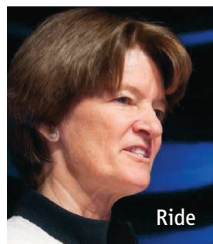
Scientists Spar Over Fukushima Radiation Effects

A new estimate of deaths likely to result from the Fukushima nuclear disaster has been challenged by radiation experts. John Ten Hoeve and Mark Jacobson of Stanford University produced a global map of fall-out from the March 2011 reactor meltdowns and calculated cancer cases using the linear no-threshold (LNT) model, which holds that any increase in radiation exposure proportionally increases the cancer risk. Their results, published online at *Energy & Environmental Science* on 17 July, show the accident could cause between 15 and 1100 cancer deaths, primarily in Japan.

The team “applied the LNT model inappropriately,” says University of Tokyo physicist Ryugo Hayano. He points to International Commission on Radiological Protection recommendations that the LNT model not be used this way with low radiation doses. And in an opinion appearing online with the paper, Nobel Prize-winning physicist Burton Richter argues that nuclear power is “better for your health” than other choices. He figured that a standard lifetime of power generation by the six Fukushima nuclear reactors would have caused fewer lost years of life (26,800) due to radiation and accidents than pollution from burning coal (124,000 years) or gas (38,000 years). <http://scim.ag/radeffects>

NEWSMAKERS

Sally Ride Dead at 61



Ride

Astronaut **Sally Ride**, the first American woman to travel to outer space, died this week of pancreatic cancer. The intensely private Ride, an astrophysicist, graduated

from Stanford University in California in 1978; the same year, she joined NASA as an astronaut candidate, one of six women chosen as the first female candidates. She traveled into space for the first time in 1983 aboard the Space Shuttle *Challenger* and made a second space flight in 1984.



A Touching Tribute

Hoping to cover a lot of ground, computer researchers are helping viewers take in the world's largest piece of community folk art. The AIDS Memorial Quilt is composed of some 49,000 hand-sewn panels commemorating more than 93,000 people who died from AIDS. It would cover more than 12 hectares if fully displayed, but small portions are typically shown at events, such as this week's International AIDS Conference in Washington, D.C. To make the quilt more accessible, Anne Balsamo of the University of Southern California in Los Angeles is creating a virtual version together with Microsoft Research, the NAMES Project Foundation, and several universities. AIDS Quilt Interactive, a touchscreen exhibit, lets viewers search for panels and view them close up. Stitching together the 500,000 images has been “a profound experience for me as a designer and technologist” says Balsamo, and “a dream come true.” The exhibit will be on display at the San Jose Museum of Quilts and Textiles in California from 7 August to 14 October.

After leaving NASA in 1987, Ride became a physics professor at the University of California, San Diego. She was also the president and CEO of Sally Ride Science, founded in 2001 to promote science and math careers for girls and young women.

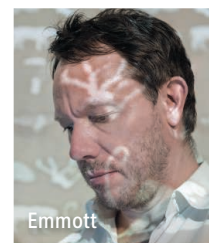
Three Q's

Earlier this month, University of Oxford neuroscientist **Stephen Emmott**, who also heads Microsoft's Computational Science Lab in Cambridge, stepped out onto the stage of the Royal Court Theatre in London to give an hourlong “performance” on the subject of population. Entitled *Ten Billion*, after the estimated world population at the end of this century, it is somewhere between

a lecture and a theatrical monologue, and has won positive reviews. “This is one of the most disturbing evenings I have ever spent in a theatre,” wrote *The Guardian's* drama critic Michael Billington. *Ten Billion* runs at the Royal Court until 11 August.

Q: What sort of a show is it?

I struggle to define it. It's an experiment: a nonscientific talk about science to a nonscientific audience in a theatre. It's about population, resource depletion, energy, water, species extinction ... how they all interlink. >>



Emmott

>>NEWSMAKERS

Q: Why population as a topic?

The Earth could carry 20 billion people, but not with our current way of living. So what is the carrying capacity of the Earth? Is it 7 billion or 10 billion or 20 billion? I think we're already past it with the way we consume now, so if there are going to be another 3 billion people this century, what are the consequences? Is there a solution?

Q: What was the audience's reaction?

I found it very difficult to judge their reaction because I couldn't see them. But

people who stayed on afterwards came up to me and said "it was absolutely life-changing," and "it made me think completely differently." So the experiment looks successful.

FINDINGS

Genetic Code Reveals Hunter-Gatherer Diversity

As prehistoric humans migrated across Africa and into Asia and Europe, their encounters with new environments sparked genetic changes. In a study

published online in *Cell*, researchers peering into the genomes of several African peoples have found signs of early divergence.

The international team, led by geneticist Sarah Tishkoff of the University of Pennsylvania, sequenced the genomes of five people from three different hunter-gatherer groups: the Hadza and Sandawe from Tanzania and the Pygmies from Cameroon, some of the most ancient lineages in the world. This is the first African population genomics study using high-coverage sequencing. According to the DNA evidence, as the groups migrated to new territories, genes responsible for immunity, taste, and smell began to change. The genetic trail suggests that the Pygmies' short stature is controlled by several large chunks of DNA involving the pituitary gland, which regulates growth, immunity, and many other functions. Perhaps most intriguing, all three groups showed signs of having intermarried with an earlier, as-yet-unidentified species, perhaps the African equivalent of the Neandertal in Europe. <http://scim.ag/huntgath>

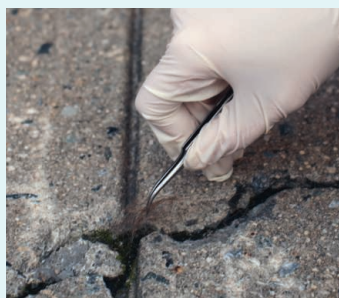
Random Sample

**Facing the Genetic Future**

Sitting in a therapist's office, New York City artist Heather Dewey-Hagborg discovered a hair lodged in a crack in the glass covering a painting on the wall. "I stared at it for an hour," she says. "I couldn't stop wondering who it belonged to, and what I could find out about that person."

After reading a story in *Science* about the new field of forensic DNA phenotyping (18 February 2011, p. 838), Dewey-Hagborg decided to turn her fascination into an art project. She collected 11 hairs left around the city by strangers and learned how to test their

DNA at a genetics lab. Now, she's printing three-dimensional masks, or approximations, of those people's faces, which will be on display—along with her own—in a January exhibition called *Stranger Visions*. The masks reflect eye color, geographical roots, sex, and other traits, but not exact facial features because forensic phenotyping can't fill in all the details. But it might one day, and with ever cheaper sequencing, an era of "genetic surveillance" is looming, says Dewey-Hagborg. "As a society, we need to have a discussion about that."



BY THE NUMBERS

\$424 million Total amount of two grant agreements signed 19 July by the Ethiopian government and the Global Fund to Fight AIDS, Tuberculosis and Malaria. The agreements aim for universal coverage of HIV treatment and to eliminate malaria deaths in Ethiopia by 2015.

34 billion Tonnes of global emissions of carbon dioxide in 2011, an increase of 3% compared with last year—and an all-time high, according to a study by the European Commission's Joint Research Centre.

Science LIVE

Join us on Thursday, 2 August, at 3 p.m. EDT for a live chat on **the future of exploration on Mars**. <http://scim.ag/science-live>

Urgent repairs. A new report finds that McMurdo Station has multiple maintenance issues.



POLAR SCIENCE

Needed Antarctic Upgrades Would Trim Science Budget

The aging scientific facilities in Antarctica are in dire need of repair and upgrades—and paying for that will require cuts to Antarctic research activities in the short-term, according to the recommendations published this week by a National Science Foundation (NSF)—organized panel. “It’s not a happy solution, but if we don’t do something soon, [U.S. Antarctic] science will disappear,” says Norman Augustine, the retired chief executive officer of Lockheed Martin Corp. who chaired the review panel.

Although painful, making those changes will ultimately pay off, by increasing the amount of science that can be supported by the U.S. Antarctic Program (USAP), the panel’s report concludes. But Antarctic scientists, weary from years of tightened research budgets, are worried about just how short-term those cuts may be.

In 2010, NSF and the White House Office of Science and Technology Policy initiated two reviews of U.S. activities in Antarctica, meant to help guide NSF’s USAP. In October 2011, a U.S. National Academies’ National Research Council panel completed the first, research-focused half of the review, publishing a report outlining U.S. science priorities and needs in the Antarctic. Now, the current report, called *More and Better Science in Antarctica Through Increased Logistical Effectiveness*, focuses on the myriad challenges of operating in Antarctica—and takes a particularly hard look at the program’s

decades-old facilities and infrastructure.

Dotting a harsh, barren landscape, NSF’s three Antarctic stations represent home and shelter to the hundreds (and, in season, more than a thousand) of U.S. scientists and staff that live at or visit the bottom of the world. Supplying and maintaining those stations, all of which are managed by USAP, poses many problems, from ensuring that they have sufficient fuel to providing communications to preventing outbreaks of disease.

The new report examines multiple issues, from transportation to communications to energy efficiency. The most urgent needs center on two USAP facilities: Palmer Station, on the Antarctic Peninsula, and McMurdo Station, the primary land, sea, and air portal to U.S. research activities in Antarctica. Both stations require numerous repairs and upgrades.

The maintenance issues are particularly urgent, the panel concludes, because they are both hazardous and busting NSF’s Antarctic budget. “If they’re going to continue as they are, it will cost a great deal in the future to bring them back up to operating capability,” Augustine noted at a 23 July press conference for the report’s release. To keep on top of needed repairs, the report pushes for the creation of a capital budget for USAP; it would be similar to NSF’s Major Research Equipment and Facility Construction account, but while MREFC’s fund is “very ad hoc,” Augustine says, what’s needed for Antarctic research is a “long-term plan with adequate reserves.”

The panel also made suggestions that it said would require a substantial financial investment up front, but that would pay off within a few years. One expense that the panel flagged is the cost of supplying the Amundsen-Scott South Pole Station, which is currently accessed primarily with 10 heavy, ski-equipped LC130 planes that can each only carry limited cargo. Because both fuel and personnel are extremely pricey in the Antarctic, the report suggests reducing that fleet to six planes that can be equipped to also do science, and developing an overland supply route from McMurdo, equipping transports with state-of-the-art ice-penetrating radar technology to detect crevasses and using driverless vehicles that follow in formation.

Meanwhile, there remains an elephant in the room: the lack of a U.S. icebreaker to service Antarctica. McMurdo Station remains the primary hub for U.S. researchers and support staff members on the continent; it allows for deep-water access by ships and a stable runway for wheeled aircraft. But the station is surrounded by sea ice each year and requires an icebreaker to cut a path to allow fuel and cargo ships to deliver supplies. Since 2006, NSF has relied on short-term contracts to use icebreakers from Russia and Sweden to help resupply its Antarctic stations. President Barack Obama has requested \$8 million in the 2013 budget to begin to design a new icebreaker for the Antarctic—an item that the panel “vigorously” supports. If that construction isn’t funded, Augustine said NSF should at least be given the authority to make longer-term agreements for icebreaker capability.

How to pay for the immediate upgrades remains the question. New money will help: The panel suggests an increase to USAP’s annual appropriation (relative to fiscal year 2012) by 6%, or \$16 million, for the next

4 years. But Congress will also want to see cuts, Augustine says. Many scientists working in the Antarctic are not fully aware of how expensive it is to maintain a presence on the ice, he notes: Like an iceberg, research may be the visible portion of the effort, but the vast, hidden base of the iceberg represents the logistics effort in Antarctica. That also means that when it comes to the expense of working on the continent, logistics is also where it

is easiest to find cuts; for example, the panel suggests reducing Antarctic-related contractor labor by 20%.

But science is also on the chopping block: The panel recommends diverting 6% of planned science expenditures over the next 4 years to help pay for the upgrades. Cutting research funds to pay for new facilities brings up sour memories for some Antarctic scientists, however. A 1997 review of

USAP (also chaired by Augustine) resulted in much-needed but decade-long renovations to the South Pole Station, completed in 2008—and Antarctic science is still recovering from the impact of that project, which took years longer than anticipated. That's the rub, says Robin Bell, a geophysicist at Lamont-Doherty Earth Observatory in Palisades, New York. "It depends if it's really a 4-year—or a permanent—cut." —CAROLYN GRAMLING

ASTRONOMY

Data Dispute Revives Exoplanet Claim

Steven Vogt is fighting to save the world—but he doesn't mean Earth. Two years ago, Vogt, an astronomer at the University of California, Santa Cruz, and colleagues made headlines when they announced the first detection of a potentially habitable planet outside the solar system. The Earth-like exoplanet was formally known as Gliese 581g after its parent star; Vogt nicknamed it Zarmina's World after his wife. But a rival group of planet hunters deflated the claim by declaring that its measurements had failed to confirm Vogt's discovery.

Now, in a paper published online in *Astronomische Nachrichten* last week, Vogt and his colleagues conclude that their own analysis of their critics' data shows that Gliese 581g exists after all. The skeptics' model showing no planet in its orbit did not take all of the data into account, they say.

But the other group, led by Michel Mayor of the Geneva Observatory, says Vogt's assertions still rest on shaky ground. "Great claims require great evidence, which is not met in Vogt *et al.*'s paper," says Xavier Bonfils, a member of that team and an astronomer at the University of Grenoble in France.

Both teams have been observing Gliese 581—a red dwarf star 20 light-years from Earth—for more than a decade, hunting planets by the "radial velocity" technique: carefully measuring the star's wobble to untangle the dance of different planets whose gravity is pulling on the star as they orbit.

Mayor's group has led the discovery of planets around Gliese 581, using data collected by the HARPS spectrometer mounted on a 3.6-meter telescope in La Silla, Chile. The group is credited with discovering four planets in the Gliese system: 581b, c, d and

e. Vogt's group has followed up on these discoveries using its own observations from the High Resolution Echelle Spectrometer (HIRES) on the Keck telescope atop Mauna Kea in Hawaii.

In September 2010, Vogt and his colleagues announced that they had analyzed a combination of HIRES and HARPS data and discovered two additional planets in the system. One had a 445-day period and was the star's outermost planet. The other, 581g, was closer in, with a period of 37 days and a potential surface temperature at which liquid

water—and hence life—could exist. Mayor's group ascribes eccentric orbits to the four planets not in dispute, which would make the system inherently unstable. "Using circular orbits produces a much better fit with their data," Vogt says.

More troubling, Vogt says, was that his group could reproduce the other team's analytical results only by removing five points from the radial velocity data set. "We conclude that certain key points were specifically excluded from their analysis that contained evidence for other planets in the system," Vogt says. Bonfils says his group didn't

omit points but weighted the data differently from Vogt.

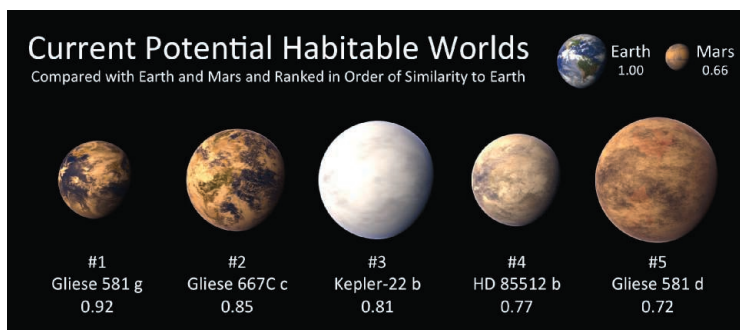
Bonfils says his group's analysis is sound. "We would be glad and proud if our HARPS program unveiled an additional planet around Gliese 581—all the more so if the planet were of low mass and in the star's habitable zone." Unfortunately, Bonfils says, the nearly 4% "false alarm probability" in Vogt's new analysis—a measure of the likelihood that the detec-

tion was a false signal—is too high for Gliese 581g's existence to be a credible claim.

Eric Ford, an exoplanet researcher at the University of Florida in Gainesville who is not connected to either study, shares Bonfils's skepticism. Most claims of planetary detection, he notes, come with a false-alarm probability of 1% to 2%. "In my judgment, we do not have extraordinary evidence for the claimed planet Gliese 581g, at least not yet," Ford says.

Vogt says he expects analysis of more data from both HARPS and HIRES observations to strengthen his case for the embattled exo-Earth. In his universe, at least, Zarmina's World is here to stay.

—YUDHIJIT BHATTACHARJEE



Look familiar? In size and temperature, Gliese 581g is the most Earthlike planet astronomers have discovered orbiting another star—if it exists.

water—and hence life—could exist.

Two weeks after the announcement, Mayor's group publicly challenged the claim at an exoplanet conference in Torino, Italy, saying that the HARPS data—considered to be more detailed than the HIRES observations—had not yielded the detections made by Vogt's group. "Most people thought our group screwed up," Vogt says. "We were roundly tarred and feathered."

After Mayor's group published the results of its analysis on the arXiv preprint server a year later, Vogt and his colleagues dug into the paper, which has been submitted to *Astronomy & Astrophysics*. "We found that their model for the system was seriously flawed," Vogt says. For one thing, he says,

BIOMEDICAL RESEARCH

Panel Votes to End Prevention Fund, Cut Economics Studies, Freeze NIH

E-mails ricocheted through a worried research community in Washington, D.C., last week after a House of Representatives panel passed a 2013 spending bill that would freeze the budget of the National Institutes of Health (NIH), impose narrowly targeted cuts and restrictions on agencies that pay for science and health care analysis, and potentially strip \$787 million from the budget of the Centers for Disease Control and Prevention. The draft bill, reflecting hostility to the Administration's 2010 health care law and a desire to trim the Department of Health and Human Services, would wipe out HHS's Agency for Healthcare Research and Quality (AHRQ), a backer of evidence-based medicine. It would also bar NIH from funding about \$200 million in economics studies.

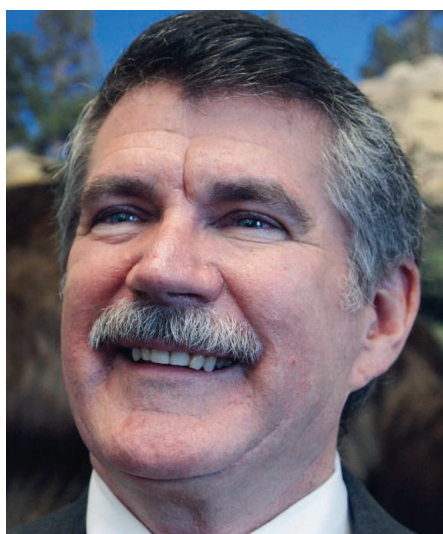
It's a "troubling sign" to have leaders back a sweeping rejection of economics at NIH, says Alan Kraut, executive director of the Association for Psychological Science in Washington, D.C.: "It's this meat ax approach that's so counter to what scientific inquiry is all about." Although the House vote may have caused alarm, observers in the biomedical community say that most, if not all, of the cuts to research will likely be removed before the bill reaches President Barack Obama.

The spending measure, part of the annual budget process, was passed by the House Appropriations Subcommittee on Labor, Health and Human Services, Education, and Related Agencies by an 8-to-6 vote. Its bottom line is consistent with the Administration's: It would provide \$30.6 billion to NIH for 2013, matching the president's request but falling \$100 million below what Senate appropriators have approved. The House bill would deny an Administration-requested increase of \$64 million for NIH's new translational science center, currently at \$575 million per year. At the same time, the bill gives a \$100 million increase (to \$376 million) to the Institutional Development Awards, which helps certain states become more competitive for NIH grants. The president wanted to trim it by \$50 million.

None of NIH's funding can be spent on "any economic research," the bill states. Howard Silver, executive director of the Consortium of Social Science Associations in Washington, D.C., says the provision appears to apply to long-running surveys

on aging and retirement as well as research on health disparities and the costs of illness. "Any research where socioeconomic status, wealth, or income are variables could be banned," he says. In 2009, NIH funded a total of about \$194 million in economics research. "To outright ban certain research makes no sense," says Jennifer Zeitzer, director of legislative relations for the Federation of American Societies for Experimental Biology in Bethesda, Maryland.

Signs of tension appeared as early as March. That's when subcommittee chair



"Why are you involved in economics when we have hundreds of federal agencies that deal with that?"

—REPRESENTATIVE DENNY REHBERG (R-MT),
SPEAKING TO NIH DIRECTOR FRANCIS COLLINS

Representative Denny Rehberg (R-MT) asked NIH Director Francis Collins about \$2.5 million in healthcare economics grants funded by NIH's Common Fund. "Why are you involved in economics when we have hundreds of federal agencies that deal with that?" Rehberg said. He thought NIH should concentrate on basic research. Kraut points out that NIH's economics grantees have included many researchers who work at the "intersection of behavioral and social sciences and neuroscience," such as Princeton University psychologist Daniel Kahneman,

a Nobel Prize winner in economics.

Several "prescriptive" policies in the bill would erode flexibility that NIH needs in tight fiscal times, says David Moore, senior director of government relations at the Association of American Medical Colleges (AAMC) in Washington, D.C. One directive would require NIH to certify to the HHS secretary that every grant it funds is of "scientific value" and will impact public health. That seems unneeded, Zeitzer says—it's what NIH's peer-review process is for.

The bill would also abolish the \$405 million AHRQ, which funds studies of the value of medical treatments. The AHRQ-supported Preventive Services Task Force, an independent advisory group that evaluates screening tests and other methods of identifying people with disease risks, would be transferred to another HHS office. In a statement, AAMC President Darrell Kirch called the proposal "particularly troubling" because of the importance of AHRQ's work in areas such as patient safety and health disparities.

Also targeted in the bill is all HHS discretionary funding for patient-centered outcomes research. The new Patient-Centered Outcomes Research Institute (PCORI) created by the health care bill would lose \$150 million of its projected \$320 million 2013 budget. In addition, because the bill zeroes out the HHS Prevention and Public Health Fund, approved as part of the 2010 health care act, the collateral loss would trim \$787 million from the budget of the Centers for Disease Control and Prevention. The Administration had proposed drawing on this fund for \$80 million in Alzheimer's research at NIH as well. If the bill passed, that research might have to be cancelled or funded by cuts elsewhere.

Rehberg said in a statement that the bill eliminates "duplicative and ineffective programs," referring specifically to the work of AHRQ and PCORI. Rehberg also claimed the bill gives NIH an extra \$675 million for basic research because it blocks a "tap" on the agency's budget used to fund other HHS programs. Lobbyists are hoping the cuts will be removed later in the legislative process, such as when the House and Senate reconcile their spending plans. Traditionally, the House subcommittee bill isn't changed much by the full Appropriations Committee, and lobbyists say interparty skirmishes could keep it from reaching the House floor anytime soon. As time runs short at year end, Congress may wrap a number of agency funding proposals into a single spending bill or even approve a broad continuing resolution that puts off specific actions until 2013.

—JOCELYN KAISER



CLIMATE CHANGE

Using Radiocarbon to Go Beyond Good Faith in Measuring CO₂ Emissions

PARIS—Many parts of the world have seen a long, hot summer—it's been the hottest year to date in the United States—and it isn't over yet. Climate experts are cautious about attributing short-term weather fluctuations to long-term global warming, but the heat helps highlight the scientific consensus that Earth's atmosphere is warming, and that human activity has a lot to do with it. While politicians worldwide debate how—and even whether—to control greenhouse gas emissions, researchers are asking a seemingly more basic question: How can they best measure such emissions, most importantly of CO₂ from the burning of fossil fuels? That's crucial for verifying any targets for reducing emissions.

At a meeting of radiocarbon experts held here earlier this month,* attendees heard the latest results from an approach many scientists think has the most promise: measuring the proportion of CO₂ in the atmosphere that contains the radioactive isotope carbon-14 (¹⁴CO₂). About one in a trillion CO₂ molecules naturally contain radiocarbon, but the carbon locked up in fossil fuels such as coal and oil has none—it lost all of its radioactivity millions of years ago, because the half-life of ¹⁴C is only 5730 years. So as the amount of CO₂ in the atmosphere from fossil fuels rises, the relative amount of ¹⁴CO₂ is depleted in a measurable way.

Other ways to produce carbon emissions numbers exist, but they are based on estimates

of how much CO₂ is generated by certain activities, such as automobile exhausts or fossil fuel-burning power plants. Those “bottom-up” numbers are provided by individual nations and amount to good-faith estimates that are subject to all kinds of errors, both intentional and unintentional. What's needed, researchers say, are “top-down” determinations based on actual scientific measurements of what's in the atmosphere. Relying solely on bottom-up figures is, a pair of researchers recently commented, “like dieting without weighing oneself” (*Science*, 4 June 2010, p. 1241). Radiocarbon is the “most promising method ... for validating bottom-up estimates,” says geochemist Heather Graven of the University of California, San Diego.

Radiocarbon meetings are usually devoted mostly to the more accurate dating of ancient human events. But the meeting here added an entire session on top-down emission measurements in Europe, North America, Asia, and Africa. Researchers are using aircraft, tall towers, and other means to sample ¹⁴CO₂ in the atmosphere under varying conditions and applying new mathematical models to extrapolate those measurements to estimates of fossil-fuel emissions. The models are also helping to correct for confounding factors, such as exchanges of CO₂ between the atmosphere and the oceans, and emissions from nuclear power plants, which generate ¹⁴C atoms.

“Over the past few years, we have made major progress in the number of sites where high-precision measurements are made,” says chemist John Miller of the U.S.

◀ **High hopes.** Radiocarbon measurements taken by tall towers and aircraft help researchers estimate CO₂ emissions from fossil fuels.

National Oceanic and Atmospheric Administration (NOAA) in Boulder, Colorado. As a result, says Soenke Szidat, a biochemist at the University of Bern in Switzerland, “we are getting close to reliable and credible [CO₂ emission] estimates, which do not depend on political willingness but on scientific measurements.”

The shrinking proportion of ¹⁴CO₂ in the atmosphere due to fossil fuel burning was first discovered in the 1950s by Austrian physicist Hans Suess and is called the “Suess effect” (*Science*, 2 September 1955, p. 415). Using it to monitor CO₂ emissions was first proposed in 2003 by physicist Ingeborg Levin and her colleagues at the University of Heidelberg in Germany. Since then, that group has monitored atmospheric ¹⁴CO₂ in Germany and other sites around the world.

In Paris, Levin presented important results from monitoring stations in the Swiss Alps and in Antarctica, indicating that the ratio of ¹⁴CO₂ to nonradioactive CO₂ is now about 0.5% lower in the Northern Hemisphere than in the Southern Hemisphere—a difference almost entirely due, she and her co-workers conclude, to a “steep increase” of fossil-fuel emissions in the more highly industrialized north. That's a reversal since preindustrial days, Graven says, when tree ring records show that the Southern Hemisphere had less ¹⁴CO₂ because upwelling of deep waters in the southern oceans brought radiocarbon-depleted CO₂ to the surface.

Estimating CO₂ emissions in urban areas, which account for about 75% of fossil-fuel emissions, can be tricky, because wind direction and seasonal variations in fossil-fuel use must be taken into account. And yet such measurements are critical to determining how nations comply with international climate treaties, researchers say.

Although the United States is the only developed nation that never ratified the Kyoto Protocol limiting emissions, NOAA's scientists and others are still working to monitor urban emissions using high towers and aircraft in U.S. cities. In Paris, Jocelyn Turnbull, a climate researcher at the National Isotope Centre in Lower Hutt, New Zealand, described one such pilot project this past spring in Indianapolis, which employed two existing cell-phone towers up to 150 meters high, light aircraft, and automobiles to take air samples at regular intervals. The project was a success, Turnbull said at the meeting, and the city will soon have 12 phone tow-

*21st International Radiocarbon Conference, 9–13 July, Paris.

ers in operation for continued monitoring. The team was surprised, however, to detect a sharp spike in CO₂ emissions at the beginning of June—until researchers realized that the Indianapolis 500 auto race had taken place just a few days before. The spike was due not to the race cars but to the 400,000 spectators who drove to Indianapolis to watch.

Despite more intensive monitoring, however, uncertainties in estimates of fossil-fuel emissions from ¹⁴CO₂ “are still large,”

Turnbull told *Science*, because accurate modeling depends on knowing all possible sources of both radioactive and nonradioactive CO₂. One confounding factor, discussed at the meeting by Graven, is emissions from nuclear power plants, which generate a significant amount of ¹⁴C in regions of Europe, North America, and East Asia where nuclear plants are concentrated, offsetting at least 20% of the reduction in ¹⁴CO₂ due to fossil fuels. But “it’s not a showstopper,” Graven says, espe-

cially if improved databases of nuclear power plant emissions—along with increased transparency and reporting of nuclear activities—are made available to modelers.

Levin agrees: “We urgently need more transparency and accuracy in bottom-up emissions reporting by different countries and the nuclear industry.” Political leaders, Levin adds, “should not make the task [of tracking emissions] more difficult.”

—MICHAEL BALTER

SCIENCE EDUCATION

U.S.’s Best Science and Math Teachers to Get Bonuses

Embracing the recommendations of a presidential advisory board, the U.S. Department of Education is launching a \$100 million program to pay select science and math teachers more money to reward excellence in the classroom. It’s the first step in what the Obama Administration hopes will become a 10,000-strong corps of master teachers working to improve STEM (science, technology, engineering, and mathematics) education in the nation’s elementary and secondary schools. That vision, however, faces stiff resistance in Congress.

The money to start the initiative comes from the department’s Teacher Incentive Fund (TIF). More than 120 school districts are vying for a share of a \$285 million pot in this year’s budget to reward teachers who have the biggest impact on student learning across all subjects.

Such performance-based compensation systems run counter to the usual teachers’ salary structure based on longevity and education, and have been viewed warily by teacher unions. But differential-pay structures are a pillar of the White House’s strategy to improve STEM education. They are seen as a valuable tool for attracting more STEM graduates into the classroom and for reducing the number of good teachers who leave for better-paying jobs outside of education.

Last month, the Education Department announced it was setting aside \$100 million within TIF for districts that want to focus on STEM education. More than 30 districts are expected to compete for those dollars by proposing innovative ways to attract and retain STEM teachers and give them leadership positions within the schools. Proposals were due on 27 July.

The idea for the new initiative comes from a September 2010 report by the President’s Council of Advisors on Science and Technology (PCAST). It called for giv-

ing annual bonuses of \$15,000 to 5% of the nation’s STEM teachers. “It will send a signal to all STEM teachers that their profession is respected,” says the report, which dealt with improving STEM education, “and will encourage them to strive to meet a nationally recognized high bar of excellence.”

Last week, the Obama Administration officially embraced that recommendation by calling on Congress to approve \$1 billion for such a program. It would offer \$20,000

message. “We have to give greater attention to STEM education, and the teacher corps is one good way to do that,” says Wheeler, a former physics teacher.

The president of the American Federation of Teachers, Randi Weingarten, also backs the idea, but with a caveat. “We share the president’s commitment to growing our STEM capacity in schools across the United States,” she says. “But on a national basis, especially in light of current budget constraints, there

have to be real checks and balances to ensure that people are receiving this because of what they know, not who they know.”

The Administration is unlikely to get what it wants from Congress this year. Last week, a House of Representatives spending panel approved a 2013 appropriations bill that contains no money for the RESPECT projects. And Representative John Kline (R-

MN), who chairs the House of Representatives committee that oversees the Education Department, has been a fierce opponent of the administration’s push for targeted new programs. Asked to comment on the teacher corps initiative, a Kline spokesperson reiterated his reaction to a government report earlier this year that tallied the hundreds of existing federal programs aimed at improving STEM education. “Investing in science, technology, engineering, and mathematics is a worthwhile endeavor,” Kline said then, “but pumping billions of dollars into programs that may be duplicative or unproductive is just plain foolish.”

—JEFFREY MERVIS

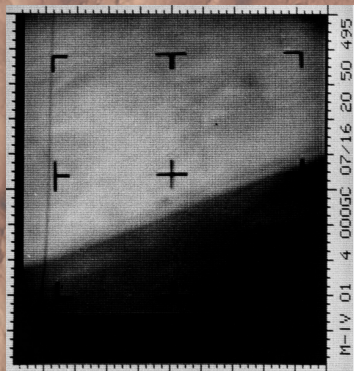


Active learning. Good teachers find fresh ways to engage students.

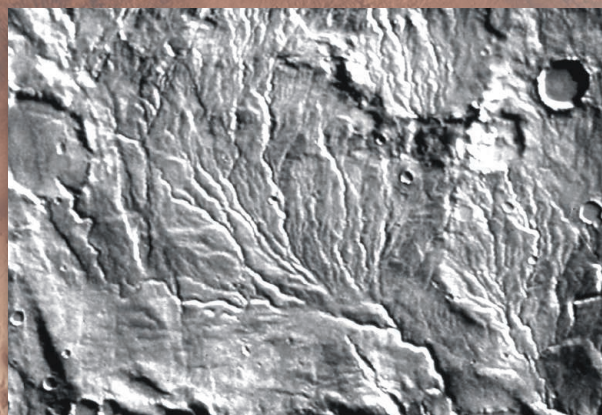
bonuses to teachers, starting with 50 teachers in each of 50 locations. The money would come from a \$5 billion initiative in the Education Department’s 2013 budget proposal that goes by the clunky acronym RESPECT (Recognizing Educational Success, Professional Excellence, and Collaborative Teaching).

“I think that school districts are more than ready for this idea,” Education Secretary Arne Duncan told reporters. “There have been pockets of creativity, but until now there has been a lack of resources.”

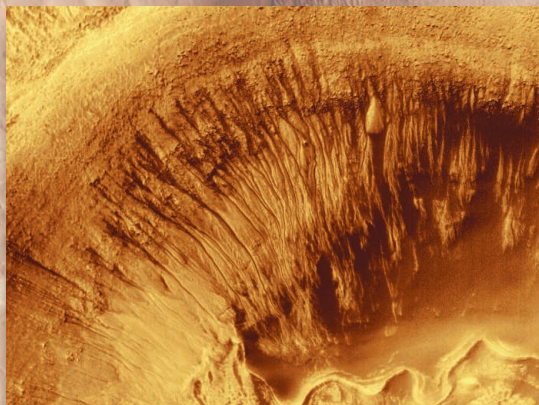
Gerry Wheeler, interim executive director of the National Science Teachers Association, thinks the extra pay would send an important



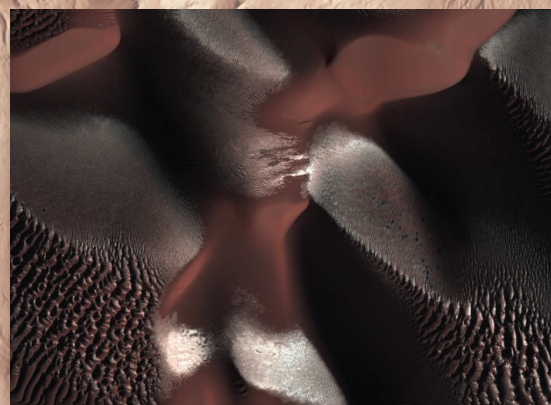
Mariner 4, 1965



Viking Orbiter, 1979



Mars Global Surveyor, 2000



Mars Reconnaissance Orbiter, 2006

Planetary Science Is Busting Budgets

A predictable escalation of the exploration of Mars has collided with limited funding, pushing Mars science into the arms of the astronauts

Exploration of the solar system over the past 50 years has been a natural progression: First, swiftly fly by your favorite planetary body, then give it its first spacecraft in orbit to map it globally, put its first rover on the surface, and then return the first rock and soil for exquisitely detailed analysis back on Earth. However natural, though, each first step of the process comes with a bigger price tag.

Mars, with its tantalizing hints of life, has been a favorite target of spacefaring nations, so it has all its firsts but one. After a barrage of flybys, orbiters, landers, and rovers, a U.S. consensus committee has recommended the return of rock and soil samples as the next logical step for Mars and indeed the highest—and by far the most expensive—priority in solar system science. Sample return also neatly answers NASA's long-standing call for new missions to be "aspirational" (read: big-

ger and better by an order of magnitude and going where no one has gone before).

But with budget cutting at a fever pitch in Washington, even Mars sample return is no shoo-in. Next month a NASA committee will report on how the cash-strapped space agency might proceed with the exploration of Mars. Ominously, all the options will involve hitching planetary science to human spaceflight—a chancy proposition. The outcome could determine whether Mars, or any planetary body, will rate one of NASA's multibillion-dollar "flagship" missions in the next decade.

Next step, please

Mars has certainly been done to death, at least up to a point. The first flyby of Mars came with Mariner 4 in 1965, an \$83 million

spacecraft (\$231 million adjusted for inflation). Mariner 4's 21 images revealed not the crisscrossing canals imagined by earthbound astronomers, but a moonscape of desolate-looking craters. In 1971, Mariner 9 became the first Mars orbiter at a price of \$137 million, revealing yawning chasms, giant volcanoes, and river channels.

Then in 1976, NASA launched an all-out, \$1 billion coordinated assault on the Red Planet with the two Viking pairs of orbiters and landers. The orbiters—sharper eyed than their predecessors—revealed delicate networks of stream valleys, clear signs that water flowed on the surface in ancient times. In the past decade, the sharper view and broader spectral range of orbiting spectrometers turned up a rainbow of water-altered minerals invisible to earlier orbiters. In the past decade, NASA's Opportunity and Spirit rovers have analyzed two such watery sites down to the atomic level.

Following any planetary first, a decline in science return tends to push scientists toward the next stage. Mars orbiters, for example, are showing signs of diminishing returns. The HiRISE camera on NASA's still-active Mars Reconnaissance Orbiter (MRO) returns images in which geologists can discern sur-

Online sciencemag.org

Podcast interview with author Richard A. Kerr (http://scim.ag/pod_6093).

CREDITS (CLOCKWISE FROM TOP LEFT): NASA/JPL; NASA/JPL/USGS; NASA/JPL/CALTECH/UNIVERSITY OF ARIZONA

Downloaded from www.sciencemag.org on July 26, 2012

Better and better. Successive spacecraft have returned increasingly sharp views of Mars.

face features as small as a meter across. Earlier orbiters had imaging resolutions of several tens of meters to a few meters. Mars geologist Michael Carr of the U.S. Geological Survey in Menlo Park, California, who was a team leader on Viking, thinks MRO has been “an outstanding mission,” but HiRISE’s “super-resolution hasn’t grabbed me,” he says. HiRISE images have confirmed hypotheses generated by images from earlier missions and revealed year-to-year changes like new impact craters, but they haven’t driven fundamental changes in the perception of Mars, he says.

Limits are looming as well for spectral imaging of Mars in the search for water-altered minerals, says Mars spectroscopist Philip Christensen of Arizona State University, Tempe, the principal investigator on Surveyor’s spectrometer. Christensen says he would love to fly a souped-up version of the instrument on a future mission. “But is that essential to our understanding of Mars? I think not,” he says. “It wouldn’t be revolutionizing. You can do only so much from orbit, no matter how good your spectrometer. We’re pretty darn close to doing what you can from orbit.”

Despite the declining science return, hundreds of thousands of images and hundreds of terabytes of data returned by five flybys, nine orbiters, three landers, and three rovers have painted a rather clear though broad-brush picture of Mars. The search from orbit has revealed a half-dozen types of ancient watery environments, from river-fed crater lakes to hot-spring deposits. Every one of them could conceivably have harbored early martian life.

To “follow the water” this far, it took 20 increasingly ambitious missions, but it also took increasing amounts of funding. “The progression is up the budget curve,” observes Noel Hinners, a former NASA official and aerospace industry manager. “The price goes up with each stage” from first flyby to first orbiter to first lander or rover.

The price also naturally goes up within a given stage of exploration. The first Mars rover, Sojourner (11 kilograms), ran \$171 million (including a lander) in 1997. The Opportunity and Spirit rovers (185 kilograms each) sent to Mars in 2004 cost about

\$410 million each. Then the lone nuclear-powered Curiosity rover (900 kilograms) that will arrive at Mars on 5 August came to \$2.5 billion.

Decision time

So with likely diminishing returns on mounting investments, what should the next big thing be at Mars, and indeed in planetary science? To decide, a committee of the National Research Council of the U.S. National Academies produced the Planetary Science Decadal Survey in March of last year (*Science*, 11 March 2011, p. 1254). Drawing on a broad polling of the few-thousand-strong U.S. planetary science community, it recommended missions for the next decade in each of the three traditional price tiers: three to five small missions costing half a billion dollars or less each, two medium missions costing \$1 billion or less each, and one multibillion-dollar flagship mission.

The decadal survey’s top-priority flagship mission—and thus the top priority for the solar system—was a rover mission to collect martian samples for eventual return to Earth. But outside cost evaluators gave it a \$3.5 billion price tag. Top priority or not, the committee concluded, that would unduly burden planetary science. The mission cost

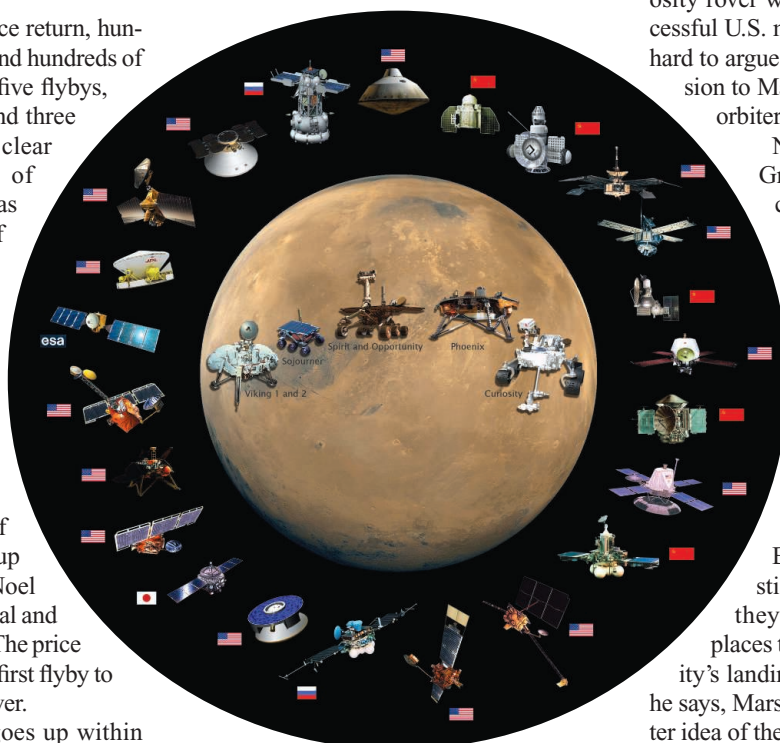
must be whittled down to \$2.5 billion, the committee stipulated; if not, it should be delayed or canceled.

“The plan in the decadal survey was very ambitious,” says space physicist Frances Bagenal of the University of Colorado, Boulder, who has chaired NASA’s Outer Planets Assessment Group. To get the samples it collects into the hands of scientists, the Mars rover recommended for the next decade would have to be followed by two more inevitably flagship-class missions, “each of which would require a considerable miracle,” Bagenal says. One would rocket the collected samples up to Mars orbit and the other would return them to Earth. All told, Mars sample return would run somewhere over \$8 billion, according to the decadal survey. Even if that cost were split equally with international partners, the Mars community was shooting for a big slice of the planetary science pie in the next couple of decades, or nothing at all for Mars. The strategy for Mars exploration had no plan B.

“My colleagues are constantly saying, ‘Phil, why did you do that?’ ” says Christensen, who chaired the Mars panel that recommended sample return to the full decadal committee. They chose the all-or-nothing plan, he says, because that was the only way they saw to keep Mars in the running. If Curiosity rover works, that would make 16 successful U.S. missions to Mars, he notes. “It’s hard to argue we need a 17th or an 18th mission to Mars” if it’s going to be just more orbiters or rovers.

Not everyone agrees. John Grotzinger is not what you would call a dyed-in-the-wool “martian,” having come to Mars research in midcareer from the Precambrian geology of Earth. But he is now Curiosity’s project scientist, and he has some ideas for less ambitious Mars exploration. Rather than going directly to sample return, he suggests two or three “boutique” rover missions in the next decade. Built on the same platform as the still-operating Opportunity rover, they would explore some of the places that were considered for Curiosity’s landing but rejected. After a decade, he says, Mars scientists would have a far better idea of the one spot to pick up samples.

Christensen doesn’t see that option flying. “No one is going to let us keep sending rovers,” he says. “Mars would lose out to other parts of the solar system ... [that] look more attractive. The small [Mars] missions aren’t



Mars Exploration Family Portrait

Successful, or not. By one count, 39 missions have gone to Mars, but about half of the flybys, orbiters, landers, and rovers have failed.

that compelling versus a comet sample return or a Uranus orbiter.” If they had suggested anything but sample return, he says, “we would have been ranked seventh.” With the decadal committee cool to the Mars panel’s smaller, less ambitious options, Christensen’s panel chose sample return. Concluding that it had the highest science return on investment of the contenders, the decadal committee ranked sample return as the highest priority among flagship missions.

Not that Mars sample return is without competitors. Nipping at its heels in the decadal survey ranking are five other flagship missions. The second choice would send an orbiter to Jupiter’s moon Europa—the first outer-planets moon orbiter—to investigate its ice-covered ocean that may harbor life. No new mission to the big moons of Jupiter or Saturn has been initiated in a quarter-century. (An impractically grandiose nuclear-fission-powered mission to orbit three icy jovian moons died in the initial design phase in 2005.) Third was a Uranus orbiter—a first for the outermost planets—with a probe to send into the planet’s atmosphere. The last ranked mission was an either-or: a mission to study the climate of Venus or one to orbit another astrobiological target, Saturn’s moon Enceladus. An Enceladus orbiter was the cheapest of the bunch but still came in at \$1.9 billion.

The big whack

The planetary science community may recommend, but it can’t fund. After adjusting for inflation, Congress’s funding of NASA has been flat the past dozen years. And that plateau is about a third lower than NASA funding in 1969, which was in turn well below 1960s funding as the Apollo program cranked up and the Viking program got started. So planetary scientists were stunned when “the planetary budget got whacked” in President Barack Obama’s fiscal year 2013 budget request to Congress, as NASA Associate Administrator for the Science Mission Directorate John Grunsfeld characterized it. Planetary science’s FY 2012 budget of \$1.5 billion took a 21% cut in the request, with three-quarters of that coming out of the Mars program for a 38.5% cut there.

NASA Administrator Charles Bolden explained that “flagships are expensive (*Science*, 24 February, p. 900). We just could not afford to do another one.” Space policy analyst John Logsdon has a more nuanced explanation of how a big-ticket item can be the first to go. A professor emeritus at George Washington University in Washington, D.C., Logsdon says that in these tight budgetary times, the White House and its Office of Management and Budget (OMB) were looking to hold NASA’s overall budget level. And within a level budget, the Administration had its own science priorities, including earth science missions and the infamously expensive

taking a “reformulation” of its Mars Exploration Program. Next month, the ad hoc Mars Program Planning Group (MPPG), chaired by one-time NASA official Orlando Figueroa, will report to NASA leadership on how robotic exploration of Mars might “remain responsive to the primary scientific goals” of the decadal survey while being “consistent with the President’s [2010] challenge of sending humans to Mars orbit,” according to the MPPG Web site.

In other words, planetary science would be riding human exploration’s coattails to Mars in the FY 2014 budget request. “That is fraught with danger,” Christensen says. “If you attach yourselves to human exploration,”

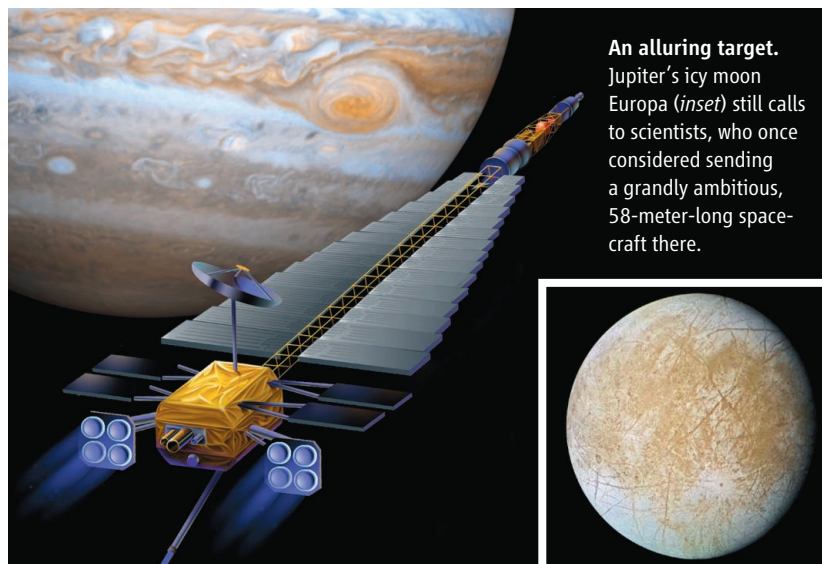
Bagenal says, “you end up tailoring your science to address the needs of human exploration. Then they change their mind. The lunar people have been down that road several times.”

Apollo astronauts did bring back 382 kilograms of moon rocks before Congress changed its mind and cut the program off short of a thorough scientific sampling of the moon. And in the 2000s, President George W. Bush directed NASA to return astronauts to the moon as a way station to Mars. That got scien-

tists a highly capable lunar orbiter, a spectacular “bombing” mission that found water ice, and a small mission to study dust lofted above the moon. Then Obama changed the executive exploration “Vision” to a new path to Mars—an asteroid as astronauts’ way station. That ended NASA’s separate lunar science program.

And then there is the question of just what science would be both consistent with sending humans to Mars and responsive to the decadal survey. Not a lot, it turns out, at least not for putting astronauts in orbit by the 2030s. “The emphasis is mostly on safety and implementation,” says Carr, who co-chaired a group advising NASA’s MPPG. “It’s very different from scientific knowledge.” However, overlap of interests “is substantial” in the area of life, he says, whether it’s potential martian life, the effects of martian dust on humans, or humans’ microbial contamination of Mars. So scientists’ best hope in their search for life in the solar system may well hang on the life we already know about.

—RICHARD A. KERR



replacement for the Hubble Space Telescope, the James Webb Space Telescope.

So “something in planetary science had to give,” Logsdon says. Even though Obama had directed NASA to send astronauts to Mars by the mid-2030s, that something was going to be Mars science. The recommended 2018 sample-collection rover alone loomed large, he says, because OMB, despite independent cost estimates made for the decadal survey, remained leery of that mission’s stated cost. And then there were the inevitable second and third flagship missions to complete sample return; they had no rigorous cost estimates whatsoever. So the ambitious and pricey sample return was just what the budget cutters at OMB were looking for. Or as one planetary scientist puts it, it was “the chicken with the long neck.”

Playing to NASA’s strong suit

But NASA isn’t giving up on Mars. It may have failed to sell the Administration on a big-ticket exploration of Mars in the fiscal year 2013 budget round, but NASA is now under-

Low water mark. The Ili's spring flow was half that needed to maintain ecosystems, Kazakh scientists say.

TRANSBOUNDARY RIVERS

For China and Kazakhstan, No Meeting of the Minds on Water

Kazakh scientists warn that low river flows from China could harm agriculture and aquatic ecosystems; bilateral talks are only treading water

DOBYN STATION, KAZAKHSTAN—Along the Ili River's withering banks, slabs of mud bake under a searing midday sun. A few weeks earlier this muck, swarming with flies, was riverbed. "I've never seen the river so low," says Vasili Gusev, chief of Dobyn Hydrological Station, 52 kilometers west of the Chinese border. The flow here in late spring—236 cubic meters per second—is five times lower than during the same period in 2005, when Gusev and his wife took up residence

and snow have increased at the river's headwaters in the Tian Shan mountains in western China's Xinjiang Uygur Autonomous Region, Chinese data show. Yet in the past several years, the Ili's flow has declined precipitously, says Murat Nurumbetov, a Kazhydromet engineer in Almaty. The "inescapable conclusion," he asserts, is that Xinjiang is drawing more heavily for irrigation, industrial use, and drinking water.

Although China is a party to many international treaties, it has avoided those that would restrict its use of transboundary waters, resource experts say. China "rejects the idea of national integrity, which asserts that states have the right not to be adversely affected in their development potential by activities of the upstream riparian countries," Elizabeth Economy, Asia studies director at the Council on



Vulnerable watershed. Scientists predict that Balkhash will break up into several small lakes if inputs from the Ili River continue to decline.

at this outpost run by Kazhydromet, the agency that manages Kazakhstan's water resources. Fish, once abundant on this languid stretch of river, are now scarce despite a spring fishing ban.

Kazakhstan blames China for the Ili's ebbing vitality. Since the mid-1980s, rain

Foreign Relations, testified before the U.S.-China Economic and Security Review Commission in January.

Transboundary watersheds have been fraught with squabbles. Some concern pollution but most are about water flow. For example, Chinese hydropower dams on the

Lancang River—the Upper Mekong—rile Laos, Cambodia, and Vietnam. And after years of assuring India and Bangladesh that it had no plans to dam the Yarlung Tsangpo River in Tibet, known downstream as the Brahmaputra, 2 years ago China embarked on a hydropower project that it insists will not significantly impede the river's flow.

Tensions are now running high on China's western flank. Under a "Go West" initiative launched in 2000, Chinese leaders have been encouraging citizens to move to Xinjiang. Since then, the arid province's population has shot up from 18.2 million to more than 22 million. China has not been forthcoming about how water resources will keep pace with Xinjiang's growth, asserts Igor Malkovsky, deputy director of the Institute of Geography in Almaty. "China doesn't inform us of the factual situation with the rivers on its side of the border. Nor does it inform us of its plans for the rivers," he claims. But based on remote-sensing and classified data, he says, "we foresee a huge increase in water consumption in China."

The Ili's deterioration is only part of the problem. Another big concern is the diminished Irtysh River to the north. Asia's fifth longest river, the Irtysh wends 4248 kilometers from Mongolia through China then into Kazakhstan and Russia. Human activity is taking a heavy toll on the Irtysh's flow, leaving it and the Ili shadows of their former selves by the time they reach Kazakhstan. That's bad news for 7 million Kazakhs—nearly half of the country's population—who depend on those two rivers and 18 smaller ones that cross the China-Kazakh border, says Zhakyrbay Dostay, a water expert at the Institute of Geography.

The scramble for water is starting to get international attention. “We are now witnessing an unfolding disaster,” says Struan Stevenson, a Scottish member of the European Parliament, who authored a report last year on Central Asia’s environmental problems. “Desertification could be a direct consequence of China’s actions.”

The Ili’s woes in particular could have severe ecological consequences. The river nourishes a delta that empties into one of the world’s great lakes, Balkhash. In recent years, marshlands in the 8000-square-kilometer delta have been beating a rapid retreat. “The area is gradually turning to desert,” Nurumbetov says. Hydrologists forecast that in the coming decade, Balkhash—a shallow lake with an average depth of just under 6 meters—will shrink and grow saltier as inputs from the Ili, which supplies 80% of its water, dwindle. “We predict an ecological catastrophe on the scale of the Aral Sea,” says Malkovsky, referring to a once-vast inland lake on the Kazakhstan-Uzbekistan border. Ravaged by Soviet mismanagement, the Aral Sea has fissured into four smaller, fragile lakes. Worried that Balkhash could meet a similar fate, the Kazakh government is drafting a law that would declare the safeguarding of water resources a matter of national security.

Despite growing apprehension about water scarcity, China and Kazakhstan have made little progress in a decade of talks over water rights, although they continue. At their latest meeting in Beijing earlier this month, Chinese officials asked for more time to come to terms on water-sharing agreements for the Ili and the Irtysh; the deadline has been shifted from the end of 2014 to the end of 2016, according to a Kazakh diplomat in Beijing. The two parties have divergent views on what is fair use. China asserts that water should be allocated by population. “They say, ‘We think it’s fair, we have more people, so we need a bigger share,’” Dostay says. The head of the Chinese delegation to the talks, Liu Weiping, director of the Water Resources and Hydropower Planning and Design General Institute in Beijing, declined to comment for this article, citing the sensitivity of the issue of transboundary rivers in China. Liu referred inquiries to China’s Ministry of Water Resources, which did not respond to requests for comment.

Kazakhstan argues that it is entitled to a share of river flow that at the minimum will sustain aquatic ecosystems and irrigation schemes. However, Malkovsky complains, in the bilateral talks “we don’t have any leverage.”

Ill omens

Shaped like a peapod, Balkhash is the 13th largest lake in the world. It covers 16,000 square kilometers, measuring 600 kilometers from east to west and only 5 to 70 kilometers wide. Located in a desert depression, its eastern half is salty. But the western end, where the Ili flows in, is fresh. How Balkhash maintains this split personality is a mystery, Malkovsky says.

There’s no mystery about what will happen if the 1400-kilometer-long Ili continues



Grim prognosis. As the Ili fades, Dobyin Station could lose its raison d’être, says Vasil Gusev.

to shrivel. “Balkhash’s level will soon begin to fall,” Nurumbetov says. Balkhash at present is stable—and in fact its level has risen in the past few years, says Pavel Propastin, a geographer at Georg August University in Göttingen, Germany, who has studied the Ili River basin. However, he says, Kazakhstan’s concerns are “reasonable.” According to Propastin’s modeling, in a worst-case scenario assuming heavy water use on both sides of the border, Balkhash in the next half-century would break up into several small lakes with a total surface area of less than 5000 square kilometers. That would imperil fisheries. And according to Dostay, enough windblown salt from the desiccated lakebed could melt glaciers in the mountains south of Almaty, possibly altering the climate regime

of Kazakhstan’s most populous city.

A failing Ili “is a nightmare,” says Nurumbetov. “If things continue like this, the river and its ecosystem will die.”

The creation of Kapchagay reservoir 60 kilometers north of Almaty illustrates the exquisite sensitivity of Balkhash to reductions in the Ili’s flow. In 1966, Soviet engineers dammed the Ili to fill Kapchagay. Over the next 20 years, Balkhash’s level fell 1.9 meters, Dostay says, as water flowed into the reservoir, evaporated from its surface, or went to irrigate rice paddies. After Kapchagay reached full capacity in 1987 and most of the Ili’s flow to Balkhash was restored, the lake’s level rebounded by 1.5 meters in a few years, recovering most of the losses.

Soviet authorities also launched massive schemes in the 1960s to divert water from the Irtysh River to irrigate wheat and cotton fields and hydrate military and industrial complexes in what is now northeastern Kazakhstan and southern Siberia. In 1971, Soviet engineers completed the Irtysh-Karaganda canal, which brings water 451 kilometers into the Kazakh heartland.

In 1998, journalists revealed that China had begun excavating a 300-kilometer-long canal in northwestern Xinjiang, to divert water from the Irtysh. “Not only did [China] not notify Kazakhstan or Russia of its plans regarding the Irtysh,” it failed to acknowledge them until they were nearing completion, says Eric Sievers, an environmental lawyer who at that time was advising the Kazakh government on transboundary water issues. Completed in 1999, the Kara Irtysh-Karamay canal now diverts 800 million cubic meters of water per year to Ulungur Lake, from which water is doled out to farms and to Karamay oil field. (In China and Mongolia, the river is known as the Black, or Kara, Irtysh.) Plans call for raising the canal’s capacity to 1 billion cubic meters per year by 2020, or about 15% of the Irtysh’s flow.

A climate change dividend will help offset some of that increased consumption. Climate models predict that higher average temperatures will result in more precipitation in the Kara Irtysh watershed, says Pang Zhonghe, a hydrogeologist at the Institute of Geology and Geophysics of the Chinese Academy of Sciences in Beijing. That’s the case throughout northern Xinjiang, his team reports in the 20 April issue of the *Journal of Hydrology*.

The Ili River basin in Xinjiang is a similar story. The terrain is ringed by mountains to the north, east, and south. They funnel in water from moisture-laden westerly winds, especially during the spring and early summer, says Chen Yaning, a hydrologist at

Xinjiang Institute of Ecology and Geography in Urumqi. The Ili basin gets more precipitation than any other part of Xinjiang, up to 550 millimeters per year. Data from seven meteorological stations accumulated from 1961 to 2007 show a clear increase in precipitation across the basin since the mid-1980s, Chen's team reported in the *Journal of Geographical Sciences* in October 2010. The Ili basin, Pang concurs, should get even wetter as temperatures rise.

It's hard to pinpoint where all this precipitation ends up. "It is difficult to quantify the impact of natural factors on river flow" in Xinjiang, because data are sparse and glacier melting and runoff processes are not fully understood, says Shang Songhao, a hydrologist at Tsinghua University in Beijing. One impediment to independent assessments, says a Chinese hydrologist who works overseas, is that "because of the sensitivity of the negotiations with Kazakhstan, it's very hard to get discharge data now from Xinjiang Water Resources Bureau." The bureau declined to comment for this article. Chen's team has found that across northern Xinjiang as a whole, runoff into rivers in recent years has increased.

If there is indeed a surfeit of water at the Ili's headwaters, China appears to be the sole beneficiary. "We know that less and less water is coming into Kazakhstan, and the water is becoming more polluted," Dostay says. The Kazakh government, he says, estimates that since 1985, the amount of arable land irrigated by the Ili in Xinjiang has tripled to 700,000 hectares. That may be a "considerable overestimate," cautions Propastin, who says the more likely figure is 500,000 hectares.

The long-term prognosis is grim. In the next couple of decades, Propastin warns, rapid melting of Tian Shan glaciers will sharply reduce discharge into the Ili. "The precipitation increase will not compensate for the rapid decrease of glacier water," he predicts.

Running out the clock?

A Chinese delegation came here to Doby in 2009 on a fact-finding mission under the bilateral water agreement. Gusev says he and other Kazhydromet personnel took them by motorboat to examine the river. A few kilometers upstream, the water level was too low for the boat to continue. They abandoned the rest of the inspection. After the Chinese returned home, the Kazakhs observed an uptick in Ili flow. "Maybe the Chinese were embarrassed and released more water," Gusev says. Or it may have been a coincidence: The more robust flow lasted only a few months before

tapering off, Gusev says.

To the Kazakhs, the bilateral talks have largely been an exercise in frustration. In 2006, the two countries agreed to conduct research together and exchange data on transboundary water quality. There hasn't been any joint research, Malkovsky says, and "we have been going around and around on what



Inescapable conclusion? Murat Nurumbetov (top) is convinced that Xinjiang Province is drawing more heavily from transboundary rivers. Water flowing into Kazakhstan is becoming more polluted, says Zhakyrbay Dostay.

data to share." Since 2009, he says, Kazakhstan has been providing China with data on flow rate, pollutants, and other indicators of river health. "We still haven't received anything in return," Malkovsky says.

The talks haven't been a total washout. At the bilateral meeting earlier this month, officials assessed a joint water-diversion scheme serving both sides of the Khorgos River, which demarcates about 100 kilometers of the China-Kazakh border. Kazakhstan can also take solace from having coaxed China to the bargaining table in the first place. This "apparent relative success,"

according to Economy, "may result from the country's value to China as a source of copper and oil." Other downstream nations, she said, "might consider adopting a strategy of linking access to their commodities or energy to Chinese willingness to negotiate water-allocation issues."

China's willingness to negotiate on the critical issue of water usage will be put to the test in the coming months. The signs are discouraging. The two sides are bogged down on which methodology to use to calculate water flow, Dostay says. It's a ridiculous point of contention, he says, because both countries already use standard methodology. Delays work in China's favor, Dostay says: "The longer China postpones resolution of the issues, the more intensive infrastructure development we see on their side of the border," says Malkovsky. Diminished flows then become the baseline for an accord, he notes.

Hoping to pressure China, Stevenson has called on the European Union to hold a conference on transboundary water problems that could focus on the Irtysh and the Ili "as an example of where things can go badly wrong." He also argues that the international community should urge China to sign transboundary water treaties, including the 1997 U.N. Convention on the Law of the Non-Navigational Uses of International Watercourses. But that could backfire. If China can demonstrate that Xinjiang residents depend on the Kara Irtysh-Karamay canal, then it could protect a higher share of Irtysh flow under the convention's "vital human needs" provision.

Kazakh officials have shown no inclination to antagonize China. At the same time, they are weighing new actions at home. "We have options," Malkovsky says. For instance, Kazakhstan is planning to build a Trans-Kazakhstan canal after 2020 that would wring the most usage out of its diminishing water resources.

It's hard to predict how much longer the Ili will remain viable. "The river is nothing like it once was," says Gusev, who was born and raised on the Ili. The minimum spring-time flow necessary to maintain river health, he says, is about 600 cubic meters per second—more than double that measured this spring. Gusev foresees a day when the Ili's level is so low that it won't be worthwhile for Kazhydromet to maintain Doby Station. In that case, he will stay put—but instead of living off the river, Gusev says, "I'll make honey and hunt wild pigs." But even that may not be possible if Kazakhstan and China fail to find a way to overcome their differences and maintain the pulse of the Ili.

—RICHARD STONE

Insulin May Guarantee the Honesty Of Beetle's Massive Horn

Rhinoceros beetles put peacocks to shame when it comes to their sexually selected trait. The head of this apricot-sized insect sports a forked "horn" that can extend to two-thirds of its body length. Males size each other up based on their horns; those with the bigger ones gain access to the females.

Horn size appears to be an honest indicator of male quality: Small male rhinoceros beetles never grow large horns to fool a rival. Biologists have long thought that's because the horns are too physiologically costly for small, undernourished males to build and support. "It's one of the central tenets of sexual-selection theory," says Sara Lewis, an evolutionary biologist at Tufts University in Medford, Massachusetts. But work presented at the meeting shows that, actually, horns are not a very big burden. Instead, the nature of the developmental pathway that leads to horns—and other sexually selected traits related to size—may be what guarantees that these traits are a true reflection of the rival's health and stature, says Douglas Emlen, an evolutionary biologist at the University of Montana in Missoula.

Other researchers are intrigued. Emlen has "got a handle on the mechanistic gears behind the story of how these amazing horns developed in these beetles," says Mark Kirkpatrick, an evolutionary biologist at the University of Texas, Austin.

To find out how much of their bodily resources male beetles devote to their horns, Emlen's graduate student Erin McCullough weighed large and small horns, before and after drying them out. While the head and thorax of a male rhinoceros beetle are 65% water and the legs 55%, the horns were lightweight, only 25% water, she reported at the meeting. All told, a horn makes up less than 3% of the insect's body mass on average.

Next, McCullough looked at how horn size affects flying ability. She positioned dead rhinoceros beetles with and without their horns in a wind tunnel to measure drag. She also clocked the speed of beetles with various sized horns in the wild with a radar gun and measured how far beetles go in a single flight. The beetles fly upright, creating so much drag that having a horn doesn't really make flying

much harder, she reported. Flight speed and endurance were likewise unaffected by having a horn, leading McCullough to conclude that small males wouldn't obviously be disadvantaged if they produced a bigger horn in order to deceive rivals.

Nor did the production of a big horn compromise the growth of other body parts: Males with big horns also had relatively large wings and eyes and developed just as quickly as their smaller peers, she noted. McCullough "did



Honest signal. A rhinoceros beetle horn may reflect how fit the beetle is because its growth is tied to the insulin pathway.

a thorough job of demonstrating clearly that the would-be costs of this enormous structure weren't there," says Adam South, an evolutionary biologist at Harvard University. "I think we might have to revise our theory," McCullough concluded.

Emlen is doing just that. He has long wondered what causes horns and other oversized, sexually selected structures to grow out of proportion with the rest of the body, as long as ample food supplies were available to the growing insect. The signaling pathway involving insulin seemed like a good bet. For 500 million years of evolution, insulin and its interacting proteins have helped cells respond to nutrients, stimulating cell division and tissue growth in good times and shutting down growth when food is scarce. These signals affect the entire body, but if an animal's sexually selected ornaments and weapons were more sensitive to these signals than the rest of the body, then they should grow disproportionately larger in good times and little to not

at all in bad times. An insulin-mediated sensitivity would make the horn a clear indicator of male quality.

Earlier research by Alex Shingleton of Michigan State University in East Lansing had shown that body parts can differ in how they respond to insulin or insulin-like growth factors. In fruit flies, sex organs grow to be the same size no matter how much food is available to the young. They are insensitive to the insulin pathway. In contrast, wings in these insects respond to this pathway such that well-fed individuals not only grow larger, but they also have proportionally larger wings.

Emlen and his colleagues tested the insulin sensitivity of rhinoceros beetles by injecting RNA matching part of the insulin receptor gene into larvae just as they were about to transform into adults. This RNA interfered with the gene's activity, reducing the number of receptors produced and greatly diminishing insulin signaling in growing tissues. The sex organs were the same size in both the RNA-treated and untreated beetles, wings were 2% shorter in the treated beetles, and horns were 16% smaller. Thus horns were eight times more sensitive to insulin signaling than the rest of the body, Emlen reported at the meeting. (His group's work is also described today online in *Science* <http://scim.ag/DEmlen>.)

Because the insulin pathway directly links nutrition to cell growth, it becomes impossible for a malnourished beetle to fake its fitness by growing a big horn. "The insulin [pathway] keeps the signal honest," says Luke Holman, an evolutionary ecologist at Australian National University in Canberra. "Females get what they expect."

Texas Wildflower's Red Keeps It a Species

It's tough to remain a separate species when close relatives live in the same place. That's apparently why a Texas wildflower, the annual phlox (*Phlox drummondii*), has light bluish purple blooms in the central part of the state but takes on a dramatically different hue in eastern Texas. There, it comes into contact with the blue-flowering pointed phlox (*Phlox cuspidata*), and the flowers of the annual phlox have evolved to become deep red. Evolutionary biologist Robin Hopkins, a post-

doctoral fellow at the University of Texas, Austin, has unearthed evidence that this red form persists because it helps keep hybrids from forming between the annual and pointed phlox, and at the meeting she reported that the eastern annual phlox is not as well adapted to its pollinators as the original variety.

Colleagues say that Hopkins's series of results illustrates how two species stay apart through a process called reinforcement. "She went soup to nuts," says Mohamed Noor, an evolutionary biologist at Duke University in Durham, North Carolina. Not only did she show how reinforcement operates, "she went and identified the individual genes that are responsible for it."

In 1889, Alfred Russel Wallace proposed that if hybrids resulting from the mating of two species were inferior, their lack of fitness would favor the evolution of traits in the two species that eliminate hybrids. (And when reinforcement occurs between two subspecies, it can help push them to become fully distinct species.) But documenting this reinforcement process has been difficult. Some researchers have found evidence of reinforcement in laboratory fruit flies, but few studies had been done in a natural setting. "[Hopkins] has identified a system in which she could study it in real time and in nature,"

says Janette Boughman, an evolutionary biologist at Michigan State University in East Lansing.

In 2011, seeking to understand why the eastern Texas annual phlox was red, Hopkins tracked down the genetic basis of the hue change. She found that the variety had mutations that altered the activity of two genes involved in producing the blue color. One genetic change makes the color more intense, leading to darker blooms, though still blue. The second mutation ramps down the production of the blue pigment, resulting in a reddish hue. Together, they produce the deep-red flower.

Hopkins also found that the color change is recessive and the intensity gene is dominant, so any hybrids between any annual phlox and the pointed phlox are dark blue. Previous studies have shown that this dark blue is less attractive to butterflies that pollinate these flowers, so Hopkins looked more closely at how pollinators used these different-colored blossoms. She crossbred the central and eastern Texas annual phlox varieties to get plants with light or dark red or light or dark blue flowers and grew these plants under the same conditions in the field. Sometimes she grew pointed phlox with the annual phlox.

When pointed phlox was present, about 40% of the offspring of the light-colored annual phlox were hybrids with the pointed phlox, while only 10% of the offspring of the dark-flowered forms were, indicating that color intensity, not color per se, was most important for reinforcement to occur. "There's been selection for a flower-color difference in order to reduce hybridization," Boughman says (*Science*, 2 March, p. 1090).

Hopkins has now tackled the question of why the red form hasn't spread beyond eastern Texas. When she grew red and blue annual phlox under the same conditions, the two varieties did equally well in terms of the number of fruits set, she reported at the meeting. But when she looked at pollinator preferences, butterflies favored the light blue over either the dark blue or dark or light red, suggesting an advantage to being light blue. "That may explain why the light blue stays" and why genetic variation is maintained in the annual phlox, she concluded. Although there is a cost for having a dark color, that cost is justified when two phlox species are present.

"She's given us a level of insight into the process of reinforcement that few other studies have done," Boughman says. The work "helps us to understand the process of speciation and the multiple ways in which speciation can happen."

—ELIZABETH PENNISI



By the Skin of Their Teeth >>

In a fast-flowing underground stream in a cave in Ecuador, a 7-centimeter-long catfish holds its own thanks to an unusual sense organ. *Astroblepus pholeter* relies on teeth to sense the water flow around it. Not the teeth in its mouth, but ones sticking out all over the catfish's body, sensory neurobiologist Daphne Soares of the University of Maryland, College Park, reported at the meeting.

Soares has long puzzled over this Ecuadorian fish, which has no functional eyes and doesn't even have a lateral line, a row of specialized hair cells along the sides of most fish that sense vibration and the movement of water. Scanning electron microscopy studies she recently conducted revealed that the catfish's body is covered with bumps that proved to be teeth—complete with enamel and dentine. The teeth protrude through the skin enough that they move back and forth as the animal swims, relaying the surrounding water's movement to the catfish's brain, Soares reported.

When she scraped the teeth off such fish, they swam crookedly, didn't orient to the water flow, and failed to stick to rocks as they normally would. The teeth hook up to a large nerve that in other fish is connected to the lateral line. When Soares examined museum specimens of other catfish, she found that they too have these dermal teeth, but only around the mouth. She thinks that when surface-dwelling catfish first became cave-locked, their lateral line was ill-suited for the high flow and eventually gave way to these dermal teeth.

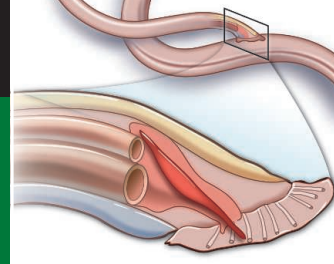
Soares has looked in other caves in Ecuador but thus far has found no other fish with this adaptation. Worried that these teeth-wielding fish may be limited to just one cave, Soares has stopped studying this population and is instead trying to get some protection for it. "It's not listed as endangered, but I think it should be," she said.

—E.P.



Phlox of a different color. Annual phlox (top) evolved a red variety (bottom) so as to keep its species separate from another phlox (inset).

CREDITS (TOP TO BOTTOM): DAPHNE SOARES; ROBIN HOPKINS/UNIVERSITY OF TEXAS, AUSTIN



LETTERS

edited by Jennifer Sills

Pollution in the Yangtze

THE NEWS FOCUS STORY “TROUBLE ON THE YANGTZE” (J. QIU, 20 APRIL, P. 288) HIGHLIGHTS potentially serious consequences of proposed and completed hydropower dams on Yangtze fish and cetaceans. Another important but largely ignored concern is water pollution (1); rising contamination and hydrological changes in the Yangtze are accelerating species losses.

A good example of these endangered Yangtze species is the finless porpoise (*Neophocaena phocaenoides*), which has declined by more than 5% annually for nearly 20 years (2, 3). Yangtze water is heavily polluted by organic and inorganic compounds (such as metals, persistent organic pollutants, and agro-fertilizers) from new large-scale industrial, agricultural, and domestic developments (4). Hydropower impoundment reservoirs (such as Three Gorges Reservoir) have exacerbated water pollution by trapping water and sediment and by increasing eutrophication, resulting in oxygen depletion (5). Heavy metal concentrations, including lead, copper, and cadmium, in Three Gorges Reservoir water have generally increased by more than 25% as the water depth increased (6). Mercury is of particular concern because anoxia promotes release of toxic methyl mercury from contaminated land inundated by rising water (7). Mercury in suspended sediment now exceeds European Union recommendations by a factor of 4 (8).

*Neophocaena phocaenoides*

Despite government cleanup campaigns for inundation areas (including sewerage construction, wastewater treatment, and dump sites), submerged polluted land and expanding human activities still contribute hugely to toxic pollution (9). The Yangtze remains in the top 10 rivers at risk from unprecedented pollution (4). Pollution and habitat changes already have pushed endangered species like the Yangtze porpoise to the edge of extinction (2). We applaud plans to suspend dam construction in the short term, but reducing pollution must be a key objective in river management policy. Without effective action, the recent extinction of the Chinese river dolphin (*Lipotes vexillifer*) (10) may be followed by more species losses.

HONG YANG,^{1,2*} PING XIE,¹ LEVI NI,¹ ROGER J. FLOWER³

¹Donghu Experimental Station of Lake Ecosystems, State Key Laboratory for Freshwater Ecology and Biotechnology of China, Institute of Hydrobiology, Chinese Academy of Sciences, Wuhan 430072, China. ²Geography and Environment, University of Southampton, Southampton, SO17 1BJ, UK. ³Environmental Change Research Centre, Department of Geography, University College London, London, WC1E 6BT, UK.

*To whom correspondence should be addressed. E-mail: hongyanghy@gmail.com

References

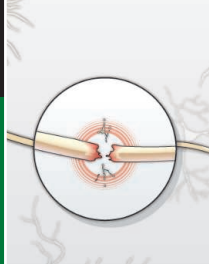
1. J. Liu, J. Diamond, *Nature* **435**, 1179 (2005).
2. D. Wang, *Chin. Sci. Bull.* **54**, 3473 (2009).
3. J. Baillie, C. Hilton-Taylor, S. N. Stuart, *2004 IUCN Red List of Threatened Species: A Global Species Assessment* (IUCN, Gland, Switzerland, 2004).
4. C. M. Wong, C. E. Williams, J. Pittock, U. Collier, P. Schelle, *World's Top 10 Rivers at Risk* (WWF International, Gland, Switzerland, 2007).
5. R. Stone, *Science* **333**, 817 (2011).
6. S. Zhang et al., *Environ. Pollut. Control* **28**, 865 (2006).
7. S. M. Ullrich, T. W. Tanton, S. A. Abdrashitova, *Crit. Rev. Environ. Sci. Technol.* **31**, 241 (2001).
8. B. Mülle et al., *Sci. Total Environ.* **402**, 232 (2008).
9. Q. Zhang, Z. Lou, *Environ. Sci. Policy* **14**, 1132 (2011).
10. S. T. Turvey et al., *Biol. Lett.* **3**, 537 (2007).

Reducing Red Tape for Research in Europe

IN 2010, THOUSANDS OF EUROPEAN researchers signed a petition—the “Trust Researchers” Declaration—calling for less bureaucracy in the funding system (1). They argued that they spent too much time on proposal writing, project management, evaluation, reporting, and audits, and therefore not enough time in labs or in the field.

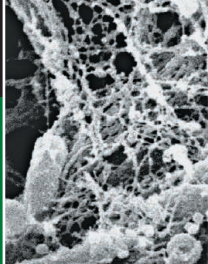
We in the European Commission and the European Parliament are listening. Our research programs should not be designed for accountants and bureaucrats, but for scientists and innovators. We have worked hard to find ways to reduce the administrative burden on Europe’s talented researchers, while remaining fully accountable to the taxpayer. We recognize that clear and simple rules, consistently applied, equal good financial control.

For 18 months, we talked to a range of stakeholders and research communities about the best way to maximize value for our investment in research. These consultations provided valuable input to the new European research and innovation program for the 2013 to 2020 period, named HORIZON 2020, and the financial rules under which it operates. We have already simplified the current research funding program. There is now greater flexibility in how personnel costs are calculated, based on the grant-holders’ usual accounting rules. Small and medium enterprise owners are now entitled to receive a flat-rate reimbursement for their work in the event that they do not receive a formal salary.



Axon self-destruction

418



Defensin nanonets

420

Horizon 2020 brings together all previous EU research and innovation funding instruments under a single program, providing funding for everything from basic research to demonstration and market uptake. The simplified program architecture streamlines access to funds and standardizes rules and criteria for proposal evaluations, intellectual property rights, and eligibility of costs.

In Horizon 2020, the current complex matrix of reimbursement categories will be replaced by a single reimbursement rate per project and a single flat rate for overheads. There will be fewer requirements for timesheets to justify personnel costs. Horizon 2020 will also allow scope for experimenting with alternatives to cost reimbursement. A results-based approach with lump sums for whole projects or the use of inducement prizes would remove the administrative effort for reporting costs incurred. However, such approaches require adequate mechanisms for establishing lump sum payments and for defining measurable deliverables against which the lump-sum or the prize would be paid. Project audits in Horizon 2020 will focus on fraud detection and prevention, rather than detecting and correcting errors as in the past. We hope this shift will lead to a reduction in the audit burden for participants.

The new approach will reduce the time and cost in making applications and reduce the cost to the European Commission of managing the schemes. We aim to cut the time from submission of proposals to signature of the grant agreement by about one-third. This will allow projects to get off the ground much more quickly. It also means that the European taxpayer will be getting more output from their investments as scientists' time is freed up for the real work.

MARIA DA GRAÇA CARVALHO^{1*} AND
MÁIRE GEOGHEGAN-QUINN²

¹European Parliament of the European Union and Rapporteur for the Specific Programme of Horizon 2020, European Parliament, B-1047 Brussels, Belgium. ²European Commission in Brussels responsible for Research, Innovation, and Science, European Commission, B-1049 Brussels, Belgium.

*To whom correspondence should be addressed. E-mail: mariadagraca.carvalho@europarl.europa.eu

Reference

1. Trust Researchers: A Declaration to the Attention of the European Council of Ministers and the Parliament (www.trust-researchers.eu).

Stemming the U.S. HIV Epidemic: Act Local

THE ANNUAL NUMBER OF NEW HIV INFECTIONS in the United States initially declined during the 1980s but has been at a plateau for more than two decades (1). This disappointing situation stands in stark contrast to the declining HIV incidence in several countries in sub-Saharan Africa (2). Prevalence rates among men who have sex with men and in subsets of women of color in the United States exceed those in the general population in countries in sub-Saharan Africa (3).

Inconsistent national targets and a paucity of local targets may be part of the problem. Although the United States has participated in global monitoring of the epidemic via the United Nations General Assembly Special Session (UNGASS) indicators, data from the United States were still unavailable by 2010 for many UNGASS indicators, such as percentage of women and men ages 15 to 49 who received an HIV test in the past 12 months and know their status (4). The CDC's "Healthy People" indicators do not include HIV counseling and testing as an objective, and knowledge of serostatus among HIV-infected persons was dropped from the list in 2010 (5).

In 2010, the United States issued its first National HIV/AIDS Strategy (NHAS),

which includes 5-year national targets, such as reducing the annual number of new infections by 25% (6). In March 2012, to help measure the impact of the NHAS, the Institute of Medicine published a set of national core indicators for HIV clinical care (7), but they focus solely on individuals already identified with HIV infection and receiving clinical services. The County Health Rankings and Roadmaps Program permits assessment of indicators at a more local level but includes only one HIV-related indicator—HIV prevalence (8).

An additional explanation may lie in a lack of targets that focus on identifying those HIV-infected persons not in care or not yet aware of their infection. Only by articulating specific targets with this focus at the state and municipality level, and even at the community level, can we seriously address the HIV emergency in the United States and achieve National HIV Strategy goals. A clinic providing HIV services should not be satisfied with providing high-quality care to those presenting for services at its facilities, but should also seek to identify and reach the estimated number of persons living with HIV in the area it covers. A concrete target, for example, would be an annual 10% increase in the number of individuals identified with HIV infection who are linked and retained in care, until a linkage rate of 90% or more is achieved by that testing site. Another example would be annual targets for the locally appropriate number of new HIV infections within a municipality.

The theme of the recently held XIX International AIDS Conference was "Turning the Tide Together." By acting locally, we can turn the tide of the U.S. epidemic.

JESSICA JUSTMAN* AND WAFAA M EL-SADR

ICAP—Columbia University, Mailman School of Public Health and College of Physicians and Surgeons, Columbia University, New York, NY 10032, USA.

*To whom correspondence should be addressed. E-mail: jj2158@columbia.edu

References

1. H. I. Hall *et al.*, *JAMA* **300**, 520 (2008).
2. UNAIDS Report on the Global AIDS Epidemic 2010 (www.unaids.org/globalreport/Global_report.htm).
3. J. Prejean *et al.*, *PLoS One* **6**, e17502 (2011); published online 3 August 2011.
4. UNGASS Country Progress Report, United States 2010 (http://data.unaids.org/pub/manual/2009/jc1676_core_indicators_2009_en.pdf).
5. CDC, Healthy People 2010 Final Review (www.cdc.gov/nchs/healthy_people/hp2010/hp2010_final_review.htm).
6. The White House Office of National AIDS Policy, National HIV/AIDS Strategy for the United States (July, 2010); www.whitehouse.gov/sites/default/files/uploads/NHAS.pdf.
7. Institute of Medicine, Monitoring HIV Care in the United States: Indicators and Data Systems (March, 2012); www.iom.edu/monitoringhivcare.
8. County Health Rankings and Road Maps (www.countyhealthrankings.org).

Letters to the Editor

Letters (~300 words) discuss material published in *Science* in the past 3 months or matters of general interest. Letters are not acknowledged upon receipt. Whether published in full or in part, Letters are subject to editing for clarity and space. Letters submitted, published, or posted elsewhere, in print or online, will be disqualified. To submit a Letter, go to www.submit2science.org.

PUBLIC HEALTH

Big Tobacco Indicts Itself

Thomas H. Brandon

An author takes a risk in using the word “holocaust.” When employed as a lazy rhetorical tool, the word can trivialize the magnitude of death and suffering inflicted on entire communities and populations during World War II. Robert Proctor (a historian of science at Stanford University) is well aware of the potency of the word he uses to describe the actions of the tobacco industry—responsible for 100 million deaths worldwide during the past century and a projected 1 billion deaths by 2100. He observes that globally smoking causes one excess death for every million cigarettes (the output of a single cigarette-making machine in under an hour). Punctuating the point, he calculates that the tobacco industry kills one person for each \$10,000 in profit. Despite general awareness that tobacco smoking is harmful, the sheer scale of destruction is often not appreciated. Proctor’s *Golden Holocaust* brings it into focus.

A meticulous prosecutor, Proctor details past and present actions of the tobacco industry and its many coconspirators, drawing heavily on over 70 million pages of internal industry documents disclosed as a result of the Master Settlement Agreement of 1998. [Archived by the American Legacy Foundation, these documents are available for public searching at (1).] The nature of the industry’s activities will not surprise the readers: It paid athletes and other celebrities to smoke. While publicly denying that cigarettes were harmful or addictive, it suppressed its own research reaching those very conclusions. It manipulates nicotine delivery to maximize addiction potential. Its filters and “light” cigarettes do not reduce the dangers of smoking. Yet Proctor documents a

breadth and depth of the industry’s duplicitous actions that is nevertheless astounding, as are the numerous direct quotations that he provides to support his indictment:

Hiram Hanmer, the American Tobacco Company’s director of research, recognized in 1953 that filters are “purely a merchandising and sales promotion proposition.” Comments by other industry research directors the same year indicate they knew about addiction and carcinogenesis: “It’s fortunate for us that cigarettes are a habit they can’t break.” “Boy! Wouldn’t it be wonderful if our company was first to produce a cancer-free cigarette. What

we could do to competition!” Describing the goals of the Tobacco Institute’s research grant program in 1970, Helmut Wakeham (Philip Morris’s research director) wrote “Let’s face it. We are interested in evidence which we believe denies the allegation that cigaret smoking causes disease.”

Proctor reserves his greatest scorn for the scientists, academicians, and physicians who aided and abetted the tobacco industry. He discusses industry funding of research at several esteemed academic institutions (e.g., Duke, Harvard, University of California Los Angeles, Sloan-Kettering, and Washington University), and he devotes an entire chap-

ter to the Medical College of Virginia and its seven-decade symbiotic alliance with the American Tobacco Company and Philip Morris. Through such academic partnerships and funding of individual researchers, the industry apparently sought to discredit and obfuscate the science behind the smoking-cancer link and to enhance its own credibility. Until dismantled by the Master Settlement Agreement, industry-created entities such as the Council for Tobacco Research, the Tobacco Institute, and the Center for Indoor Air Research awarded grants for research that posed no risk of harming the industry’s image or profits.

Academics were not alone in their partnerships with tobacco. Proctor reminds us, for example, that the American Medical Association soft-peddled the risks of smoking in return for the industry’s alliance against “socialized medicine.” Serving as a paid expert witness, a former (mid-1990s) president of the American Heart Association denies the link between smoking and disease. Merrell Dow Pharmaceuticals initially backed off its marketing of nicotine chewing gum for smoking cessation when Philip Morris threatened to stop doing business with Dow Chemical. The American Civil Liberties Union accepted tobacco funding and supported the rights of workplace smokers against those of co-workers to breathe clean air. And governments worldwide have become “addicted” to the revenue generated by tobacco taxes.

The author does not spare his own discipline. Historians have testified for the industry in court and have been engaged to write favorable histories of, for example, tobacco use in American life or the medical evidence regarding tobacco and cancer. The industry has also used them to buttress its courtroom argument that the harmful effects of smoking have long been general knowledge (except, apparently, to the industry itself). Proctor attributes roughly 160 annual tobacco-related deaths to the role played by historians in tobacco litigation.

Having build a strong case against the tobacco industry, Proctor calls for the death penalty—a total ban on the sale and manufacture of cigarettes. Such action would be justified on humanitarian grounds, not to mention as suitable punishment for the decades of misdeeds by the industry. How-

Golden Holocaust
Origins of the Cigarette
Catastrophe and the Case
for Abolition

by Robert N. Proctor

University of California Press,
Berkeley, 2012. 772 pp. \$49.95.
£34.95. ISBN 9780520270169.



Truthful ad. Hans Rudi Erdt’s 1912 poster for Turkish cigarettes produced in Berlin.

The reviewer is at the Department of Health Outcomes and Behavior, Moffitt Cancer Center, and the Department of Psychology, University of South Florida, Tampa, FL 33620, USA. E-mail: thomas.brandon@moffitt.org

ever, Proctor gives little attention to the potential societal consequences. Drug prohibitions, exemplified by the ongoing “war on drugs,” do not have a good track record. They usually spawn black markets, organized crime, dangerously adulterated product, and the emergence of other popular substances of abuse. Proctor argues that a tobacco ban would be different because smoking does not provide the immediate pleasurable intoxication of most other addictive drugs and the vast majority of smokers would like to quit. Although reinforcement effects of nicotine are more subtle, they are nevertheless potent. For example, recent evidence suggests that smoking may enhance cognitive performance (2) and restore depleted self-control resources (3). Moreover, nicotine also appears to enhance the reward experienced from other activities (4). The “satisfaction” obtained by smoking appears to be more than merely the relief of unpleasant nicotine withdrawal symptoms (as Proctor suggests), which is why smoking relapse rates are high even long after withdrawal subsides. Historically, the social chaos caused by cigarette rationing in postwar Germany and the “nicotine riots” that ensued in the Soviet Union during cigarette shortages suggest that tobacco prohibition would not come easily. It could be argued, of course, that these social costs are acceptable when weighed against nearly a half-million annual deaths in the United States alone—far more than attributable to all other drugs combined.

As his fall-back position, Proctor advocates a mandated reduction of nicotine content in cigarettes to sub-psychoactive levels along with raising the pH back to levels that discourage smoke inhalation (akin to pipe or cigar smoke and to cigarette smoke before the advent of milder flue-cured tobacco). The Food and Drug Administration, which has had regulatory authority over tobacco products since 2009, is currently funding research on the effects of nicotine reduction in cigarettes. But again the issue is more complex than implied by Proctor, with possible unintended consequences that merit attention (5).

Proctor offers another 18 reasonable recommendations for reducing the burden of tobacco. These include increased taxes (on cigarettes and cigarette-making machines), a complete ban on public smoking (indoors and out), bans on marketing and promotion of tobacco, R ratings for films depicting smoking, more-graphic warning labels, and restricting sales to only state-licensed outlets. He also argues that the public health

community must reclaim the rhetorical high ground through language that does justice to the unparalleled human toll exacted by the tobacco industry. Ergo the title of his book.

References

1. <http://legacy.library.ucsf.edu>.
2. D. E. Evans, D. J. Drobes, *Addict. Biol.* **14**, 32 (2009).
3. B. W. Heckman, J. W. Ditte, T. H. Brandon, *J. Abnorm. Psychol.* **121**, 244 (2012).
4. P. J. Kenny, A. Markou, *Neuropsychopharmacology* **31**, 1203 (2006).
5. D. K. Hatsukami et al., *Tob. Control* **19**, e1 (2010).

10.1126/science.1222146

PUBLIC HEALTH

At Work to Save Lives

Jerry C. H. Tam

On 26 August 1976, a schoolteacher in Yambuku, Zaire (now Democratic Republic of Congo), came to a hospital with a raging fever similar to malaria but with hemorrhagic symptoms. His was the first case in an erupting epidemic in which over 80% of those infected died. In mid-

October, Peter Piot, a junior member of a small lab in Belgium, was sent to the epicenter of the new disease, where he worked as part of the team that identified and named the causative agent—Ebola. Five years later, reports of impaired

immunity leading to opportunistic infections, with a link to Kaposi's sarcoma, were released. Human immunodeficiency virus (HIV) would soon become one of the worst pandemics in human history and central to Piot's work. *No Time to Lose's* subtitle, *A Life in Pursuit of Deadly Viruses*, is definitely well deserved.

In the preface, Piot warns that the book is not an autobiography or a history of the discovery of Ebola and HIV. Nor is the book filled with details about the viruses themselves. Instead, he offers a whistle-stop overview of the human side of these epidemics, the several roles he has filled (clinician, scientist, activist, and politician), and a sense of the importance of cooperation among these groups. Although these roles are often seen

as separate (even antagonistic), Piot reminds us that, especially with the AIDS pandemic, all are important to bring about desired outcomes: “Science without politics has no impact, politics without science can be dangerous, and without programs people don't benefit.” With his experiences—as an early investigator of these diseases, worker on Project SIDA, president of the International AIDS Society, assistant director of the World Health Organization's Global Programme on AIDS, and founding executive director of UNAIDS—Piot is well placed to comment on the struggles and successes of balancing the various roles while remaining true to the aim of saving lives.

While presenting extremely candid views of his interactions with the frontline workers, bureaucrats, activists, politicians, and religious leaders, Piot always recognizes that the medical disasters could bring out the best or worst of people in those positions. Refreshingly, he doesn't present developments as mere historical facts but provides insights into the emotions that drove the actions of many dedicated people. Toward the end of the book, Piot reminds us that the struggle against AIDS is still far from over. In addition, we face the challenges of future emerging pathogens as well as pandemic noncommunicable diseases (e.g., obesity and cancer).

The author's philosophy on global health can be best described using a quote attributed to neurosurgeon Harvey Cushing: “A physician is obligated to consider more than a diseased organ, more even than the whole man—he must view the man in his world.” Throughout this book, readers will encounter the ethos of collecting good, accurate data while understanding the culture and practices of the people involved—a mixture of quantitative and qualitative research. That is highlighted in several narratives about what Piot found on his travels, such as the way that funeral practices in Zaire contributed to the spread of Ebola. Clearly these same principles of understanding people should also be applied to other aspects of health and international development, not just to communicable diseases.

No Time to Lose contains strong lessons about attitudes to health and societal problems. The book also provides a very personal account, focusing on the lives of those in the front line against deadly viral diseases and those involved in policy-making. But above all, it offers an inspirational account of one person's career and how Piot's following his heart on science, integrity, and justice helped change our world for the better.

10.1126/science.1224879

No Time to Lose A Life in Pursuit of Deadly Viruses by Peter Piot

Norton, New York, 2012.
415 pp. \$28.95, C\$31, £17.99.
ISBN 9780393063165.

The reviewer is at the Medical Research Council Laboratory of Molecular Biology, Hills Road, Cambridge CB2 0QH, UK.
E-mail: jtam@mrc-lmb.cam.ac.uk

Challenges to India's Pharmaceutical Patent Laws

Bhaven N. Sampat,^{1*} Kenneth C. Shadlen,² Tahir M. Amin^{3,4}

The Indian Supreme Court will soon hear final arguments in a challenge by the pharmaceutical company Novartis against the Indian Patent Office's (IPO) rejection of a patent for the leukemia drug Glivec. We discuss key issues, particularly the patentability of new compounds versus variants of existing compounds, and how the outcome of the case might affect patent terms and access to drugs in the developing world.

The World Trade Organization's (WTO's) Agreement on Trade-Related Aspects of Intellectual Property Rights (TRIPS), in effect since 1995, requires all WTO countries to allow patenting of pharmaceutical products and processes. Global extension of pharmaceutical patents, which will be the effect of

until 2005. India also introduced a clause designed to restrict the number and type of pharmaceutical patents granted: Section 3(d) of the Patent Act prohibits patents on variants of existing compounds that do not show enhanced efficacy.

Section 3(d) has been extremely contentious since its introduction in 2005. The transnational pharmaceutical industry and the U.S.-India Business Council regard it as establishing an unacceptably high barrier to patenting (1, 2). Echoing this criticism, the U.S. Trade Representative regularly cites 3(d) among reasons to keep India on its list of countries whose intellectual property regimes are of concern (3). But many observers, including the United Nations Programme

An Indian Supreme Court decision about variants of existing compounds could affect access to affordable drugs.

that section 3(d) has in India's ability to supply low-cost generic pharmaceuticals domestically and abroad (6).

Evergreening, Patent Policy, and Glivec

The core issue in this debate is not whether newly discovered molecules will be protected by patents in India or open for generic production. Rather, the main issues are whether and how countries with newly introduced pharmaceutical patent regimes limit "evergreening" of existing molecules and patent portfolios. Evergreening is a term used to describe the sequential accumulation of secondary patents on drugs, including alternative forms of active ingredients, new formulations, dosages, and uses (9). Pharmaceutical companies refer to this as "life-cycle management" (10). Because secondary patents tend to be filed later in the life of a drug than primary chemical compound patents, they can extend monopoly terms (11). Some scholars argue that innovative efforts associated with secondary patents are less substantial, although that is subject to debate (5). There is broader agreement that secondary patents are less likely to satisfy traditional patentability criteria and thus are more vulnerable legally (5, 12).

Across industries, in developed and developing countries, policy-makers wrestle with how to weed out "low-quality" patents (13). In the United States, the Hatch-Waxman Act of 1984 provides financial incentives for generic firms to identify and challenge pharmaceutical patents that they believe were improperly issued by the U.S. Patent and Trademark Office. Challenges disproportionately target secondary patents and appear to be successful: Despite the proliferation of secondary patents and expansion of nominal patent terms since Hatch-Waxman (11), the time to generic entry in the United States has remained fairly stable (9).

In the United States, then, litigation constitutes an ex post way to subject legally questionable patents to a strong second look and thus curb evergreening. India, in contrast, has adopted an ex ante mechanism: Section 3(d) attempts to scrutinize secondary patents preemptively, before they are issued (14). Apart from timing, 3(d) differs

... Hatch-Waxman challenge provisions and 3(d) [of India's Patent Act] ... aim to prevent low-quality patents from delaying generic entry.

TRIPS when fully implemented over various transition periods by all WTO members, has fueled concerns about drug prices and, subsequently, access to lifesaving medications.

The introduction of pharmaceutical patents in India has been particularly controversial. Indian producers have long been suppliers of low-cost medicines (including key HIV/AIDS treatments), domestically and also to other low- and middle-income countries. In amending its patent law to meet new international obligations, India, like many developing countries, attempted to take advantage of flexibilities in TRIPS to ameliorate potentially negative effects that pharmaceutical patents might have on the supply of medicines. India used its full transition period, waiting to introduce pharmaceutical product patents until 2005 (pharmaceutical process patents were already available prior to TRIPS). Applications dating from 1995 onward were received but were not examined

on HIV/AIDS (UNAIDS) and civil society groups, defend 3(d) and point to India as a model for developing countries attempting to use TRIPS flexibilities to promote public health (4–6).

In 2006, the IPO, citing 3(d), rejected Novartis's application for a patent on a crystalline form of Glivec's basic compound, imatinib mesylate. Glivec is widely recognized as having revolutionized treatment of chronic myeloid leukemia and demonstrated the potential for targeted drug development (7). As a result of the IPO's decision, Glivec is not protected by a patent in India.

Novartis appealed against the rejection, and the case has worked its way to the Supreme Court. Although the case is meant to determine whether the rejection was appropriate, the broader issues of how the IPO interprets and applies 3(d), and the validity of the provision itself, are likely to be considered by the court, making the case a referendum on 3(d). Novartis, making its case before the court of public opinion, has emphasized that the drug has received patents in more than 40 other countries, implying that if even Glivec cannot be patented in India, 3(d) must be setting unreasonable standards (8). Meanwhile, civil society groups have called on Novartis to drop the suit, emphasizing the crucial role

¹Health Policy and Management, Columbia University, New York, NY 10032, USA. ²International Development, London School of Economics (LSE), London WC2A 2AE, UK. ³Initiative for Medicines, Access, and Knowledge, New York, NY 10016, USA. ⁴Department of Global Health and Social Medicine, Harvard Medical School, Boston, MA 02115, USA.

*Author for correspondence. E-mail: bns3@columbia.edu

from the U.S. approach in that it relies on tests of efficacy in addition to the traditional “novelty” and “inventive step” standards to determine whether variants on old molecules receive patents.

Notwithstanding differences in form, Hatch-Waxman challenge provisions and 3(d) share the same goal: Both aim to prevent low-quality patents from delaying generic entry. Indeed, their effects may be similar, as Glivec itself illustrates. The same patent at issue in the Novartis case in India was the target of a Hatch-Waxman challenge in the United States in 2007 (15). Novartis does not appear to be litigating in response to this challenge, which suggests that it accepts the patent as questionable even in the United States. It is noteworthy that in the United States (and elsewhere), Novartis has an earlier patent on the drug’s basic compound, filed in 1993, which protects Glivec until 2015. This earlier application was not filed in India because India did not grant pharmaceutical products patents before TRIPS and does not recognize pre-1995 applications. In the absence of this primary patent, the only protection possible for Glivec in India would be via the secondary patents that cover alternative structural forms of the base molecule.

As a case study, Glivec is peculiar and unlikely to be representative going forward. Had it been invented a few years later (or TRIPS implemented a few years earlier), Glivec likely would be patented in India, even under 3(d) standards. Newly discovered compounds are likely to receive basic patents and to be less vulnerable to 3(d) rejections.

In the short term, whether drugs whose primary patents predate TRIPS receive any patent protection in India—and thus whether low-cost generic provision of these drugs for patients in India and abroad remains possible—may turn on whether 3(d) stands or falls. Applications for secondary patents on these drugs are vulnerable to rejections based on this provision. However, the long-term effects of 3(d) are likely to differ. Most new drugs typically have primary (compound) patents (11). For these drugs, the effects of 3(d) will be on the length of effective patent terms, not the existence of patents. Because of 3(d), consumers may benefit from generic competition on these drugs sooner, but they will not be able to count on the denial of patents altogether.

Laws on the Books Versus Laws in Practice

Although Novartis and its allies see a problem of false-positives, where 3(d) is applied injudiciously to deny patent protection to innovative drugs, another concern is poten-

INDIAN PATENT OFFICE OUTCOMES	
Outcome	Number
Granted	75
Pending	79
Withdrawn	35
Rejected	25
• on grounds including 3(d)	16
• exclusively on 3(d) grounds	3
• on grounds other than 3(d)	6

Indian Patent Office Outcomes. As of March 2012, outcomes for 214 Indian patent applications associated with drugs approved for U.S. marketing between 1996 and 2004. See the Supplementary Materials for details.

tial false-negatives: that the IPO, under severe resource constraints and pressures to clear applications (16), may not be well positioned to deploy 3(d) with sufficient robustness to block patents that perhaps should not be granted (17). Indeed, data on a set of 214 Indian patent applications associated with drugs approved by the U.S. Food and Drug Administration between 1996 and 2004 indicate that only 19 had rejections on 3(d) grounds (see the table). In 16 of the cases where there was a 3(d) rejection, the decision cited other grounds as well, which suggests that these may have faced difficulties even without 3(d). Although it is difficult to know what share of application withdrawals were responses to 3(d) rejections, or the extent to which granted patents had their scope narrowed because of 3(d), the data suggest that outright refusals based on the provision are surprisingly rare.

The issues that emerge from an assessment of 3(d) as insufficiently effective relate to broader challenges in patent policy. Arguments that applications should be rejected because of 3(d) are often brought to the attention of the IPO through third-party “oppositions” that provide a rationale for why a drug should not be patented (18). But oppositions are public goods and subject to coordination problems among and between civil society groups and generic firms.

The Supreme Court is expected to clarify exactly how and when 3(d) will be applied—and perhaps how terms such as “efficacy” should be understood (19). The IPO may need more than just clarity. Increased resources may be necessary, not only for proper implementation of 3(d) but also for improving patent examination in general. In addition to reducing the grant of low-quality patents, which would benefit generics and consumers, more resources would increase examination speed, which would benefit patenting

firms. Increased funding for the IPO implies reallocation of resources from other areas, and thus is easier said than done, but it is an area where pharmaceutical firms (patent-based and generic) and treatment advocates may find common ground.

How might limitations on secondary patents in India affect pharmaceutical innovation, generic competition, and, subsequently, prices and utilization? Accepting that restrictions on evergreening are desirable (as other countries do) raises questions of institutional design: How high should standards for patentability be? Where in the patent process should they be implemented? How much should be invested in their functioning? These issues, straightforward to enumerate although difficult to answer, are important not only in India but also in other developing (and developed) countries aiming to improve patent examination and to balance innovation and access.

References and Notes

1. Pharmaceutical Research and Manufacturers of America, Special 301 Submission (PhRMA, Washington, DC, 2010).
2. U.S.-India Business Council, *The Value of Incremental Pharmaceutical Innovation: Benefits for Indian Patients and Indian Businesses* (USIBC, Washington, DC, 2009).
3. Office of the U.S. Trade Representative, Special 301 Reports, 2010–2012 (USTR, Washington, DC, 2012).
4. UNAIDS, *DOHA+10: TRIPS Flexibilities and Access to Anti-retroviral Therapy: Lessons from the Past, Opportunities for the Future* (UNAIDS, Geneva, 2011).
5. C. Correa, *Guidelines for the Examination of Pharmaceutical Patents: Developing a Public Health Perspective* (WHO-ICTSD-UNCTAD, Geneva, 2007).
6. K. Grogan, *PharmaTimes*, 24 February 2012.
7. L. Pray, *Nat. Educ.* **1**, 565 (2008).
8. Novartis, Glivec Patent Case in India: Fact vs. Fiction; www.novartis.com/downloads/newsroom/glivec-information-center/Fact_vs_fiction_of_Glivec_India_Case.pdf.
9. C. S. Hemphill, B. N. Sampat, *J. Health Econ.* **31**, 327 (2012).
10. M. E. Furrow, *Food Drug Law J.* **63**, 275 (2008).
11. S. Hemphill, B. N. Sampat, *J. Empir. Legal Stud.* **8**, 613 (2011).
12. R. Eisenberg, *Lewis & Clark Law Rev.* **12**, 375 (2008).
13. A. Jaffe, J. Lerner, *Innovation and Its Discontents: How Our Broken Patent System Is Endangering Innovation and Progress, and What to Do About It* (Princeton Univ. Press, Princeton, NJ, 2006).
14. Patents can be revoked using 3(d) as well, via postgrant opposition.
15. ParagraphFour.com, Gleevec (imatinib) tablets; www.paragraphfour.com.
16. A. Kapczynski, *Calif. Law Rev.* **97**, 1571 (2009).
17. C. H. Unnikrishnan, LiveMint.com, 10 December 2008; www.livemint.com/2008/12/10000020/India-granting-drug-patents-fo.html.
18. S. Basheer, Patent Oppositions in India: The “Efficacy” of Section 3(d); www.spicyipindia.blogspot.com/2009/09/patent-oppositions-in-india-efficacy-of.html.
19. S. Basheer, P. Reddy, *SCRIPTed* **5**(2), 232 (2008); www.law.ed.ac.uk/ahrc/script-ed/vol5-2/basheer.asp.

Acknowledgments: An LSE-Columbia Seed Research Grant and the Robert Wood Johnson Foundation’s Public Health Law Research Program supported this research. We thank S. Hemphill for his comments on the manuscript.

Supplementary Materials

www.sciencemag.org/cgi/content/full/science.1224892/DC1

10.1126/science.1224892

NEUROSCIENCE

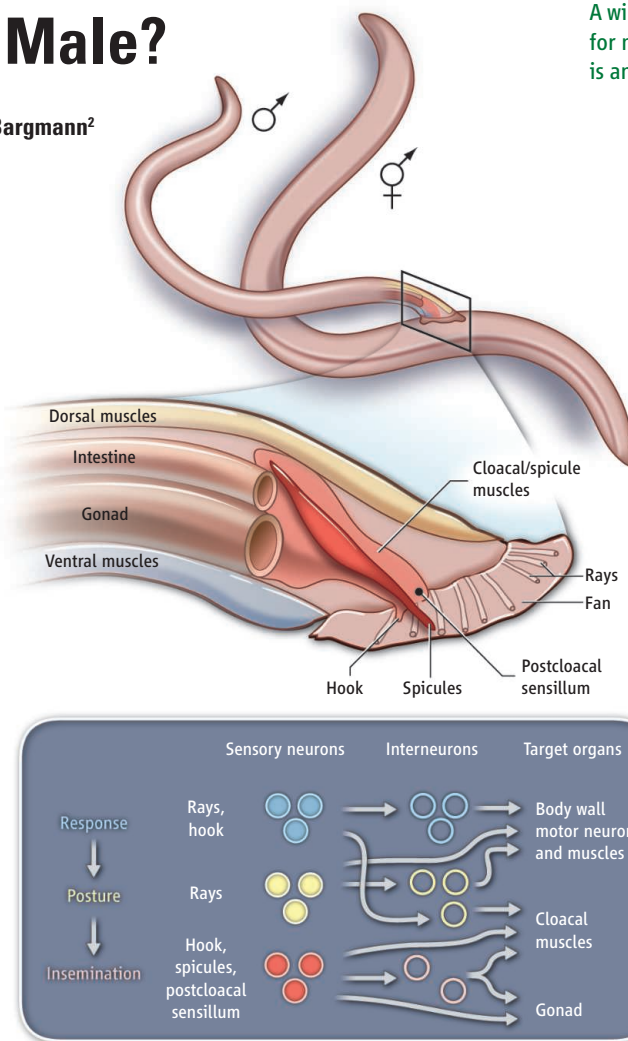
The Mind of a Male?

Dmitri B. Chklovskii¹ and Cornelia I. Bargmann²

When a major computer chip manufacturer brings a new integrated circuit to the market, its competitors often rush to reverse-engineer the chip to understand how it works. They shave off thin layers of the semiconductor material while imaging each newly revealed surface under an electron microscope. By tracing the wires in the electron micrographs, computer engineers assemble the wiring diagram of the chip, which allows them to eventually deduce its function. Similarly, neuroscientists hope to gain insights into the way the nervous system generates behavior by reconstructing its wiring diagram. Like the solid-state wires in computer chips, biological “wires” that carry electrical signals are tens of nanometers in diameter, requiring electron microscopes and ultrathin sectioning to image them. On page 437 of this issue, Jarrell *et al.* (1) use this approach to reconstruct the nervous system in the tail of a male *Caenorhabditis elegans* roundworm.

Why did they choose this seemingly exotic circuit to reconstruct? *C. elegans* is less than 1 mm long, and the subsystem in question contains only 170 neurons and 64 muscles, making complete reconstruction possible. Yet the mating behavior of the *C. elegans* male is considered the most complex innate behavior of the animal and has interesting decision-making features (2). Previous circuit reconstructions of *C. elegans* hermaphrodites (essentially females) (3, 4) showed that their wiring is largely stereotyped, allowing comparisons between individuals and sexes. The male worm chosen for reconstruction was fixed and sectioned decades ago, by the same group that performed the early hermaphrodite reconstructions (4); this choice aids com-

¹Howard Hughes Medical Institute, Janelia Farm Research Campus, Ashburn, VA 20147, USA. ²Howard Hughes Medical Institute, The Rockefeller University, New York, NY 10065, USA. E-mail: cori@mail.rockefeller.edu; chklvskiid@janelia.hhmi.org



The mating circuit. The mating structures in the tail of the male worm *C. elegans* are shown. The colors correspond with a simplified summary of the neuronal circuits that control the indicated mating behaviors.

parisons and also hints at the element of black magic that still characterizes sample preparation for electron microscopy.

The elementary building blocks of the nervous system are neurons and synapses. A *C. elegans* male has 383 neurons, compared to 302 in the hermaphrodite; nearly all male-specific neurons are associated with a delicate, fan-shaped mating structure in the tail (see the figure). Accordingly, the tail reconstruction encompasses 81 male-specific neurons as well as 89 neurons that are shared by both sexes. Neurons are classified as sensory neurons based on specialized externally directed structures, as motor neurons if they mainly synapse onto muscles or the gonad, or as interneurons if they mainly form synapses with other neurons. Most male-specific neurons are sensory neurons (52 in the reconstruction); the interneurons are a mix

A wiring diagram of neuronal circuits for mating behaviors in the male worm is anatomically reconstructed and analyzed.

of male-specific and shared, and motor neurons are mostly shared between sexes. This cellular division suggests that mating decisions are driven by specialized sensory input.

Synapses fall into two classes: those that use chemical neurotransmitters to signal between neurons, and gap junctions that form electrical connections between two cells. Chemical synapses are intrinsically directed, whereas gap junctions can be symmetrical or asymmetric. The male tail has as many reconstructed synaptic connections as the entire hermaphrodite nervous system, with a slightly stronger bias toward gap junctions (28% versus 19%). The wiring from start to finish is remarkably compact: About half of the synapses onto muscles come directly from sensory neurons, and most neurons are only one synapse away from a muscle or the gonad. The dominant direction of the synapses is feedforward, from sensory neuron toward muscle. This directionality is supplemented by synapses between different classes of sensory neurons, potentially bidirectional gap junctions, and limited feedback from interneurons.

The wiring diagram of a nervous system can be represented by a graph whose nodes are neurons or muscle, and whose edges are synapses. Jarrell *et al.* reconstruct this graph for the male wiring diagram. Rather than merely counting the number of synapses, as was previously done for the hermaphrodite, they estimate the strength of connections by taking their total size (which can vary by a factor of 100) into account. They then use the graph to formulate both concrete and abstract hypotheses about the logic of the mating circuit. At a concrete level, they identify five modules, or highly connected groups of neurons, and suggest mating-related behaviors that the modules might control: the response to hermaphrodite contact, locomotion, posture (two modules), and insemination. At an abstract level, they analyze the reconstructed wiring diagram using the tools of network science (5): They report degree

and connection strength distributions, find that the network is small-world, and identify its community (module) structure. They find overrepresented connectivity motifs among connected triplets of neurons, including feed-forward motifs, which are also common in the hermaphrodite wiring diagram (6, 7) and the mammalian cortex (8). The broad statistical similarity between these graphs and those reported for the mammalian cortex (8, 9) suggests that fundamental principles of circuit operation gleaned from the worm may help us understand how mammalian brains generate behavior.

The challenge going forward is to convert the reconstruction into detailed knowledge of circuit function. First is the question of what the neurons (nodes) do. Of the 302 neurons of the hermaphrodite, functions are known for about 60%; 30% have also been characterized by functional calcium imaging, and 15% by electrophysiological recordings—a respectable fraction of the nervous system. For many male-specific neurons,

functions remain to be assigned, and the neuronal activity patterns are unknown. Moreover, in the new reconstructions, two-thirds of the neurons that males share with hermaphrodites are strongly sexually dimorphic in their wiring, which suggests that the male worm is a new animal whose neurons cannot be assumed to have the same functions as those of his sisters (10).

At the circuit level, an anatomically reconstructed wiring diagram leaves many unanswered questions about synapses (edges). For example, electron micrographs do not reveal whether a chemical synapse is excitatory or inhibitory, or whether an electrical synapse is asymmetric or symmetric. Information about these properties and about neuronal dynamics is essential for understanding circuits, even for simple elements such as the feedforward motif. An anatomical map of synapses also fails to show neuromodulators that act at a distance, which play important roles in modifying functional connectivity between neurons. Which of these “nonanatomic” fea-

tures are necessary to understand circuit function? The importance of the complete reconstruction is the ability to pose this question in a rigorous way. With advances in quantitative microscopy and genetically encoded sensors, it seems increasingly feasible to examine neuronal activity during mating behavior; such measurements would reveal whether attractor networks, perceptrons, and other models for circuit function are embodied in the male nervous system.

References

1. T. A. Jarrell *et al.*, *Science* **337**, 437 (2012).
2. K. S. Liu, P. W. Sternberg, *Neuron* **14**, 79 (1995).
3. L. R. Varshney, B. L. Chen, E. Paniagua, D. H. Hall, D. B. Chklovskii, *PLOS Comput. Biol.* **7**, e1001066 (2011).
4. J. G. White, E. Southgate, J. N. Thomson, S. Brenner, *Philos. Trans. R. Soc. London Ser. B* **314**, 1 (1986).
5. M. E. J. Newman, *Networks: An Introduction* (Oxford Univ. Press, Oxford, 2010).
6. R. Milo *et al.*, *Science* **298**, 824 (2002).
7. M. Reigl, U. Alon, D. B. Chklovskii, *BMC Biol.* **2**, 25 (2004).
8. S. Song *et al.*, *PLoS Biol.* **3**, e68 (2005).
9. O. Sporns, R. Kötter, *PLoS Biol.* **2**, e369 (2004).
10. K. Lee, D. S. Portman, *Curr. Biol.* **17**, 1858 (2007).

10.1126/science.1225853

MATERIALS SCIENCE

A Roadmap for the Assembly of Polyhedral Particles

Joost de Graaf¹ and Liberato Manna^{2,3}

Self-assembly of atomic, molecular, or artificial nanoscale units into superstructures is a prevalent topic in science. Advances in control over the synthesis of colloidal nanoparticles (1, 2), in their organization into ordered structures (3–7), and in modeling of assembly (8–10) have boosted interest in this topic. Yet predicting what types of superstructures will be formed from specific building blocks according to the shape of the blocks and their interactions remains an open problem (11). Even if the shape is spherical and interactions between blocks do not depend on their mutual orientation, one cannot model the finite-pressure assembly on the basis of simple close-packing arguments; more elaborate approaches are required. On page 453 of this issue, Damasceno *et al.* (12) report the most extensive and systematic study thus far on the

assembly behavior of polyhedral “hard” particles of many different shapes. The study exploits a large set of shapes to determine simple predictive criteria for assembly.

Modeling anisotropic hard-particle assembly began many decades ago. In 1949, Onsager predicted that hard cylinders with hemispherical caps (spherocylinders) spontaneously form a nematic liquid crystal past a threshold in volume fraction (13). The organization is driven by maximization of the configurational space that is made available to the particles (in other words, a maximization in the positional and orientational entropy of each cylinder). This assembly works best when spherocylinders are organized parallel to each other.

For hard particles with flat facets, entropy maximization favors mutual alignment of particles along these facets (14). This requirement translates into directional interactions of each particle with its neighbors [so-called “directional entropic forces” (14)]. The concept of directional entropic forces is similar to the directional bonding between atoms

How particles pack together as a solid can often be predicted just from their shape and how many neighbors they have in the fluid phase.

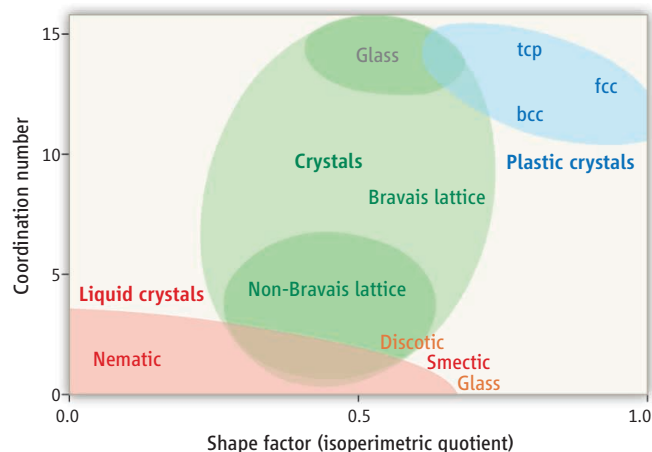
in solids, and the connection is exploited by Damasceno *et al.* to draw parallels between the results of their calculations for hard particles and the types of bonds found in solids.

Slow compression of particles from the fluid phase, as done in these calculations, mimics the assembly of colloidal nanoparticles by controlled evaporation of the solvent in which they are dissolved—a process that steadily increases the volume fraction of particles. The calculations show that, depending on their initial shape, hard polyhedra will assemble in one of four ways. They can form crystals (ordered structures in which units are positionally and orientationally blocked at their sites), plastic crystals (ordered structures in which units are free to rotate but remain positionally fixed at their sites), liquid crystals (structures that have positional disorder but have a strong orientational order), or fully disordered structures.

Some of the individual results of the simulations are unexpected. For example, square pyramids first assemble into cubes and then into sheared cubic lattices—a case of hier-

¹Soft Condensed Matter, Debye Institute for Nanomaterials Science, Utrecht University, 3584 CC Utrecht, Netherlands.

²Istituto Italiano di Tecnologia, 16145 Genova, Italy. ³Kavli Institute of NanoScience, TU Delft, 2628 CJ Delft, Netherlands. E-mail: liberato.manna@iit.it; j.degraaf1@uu.nl



archical assembly. However, a unified view is found when results are mapped in terms of two parameters: the “coordination number” in the fluid phase (that is, the number of nearest neighbors surrounding each polyhedron in the fluid) and the isoperimetric quotient, which depends on the particle shape and measures the deviation of the shape from the sphere. Damasceno *et al.* determined that highly faceted polyhedra, which are almost spherical and also have a high coordination number, will assemble into plastic crystals. Polyhedra that are highly nonspherical, with a smaller number of facets and a low coordination number, tend to form liquid crystals. Nonspherical polyhedra that have an intermediate coordination number will assemble into crystals. Almost the entire set of polyhedra that crystallized, according to simulations, fell into one of these three major regions (see the figure).

The coordination number in the fluid phase and the coordination number in the ordered phase were nearly identical in almost all cases. Thus, the packing category for a new type of nanoparticle (whether synthesized in the laboratory or computer-generated) can be determined using the map drawn by Damasceno *et al.*, given its coordination number in the fluid and its shape parameter (both easily determined).

A conspicuous number of polyhedra formed glassy states, and there are overlapping regions where two or even more types of structures could arise from the same polyhedra. The frequent formation of glassy states, possible improvements in mapping, and the investigation of other cases not yet probed by systematic calculations all require further research. In addition, particles with more complex shapes—for example, with concave surfaces or branches—are more likely to become trapped into locally “jammed” configurations and to form disordered assem-

blies when the volume fraction is increased. These types of particles can, however, still spontaneously assemble into ordered superstructures if they follow hierarchical assembly schemes like those adopted by biomolecules, in which complicated building blocks sequentially organize into assemblies of growing complexity.

An example is the organization of DNA into symmetric supramolecular structures, which do not require high volume fractions of units to form (15), but where favorable kinetic and thermodynamic paths drive organization even at very low volume fractions of the units. A nanoparticle analog of hierarchical self-assembly was recently reported for colloidal branched nanocrystals (16), which did not form close-packed structures but nonetheless self-organized in a hierarchical way. Many more examples can be expected as the synthesis of monodisperse colloidal

An assembly map. Damasceno *et al.* have charted the types of superstructures into which polyhedral particles can assemble using only two readily determined parameters, a shape factor and a coordination number. For any given polyhedron, the map predicts its assembly category (one of the shaded areas in the map). In a Bravais lattice, all lattice points are equivalent, which is not the case for a non-Bravais lattice. Abbreviations: fcc, face-centered cubic; bcc, body-centered cubic; tcp, topologically close-packed.

nanoparticles with unconventional shapes progresses. For now, a comprehensive framework for predicting the assembly of any particle based only on the shape and interparticle forces is still out of reach (17).

References and Notes

1. Y. Yin, A. P. Alivisatos, *Nature* **437**, 664 (2005).
2. S. C. Glotzer, M. J. Solomon, *Nat. Mater.* **6**, 557 (2007).
3. D. V. Talapin *et al.*, *Chem. Rev.* **110**, 389 (2010).
4. A. G. Dong *et al.*, *Nature* **466**, 474 (2010).
5. J. Henzie *et al.*, *Nat. Mater.* **11**, 131 (2012).
6. S. C. Glotzer, *Science* **306**, 419 (2004).
7. Z. H. Nie *et al.*, *Nat. Nanotechnol.* **5**, 15 (2010).
8. U. Agarwal, F. A. Escobedo, *Nat. Mater.* **10**, 230 (2011).
9. W. H. Evers *et al.*, *Angew. Chem. Int. Ed.* **48**, 9655 (2009).
10. S. Torquato, Y. Jiao, *Nature* **460**, 876 (2009).
11. S. M. Woodley, R. Catlow, *Nat. Mater.* **7**, 937 (2008).
12. P. F. Damasceno *et al.*, *Science* **337**, 453 (2012).
13. L. Onsager, *Ann. N.Y. Acad. Sci.* **51**, 627 (1949).
14. P. F. Damasceno *et al.*, *ACS Nano* **6**, 609 (2012).
15. Y. He *et al.*, *Nature* **452**, 198 (2008).
16. K. Miszta *et al.*, *Nat. Mater.* **10**, 872 (2011).
17. S. M. Rupich, D. V. Talapin, *Nat. Mater.* **10**, 815 (2011).

Acknowledgments: L.M. holds a European Research Council starting grant (EU-FP7, contract 240111).

10.1126/science.1226162

NEUROSCIENCE

dSarm-ing Axon Degeneration

Xiaomeng Milton Yu and Liqun Luo

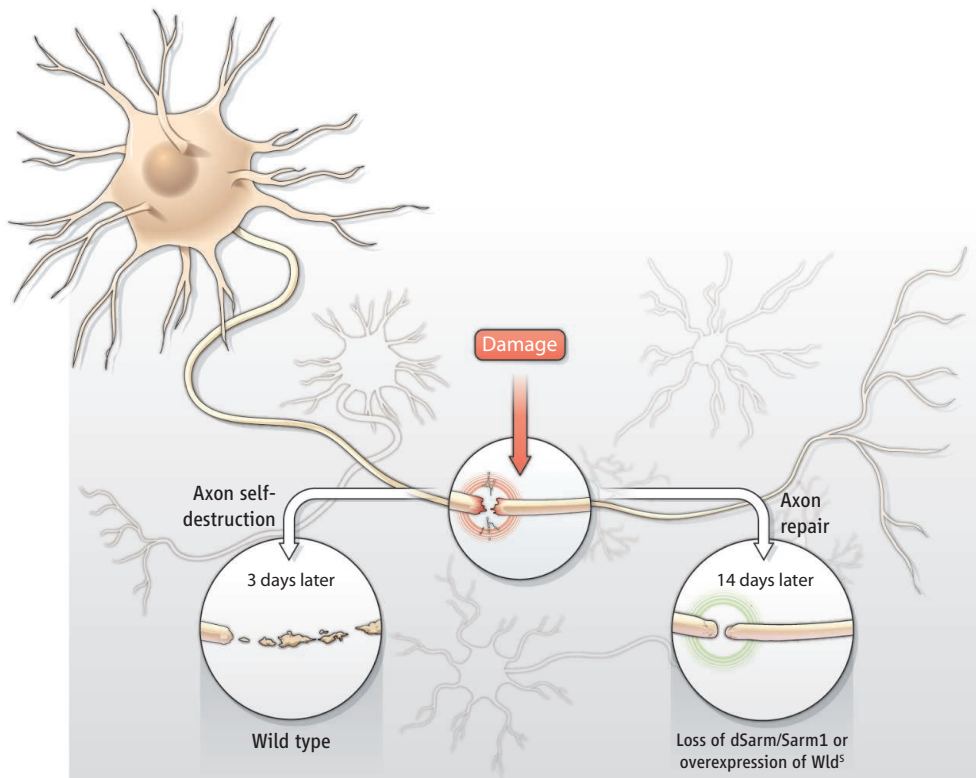
An axon self-destruction program may underlie neurodegeneration in injury and diseased states.

Plucked from the tree, a leaf withers. Such a loss of vitality upon removal from the whole appears so natural that one may take it for granted as a passive and unstoppable process. But is it? Although cell death was long thought to be a passive process, we now know that at least one form of cell death, apoptosis (from Greek “falling away”), is an active process that can be blocked by inhibiting a specific signaling pathway (1). On page 481 of this issue, Osterloh *et al.* (2) find that the death of a portion of a nerve cell, the axon, after it is sev-

ered from the cell body, can be dramatically slowed by the inactivation of just one gene. The discovery has important implications for understanding the molecular mechanisms of axon degeneration, as well as for developing drugs against neurodegenerative diseases.

An axon is a long, polarized extension from the neuronal cell body that transmits a neuron’s output signals to downstream cells. When an axon is acutely injured, the segment distal to the lesion site undergoes morphological changes that lead to its fragmentation and clearance within a few days (see the figure). This process of “Wallerian degeneration,” named after Augustus Waller who described it in 1850 (3), was traditionally viewed as passive deterioration due to the lack of cell

Howard Hughes Medical Institute, Department of Biology, Stanford University, Stanford, CA 94305, USA. E-mail: lluo@stanford.edu



Degeneration delayed. After an axon is severed from the neuronal cell body, the segment distal to the lesion normally undergoes a series of morphological changes that include granulation and fragmentation before it completely disintegrates within 3 days. If the neuron expresses the *Wld^s* fusion protein, or lacks dSarm (in fly) or Sarm1 (in mice), the distal axon segment remains intact for 2 to 4 weeks after the lesion.

body-derived nutrients. However, in 1989, a mutant mouse strain, *Wallerian degeneration slow* (*Wld^s*), showed that severed axons remain intact for weeks, as opposed to 3 days in wild-type mice (4). This suggested that Wallerian degeneration is normally mediated by an active process, as with apoptosis. However, unlike apoptosis (5), little is known about the constituents of this putative axon self-destruction pathway. The axon protection seen in *Wld^s* mice is caused by a chromosomal rearrangement that results in the overexpression of *Wld^s*, a chimeric protein consisting of the amino-terminal part of an enzyme for polyubiquitination and NMNAT, a biosynthetic enzyme for nicotinamide adenine dinucleotide (6). *Wld^s* is not made in normal mice and thus does not inform on the endogenous mechanisms that mediate axon degeneration. Candidate gene studies have yielded only two in vivo examples of axon degeneration inhibition: a mutation in *DLK/Wnd* delays Wallerian axon degeneration in both fly and mouse (7); and suppression of ubiquitin proteasome activity, which slows injury-induced axon degeneration in flies (8). In both cases, the inhibition of axon degeneration is considerably weaker than that caused by *Wld^s* overexpression. Therefore, major players in Wallerian degeneration, if they exist, remain to be identified.

Enter *dsarm/Sarm1* (*Drosophila* sterile alpha and Armadillo motif and its mouse

ortholog *Sarm1*), the first mutant whose inhibition of axon degeneration rivals that of *Wld^s* protection. Osterloh *et al.* discovered *dsarm/Sarm1* using a forward genetic screen, wherein animals with randomly generated mutations are screened for a desired phenotype and relevant genes are identified only after such mutants are isolated. In contrast to a candidate gene approach, forward genetic screens do not rely on any hypotheses regarding which genes may control axon degeneration. Osterloh *et al.* carried out their screen with an established Wallerian degeneration model in the fruit fly *Drosophila melanogaster* (9). Using *Drosophila* enabled them to base the screen on genetic mosaic analyses, a unique advantage that allows the isolation of mutant genes that could otherwise be lethal. Both the unbiased nature and mosaic design of the screen were crucial for their discovery. *dsarm* encodes a highly conserved Toll-like receptor signaling adaptor (10) with no previous link to axon degeneration. Although the fly *dsarm* mutation is lethal, the authors created mosaic animals in which only olfactory receptor neurons lost the *dsarm* gene. When the neuronal cell bodies were removed, their severed axons in the brain remained intact for 30 days, more than half the lifetime of a fly. This is in astonishing contrast to severed wild-type axons, which degenerate and are completely cleared within a week. Remarkably, the axon pro-

tection effect of dSarm is well conserved in mammals. Transected axons of sciatic nerves in *Sarm1* mutant mice were protected from degeneration for 2 weeks; denervation of neuromuscular terminal was delayed to over 6 days. Both phenotypes are comparable in extent to *Wld^s* protection.

The identification of dSarm/Sarm1 provides direct evidence for an endogenous axon self-destruction program. Understanding this mechanism has wide implications, as Wallerian degeneration shares morphological similarities with axon degeneration during normal brain development (axon pruning) and with the “dying back” degeneration in neurodegenerative diseases. There are similarities and differences in these processes. For example, whereas inhibiting the ubiquitin-proteasome system blocks developmental axon degeneration and delays axon degeneration after injury, *Wld^s* only protects axon degeneration after injury (8, 11, 12). In that regard, dSarm/Sarm1 resembles *Wld^s* because its function also appears to be highly specific for injury-induced axon degeneration. *Wld^s* also attenuates the progression of pathological symptoms in several mouse models of neurodegenerative diseases, such as Parkinson’s disease, multiple sclerosis, motor neuron disease, and glaucoma (13). Thus, it will be of particular interest to determine whether Sarm1 also plays a role in the axon loss in mouse models of neurodegenerative diseases; if so, Sarm1 represents an attractive drug target for combating these diseases.

If there is a specific process that actively triggers axon death, as seems likely, what is its function during normal conditions? The success of the approach taken by Osterloh *et al.* suggests that additional components in the Wallerian degeneration pathway could be identified in a similar fashion, thereby providing clues to answer this question.

References

1. J. Yuan, S. Shaham, S. Ledoux, H. M. Ellis, H. R. Horvitz, *Cell* **75**, 641 (1993).
2. J. M. Osterloh *et al.*, *Science* **337**, 481 (2012).
3. A. Waller, *Philos. Trans. R. Soc. Lond.* **140**, 423 (1850).
4. E. R. Lunn, V. H. Perry, M. C. Brown, H. Rosen, S. Gordon, *Eur. J. Neurosci.* **1**, 27 (1989).
5. I. Budihardjo, H. Oliver, M. Lutter, X. Luo, X. Wang, *Annu. Rev. Cell Dev. Biol.* **15**, 269 (1999).
6. T. G. Mack *et al.*, *Nat. Neurosci.* **4**, 1199 (2001).
7. B. R. Miller *et al.*, *Nat. Neurosci.* **12**, 387 (2009).
8. E. D. Hoopfer *et al.*, *Neuron* **50**, 883 (2006).
9. J. M. MacDonald *et al.*, *Neuron* **50**, 869 (2006).
10. I. Akhouchayri, C. Turc, J. Royet, B. Charroux, *PLoS Pathog.* **7**, e1002319 (2011).
11. R. J. Watts, E. D. Hoopfer, L. Luo, *Neuron* **38**, 871 (2003).
12. Q. Zhai *et al.*, *Neuron* **39**, 217 (2003).
13. M. P. Coleman, M. R. Freeman, *Annu. Rev. Neurosci.* **33**, 245 (2010).

10.1126/science.1226150

IMMUNOLOGY

HD6 Defensin Nanonets

André J. Ouellette and Michael E. Selsted

The lining of the mammalian small intestine—the epithelium—is the main organ for nutrient absorption and also prevents gut microbes from crossing the gut wall and establishing systemic infections. Although humans benefit from interactions with resident gut microbes (1, 2), mechanisms exist to maintain a balance between supporting gastrointestinal microbiota and ensuring the integrity of the gastrointestinal epithelial barrier. For example, peptides called α -defensins influence the composition of the microbial consortium while also providing immunity against certain mucosal infections (3, 4). On page 477 of this issue, Chu *et al.* (5) report that human α -defensin (HD) 6 molecules self-assemble to form nanonets that entrap microorganisms and block their translocation across the epithelial barrier.

α -defensins secreted by Paneth cells in the small intestine (see the figure) are microbicides that are active against diverse microbes and certain viruses (6). Mature HD6 has 32 amino acids, and its nine conserved residue positions include Arg and Glu positions that form a salt bridge, a conserved Gly residue on a β -turn, and six Cys residues. The latter form the tridysulfide array that determines the triple-stranded β -sheet topology common to all α -defensins.

These canonical features are highly conserved, but the remaining residue positions may be occupied by a range of amino acids. The resulting α -defensin peptide diversity creates molecules with differing target cell specificities and mechanisms of action. For example, in the two α -defensins secreted by human Paneth cells, HD5 and HD6, only five nonconserved residues are the same or have conservative substitutions. Like most α -defensins, HD5 has direct microbicidal effects *in vitro* against various microbial species, but HD6 lacks this activity (7).

In vitro, α -defensins kill bacteria by two main mechanisms. At high peptide concentrations, they disrupt the bacterial cell membrane through electrostatic and hydrophobic interactions with the bacterial cell envelope.

At low peptide concentrations, α -defensins inactivate lipid mediators of bacterial cell wall biosynthesis to inhibit cell growth. Because HD6 does not kill bacteria directly *in vitro*, it has remained unclear whether, and if so how, HD6 might influence immunity of the intestinal mucosa.

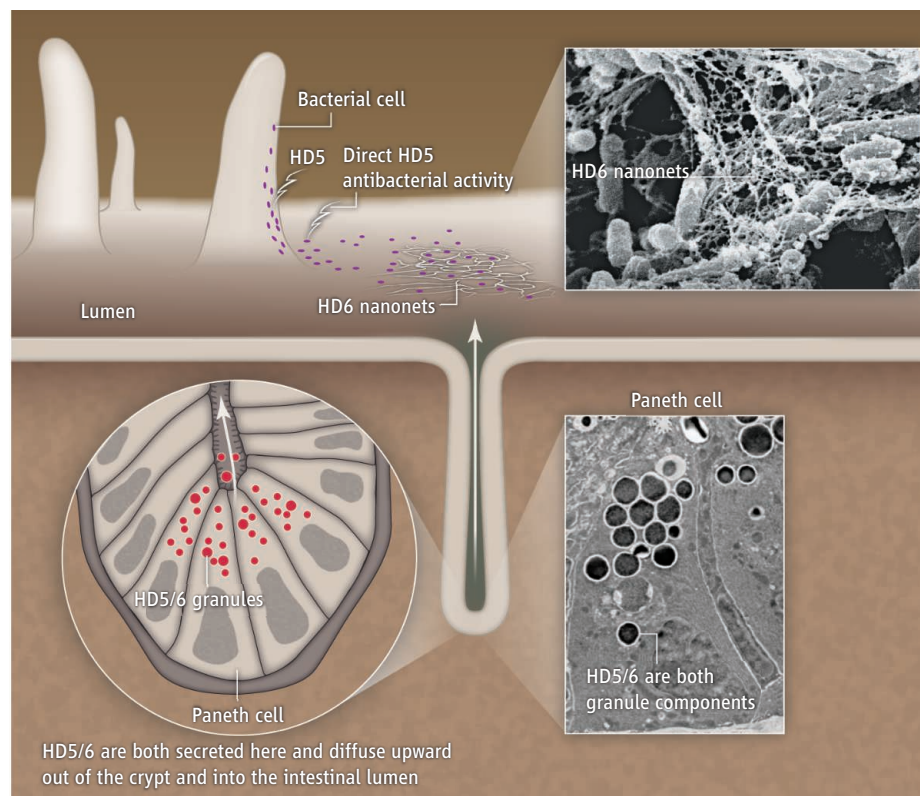
The elegant and comprehensive study of Chu *et al.* now provides the answer. To test for a role for HD6 in mucosal immunity, the authors adopted a transgenic approach similar to that previously used to study the role of HD5 *in vivo*. In the earlier HD5 work, transgenic, Paneth cell-specific HD5 minigene expression in mice altered the composition of the ileal microbiota and also dramatically reduced survival of *Salmonella enterica* serovar Typhimurium (STM) in the small intestine (3, 4). Chu *et al.* now report that HD6 transgenic mice of similar experimental design expressed HD6 at levels compa-

The human α -defensin 6 peptide fights infection in the human intestine by forming nanonets that entrap the microbial cells.

able to those of transgenic HD5 mice and of endogenous mouse α -defensins.

Similar to the protective effects of HD5 transgene expression, HD6 transgenic mice challenged with oral STM had increased survival compared with controls. However, the mechanisms that promoted survival were different. In STM-infected HD5 transgenic mice, the number of viable STM recovered from the intestinal lumen was greatly reduced, but in HD6 transgenic mice, luminal STM survival was the same as in infected, nontransgenic control mice. STM translocation from the lumen to Peyer's patches and spleen was markedly inhibited in HD6 transgenics and similar to what is seen with noninvasive strains of the same organism.

The authors go on to show that HD6 has a structure-based mechanism of action that differs from all previously investigated α -defensins. Higher-ordered self-assem-



HD6 nanonets confer mucosal immunity. From the base of small intestinal crypts, human Paneth cells secrete granules containing two α -defensins, HD5 and HD6 (9). The granules dissolve rapidly after secretion, releasing HD5 and HD6 into the small intestinal lumen. HD5 reduces the survival of certain microbial species by direct microbicidal effects. Chu *et al.* show that HD6 instead entraps bacteria in peptide nanonets, preventing translocation across the gut wall without affecting microbial viability.

Department of Pathology and Laboratory Medicine, USC Norris Cancer Center, Keck School of Medicine, University of Southern California, Los Angeles, CA 90089–9601, USA. E-mail: aouellet@usc.edu

blies of HD6 dimers entrap bacteria, both on cell culture monolayers and in mouse ileal loops. Crystallographic analyses showed that HD6 dimers associate further to produce stable tetramers. The latter are the repeating units of elongated HD6 structures that self-assemble to form nanonets (see the figure).

A histidine at position 27 is critical for tetramer formation, higher-order oligomerization, and the ability to form nanonets. Replacement of His²⁷ with Trp abrogated the HD6 peptide's unique biochemical attributes and its in vitro and in vivo antimicrobial activities. Thus, His²⁷ confers an activity on HD6 that is, to our knowledge, lacking in all other α -defensins.

Chu *et al.* show that nanonets also form in vivo. In ileal loops from HD6 transgenic mice, induced Paneth cell secretions

trap luminal STM in a net-like meshwork of fibrils not seen in other mouse strains or in HD5 transgenic loops. The in vivo nets were seen only in HD6 mice, and they also formed in intestinal aspirates from human subjects. Superficially, the mechanism resembles that by which neutrophil extracellular traps form at sites of neutrophil recruitment and cytolysis (8), except that nanonet formation is uniquely dependent on the HD6 peptide entity.

Aside from delineating the role of HD6 and its unusual mechanism of action, the report by Chu *et al.* should give us pause for reflection. HD6 has no evident activity in in vitro assays, yet it affects mucosal immunity profoundly. Thus, in vitro bactericidal assays, although useful for comparing peptides in structure-activity studies, may not predict or even hint at the potential impact

of a peptide in vivo. Given the diversity of in vitro biological functions that have been associated with defensins and other host-defense peptides, the challenge is to establish the physiological relevance of those activities.

References

1. J. K. Nicholson *et al.*, *Science* **336**, 1262 (2012).
2. L. V. Hooper *et al.*, *Science* **336**, 1268 (2012).
3. N. H. Salzman *et al.*, *Nat. Immunol.* **11**, 76 (2010).
4. N. H. Salzman, D. Ghosh, K. M. Huttner, Y. Paterson, C. L. Bevins, *Nature* **422**, 522 (2003).
5. H. Chu *et al.*, *Science* **337** 477 (2012).
6. M. E. Selsted, A. J. Ouellette, *Nat. Immunol.* **6**, 551 (2005).
7. B. Ericksen, Z. Wu, W. Lu, R. I. Lehrer, *Antimicrob. Agents Chemother.* **49**, 269 (2005).
8. V. Brinkmann *et al.*, *Science* **303**, 1532 (2004).
9. A. J. Ouellette, *Cell Mol. Life Sci.* **68**, 2215 (2011).

10.1126/science.1225906

MOLECULAR BIOLOGY

Use and Abuse of RNAi to Study Mammalian Gene Function

William G. Kaelin Jr.

For decades, scientists studying mammalian cells could only marvel at the genetic tools available to scientists who studied organisms such as yeasts or drosophila. However, many genes linked to human diseases do not have orthologs in such model organisms, or they require an appropriate cellular context to display their disease-relevant phenotypes. The wish for a facile method to disrupt gene function in somatic mammalian cells appeared to be granted with the discovery of RNA interference (RNAi) and small interfering RNA (siRNA) (or short hairpin RNA, shRNA), which brought with them great promise—particularly for discovering novel drug targets through the use of genetic screens (1–3). However, the honeymoon is now over, and although some new discoveries have been made, the yield has fallen far short of expectations. Many drug targets identified by means of si/shRNA technology in academic laboratories are not robust when tested in industrial laboratories (4, 5). Avoiding this fate requires a more sophisticated interpretation of si/shRNA results, especially in the context of high-throughput screens.

As with any new technology, the initial euphoria is now being tempered by a growing awareness of the pitfalls. Perhaps the most damaging of these is the potential for any given si/shRNA to affect genes other than its intended target (off-target effects) (6). This concern is compounded when the phenotype being scored could also reflect a loss of cellular fitness, such as a decrease in cell proliferation or viability, which is regulated by many genes. More generally, inhibiting a complex biological phenotype (an “off” or “down” assay) is more susceptible to spurious results than the activation or restoration of a complex phenotype (an “on” or “up” assay). The common practice of focusing on the si/shRNAs for a given gene that have the strongest phenotypes in off/down screens regardless of their relative knockdown efficiencies runs the risk of enriching for off-target effects.

The minimum standard in the field is to show that the same phenotype is observed with two or more independent si/shRNAs targeting the same gene, ideally linked to a statement as to how many si/shRNAs were actually tested. In theory, the degree of target knockdown achieved with individual si/shRNAs would also correlate with the magnitude of their phenotypic effects. In practice, however, this is often not the case, presum-

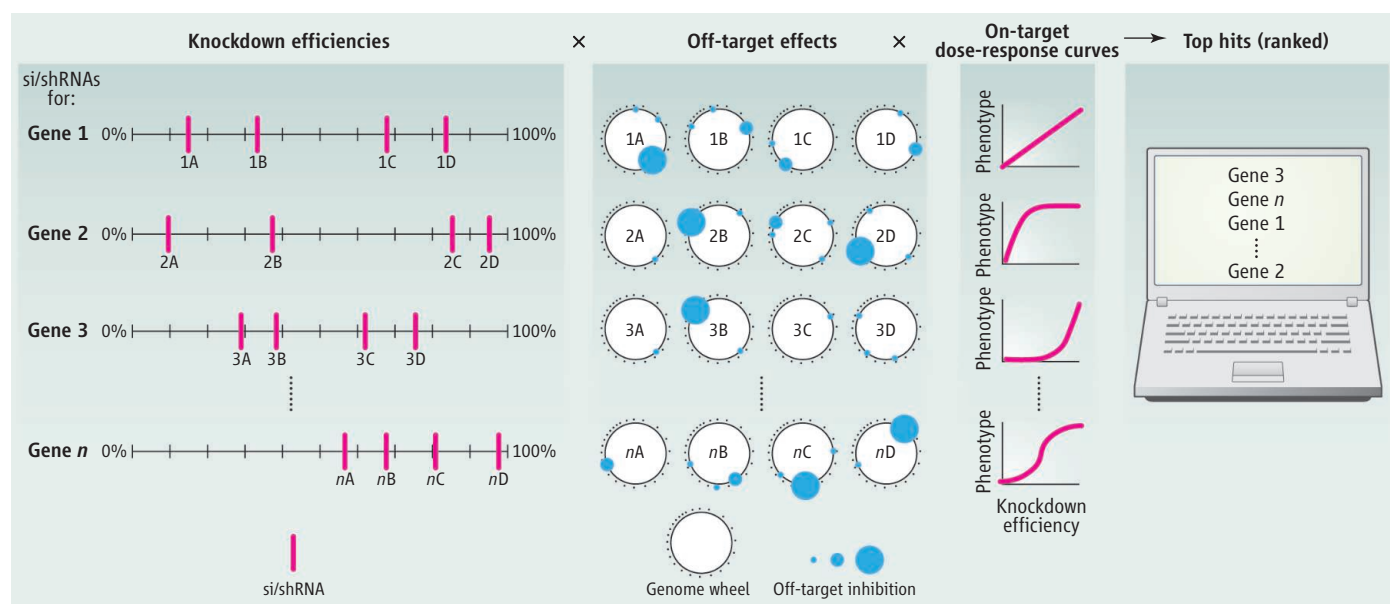
Realizing the full potential of si/shRNA technology requires more sophisticated approaches to address the pitfalls.

ably because the gene activity–phenotype relationship for many genes is not linear and/or because si/shRNA off-target effects can suppress or enhance the on-target phenotype.

In principle, the gold standard for confirming that a si/shRNA phenotype is on-target is the demonstration that the phenotype can be reversed (“rescued”) by a si/shRNA-resistant mRNA for the gene of interest. However, this is again often difficult in practice. For example, it might be necessary to recapitulate the physiological expression of the targeted gene, in which case conventional expression vectors will usually be inadequate. The use of minigenes or bacterial artificial chromosomes might be helpful here (7). However, even when successful, rescue experiments do not exclude that the observed si/shRNA phenotype requires inhibition of the intended target and one or more off-target effects (that is, reflects synthetic interactions between the target gene and other genes).

It is therefore highly desirable to corroborate si/shRNA findings with alternative approaches, of which there are many available. For example, dominant-negative mutants and pharmacological agents are especially useful when the goal is to credential a drug target, because absence of a target (such as achieved with a si/shRNA) need not phe-

Department of Adult Oncology, Office M457, Dana-Farber Cancer Institute, 450 Brookline Avenue, Boston, MA 02215, USA. E-mail: william_kaelin@dfci.harvard.edu



si/shRNA screen variables. For a phenotypic si/shRNA screen involving n genes, the ranking of any one gene will be influenced by the knockdown efficiencies of the si/shRNAs (A to D in the example shown) for that gene, their off-target effects (for simplicity, on-target effects not shown), and the dose-response curves linking the activity of that gene and the phenotype being measured (for example, loss of viability).

nocopy an inactive protein (such as achieved with a drug). Another useful approach, especially for off/down si/shRNA phenotypes, is to show that increasing the activity of the si/shRNA target (such as through overexpression) induces changes that are the opposite of those seen with the si/shRNA. In some cases, known epistatic relationships can also be exploited to reverse si/shRNA phenotypes and to strengthen the case for an on-target relationship. Finally, other methods for inactivating gene function, such as adeno-associated virus-based homologous recombination and TAL (transcription activator-like) effector endonucleases (8, 9), might help but are currently low throughput. It may be feasible to conduct unbiased, relatively high-throughput, insertional mutagenesis screens in human haploid cancer cells (10).

These issues are potentially compounded by problems related to multiple hypothesis testing when large si/shRNA libraries are used in high-throughput screens. Many of the first-generation screens used libraries containing three to five si/shRNAs per target gene where the knockdown efficiencies and off-target effects of the individual si/shRNAs were unknown. In such large screens, and especially those approaching genome-wide scale, the probability that two or more si/shRNAs for a given gene will have similar phenotypes

(especially in off/down screens) because of random off-target effects increases, leading to false discoveries. Although these screens clearly do generate valuable data, the extent to which false-positives contaminate the results is currently unclear.

These concerns can be partially mitigated through the use of algorithms that weigh the behavior of each of the si/shRNAs for a given gene to generate a gene score that can then be compared to the scores obtained for the other genes in the library. At three to five si/shRNAs per gene, however, different algorithms that are reasonable a priori can give very different scores. For example, one algorithm might place greater weight on the “top scoring” one, two, or three si/shRNAs out of a set, and another might place greater weight on the absence of outlier si/shRNAs within a set.

Ranking genes relative to one another becomes even more challenging because the rank for a given gene will potentially reflect a number of variables that are unknown (or unknowable), including the knockdown efficiencies of the si/shRNAs targeting that gene, their off-target effects, and the dose-response curve linking the activity of that gene to the phenotype being scored (see the figure and fig. S1). It is therefore not surprising that screens designed to achieve the same end (for example, to kill cells harboring a particular pathogen or cancer-relevant mutation) but using different libraries and different ranking algorithms can yield very different results (11–15).

So, what’s the best way forward? In the short term, one approach would be to conduct more focused screens, perhaps involving fewer than 100 genes, to allow deeper

interrogation of primary screen hits in lower-throughput secondary screens. For example, one might focus on the genes within a particular disease-associated amplicon or that encode a particular family of enzymes. In the long term, the performance of genome-scale screens will improve with further library enhancements (including increasing the number of si/shRNAs per gene and eliminating si/shRNA empirically found to produce false-positives across multiple screens), the use of algorithms that take into account si/shRNA knockdown efficiencies, and incorporation of orthogonal data sets (for example, data from genomic studies or chemical screens). In the meantime, greater prudence is needed when analyzing si/shRNA data if we are to remain in love beyond the honeymoon.

References

1. S. M. Elbashir *et al.*, *Nature* **411**, 494 (2001).
2. T. R. Brummelkamp *et al.*, *Science* **296**, 550 (2002).
3. G. Sui *et al.*, *Proc. Natl. Acad. Sci. U.S.A.* **99**, 5515 (2002).
4. F. Prinz, T. Schlange, K. Asadullah, *Nat. Rev. Drug Discov.* **10**, 712 (2011).
5. C. G. Begley, L. M. Ellis, *Nature* **483**, 531 (2012).
6. C. J. Echeverri *et al.*, *Nat. Methods* **3**, 777 (2006).
7. R. Kittler *et al.*, *Proc. Natl. Acad. Sci. U.S.A.* **102**, 2396 (2005).
8. I. F. Khan *et al.*, *Nat. Protoc.* **6**, 482 (2011).
9. A. J. Bogdanove, D. F. Voytas, *Science* **333**, 1843 (2011).
10. J. E. Carette *et al.*, *Science* **326**, 1231 (2009).
11. N. J. Barrows, C. Le Sommer, M. A. García-Blanco, J. L. Pearson, *J. Biomol. Screen.* **15**, 735 (2010).
12. S. P. Goff, *Cell* **135**, 417 (2008).
13. J. Luo *et al.*, *Cell* **137**, 835 (2009).
14. C. Scholl *et al.*, *Cell* **137**, 821 (2009).
15. D. A. Barbie *et al.*, *Nature* **462**, 108 (2009).

Supplementary Materials

www.sciencemag.org/cgi/content/full/337/6093/421/DC1
Fig. S1

10.1126/science.1225787

RETROSPECTIVE

Phillip V. Tobias (1925–2012)

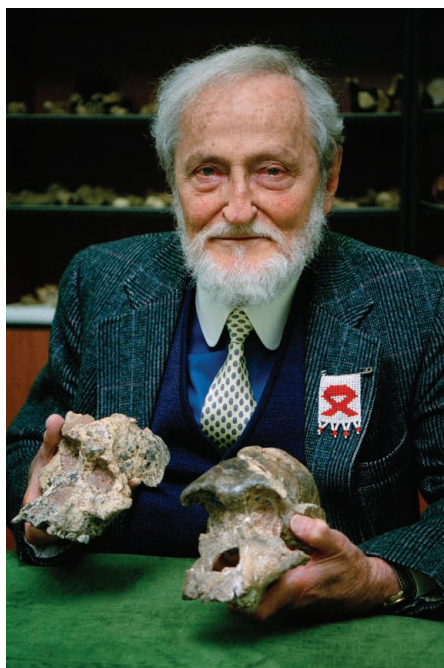
Tim D. White

In his 1888 Royal Society remembrance, Thomas Huxley noted that Charles Darwin might have become a physician but for his professor whose anatomy lectures were “as dull as he was himself.” Evolutionary biology has much to thank for Darwin’s inadequate medical instruction. Thankfully for human evolutionary studies, the opposite happened at South Africa’s University of the Witwatersrand (“Wits”), where Phillip Tobias was inspired by the anatomist Raymond Dart. In his words, for more than 40 years, Dart was “a kind of father figure and surrogate academic parent to me.” Tobias went on to become legendary for research, scholarship, principles, and educational impacts. Africa has now lost one of her greatest scientists.

Tobias (known professionally as PVT) often noted that he was born the year Dart revealed *Australopithecus*—and the year of Tennessee’s Scopes “Monkey Trial.” Born in Durban, South Africa, he moved to Johannesburg in 1942. For the next 70 years, from freshman to emeritus professor, he was associated with Wits. As a student, Tobias grounded himself in a wide range of disciplines, undertaking postdoctoral work in the mid-1950s at Cambridge, Rockefeller, Michigan, and Chicago. He was well prepared to succeed Dart and led the Department of Anatomy at Wits from 1959 to 1990. This long administrative tenure was one of dozens he assumed for his university, country, and world. From the presidency of the South African Speleological Association to the first chairmanship of the South African National Commission for UNESCO, it seemed like Tobias was omnipresent.

Dart only indirectly planted PVT’s feet in paleoanthropology. Redirecting his career away from studies of living Africans was left to Louis and Mary Leakey, who invited him in 1959 to describe Tanzania’s “Zinj” cranium from Olduvai. In short order, Tobias published his magnificently detailed 1967 Cambridge monograph on the new species *Au. boisei*. He described *Homo habilis* with Louis Leakey and John Napier in 1964 and monographed the fossils in two 1991 volumes.

Tobias was an effective advocate for con-



servation and outreach. In the 1960s, he began to preserve and manage the Sterkfontein fossil site, undertaking and overseeing paleoanthropology’s longest continuously running excavation. His efforts led to UNESCO World Heritage protection in 1999. PVT appreciated the value of human osteological collections and wrote persuasively about their preservation. He generously made himself available to the public, most notably in the 6-week television series for the South African Broadcasting Corporation entitled “Tobias’s Bodies.”

Monuments to his productivity are his many honors and an incredible publication record (more than 1300 titles, ranging from human stature to cytogenetics and from embryology to medical education). Asked in 1988 how he managed, PVT, then 63, replied that “the story that I survive on three hours’ sleep a night is not true; it’s more like four or five.” He described his life’s concerns as “all things human, humane, humanitarian, and humanistic.” In 1999, in the last public act of his presidency, Nelson Mandela presented Tobias with the Order of the Southern Cross of South Africa. Visual remembrances of this gentle giant of paleoanthropology abound, one of the most poignant and current within the “21 Icons” project (www.youtube.com/watch?v=QU90FGunarA).

The preeminent paleoanthropologist’s courage, humanity, and research led the way in African academia and paleoanthropology.

Since his student days, Tobias had been heavily involved in fighting compulsory racial segregation at South African universities, emphasizing that “race is irrelevant in matters of the mind and spirit.” In 1948, only months after the National Party took power in South Africa, the nonracial National Union of South African Students elected PVT its president. His cause was a 40-year struggle during which “we kept alive the flickering flame of academic freedom, the spirit of resistance and of anti-racism, for all those bitter and painful years.” Throughout, PVT conducted an extensive correspondence with his global extended family (a “Civitas Academica”) as protection from a government whose policies he courageously opposed. By 1996, Tobias was finally able to convey in his seasonal “nuggets of news” letter to colleagues (which annually recounted his tireless global travels and extended acquaintances), “How happy I am to have lived to see the end of statutory racism, discrimination, and segregation and the other evils of the apartheid era.”

Generous in his praise and restrained in his advice, Tobias was renowned for his lengthy but engrossing lectures, his command of many languages, his alliance with justice, and his few detractors. He was meticulous with words and fossils, an eternal optimist whose kindness, respect, and generosity were bestowed liberally. He was always first with a word of congratulation for a fossil newly found, a paper well presented, or a custodian in the hallways.

Tobias never really retired. In 1998, he and Ron Clarke, his partner in the ongoing work at Sterkfontein (following Alun Hughes), announced the discovery of one of Africa’s most important hominid skeletons, “Littlefoot.” Rather than rushing its preparation and analysis, Clarke has followed the careful, meticulous approach of his mentor; any other approach, PVT would have accurately termed malpractice.

Huxley wrote about Darwin, “In science no man can safely speculate about the nature and relation of things with which he is unacquainted at first hand.” Phillip Tobias was better acquainted with *Homo sapiens* than any other scientist. As Francis Thackeray, his Wits successor, eulogized: “We have lost a great and special representative of our species.”

10.1126/science.1225988

Human Evolution Research Center, University of California at Berkeley, Berkeley, CA 94720, USA. E-mail: timwhite@berkeley.edu

CREDIT: SELWYN TAIT/SYGMA/CORBIS

Aipotu: Simulation from Nucleotides to Populations and Back Again

Aipotu, the IBI Prize-winning module, creates a world where students manipulate the DNA of virtual organisms and examine resulting effects.

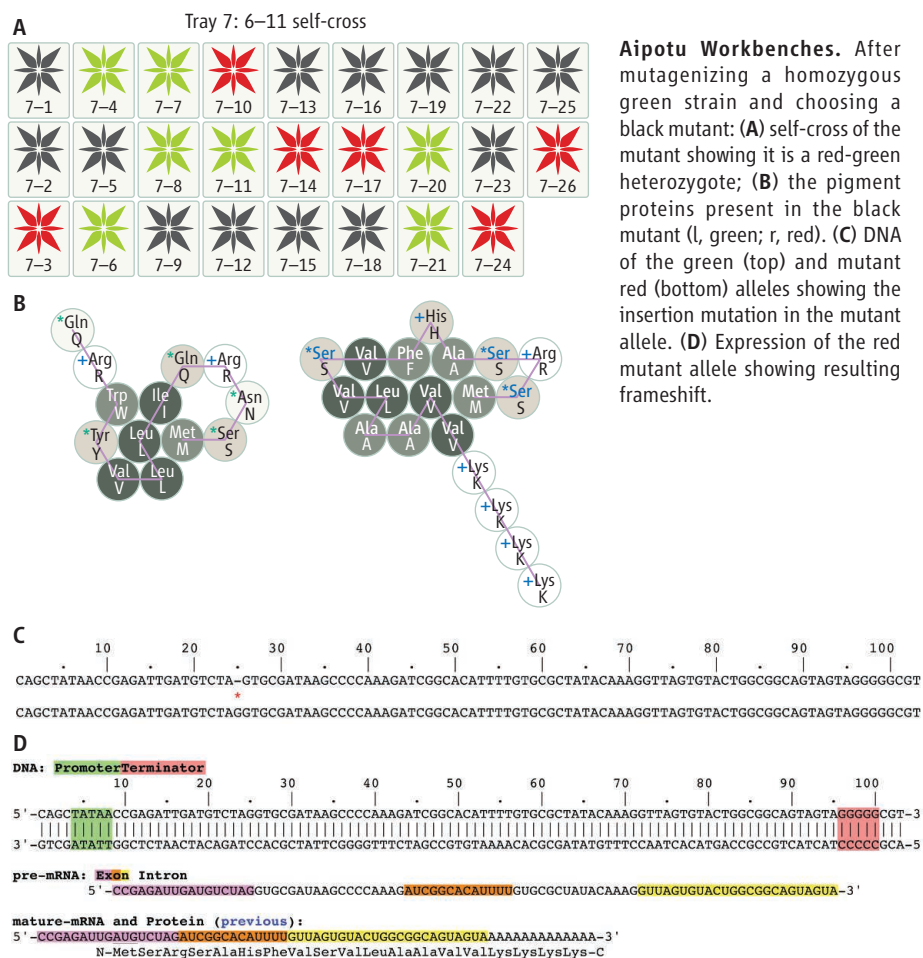
Brian T. White

Imagine an undergraduate research project where students are given samples of an uncharacterized plant species. The flowers in these samples appear in several different colors, and the students' task is to not only discover how these colors are produced but also construct a plant with a novel flower color. They begin by crossing plants to determine what color alleles are present and how these alleles interact. Students then investigate the biochemical mechanism behind color formation and the DNA sequences responsible for each color allele and use this information to engineer a transgenic plant strain with a novel flower color. Finally, they undertake a long-term study of the evolution of flower color in this species. This "flower-engineering" project would give students the opportunity to develop and test hypotheses in an authentic research environment.

Unfortunately, the time, equipment, and expertise required for this type of experience are not typically available in undergraduate teaching laboratories. For this reason, I built Aipotu to provide a virtual microworld where students could carry out a reasonable approximation of this flower-engineering project. In Aipotu, organisms can be manipulated at the DNA level with resulting effects on RNA, protein, phenotype, and populations. The Aipotu software and associated lab activities retain many of the pedagogically relevant features of the flower-engineering project in a form that can be completed by high school or beginning undergraduate students. These activities have been developed over the past 5 years through collaboration with Ethan Bolker (Mathematics and Computer Science, University of Massachusetts, Boston), several dozen teaching assistants, and more than 2000 students who have taken my courses since Aipotu was first tested in 2007. The Aipotu software is part of the Bio-QUEST Collection (1) and runs on Windows, OS X, and Linux. You can download Aipotu software, documentation, and lab manuals free from <http://aipotu.umb.edu>.

Biology Department, University of Massachusetts, Boston, 100 Morrissey Boulevard, Boston, MA 02125, USA. E-mail: brian.white@umb.edu

*IBI, Science Prize for Inquiry-Based Instruction; www.sciencemag.org/site/feature/data/prizes/inquiry/.



Aipotu Workbenches. After mutagenizing a homozygous green strain and choosing a black mutant: (A) self-cross of the mutant showing it is a red-green heterozygote; (B) the pigment proteins present in the black mutant (l, green; r, red). (C) DNA of the green (top) and mutant red (bottom) alleles showing the insertion mutation in the mutant allele. (D) Expression of the red mutant allele showing resulting frameshift.

Each aipotian organism contains two DNA sequences, one from each parent. Students can use the software to analyze the DNA sequences to determine the phenotype of the organism in a manner that includes many of the pedagogically relevant features of real-world organisms (2). Each DNA sequence is scanned for specific promoter and transcription terminator sequences. Any resulting pre-mRNA is then scanned for specific splicing control sequences, spliced, and processed, and any resulting open reading frame is then translated. The structure of the protein is then determined by an energy-minimization algorithm that uses ionic bonds, hydrogen bonds, and the hydrophobic effect to fold the protein on a two-dimensional hexagonal lattice. The software determines the function of the protein on the

basis of its shape and amino acid composition. Proteins with a specific shape can be colored, and the particular color depends on the particular amino acids in a critical region of the protein (this is analogous to the mechanism of color formation in rhodopsins and green fluorescent protein). Finally, the overall color of the flowers produced is determined via a set of color combination rules encoded in the software.

To compress the real world into a practical simulation, I have taken some significant biochemical liberties. Real protein folding is a three-dimensional and highly complex process and flower color typically results from enzymatic production of small pigmented molecules rather than from pigmented proteins. However, the purpose of Aipotu is not to illustrate how flowers are

colored in nature but to allow students to explore a biological phenomenon in detail. aipotian proteins fold in a manner that is explicable, if not predictable, in terms taught in introductory-level biology courses, and the mechanism of color formation is not unreasonable from a student's point of view. Previous studies of this protein-folding simulation show that it leads to significant increases in students' understanding of protein structure and does not leave a significant number of students with the misconception that proteins are two-dimensional (3). Most important, this model of protein folding, in which structures and phenotypes can be determined in less than a second, allows the students to carry out their studies in a reasonable amount of time.

Aipotu invites students to work at four Workbenches—Genetics, Biochemistry, Molecular Biology, and Evolution—and a virtual Greenhouse allows organisms to be passed from one Workbench to another. At the start of the exercises, the Greenhouse contains four organisms with different-colored flowers: white, red, and two green strains. In time, students discover that one is homozygous green and the other a yellow-blue heterozygote. These choices can be customized by the instructor, as can the order of the exercises.

In the Genetics lab session, students use the tools in the Genetics Workbench to cross organisms of their choice in order to characterize the color alleles present. Students are then introduced to two ongoing themes that will frame their work in the following labs. In the first of these, students are challenged to engineer a pure-breeding purple organism. In the second framing task, each group of students creates an organism with a novel color by introducing a random mutation and saving it to the Greenhouse. They will use their developing understanding of the molecular mechanism of color formation to explain the properties of this mutant as they carry out the remaining labs.

The Biochemistry Workbench provides tools for students to determine the relations among protein sequence, protein shape, and protein color. By examining the structures of proteins present in the Greenhouse strains, students use the existing colored proteins to develop hypotheses about the factors that influence color and test their hypothesis by observing the colors that result from protein sequences they have designed. Students post hypotheses, experiments, and results to a lab blog (see Supplementary Materials). At regular intervals throughout the lab session, the instructor holds a classwide

“minisymposium” to review the class's work so far, to determine which hypotheses have been supported or refuted, to identify remaining open questions, and to design the next round of experiments. At the end of this 3-hour session, students use what they have discovered to explain the color of their mutant and to design a purple protein.

Students use the Molecular Biology Workbench to explore the DNA sequences of the various color alleles, to complete their explanation of the color of their mutant strain, and to construct a gene encoding the purple protein they engineered in the Biochemistry lab. They then construct an organism with two copies of this DNA sequence, save it to the Greenhouse, and use the crossing tools in the Genetics Workbench to show that it is true-breeding. A series of screenshots (see the figure) illustrates the steps in this process.

To conclude the module, students select organisms from the Greenhouse to form a starting population of 100 individuals in the Evolution Workbench. This population is then subjected to random mutations at the DNA level followed by natural selection with user-adjustable fitness for each color. Tools from other Workbenches can be used both to create organisms for study and to analyze the organisms that result. Students use multiple evolution runs to address particular misconceptions about evolution, including “selection causes beneficial mutations,” “mutations are always deleterious,” and “mutations cannot create new features.” Experiments that target these include observing the evolution of particular colors in the presence and absence of selection, as well as the evolution of colored flowers from colorless ancestors.

Students are sometimes frustrated by the open-ended nature of these labs. They expect that the software will “tell them the answer” rather than act as a tool that they must thoughtfully wield in order to discover the answer. Also, they do not often see how all the pieces of this project fit together until the Evolution Workshop, where they take a newly evolved organism and explore the specific changes in DNA and the resulting changes in RNA and protein that give rise to its new phenotype. It is important to emphasize that this is constructive frustration that leads to a deeper understanding of how biologists investigate and understand living things.

Aipotu provides a virtual microworld where students can explore a biological

About the author

Brian T. White is an associate professor in the Biology Department at the University of Massachusetts, Boston, where he teaches the introductory courses for Biology majors and studies the development and evaluation of materials for teaching biology. He has developed many different simulations and activities for teaching introductory biology (<http://intro.bio.umb.edu/BW/>). He earned a B.S. in Biology from Massachusetts Institute of Technology and a Ph.D. in Biological Sciences from Stanford University. He is an active member of the BioQUEST Curriculum Consortium (which has been a constant source of inspiration and encouragement throughout this project), as well as the Center for Scientific Teaching (cst.yale.edu).



phenomenon using tools from some of the key domains in modern biology. Because the aipotian organisms' simulated biology includes some of the detail and complexity found in living organisms, students can directly explore the connections between these domains in depth, using a wide range of approaches. Furthermore, a far wider range of activities is possible, limited chiefly by the imagination of the instructor. For example, the Workbenches can be used independently to explore these domains on their own or in any order. Going further, students could design genes that encode proteins with specific shapes, explore the effects of different types of mutations, and compare evolution in different worlds. Finally, future software development could include other organisms, genes, phenotypes, and multigene interactions—a world of aipotian creatures. I look forward to working with fellow “aipotian explorers” to develop both the software and activities to their full potential.

References and Notes

1. BioQUEST Curriculum Consortium, <http://bioquest.org>.
2. B. T. White, E. D. Bolker, Interactive computer simulations of genetics, biochemistry, and molecular biology. *Biochem. Mol. Biol. Educ.* **36**, 77 (2008).
3. B. White, A. Kahrman, L. Luberic, F. Idleh, Evaluation of software for introducing protein structure: Visualization and simulation. *Biochem. Mol. Biol. Educ.* **38**, 284 (2010).

Supplementary Materials

www.sciencemag.org/cgi/content/full/337/6093/424/DC1

10.1126/science.1215105

Case It!, an IBI prize-winning module, provides computer simulations that enable student analysis of biological materials not usually available in laboratories.

Case It! (www.caseitproject.org) originated at the 1995 BioQUEST Summer Workshop (1) and has developed over the years into an effective system for case-based learning useful for both high school and university educators (2, 3). National Science Foundation support has enabled us to distribute all project materials at no cost.

Case It v6.06 is a computer simulation that enables students to input DNA or protein sequences and to generate realistic results for procedures including Southern, Western, and dot blotting; simple and multiplex polymerase chain reaction (PCR); single-nucleotide polymorphism (SNP) and expression microarrays; and enzyme-linked immunosorbent assay (ELISA). The free download includes Case It v6.06 and folders containing sequences for case scenarios based primarily on genetic and infectious diseases.

Students first read case descriptions from the Case It! Web site, then use Case It v6.06 to open sequence files associated with particular case scenarios. They select and run the appropriate procedure to analyze the sequences, generating results in the form of images that can then be incorporated into presentations or reports.

The simulation can be used in a variety of ways for inquiry-based instruction at different learning levels. At the introductory-biology level, students can assume roles of persons in the cases, such as health-care professionals, lab technicians, researchers, or hypothetical family members. They then discuss results either in person or online. Substantial inquiry



Undergraduate research assistants developing new cases on honeybee biology. (Left to right) Samuel Master, Kathryn Hoffman, Ryan Debner, Brianna Jacques, Jennifer Brooks, Jamie Bolwerk.

occurs when students have to answer questions in the role of a physician or counselor and discuss ethical and social ramifications of the results (e.g., genetic testing). Playing the role of a person in the case requires them to develop pertinent questions leading to rich interactions with their peers (4).

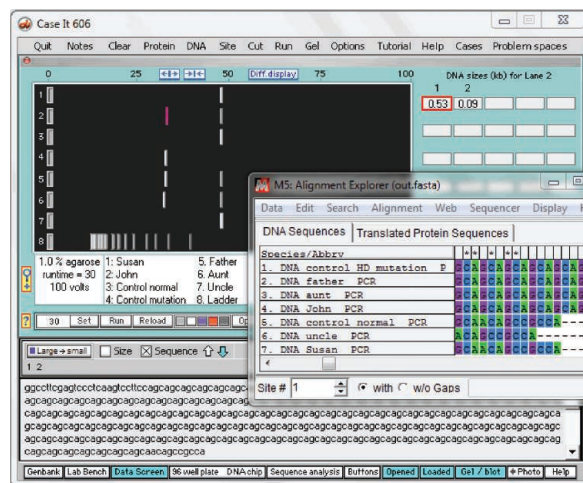
For example, in the Huntington's disease case, students enter sequences representing patient samples, perform PCR on these samples, and then analyze the gel results to determine who has inherited the mutation associated with this disease. The sequence of each PCR product can be viewed in Case It v6.06 or aligned using MEGA software (5) to illustrate the variable nature of the triplet repeat mutation. Because this is a dominant mutation, anyone with one mutated allele will likely progress to the disease, for which there currently is no cure or treatment. In one scenario of this case, Susan talks her brother John into being tested for the disease, but he is the one who tests positive for the mutation, and her results are normal (see the screen shot at right). Students playing the roles of Susan or John must then imagine what it is like to be in this situation and respond

accordingly. In our experience, this kind of interaction enhances learning by making molecular biology more interesting and relevant (6).

We have found that role-playing works best when students post case results and communicate with their peers online, switching roles as family members and health counselors. They preferred online discussions to other types of interactions (4) and became so engaged in asking ques-

tions and responding that they frequently forgot that the class period was about to end. Students felt that they could give more thoughtful and accurate answers online, because more time was available to reflect and consult sources before responding.

Another case example involves Anna, a woman diagnosed with HIV during the second trimester of her pregnancy. Students use Case It v6.06 to test for the presence of HIV-specific antibodies in samples from Anna, her baby, and her boyfriend and then use a bioinformatics extension of the case to examine



PCR results from Case It v6.06, and alignment results from MEGA 5, for a Huntington's case scenario. The sequence for the selected (pink) band is shown.

¹Biology Department, University of Wisconsin–River Falls, River Falls, WI 54022, USA. ²Computer Science Department, Winona State University, Winona, MN 55987, USA.

³ Faculty of Science and Technology, Inter American University of Puerto Rico, Metropolitan Campus, San Juan, Puerto Rico 00919. ⁴ Department of Biology, Chemistry, and Environmental Sciences, Post Office Box 5100, Inter American University of Puerto Rico, San Germán Campus, Puerto Rico 00683. ⁵ Biology Department, North Carolina A&T State University, Greensboro, NC 27411, USA. ⁶ Department of Fisheries and Wildlife, Michigan State University, East Lansing, MI, 48824, USA.

*IBI, Science Prize for Inquiry-Based Instruction; www.sciencemag.org/site/feature/data/prizes/inquiry/ †Author for correspondence. E-mail: mark.s.berglund@uwrf.edu

relations among the virus sequences of these individuals. They discuss how Anna may have become infected with HIV and provide suggestions for how she can care for herself and her infant.

This example and other Case It! scenarios from the United States and Africa help in understanding how culture, geography, and other social issues affect people infected with HIV. The following quote from a student at the University of Zimbabwe illustrates how the Case It! project is helping students worldwide to better understand principles of molecular biology and their relevance to everyday life: "Case It! is a very useful project for all schools if adopted in Zimbabwe. It will help many in understanding HIV and AIDS in general. ... Since Zimbabwe is hard hit by HIV it is important to have this project." Online communication allows collaborations among students at different institutions, so that they experience other perspectives on the issues. After interacting with peers at the University of Wisconsin–River Falls (UWRF), a Zimbabwean student said: "[Case It!] gave me an opportunity to simulate HIV tests and play the role of a medical practitioner and counselor by

giving advice to people affected by HIV. It was also interesting to network with international students via conferencing. Indeed, the world is a global village."

Case It v6.06 can also be used as an introduction to quantitative techniques, such as the calculations used in SNP microarrays, as illustrated with a prostate cancer case. In one scenario, Greg, who has just turned 50, is told that his blood level of prostate-specific antigen (PSA) is higher than the normal range. Greg's physician recommends SNP testing to see if his PSA levels may naturally be higher than average and not necessarily linked to prostate disease. Greg's results can be compared with outcomes of DNA testing from individuals determined to have high and low blood PSA levels, and users can search using BLAST probe sequences or gather information from the NCBI SNP database (7). Students can determine whether Greg should get further testing, such as a needle biopsy, even though he has no symptoms.

The open-ended nature of the simulation encourages inquiry by enabling users to analyze any DNA sequence, including entire viral or bacterial genomes, with any probe, primer, or restriction enzyme.

For example, freshmen at UWRF participating in the Howard Hughes Medical Institute (HHMI) SEAPHAGES project (8, 9) use Case It v6.06 to generate virtual digests of known phage genomes for comparison with actual gels of their newly discovered phages. They can then use the simulation to search the sequence of any band on the gel via a BLAST search and conduct additional bioinformatics analyses. Another strategy is to engage students in developing new cases, using information from research articles and online databases. They create a case scenario; determine techniques; and obtain sequences and tools, such as PCR primers. Creating new cases can be challenging even for advanced undergraduates, but it helps them to analyze original research and to apply results in a novel context. Undergraduates at UWRF (see the first photo) have found this

experience to be valuable and engaging.

Case It! pedagogy has been extensively assessed by means of focus group interviews, analysis of posters and conferencing logs, and pre- and posttests (4, 6). We videotaped groups working through Case It! and found them engaged in interpretation and verification of results and procedures. Creating a Web poster for discussion with peers challenged students to integrate knowledge and to articulate their ideas (3). Case It! made them aware of the social contexts involved in global issues, promoted scientific competence, and positively influenced performance (4, 6, 10).

A final point relates to how simulations can help educators enhance laboratory experiences and undergraduate research in an era of tight budgets. Simulations such as Case It v6.06 can extend wet labs by enabling students to analyze sequences that they could not otherwise access, such as sequences from HIV patient blood samples, and also allows them to conduct research in a cost-effective manner using sequences from online databases.

Our goal is to foster a community of users willing to share their ideas for Case It! via meetings, workshops, and discussion forums at www.caseitproject.org. We welcome your participation in this effort.

References and Notes

1. The BioQUEST Curriculum Consortium, <http://bioquest.org>. Original team members at the 1995 workshop included M. Bergland, K. Klyczek, J. Cadwallader, V. Carson, and W. Coleman.
2. M. A. Lundeberg, M. Bergland, K. Klyczek, D. Hoffman, *J. Interact. Online Learn.* **1**(3), (2003).
3. M. A. Lundeberg et al., *J. Coll. Sci. Teach.* **32**, 64 (2002).
4. M. Bergland et al., *Am. Biol. Teach.* **68**, 81 (2002).
5. K. Tamura et al., MEGA5: Molecular evolutionary genetics analysis using maximum likelihood, evolutionary distance, and maximum parsimony methods. *Mol. Biol. Evol.* **28**, 2731 (2011).
6. B. H. K. Wolter et al., *J. Sci. Educ. Technol.* **10**, 1007/s/0956-012-9387-7 (2012).
7. National Center for Biotechnology Information database, <http://www.ncbi.nlm.nih.gov>.
8. The Phage Hunters Advancing Genomics and Evolutionary Science (PHAGES) program is part of the HHMI Science Education Alliance; www.hhmi.org/grants/sea.
9. G. F. Hatfull et al., Exploring the mycobacteriophage metaproteome: Phage genomics as an educational platform. *PLoS Genet.* **2**, e92 (2006).
10. H. Kang, M. A. Lundeberg, Participation in science practices while working in a multimedia case-based environment. *J. Res. Sci. Teach.* **47**, 1116 (2010).

Acknowledgments: Major funding provided by NSF (DUE 9752268, 0229156, and 0717577) and the University of Wisconsin–River Falls. Opinions expressed are those of the authors and not necessarily those of the NSF. K. Mogen, D. Johnson, and E. Ribbens assisted in case development.

Supplementary Materials

www.sciencemag.org/cgi/content/full/337/6093/426/DC1

10.1126/science.1215225

About the authors



(Left to right) Dinitra White, Assistant Professor of Computational Biology, North Carolina A&T State University. Karen Klyczek, Professor of Biology, UWRF. Arlin Toro, Associate Professor, Department of Biology, Chemistry and Environmental Sciences, Inter American University of Puerto Rico, San Germán Campus. Chi-Cheng Lin, Professor of Computer Science, Winona State University. Mary Lundeberg, former Chair of Teacher Education, Michigan State University. Mark Bergland, Professor of Biology, UWRF. Rafael Tosado-Acevedo, Associate Professor, Graduate Program in Medical Technology, Inter American University of Puerto Rico, Metropolitan Campus. (Right) Bjørn Wolter, Adjunct Faculty, Department of Fisheries and Wildlife, Michigan State University.





SCIENCE POLICY

Poverty Can Harm Early Brain Development, Researchers Say

A host of recent studies show that growing up in poverty can shape the wiring and even the physical dimensions of a young child's brain, with negative effects on language, learning, and attention. Those findings raise important policy questions in areas ranging from education and health to juvenile justice and social welfare, researchers said at a Capitol Hill briefing organized by AAAS.

Scientists have long known that brain development can be harmed by factors such

children may be more likely to raise their own children in poverty, "and there you have a vicious cycle.

"The promise of neuroscience," Farah added, "is to understand how this works so that you can intervene" to disrupt that cycle.

Recent technological advances, such as functional magnetic resonance imaging, are giving neuroscientists a window into some of the brain's deepest structures and innermost workings. But in a culture that

tends to venerate free will and view poverty as evidence of weak character and moral breakdown, the emerging insights face an uncertain road to acceptance.

The briefing, held 26 June, drew an audience of over 100 people, including congressional staff, federal scientists, and journalists. It was held with the support of U.S. Representatives Chaka Fattah (D-Pennsylvania) and Brian Bilbray (R-California), and was the first in a series of three Capitol Hill briefings on neuroscience organized by the AAAS Office of Government Relations with sup-

port from The Dana Foundation.

In the opening presentation, James Griffin, director of the Early Learning and School Readiness Program at the National Institutes of Health, described the early growth of the brain. By the time a child is 3, the brain is 80% the size of an adult's, with 1000 trillion neuron connections that will be critical to continuing development. Areas such as the prefrontal cortex that govern more complex functions—language, problem-solving, self-regulation, and social bonding—develop most rapidly from ages 1½ to 4.

"This really is a crucial period in brain development," Griffin explained. "We know we need to...take full advantage of what we can do for children (at that age) so they reach their full potential."

That's the importance of cognitive nurturing, the researchers said. When parents or caregivers spend time reading with a child, the intellectual activity helps build neural connections. Without that engagement, important connections will not be activated—and those not activated often are pruned away as the brain develops.

Stressful lives can cause parents to engage less with children, and stress also acts directly on young brains, leaving a physical signature. Farah said her lab and others are finding that higher income levels are associated with greater volume in the prefrontal cortex and in the hippocampus, a center for memory and learning.

Related studies suggest disparities in brain function between low-income and higher-income children. Farah cited "highly robust, sizeable differences" in the functions of these areas, affecting language, self-regulation, and working memory.

Both Griffin and Farah emphasized that the brain can recover from effects of childhood poverty. But, they said, preventing harm is more efficient than repairing it.

Developing strategies to address these issues would require broad shifts in public policy. Even without that, the researchers said that parents and caregivers can have a constructive impact just by talking and reading to their children and doing what they can to build a sense of security.

For children, the future "depends on us understanding really, fully, what is the science... and how do we put it into practice," said Annapurni Jayam-Trouth, chair of the Department of Neurology at Howard University. "The science must be transmitted via many channels of education to the general public, especially to low-income communities, so intervention can begin early at home."



Deep insight. Functional magnetic resonance imaging allows neuroscientists to assess the structure and function of children's brains.

as poor nutrition and exposure to lead. But researchers at the briefing cited studies that are probing how a lack of "cognitive nurturing"—talking and reading to a child, for example—and sustained exposure to "toxic stress" set off a cascade of hormonal and neural responses far different than those in a child who is raised in a more secure, stimulating environment.

"Where a child grows up in impoverished conditions...with limited cognitive stimulation, high levels of stress, and so forth, that person is more likely to grow up with compromised physical and mental health and lowered academic achievement," said Martha Farah, director of the Center for Neuroscience and Society at the University of Pennsylvania. Once grown up, those



2011 Annual Report

Download the Report at www.aaas.org/publications/annual_report/.

AAAS Delegation Makes “Positive” Visit to Iran

A small delegation led by Nobel laureate and former AAAS President Peter Agre delivered a series of lectures and met with Iranian science leaders, researchers, and students during a week-long science diplomacy visit to Tehran.

Although the visit came at a time of tension centered on Iran’s disputed nuclear research and tightening Western economic sanctions, the presentations and meetings focused on shared interests in research and building a dialogue based on science. And, Agre said, the Americans were warmly received.

“Overall, it was a very positive visit,” said Agre, the 2009 AAAS president. “Our meetings with faculty and students were always positive—it seems to me that we all have a lot to share.... From a scientific viewpoint, the doors are certainly open.”

The AAAS visit was “a milestone,” said Abolhassan Vafai, a professor at Sharif University of Technology. “[The meetings] created a very conducive and fruitful atmosphere for establishing scientific dialogue between the two nations.”

The delegation was invited and hosted by Nasrin Soltankhah, Iran’s vice president for science and technology. The visit was initiated earlier this year when AAAS representatives met in New York with Iranian Foreign Minister Ali Akbar Salehi, who 35 years ago earned a Ph.D. at MIT.

Traveling with Agre were his wife, Mary, a preschool teacher, and Norman P. Neureiter, senior adviser to the AAAS Center for Science Diplomacy and chair of the

senior advisory board at *Science & Diplomacy*, AAAS’s new online quarterly. While in Iran from 6 to 13 June, they spoke at elite universities and civic organizations and met with top government and science policy officials, scholars, and students.

The delegation also was invited to a brief visit with Iranian President Mahmoud Ahmadinejad in his private reception area. Speaking in Farsi, the president offered cordial remarks that emphasized the universal values of science and the belief that knowledge produced by research should benefit all of humanity.

While in Iran, Agre was named an honorary member of the Sharif University faculty and given an office there; he agreed to return every year for 10 days of lectures and other scholarly activity.

Support for science diplomacy by AAAS and others worldwide is based, at least in part, on a basic principle: Common scientific interests and joint research can create engagement and build trust between nations even when governmental relations are strained or broken.

Scientific research has provided a continuing basis for Iran-U.S. engagement. Iran has an accomplished science sector, with focus areas including medical and stem cell research, petroleum engineering, space exploration, and nanotechnology. Many of Iran’s science policy leaders and university faculty members were educated in the United States or Europe, and 5600 young Iranian scientists last year had student visas to live in the United States while studying



Landmark of learning. The Avicenna Building at Sharif University of Technology is named for the influential Persian polymath who lived a thousand years ago.

in nonsensitive fields. The U.S. National Academy of Sciences since 2000 has had an agreement to foster cooperation with the Iranian Academy, and some 20 seminars and workshops have been held in Iran, the United States, and occasionally other countries.

After the AAAS delegation returned, Neureiter discussed the Iran trip during an hour-long look at science diplomacy on The Kojo Nnamdi Show, on WAMU-FM in Washington, D.C. [Listen to the archived show at www.aaas.org/go/kojo/].

AAAS

New Dues Rates Approved for 2013

The AAAS Board of Directors has approved a dues increase for 2013. The Board authorizes increases to cover two kinds of expenses: unavoidable costs associated with running AAAS and publishing *Science*, and new expenses that add value to membership. Postage and paper increases and improving online resources are examples of the kinds of expenses the Board anticipated in setting the 2013 rates.

The new rates are effective for membership terms beginning after 31 December 2012. As listed at right, they do not include

postage or taxes for international members, which are additional.

For further information, including subscription rates for *Science Online*, librarians should contact AAAS or their subscription agents, or go to the *Science Online* Web site.

All members will be advised of the new dues rates on their renewal notices for 2013. Member dues and voluntary contributions form the critical financial base for a wide range of AAAS activities. For more information, contact the AAAS Membership Office at 202-326-6417 or www.aaas.org/membership.

Regular professional members	\$151
Postdocs and K-12 teachers	\$99
Emeritus members who receive print <i>Science</i>	\$115
Students	\$75
Patrons	\$310
Institutional rate for print for high schools and public libraries	\$360
All other institutions receiving print	\$1176

New Paradigms in Type 2 Immunity

Bali Pulendran^{1*} and David Artis^{2*}

Nearly half of the world's population harbors helminth infections or suffers from allergic disorders. A common feature of this population is the so-called "type 2 immune response," which confers protection against helminths, but also promotes pathologic responses associated with allergic inflammation. However, the mechanisms that initiate and control type 2 responses remain enigmatic. Recent advances have revealed a role for the innate immune system in orchestrating type 2 responses against a bewildering array of stimuli, from nanometer-sized allergens to 20-meter-long helminth parasites. Here, we review these advances and suggest that the human immune system has evolved multiple mechanisms of sensing such stimuli, from recognition of molecular patterns via innate immune receptors to detecting metabolic changes and tissue damage caused by these stimuli.

More than 3 billion people worldwide are infected with parasitic worms called helminths or suffer allergic disorders such as asthma, allergic rhinitis, food allergies, and eczema (1, 2). A common feature of these infectious or inflammatory conditions is the so-called allergic or "type 2" immune response (3–6). Type 2 immune responses are induced by and confer protection against helminths, but can also play pathologic roles, promoting acute and chronic inflammatory responses against a myriad of allergens. Although type 2 immune responses have been explored largely in the context of helminth infections and allergies, they are also induced by venoms, vaccine adjuvants such as alum (7, 8), several endogenous ligands in the host, and some bacterial and viral infections (although allergic reactions to the latter are the exception rather than the rule) (Fig. 1). Despite the medical and economic impact of type 2 inflammatory responses, how such diverse stimuli trigger prototypic type 2 responses, the nature of the cellular and molecular networks that orchestrate these responses, and whether there are distinct kinds of type 2 responses that play protective versus pathologic roles in various infectious or inflammatory settings are still unclear.

Type 2 Immunity: An Overview

Type 2 responses are characterized by the induction of CD4⁺ T helper (T_H) 2 cells, which secrete cytokines such as interleukin-4 (IL-4), IL-5, IL-9, and IL-13. T_H2 cells promote B cell responses and immunoglobulin E (IgE) secretion through their production of IL-4 (3–6). IgE immune complexes bind to high-affinity IgE receptors (FcεR1) on basophils and mast cells, leading to their activation and secretion of several cytokines and inflammatory mediators such as histamine, heparin, and serotonin (3–6). These factors mediate a range of effector functions character-

istic of type 2 inflammation, including recruitment of alternatively activated macrophages and granulocytes, smooth muscle contractility, and mucus hypersecretion (3–6). Because many different cell types are involved in the orchestration of T_H2 cell responses, the term "type 2 response" will be used to describe the overall response.

T_H2 cell responses belong to a larger spectrum of distinct T_H responses that have evolved to protect the host against a spectrum of pathogens. Different types of T_H cells are characterized by distinct cytokines and transcription factor profiles and also the types of pathogens they control. For example, infection with intracellular bacteria such as *Mycobacterium tuberculosis* or viruses typically induces strong CD4⁺ T_H1 cell responses that result in the secretion of interferon-γ and the elicitation of CD8⁺ cytotoxic T cells that can kill infected cells (3, 4). In contrast, T_H2 cell responses are typically induced by helminths but play a central role in mediating allergic disorders and asthma. Other T_H subsets include T_H17 cells, which contribute to immunity against extracellular bacteria and fungi and the pathogenesis of multiple chronic inflammatory diseases (3, 4);

T follicular (T_{FH}) cells, which promote differentiation of memory B cells (4); and regulatory T cells (T_{regs}), which suppress T_H1, T_H2, and T_H17 responses (4).

Despite the notable developments in understanding the cellular and molecular mechanisms that control T_H1 and T_H17 cell responses, much less is understood about how T_H2 cell responses are initiated and orchestrated. Furthermore, the question of why type 2 responses are generated to allergens and helminths remains a mystery. The diversity of stimuli that induce type 2 responses (Fig. 1), the assembly of different cell types that seem to play key roles, and the fact that there appear to be variants of type 2 responses are all challenges in studying type 2 inflammation. However, several conceptual advances in recent years have begun to shed light on the pathways that initiate and regulate type 2 responses. In the present Review, we examine this recent progress. First, we discuss the apparent heterogeneity of cytokine profiles within the T_H2 cells (the T_H2 medley) and consider the physiological relevance of this heterogeneity in vivo. Second, we reflect on how the immune system senses a staggering diversity of allergens, helminth products, and other microbes to initiate type 2 responses. Third, we consider how type 2 responses are initiated and orchestrated. We discuss the current knowledge of the cell types, innate receptors, and signaling pathways that orchestrate T_H2 responses. Finally, we conclude by highlighting some key questions that must be answered to facilitate the rational design of therapeutics against type 2 inflammatory disorders.

The T_H2 Medley

Traditionally T_H2 cells have been defined as those T cells that produce IL-4, IL-5, IL-13, IL-9, and IL-10 and express the transcription factors GATA-binding protein 3 (GATA-3), signal transducer and activator of transcription-5 (STAT-5), and

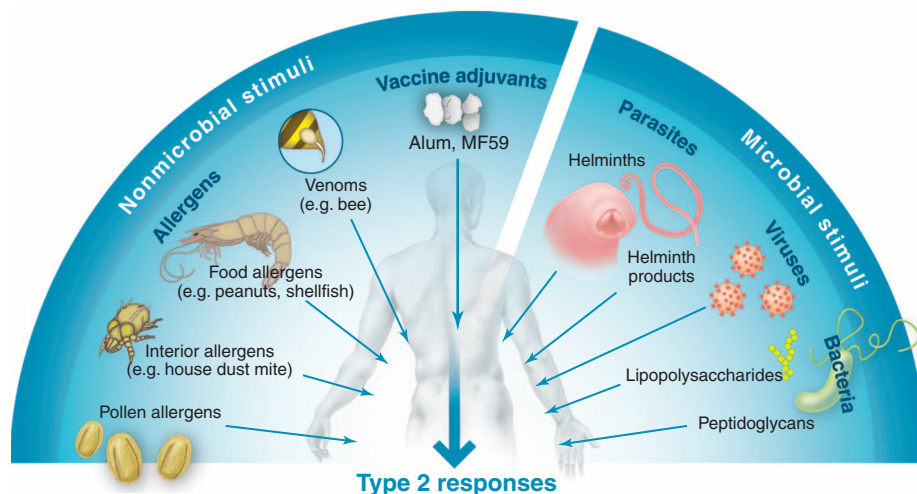


Fig. 1. Diversity of stimuli that induce type 2 immune responses. Such stimuli range from nanometer-sized allergens to 20-m-long helminth parasites. Despite marked differences in size, shape, structure, and physical and chemical properties, all of these stimuli induce type 2 immune responses.

¹Department of Pathology, Emory Vaccine Center, Yerkes National Primate Research Center, 954 Gatewood Road, Atlanta, GA 30329, USA. ²Department of Microbiology and Institute for Immunology, Perelman School of Medicine, University of Pennsylvania, Philadelphia, PA 19104, USA.

*To whom correspondence should be addressed. E-mail: bpulend@emory.edu (B.P.); dartis@mail.med.upenn.edu (D.A.)

STAT-6 (3–6). However, single-cell analysis has revealed a marked degree of heterogeneity in the cytokine profiles of T_H2 cells (9). Furthermore, ex vivo restimulation of human T cells isolated from blood revealed a population of T_H2 cells that produce IL-4, IL-5, and IL-13 but not IL-10. In contrast, this cell population expressed high levels of the proinflammatory cytokine tumor necrosis factor- α (TNF- α) (10). Because IL-10 is a cytokine that is known to suppress allergic inflammation, T_H2 cells that coexpress proinflammatory cytokines have been termed “inflammatory T_H2 cells” to distinguish them from the canonical “noninflammatory T_H2 cells” that do produce IL-10. Consistent with this, IL-13⁺/TNF- α ⁺ inflammatory T_H2 cells have also been isolated from human breast cancer biopsies and are believed to contribute to an inflammatory milieu that promotes tumor progression (11). Whether the T_H2 cells that cause allergic disease display a more proinflammatory phenotype is poorly understood. Moreover, certain microbial stimuli can stimulate T_H2 -like cells that cannot be pigeonholed into the canonical T_H2 phenotype. For example, *Porphyromonas gingivalis*-derived lipopolysaccharide (LPS) promotes T_H2 cell-like responses in which T_H cells produce IL-13, IL-5, and IL-10 but not IL-4 (12). Other stimuli, such as certain ligands for Toll-like receptor 2 (TLR2), promote a mixed T_H2 and T_H17 response (13), and subsets of T cells that secrete both IL-4 and IL-17 and coexpress the transcription factors GATA3 and ROR γ t have been described and linked to bronchial hyperactivity in humans (14). In addition, T_H2 cells can acquire IL-9 production when stimulated with transforming growth factor- β (15).

It is important to note that many studies that indicate heterogeneity within a population of T_H2 cells have employed restimulation of T cells ex vivo. Although these approaches reveal the potential of a given T_H2 cell to express different effector cytokines, they do not illuminate what the cell actually secretes within the tissue microenvironment. Therefore, an important challenge for the field is to evaluate the heterogeneity of T_H2 cell responses in vivo. Employing genetically engineered reporter mice in which the temporal and spatial expression of a given cytokine by antigen-specific T cells can be visualized in vivo has proven to be a fruitful approach to addressing this question. For example, the use of this approach to assess the temporal and spatial production of these cytokines in vivo revealed that in lymph nodes, IL-4 but not IL-13 was produced by T_{FH} cells (16). In contrast, T_H2 cells in tissues produced both cytokines.

Such heterogeneity in cytokine expression may exist within populations of T_H2 cells because subsets of T_H2 cells may be functionally distinct.

Thus, IL-4-producing T_{FH} cells in the germinal center may induce isotype switching of B cells to IgE, whereas IL-4⁺IL-13⁺ T_H2 cells in tissues may contribute to tissue remodeling. An alternative, though not mutually exclusive, possibility is that the heterogeneity represents the dynamic nature of T_H2 cell responses, in which the cytokine profiles of individual T cells within the T_H2 compartment are dependent on the number of cell divisions and the tissue microenvironment in which the T cells reside. If the T_H2 cell variants

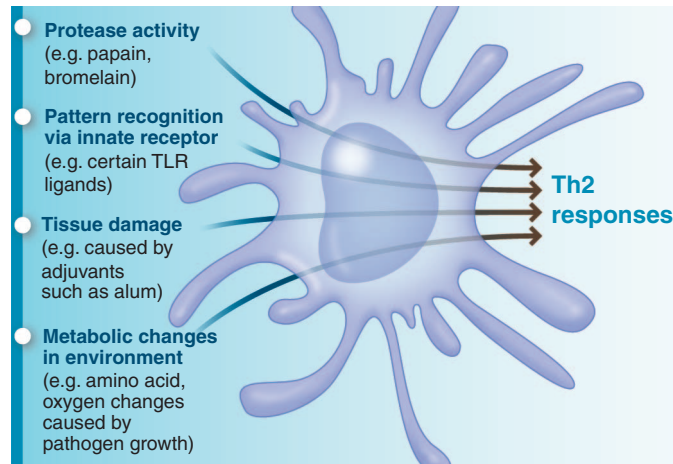


Fig. 2. Diverse mechanisms by which the innate immune system senses type 2-inducing stimuli. The host appears to have evolved multiple mechanisms to sense a bewildering array of stimuli that induce type 2 immune responses. Many pathogens and allergens can be sensed by pattern recognition receptors. In addition, proteolytic cleavage of host proteins by the protease activity of allergens, as well as tissue damage and metabolic changes caused by stimuli, may also be sensed by cells such as dendritic cells. Such diverse signals are decoded by dendritic cells to program type 2 immunity.

indeed have distinct functions, then learning whether one variant (for instance, pathologic) can be reprogrammed to another (e.g., protective) has therapeutic relevance in the context of allergic disorders and asthma.

How Are Type 2-Inducing Stimuli Sensed?

In the immune system, pathogen recognition receptors (PRRs) have evolved to sense a diverse array of stimuli (17–19). PRRs include TLRs, C-type lectin-like receptors (CLRs), and NOD-like receptors (NLRs), which are expressed on the surface and in intracellular compartments of a variety of cell types, including dendritic cells (DCs) and epithelial cells. Triggering of such PRRs results in the activation of DCs, which then stimulate antigen-specific T cells and tune the type of T_H cell response that is generated. Indirect activation of DCs can also occur, for example, via epithelial cell-derived factors such as thymic stromal lymphopoietin (TSLP), which conditions DCs to induce T_H2 cell responses (3–6).

Although recent studies have highlighted the role of PRR triggering of DCs in orchestrating type 2 responses, emerging insights suggest that this paradigm may not be the only way to induce type 2 immunity. Other pathways

such as the enzymatic activity of allergens, or recognition of tissue damage and/or metabolic changes caused by allergens or helminths, may also trigger type 2 immunity (Fig. 2).

Given the notable array of microbial (e.g., helminth products, bacterial LPS, viruses) and nonmicrobial (allergens from pollen, mites, animal dander, insects, molds, foods, venoms, and adjuvants) stimuli that provoke type 2 responses, it may be necessary to look beyond the classical PRR-DC paradigm when thinking about how type 2 responses are generated. Are the known sets of PRRs sufficient to account for type 2-inducing stimuli, or do we have to posit an undiscovered family of PRRs or other innate sensors that promote these responses? Although the role of TLRs in inducing T_H1 cell responses is appreciated, there are also several examples in which stimuli that activate TLRs (e.g., *P. gingivalis* LPS, synthetic TLR2 ligands, helminth extracts, low doses of lipopolysaccharides) signal DCs to induce T_H2 cell responses (6). Furthermore, recognition of bacterial peptidoglycans by NOD1 and NOD2 or by the C-type lectin DC-SIGN induces type 2 responses in some scenarios (6).

In the case of allergens, there is evidence that they can be sensed by PRRs. For example, extracts of the ubiquitous house dust mite (HDM) allergens signal through TLR4 on airway structural cells to produce cytokines such as TSLP, granulocyte-macrophage colony-stimulating factor (GM-CSF), IL-25, and IL-33, which condition DCs and other accessory cells to promote a T_H2 response and airway inflammation (20). HDM extract contains endotoxin, which signals through TLR4 and modulates allergic sensitization in children (21). Furthermore, it has been proposed that low-dose LPS promotes T_H2 cell responses, whereas high doses promote T_H1 cell responses (22). The induction of TSLP, GM-CSF, IL-25, and IL-33 in a TLR4-dependent manner may reflect contaminating LPS (20). In addition, the main kind of HDM called Der p 2 is structurally and functionally homologous to MD2 (the LPS binding component of the TLR4 complex) and directly interacts with TLR4 to facilitate TLR4 signaling-dependent, T_H2 -mediated allergic inflammation (23). Now, there is increasing evidence that other allergens also trigger TLR4 by a similar mechanism. For example, a nickel allergy, one of the most frequent causes of contact hypersensitivity in industrialized countries, is triggered by an inflammatory response via TLR4 signaling (24). Interestingly, the cysteine protease papain also induces type 2 in vivo, through a mechanism dependent on TLR4 (25). Finally, HDMs can also activate DCs through the C-type lectin dectin-2 to induce T_H2 responses (26).

Sensing a universe of allergens. Currently more than 1000 protein allergens from mites, animal dander, pollens, insects, and foods have been cloned and sequenced, and through structural biology and bioinformatics approaches, the secondary and tertiary structures of more than 200 allergens have been determined (27–29). Although most allergens can be classified into structural families on the basis of their protein folds (e.g., antiparallel β strands and antiparallel β strands associated with one or more α helices), these structural features do not allow discrimination between allergens and nonallergens (27–29). Moreover, functional analyses of allergens reveal that they consist of proteins with diverse biological functions, such as proteases, lipid-transfer proteins, and calcium-binding proteins (27–30).

One feature that contributes to the induction of type 2 responses by some allergens is the serine or cysteine protease activity of allergens such as the HDM group I allergens Der p1 and Der f1, papain, and allergens from *Aspergillus* and ragweed (27–29). The proteolytic activity of Der p1 and papain seem essential, as inactive forms of these proteins do not induce type 2 responses, although whether this is due to loss of enzymatic activity or to the shorter half life of inactive allergens is unknown (Fig. 2). It has also been reported that a cysteine protease from the parasite *Leishmania mexicana* induces type 2 responses in mice and that this effect could be abrogated by protease inhibitors (27–29). It is not clear what targets of such proteases are relevant for the induction of type 2 responses. Although protease-activated receptors (PARs) are activated by serine proteases, the ability of PARs to recognize cysteine protease activity and mediate T_H2 responses is poorly understood (30). Recently, PAR-2 was shown to mediate, in part, the induction of the T_H2 cell-inducing cytokine TSLP from airway epithelial cells in vitro in response to the protease activity of the common environmental fungus *Alternaria alternata* (31). Moreover, the serine protease kallikrein-5 induces atopic dermatitis-like lesions through PAR-2-mediated induction of TSLP in Netherton syndrome, a persistent atopic skin disease caused by mutations in the gene encoding serine protease inhibitor Kazal-type-5 (SPINK5, also known as LEKTI) (32). This protease inhibitor mutation results in unregulated kallikrein-5 activation of PAR-2, with the induction of the pro- T_H2 mediators TSLP, thymus and activation-regulated chemokine, and macrophage-derived chemokine. However, the targets of other proteases such as papain are not known. Moreover, other allergens such as those isolated from cats and cockroaches do not appear to have any protease activity, indicating that protease activity is not the only pathway to promote type 2 inflammation. Consistent with this observation, many proteases such as bacterial proteases, metalloproteases, and aspartic proteases do not appear to induce type 2 responses, suggesting that protease activity alone may not be sufficient.

Tissue damage and metabolic changes. Besides pattern recognition and protease activity, it is conceivable that certain allergens and helminth-derived factors induce type 2 immune responses as a result of tissue damage caused by cell death (33). Many endogenous molecules released by tissue damage are potent inducers of type 2 responses. For example, induction of T_H2 responses by the vaccine adjuvant alum does not seem to depend on any of the known PRRs (6, 7), but rather on tissue damage that results in the release of uric acid crystals, which programs DCs to induce type 2 responses (34). Furthermore, a recent report suggests that in mice, alum causes cell death and the subsequent release of host DNA, which acts as a potent endogenous adjuvant that triggers T_H2 responses, partly through an interferon response factor 3-dependent mechanism (35). In addition, our recent work suggests that immunization with papain results in the induction of reactive oxygen species (ROS) in epithelial cells at the site. ROS orchestrated T_H2 cell responses, in part, by inducing oxidized lipids that triggered the induction of TSLP by epithelial cells mediated by TLR4 and the adaptor protein TRIF (25). Consistent with this observation, two other signals of tissue damage—high mobility group nucleosome binding protein 1 (a nonhistone chromatin binding protein that is released upon cell death) and matrix metalloproteinase-2 (a proteolytic enzyme that degrades the extracellular matrix)—activate DCs via a TLR4-dependent pathway to induce T_H2 cell responses (36, 37).

Given these examples, a critical question is why such tissue damage-associated molecules induce type 2 responses? It has been proposed that type 2 responses represent a rapid repair response to tissue damage (33). Consistent with this idea, synthesis of collagen I and III during wound repair after helminth infections is dependent on IL-4 and IL-13. Furthermore, in an experimental model of helminth infection in mice, although there was initial production of IL-17 and concomitant inflammation and tissue damage, subsequent signaling via the IL-4 receptor resulted in a suppression of IL-17 production, enhanced expression of IL-10, and generation of anti-inflammatory macrophages, all of which lead to rapid tissue repair (38).

Finally, we can speculate that metabolic changes in the local milieu [for example, amino acid starvation or oxygen deprivation leading to the so-called integrated stress response (39)] may program DCs and other innate cells at the site of inflammation to induce type 2 responses. How might T_H2 -inducing stimuli cause such metabolic changes? In the case of helminths, it is possible that growth and development consumes nutrients such as amino acids and oxygen from the local milieu, thus triggering the stress response. Furthermore, tissue damage caused by the migration of helminths may also trigger stress responses (i.e., oxidative stress) that are associated with type 2 inflammation. In the case of allergens such as papain, their protease activity may trigger tis-

sue damage and elicit the stress response. Future experimental evaluation of such scenarios will be necessary to elucidate their influence on type 2 inflammation in vivo. Taken together, there is growing evidence that T_H2 -inducing stimuli are sensed by a broad range of mechanisms, including PRR-mediated activation of DCs, as well as by the enzymatic activity of allergens or recognition of tissue damage and/or metabolic changes caused by allergens or helminths.

How Are Type 2 Responses Orchestrated?

As stated above, the current paradigm in innate immunity ascribes a central role for DCs in sensing microbial stimuli via PRRs and influencing the differentiation of lymphocytes into distinct effector cell populations. However, exposure to an allergen or pathogen can result in the activation of a spectrum of cell types of the innate immune system, including basophils, mast cells, natural killer T cells, innate lymphoid cells (ILCs), tissue epithelial cells, and stromal cells (Fig. 3).

DCs have been shown to play a central role in coordinating the actions of such cell types. Therefore, a unified picture of how allergens and helminths initiate type 2 responses must account for the interaction of a network of many different cell types in the innate immune system. In this context, it is instructive to consider the different hierarchies or organization in the innate immune system (Fig. 3) (6). Given their key role in orchestrating immune responses, one could envision DCs as the “ground level” and the innate receptors and signaling networks representing higher-resolution views of the hierarchy. A more global view of the hierarchy includes multicellular cooperation (for example, between DCs, basophils, ILCs, and stromal cells) and the influence of tissue microenvironments (for instance, intestine versus lung). Such a hierarchical model can be applied to most biological systems, but given that recent studies have highlighted the diverse cell types that orchestrate type 2 responses, the model may be especially apt here. Importantly, such a view may provide insights into how allergic inflammation can be prevented at one or more levels of the hierarchy (Fig. 3).

The cell level. A key question in the field is what cell types are responsible for initiating T_H2 responses. DCs play a central role in this process. For example, particular subsets of DCs seem to have an intrinsic capacity to induce type 2 responses. Thus, in mouse spleens the $CD11c^+CD8\alpha^+$ DCs versus $CD11c^+CD8\alpha^-$ DCs produce different amounts of the T_H1 -inducing cytokine subunit IL-12p70 and differentially induce T_H1 versus T_H2 cell responses, respectively (6, 19). In mouse lungs, it has been demonstrated that type 2 responses after exposure to house dust mite allergens are induced by a subset of inflammatory DCs that express Fcε receptor 1 (40). In humans, plasmacytoid DCs (6, 19, 41) in the blood and Langerhans cells (42) in the skin can preferentially induce type 2 responses. Besides their functional specializations, DCs also show a great

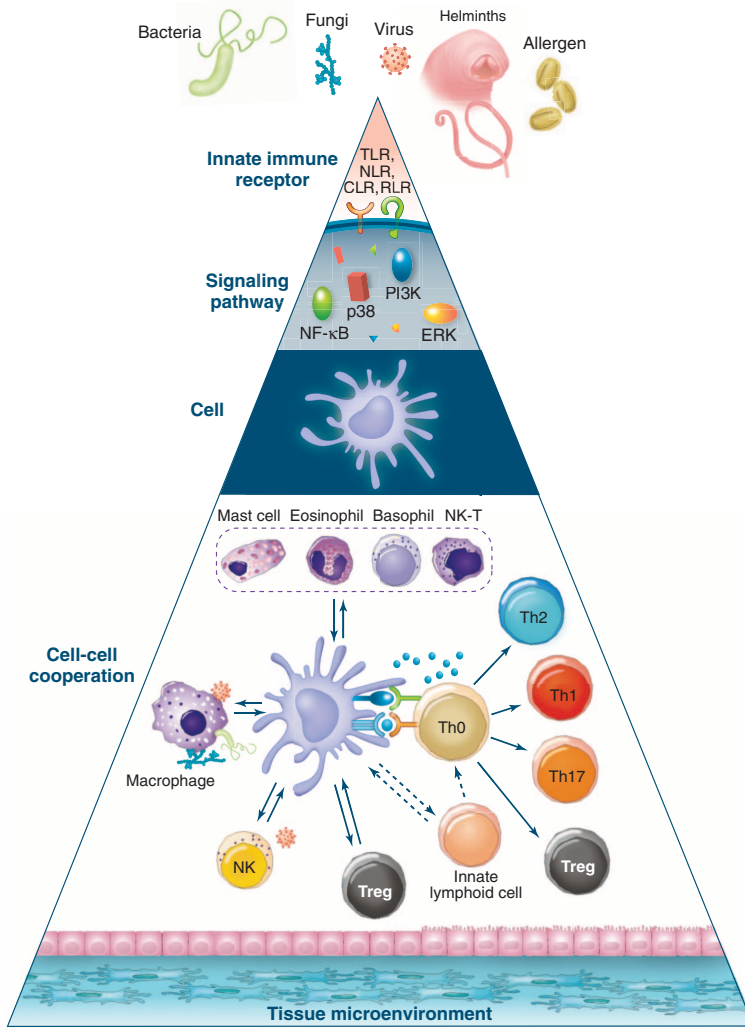


Fig. 3. Hierarchies of organization in the innate immune system. The complexity of the innate immune system in sensing stimuli and orchestrating type 2 immune responses can be conceptualized as occurring in different hierarchies of organization. The cell (that is, the dendritic cell) can be considered as the ground level; the innate receptors expressed by the cell and the signaling networks within the cell represent higher-resolution levels of the hierarchy. Conversely, cell-cell cooperation and the impact of the tissue microenvironment represent more global views of the hierarchy. This model offers a conceptual framework for therapeutic interventions to allergic inflammation. Thus, one might envision targeting the signaling level (for instance, by inhibiting ROS in DCs), the cellular level (for example, by inhibiting migration of cells such as DCs or basophils), or the cell-cell cooperation level (by inhibiting molecules such as TSLP, IL-25, and IL-33 that mediate cell interactions). RLR, RIG-I-like receptors; PI3K, phosphatidylinositol 3-kinase; NK-T, natural killer T cells.

antigen presentation to T cells during the initiation of T_H2 cell responses to allergens and helminths (53–55). Consistent with this notion, although DCs were required for T_H2 cell responses, depletion of basophils using an antibody against basophils resulted in impaired T_H2 responses to *Trichuris muris* (55). New genetic tools that have allowed the deletion of the majority of basophils in vivo suggest that type 2 responses can develop in the absence of basophils in some circumstances (57, 58). However, in these mice, basophils were constitutively deleted from birth, but not all basophils were deleted, so it is not clear whether compensatory mechanisms such as enhanced T_H2 -inducing capacities of other cells such as mast cells and DCs may contribute to developing type 2 responses in these settings. The extent to which DCs or basophils contribute to developing type 2 responses appears to be context-dependent. Differences in the relative roles of these two cell types observed in different studies may reflect differences in experimental conditions and models or, alternatively, may illuminate heterogeneity in the pathways that promote type 2 inflammation that can be influenced by stimulus- or tissue-dependent factors. This is clearly an area requiring further investigation.

What signals do DCs and basophils impart to promote T_H2 cell differentiation? In the case of T_H1 cells, IL-12 produced by DCs is essential, and it has been proposed that stimuli

deal of functional plasticity. Thus, pathogen products such as LPS from *P. gingivalis* (12), omega-1 [a T2 ribonuclease glycoprotein derived from *Schistosoma mansoni* egg antigen (SEA)] (43, 44), helminth-derived stimuli (45), cholera toxin (46), or allergens (47, 48) can all condition DCs to promote type 2 responses. Furthermore, the mediators of the allergic response, such as TSLP (which is produced by stromal cells and histamine), can stimulate DCs to induce T_H2 responses (49). Thus, certain DC subsets appear to have an intrinsic capacity to induce type 2 responses, and a multitude of microbial stimuli are reported to “condition” DCs to stimulate T_H2 responses.

But are DCs necessary and sufficient to induce type 2 responses against helminths or allergens? Several recent studies demonstrate that DCs are necessary for type 2 responses in vivo. For example, conditional ablation of DCs in vivo using CD11c–diphtheria toxin (DTR) mice abrogates T_H2 cell responses and allergen-induced asthma in an ovalbumin-driven asthma model (50). Furthermore, ablation of DCs in CD11c–DTR mice before immunization with antigen plus papain resulted in diminished T_H2 cell responses (25) and diminished T_H2 responses to

Nippostrongylus brasiliensis and *S. mansoni* (51, 52). Finally, a subset of FcεR1⁺ CD11c⁺ inflammatory DCs were shown to be necessary for the induction of T_H2 responses to inhaled HDM antigens (40).

Although DCs are important in the development of type 2 responses in many circumstances, several studies suggest that DCs were not sufficient for optimal type 2 responses after exposure to some allergens or helminth parasites (53–55). Subsequent studies demonstrated a role for basophils in cooperation with DCs in promoting T_H2 responses (25). Basophils constitute a minor population (<1%) of leukocytes in the blood and spleen and, upon activation, produce several effector molecules such as histamines, platelet-activating factors, leukotrienes, and the T_H2 cytokines IL-4 and IL-13 (56). These cells were believed to represent an innate source of T_H2 cytokines required for optimal type 2 responses. Consistent with this idea, basophils are rapidly recruited to the draining lymph nodes of mice injected with helminths or allergens within 24 hours and before the appearance of T_H2 cells (25, 53–55). Besides producing T_H2 -associated cytokines, in some circumstances basophils, and potentially other granulocytes, can contribute to

that fail to induce IL-12 in DCs program them to induce T_H2 responses (3, 4, 6). Evidence for this “default mechanism” of T_H2 cell response is observed with stimuli such as certain TLR2 ligands or allergens or helminth products that do not induce IL-12 (6). However, despite their failure to produce IL-12, DCs exposed to papain were incapable of inducing T_H2 responses (25). Rather, such DCs induced greatly diminished T_H1 cell responses, but T_H2 cell responses were not induced. An exogenous source of IL-4 (from basophils) was necessary for optimal T_H2 cell development (25). This is consistent with a number of previous studies demonstrating a key role for IL-4 in T_H2 cell responses after helminth infection. Basophils and mast cells are key producers of IL-4 during T_H2 cell development and rapidly produce IL-4 upon cross-linking of their FcεR1 receptors through preexisting antigen-IgE complexes (3, 4, 56, 59). This may be relevant in memory responses, in which preexisting antigen-specific T_H2 cells would have helped the production of antigen-specific IgE (59). However, in primary immune responses, activation of basophils and mast cells by allergens and helminths may lead to IL-4 production. Indeed, a recent report of heterogeneity within the basophil

population has revealed that TSLP-dependent basophils are activated independently of IgE and are more potent sources of IL-4 compared with classical IL-3-dependent basophils (60). Besides IL-4, other molecules on DCs, such as OX40-l (10) and the Notch ligands Jagged-1 and Jagged-2, can promote T_H2 responses (61).

Innate immune receptors. As discussed above, many TLR2 ligands induce type 2 responses (6). Furthermore, low doses of LPS have also been shown to induce T_H2 cells in response to intranasal immunization with protein antigens, by means of a TLR4- and MyD88-dependent mechanism (22). NLRs, which include Nod1 and Nod2, are a family of cytosolic proteins that sense peptidoglycans or peptides derived from their degradation. Immunization of mice with ligands specific for Nod1 or Nod2 induces T_H2 -biased responses (62). CLRs belong to a large superfamily of transmembrane and soluble proteins that sense carbohydrate components of several pathogens, as well as self-glycoproteins. Certain microbial stimuli that signal via DC-SIGN, a CLR with broad pathogen recognition specificity, induce T_H2 responses. For example, the LPS Lewis antigen (Le) of *Helicobacter pylori* induces T_H2 -biased responses through DC-SIGN (63).

Signaling networks. Very little is known about the signaling networks that program innate cells such as DCs to induce type 2 responses. Enhanced duration and magnitude of the extracellular signal-regulated mitogen-activated protein kinase (ERK MAPK), induced in DCs by certain TLR2 ligands or SEA, inhibits the production of IL-12p70, enhances IL-10 production, and programs DCs to stimulate T_H2 cell-biased responses (64). Enhanced and sustained ERK signaling results in phosphorylation and stabilization of the early growth transcription factor c-Fos, which suppresses IL-12p70 production (64). Additionally, more recent studies have revealed a role for the MAPK3 (Tpl2) in ERK activation in DCs. Macrophages from *Tpl2*^{-/-} mice display reduced c-Fos expression (65). Taken together, these results demonstrate an important role for ERK-fos signaling in inhibiting IL-12 in DCs and promoting T_H2 -biased responses. There are now several examples of diverse stimuli (e.g., Lactobacilli strains, complement proteins C5a and iC3b, ligands that activate DC-SIGN) that suppress IL-12 production via this pathway (6). Further work is required to assess the degree to which allergens and helminth products activate this pathway to promote type 2 responses.

Cell-cell cooperation and tissue microenvironment. DCs and basophils have been demonstrated to cooperate in the induction of type 2 immune responses, and this has been reviewed in detail elsewhere (6, 25). Furthermore, recent studies identified heterogeneous populations of ILCs (including natural helper cells, multipotent progenitor type 2 cells, nuocytes, and innate type 2 helper cells) as potent sources of T_H2 -associated cytokines that can promote type 2 responses. ILCs are activated by IL-25 and IL-33 secreted by epithelial cells and are a critical and early source of IL-5 and IL-13 (66–69). Influenza virus-induced airway hyperreac-

tivity is mediated by ILCs and activated by IL-33 produced from virus-triggered macrophages and epithelial cells. In allergen-mediated asthma, IL-25, IL-33, and TSLP produced by epithelial cells activate ILCs and can promote type 2 inflammation (66–69). Finally, the influence of T_{reg} s on type 2 inflammation has been well characterized and discussed extensively elsewhere. The recent report that extrathymically generated T_{reg} s control mucosal type 2 inflammation (70) and that deletion of the transcription factor interferon regulatory factor 4 (which is essential for T_H2 cell differentiation) from T_{reg} s led to allergic inflammation (71) highlights the intricate cellular network that promotes and regulates type 2 responses.

Summary and Future Challenges

A marked feature of type 2 responses is their diversity. There is diversity in terms of the array of stimuli that trigger type 2 responses, the mechanisms by which the innate immune system senses such stimuli, and the cellular and molecular pathways that orchestrate the response. Indeed, there even appears to be diversity in the cytokine profiles of responding cells in a T_H2 cell response, although whether such variants are functionally distinct remains to be established. We propose a conceptual framework to obtain an integrated understanding of how type 2 responses are initiated and controlled: The cell (the dendritic cell in this case) can be considered as the ground level, with innate receptors and signaling networks representing the subcellular levels and cell-cell cooperation and tissue microenvironments representing the supercellular levels (Fig. 3) (6). This hierarchy illuminates major challenges for the future, and we believe that such integrated understanding will come about from studying every level of the hierarchy with the use of systems biology approaches. Such approaches are likely to be particularly fruitful when used to study type 2 immune responses in humans in the context of helminth infections, allergic disorders, or vaccination (72). Greater access to human samples coupled with standardization of high-throughput technologies and reagents will accelerate progress in identifying putative molecular networks that orchestrate type 2 responses in human disease. The functional validation of such networks, involving their perturbation, will be facilitated by the establishment of more sophisticated animal models of type 2 inflammation.

References and Notes

- Pawankar, G. W. Canonica, S. T. Holgate, R. F. Lockey, *Curr. Opin. Allergy Clin. Immunol.* **12**, 39 (2012).
- P. J. Hotez et al., *N. Engl. J. Med.* **357**, 1018 (2007).
- W. E. Paul, J. Zhu, *Nat. Rev. Immunol.* **10**, 225 (2010).
- J. Zhu, H. Yamane, W. E. Paul, *Annu. Rev. Immunol.* **28**, 445 (2010).
- B. N. Lambrecht, H. Hammad, *Annu. Rev. Immunol.* **30**, 243 (2012).
- B. Pulendran, H. Tang, S. Manicassamy, *Nat. Immunol.* **11**, 647 (2010).
- R. L. Coffman, A. Sher, R. A. Seder, *Immunity* **33**, 492 (2010).
- N. W. Palm, R. K. Rosenstein, R. Medzhitov, *Nature* **484**, 465 (2012).
- A. Kelso, P. Groves, L. Ramm, A. G. Doyle, *Int. Immunol.* **11**, 617 (1999).

- T. Ito et al., *J. Exp. Med.* **202**, 1213 (2005).
- A. Pedroza-Gonzalez et al., *J. Exp. Med.* **208**, 479 (2011).
- B. Pulendran et al., *J. Immunol.* **167**, 5067 (2001).
- M. H. Wenink et al., *J. Immunol.* **183**, 6960 (2009).
- Y. H. Wang et al., *J. Exp. Med.* **207**, 2479 (2010).
- M. Veldhoen et al., *Nat. Immunol.* **9**, 1341 (2008).
- H.-E. Liang et al., *Nat. Immunol.* **13**, 58 (2012).
- P. C. Ronald, B. Beutler, *Science* **330**, 1061 (2010).
- T. Kawai, S. Akira, *Nat. Immunol.* **11**, 373 (2010).
- R. M. Steinman, J. Banchereau, *Nature* **449**, 419 (2007).
- H. Hammad et al., *Nat. Med.* **15**, 410 (2009).
- C. Braun-Fahrlander et al., *N. Engl. J. Med.* **347**, 869 (2002).
- S. C. Eisenbarth et al., *J. Exp. Med.* **196**, 1645 (2002).
- A. Trompette et al., *Nature* **457**, 585 (2009).
- M. Schmidt et al., *Nat. Immunol.* **11**, 814 (2010).
- H. Tang et al., *Nat. Immunol.* **11**, 608 (2010).
- N. A. Barrett et al., *J. Exp. Med.* **208**, 593 (2011).
- L. K. Poulsen, *Clin. Exp. Allergy* **39**, 623 (2009).
- C. Traidl-Hoffmann, T. Jakob, H. Behrendt, *J. Allergy Clin. Immunol.* **123**, 558 (2009).
- M. D. Chapman, A. Pomés, H. Breiteneder, F. Ferreira, *J. Allergy Clin. Immunol.* **119**, 414 (2007).
- R. Ramachandran, F. Noorbakhsh, K. Defea, M. D. Hollenberg, *Nat. Rev. Drug Discov.* **11**, 69 (2012).
- H. Kozuaki, S. M. O'Grady, C. B. Lawrence, H. Kita, *J. Immunol.* **183**, 1427 (2009).
- A. Briot et al., *J. Exp. Med.* **206**, 1135 (2009).
- J. E. Allen, T. A. Wynn, *PLoS Pathog.* **7**, e1002003 (2011).
- M. Kool et al., *Immunity* **34**, 527 (2011).
- T. Marichal et al., *Nat. Med.* **17**, 996 (2011).
- D. Yang et al., *J. Exp. Med.* **209**, 157 (2012).
- E. Godefroy et al., *Cancer Cell* **19**, 333 (2011).
- F. Chen et al., *Nat. Med.* **18**, 260 (2012).
- H. P. Harding, M. Calton, F. Urano, I. Novoa, D. Ron, *Annu. Rev. Cell Dev. Biol.* **18**, 575 (2002).
- H. Hammad et al., *J. Exp. Med.* **207**, 2097 (2010).
- M.-C. Rissoan et al., *Science* **283**, 1183 (1999).
- E. Klechevsky et al., *Immunity* **29**, 497 (2008).
- B. Everts et al., *J. Exp. Med.* **206**, 1673 (2009).
- S. Steinfelder et al., *J. Exp. Med.* **206**, 1681 (2009).
- M. Whelan et al., *J. Immunol.* **164**, 6453 (2000).
- M. C. Braun, J. He, C. Y. Wu, B. L. Kelsall, *J. Exp. Med.* **189**, 541 (1999).
- C. Traidl-Hoffmann et al., *J. Exp. Med.* **201**, 627 (2005).
- W. G. Shreffler et al., *J. Immunol.* **177**, 3677 (2006).
- V. Soumelis et al., *Nat. Immunol.* **3**, 673 (2002).
- L. S. van Rijk et al., *J. Exp. Med.* **201**, 981 (2005).
- C. Ohnmacht et al., *Immunity* **33**, 364 (2010).
- A. T. Phytlian-Adams et al., *J. Exp. Med.* **207**, 2089 (2010).
- T. Yoshimoto et al., *Nat. Immunol.* **10**, 706 (2009).
- C. L. Sokol et al., *Nat. Immunol.* **10**, 713 (2009).
- J. F. Perrigoue et al., *Nat. Immunol.* **10**, 697 (2009).
- H. Karasuyama, K. Mukai, K. Obata, Y. Tsujimura, T. Wada, *Annu. Rev. Immunol.* **29**, 45 (2011).
- D. Voehringer, *Curr. Opin. Immunol.* **23**, 789 (2011).
- B. M. Sullivan et al., *Nat. Immunol.* **12**, 527 (2011).
- M. V. Khodoun, T. Orekhova, C. Potter, S. Morris, F. D. Finkelman, *J. Exp. Med.* **200**, 857 (2004).
- M. C. Siracusa et al., *Nature* **477**, 229 (2011).
- D. Amsen et al., *Cell* **117**, 515 (2004).
- J. H. Fritz et al., *Immunity* **26**, 445 (2007).
- M. P. Bergman et al., *J. Exp. Med.* **200**, 979 (2004).
- S. Agrawal et al., *J. Immunol.* **171**, 4984 (2003).
- F. Kaiser et al., *J. Exp. Med.* **206**, 1863 (2009).
- K. Moro et al., *Nature* **463**, 540 (2010).
- S. A. Saenz et al., *Nature* **464**, 1362 (2010).
- D. R. Neill et al., *Nature* **464**, 1367 (2010).
- H. Spits, T. Cupedo, *Annu. Rev. Immunol.* **30**, 647 (2012).
- S. Z. Josefowicz et al., *Nature* **482**, 395 (2012).
- Y. Zheng et al., *Nature* **458**, 351 (2009).
- T. D. Querec et al., *Nat. Immunol.* **10**, 116 (2008).

Acknowledgments: Research in the Pulendran lab is supported by the NIH (grants U19AI090023, HHSN266200700006C, U54AI057157, R37AI48638, R37DK057665, U19AI057266, and N01 AI50025 to B.P.) and the Bill and Melinda Gates Foundation. Research in the Artis lab is supported by the NIH (grants AI061570, AI087990, AI074878, AI083480, AI095466, and AI095608 to D.A.) and the Burroughs Wellcome Fund Investigator in Pathogenesis of Infectious Disease Award (D.A.). We sincerely apologize to our colleagues that, owing to limitations of space, we were unable to cite many relevant references.

10.1126/science.12211064

Explosive Backpacks in Old Termite Workers

J. Šobotník,^{1*} T. Bourguignon,^{2,3*} R. Hanus,^{1,2†} Z. Demianová,¹ J. Pytelková,¹ M. Mareš,¹ P. Foltynová,⁴ J. Preisler,⁴ J. Cvačka,¹ J. Krasulová,^{1,5} Y. Roisin²

We send our young men to war; ants send their old ladies (*1*). This metaphor illustrates a long-known feature of insect societies: Older workers generally assume a larger share of defense, which may involve self-sacrifice (*2, 3*). In some termites, suicidal defense by bursting is performed by soldiers (*4*), but, because defense is their sole function, there is little potential for age dependence. However, in a few species, workers are known to rupture and release a sticky fluid (*4*). Because workers perform a variety of tasks, this readiness for suicidal defense would be expected to increase as their aptitude for other tasks declines.

Neocapritermes taracua is a neotropical termite commonly found in decayed wood on which it feeds (*5*). Close examination of workers reveals in many (hereafter blue workers) a pair of dark blue, elongated dorsal spots at the thorax-abdomen junction (Fig. 1A). These spots are variously developed among workers and are lacking in some individuals (white workers). During aggressive encounters with other termites, blue workers actively bite and, when hampered, burst and emit a drop of fluid, which in a few seconds becomes sticky as the blue color fades out (Fig. 1B and movie S1).

The blue spots are a pair of crystal-like structures (Fig. 1C) enclosed within pouches formed by posterior outgrowths of the metanotum over the first abdominal segment. The crystals are produced by a pair of glands (crystal glands) located below the epidermal cell layer at the anterior part of each pouch (Fig. 1D). The dorsal apparatus also comprises the salivary glands, producing secretion granules stored below the dorsal wall (Fig. 1D).

Mandibles of *Neocapritermes* workers wear out with time and usage because they cannot be renewed by molting (*6*) (fig. S1A). Mature workers showed a positive correlation between fresh weight and mandible sharpness index and a negative relationship between crystal weight and mandible sharpness index, indicating that, as the feeding efficiency of workers decreases, they build up their backpacks for suicidal fighting (fig. S1, B and C).

Blue workers were more aggressive than white workers toward other soil-feeding termites, such as *Labiatermes labralis*, and they burst sooner after being seized by their oppo-

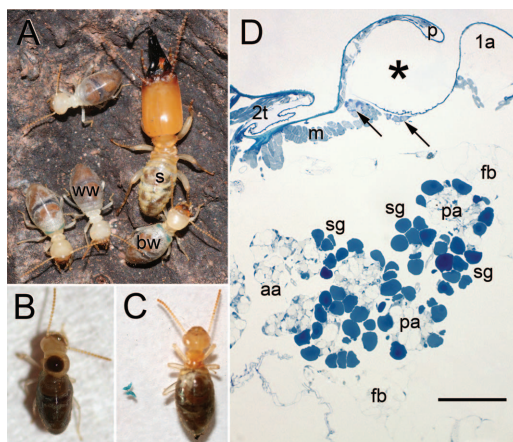


Fig. 1. Anatomy of the defensive apparatus of *N. taracua*. (A) Soldier (s) with two blue (bw) and two white workers (ww). (B) Blue worker after autothysis triggered by grasping it with tweezers. (C) Blue worker after removal of the blue crystals (placed next to it). (D) Section of anterior abdomen of a blue worker. Asterisk marks crystal-bearing pouch (crystal dissolved); arrows mark crystal gland cells. Scale bar, 200 μ m. 1a, first abdominal segment; 2t, mesothorax; aa, anterior acini (clumps of secretory cells); fb, fat body; m, muscles; p, dorsal part of the crystal-bearing pouch; pa, posterior acini; sg, aggregates of secretion granules budding off posterior acini.

nent (fig. S2). Bursting liquid from blue workers was more effective than liquid from white workers against *L. labralis* (table S1). Removing the blue crystals reduced the toxicity of blue workers to the level of white workers. Reciprocally, the toxicity of white worker bursting fluid was enhanced by the addition of blue crystals but remained lower than that of blue workers (table S1). This pinpoints the importance of the reaction between blue crystals and salivary secretion to achieve toxicity.

An important component of the blue crystal is a 76-kD protein (hereafter called BP76) as judged from the protein pattern on a 15% SDS-polyacrylamide gel electrophoresis (PAGE), and by a single blue band on the 10% native PAGE gel (fig. S3A). By using mass spectrometric meth-

ods, we confirmed the molecular weight of BP76 (fig. S3B) and detected the presence of 9 ± 2 ng (SD) of copper per crystal (fig. S3, C and D). Its molecular weight, color, and copper content suggest that BP76 is an oxygen-binding type III copper protein of the hemocyanin/phenoloxidase family, known to occur in arthropods (*7*).

The defensive apparatus of *N. taracua* is exceptional. First, it involves a previously unknown exocrine gland, unusual in its product (the copper-containing blue crystal protein) and its storage (the external “backpack” pouches). Second, its efficacy derives from the reaction, upon autothysis, of the labial gland secretion and the blue crystals. Consistent with theory, workers develop this weaponry and increase their proneness to use it as their feeding efficiency decreases when their mandibles become worn.

References and Notes

1. B. Hölldobler, E. O. Wilson, *The Ants* (Springer, Berlin, 1990), p. 179.
2. G. E. Robinson, *Annu. Rev. Entomol.* **37**, 637 (1992).
3. J. R. Shorter, O. Rueppell, *Insectes Soc.* **59**, 1 (2012).
4. J. Šobotník, A. Jirosová, R. Hanus, *J. Insect Physiol.* **56**, 1012 (2010).
5. T. Bourguignon *et al.*, *Ecol. Entomol.* **36**, 261 (2011).
6. P. Kaiser, *Mitt. Hamb. Zool. Mus. Inst.* **54**, 129 (1956).
7. H. Decker, F. Tuzek, *Trends Biochem. Sci.* **25**, 392 (2000).

Acknowledgments: We are grateful to P. Cerdan and the staff of the Hydreco lab at Petit Saut for logistical help. Support was provided by the Fund for Scientific Research (F.R.S.-FNRS, Belgium); the Japan Society for Promotion of Science (no. 22-00393); the Grant Agency of the Czech Republic (P600/525/09, P206/12/0538); the Institute of Organic Chemistry and Biochemistry, Academy of Sciences of the Czech Republic (Z4050506); and the project CEITEC (CZ.1.05/1.1.00/02.0068) from the European Regional Development Fund. The data reported in this paper are presented in the supplementary materials.

Supplementary Materials

www.sciencemag.org/cgi/content/full/337/6093/436/DC1
Materials and Methods
Figs. S1 to S3
Table S1
References (8–11)
Movie S1

13 January 2012; accepted 12 April 2012
10.1126/science.1219129

¹Institute of Organic Chemistry and Biochemistry, Academy of Sciences of the Czech Republic, 166 10 Prague, Czech Republic.

²Evolutionary Biology and Ecology, Université Libre de Bruxelles, 1050 Brussels, Belgium. ³Graduate School of Environmental Science, Hokkaido University, Sapporo 060-0810, Japan. ⁴CEITEC (Central European Institute of Technology) and Department of Chemistry, Faculty of Science, Masaryk University, 625 00 Brno, Czech Republic. ⁵Department of Analytical Chemistry, Faculty of Science, Charles University in Prague, Albertov 6, 128 43 Prague, Czech Republic.

*These authors contributed equally to this work.

†To whom correspondence should be addressed. E-mail: robert@uochb.cas.cz

The Connectome of a Decision-Making Neural Network

Travis A. Jarrell,^{1*} Yi Wang,^{1*} Adam E. Bloniarz,^{1†} Christopher A. Brittin,¹ Meng Xu,¹ J. Nichol Thomson,² Donna G. Albertson,^{2‡} David H. Hall,³ Scott W. Emmons^{1,3§}

In order to understand the nervous system, it is necessary to know the synaptic connections between the neurons, yet to date, only the wiring diagram of the adult hermaphrodite of the nematode *Caenorhabditis elegans* has been determined. Here, we present the wiring diagram of the posterior nervous system of the *C. elegans* adult male, reconstructed from serial electron micrograph sections. This region of the male nervous system contains the sexually dimorphic circuits for mating. The synaptic connections, both chemical and gap junctional, form a neural network with four striking features: multiple, parallel, short synaptic pathways directly connecting sensory neurons to end organs; recurrent and reciprocal connectivity among sensory neurons; modular substructure; and interneurons acting in feedforward loops. These features help to explain how the network robustly and rapidly selects and executes the steps of a behavioral program on the basis of the inputs from multiple sensory neurons.

Animal nervous systems are composed of very large numbers of electrical cells intricately coupled together in complex dynamic networks. Connectionist theories of the nervous system propose that its function is an emergent property of network connectivity. Although the question has been extensively addressed theoretically, the sets of physical connections between neurons within actual nervous systems remain to be described. This is due to the necessity of using electron microscopy (EM) to visualize the subcellular organelles that create the synapses, a technique not amenable to analyzing large structures. To date, the anatomical wiring diagram of only a single animal nervous system has been obtained, that of the adult hermaphrodite of *Caenorhabditis elegans*, published more than 25 years ago (1, 2).

We identified all the chemical and gap junction synapses, the connectome, in the posterior nervous system of the *C. elegans* adult male. This part of the male nervous system contains the circuits and end organs that govern mating behavior (Fig. 1, A and B). In spite of having a relatively simple nervous system, comprising just 302 neurons in the adult hermaphrodite and 383 in the adult male, *C. elegans* expresses a rich and com-

plex behavioral repertoire (3, 4). Many of these behaviors, most notably the sexual behaviors of the male, model the goal-oriented, purposeful activities controlled by decision-making processes characteristic of animal behavior (5). The well-fed adult male actively seeks out the hermaphrodite mating partner (6–9). Physical contact with the hermaphrodite triggers copulation. Copulation consists of a series of stereotyped actions that lead the male to locate the hermaphrodite's vulva, insert its spicules, and transfer sperm (10, 11) (Fig. 1A and movie S1). This multistep behavioral pathway is guided by the activities of 52 sensory neurons located in sexual structures in the tail acting both directly and through interneurons and motoneurons to control 64 muscles and the gonad (Figs. 1B and 2). For success, the male's reactions must be quick (<1 s), because self-fertile *C. elegans* hermaphrodites do not cooperate and may even be resistant to mating (12, 13). The *C. elegans* male posterior nervous system shows how the nervous system evaluates a multiplicity of environmental inputs, makes a rapid behavioral choice, and generates coherent, purposeful behavior.

EM reconstruction of the mating circuits. We determined the male posterior connectome by serial section EM (Fig. 1, C to H) (14). The feasibility of comprehensive synapse-level nervous system reconstruction by this method was a primary reason for the initial selection of *C. elegans* as an experimental model (15). We developed a PC-based software platform to facilitate assembly of a connectome from electron micrographic images. The connectome is of a single adult animal and was produced from a series of 5000 serial thin sections of 70 to 90 nm encompassing the posterior one-half of the body (fig. S1 and databases S1 to S4) (16). It comprises the processes of 170 neurons (89 shared with the hermaphrodite and 81 male-specific) and 64 muscles (24

shared and 40 male-specific) (databases S5 and S6). Among the 170 neurons, 144 lie on synaptic pathways connecting sensory inputs to the end organs involved in mating. These generate the presumptive mating circuits. The remaining 26 neurons, not considered further here, are present in the hermaphrodite as well, with little difference in connectivity and have little or no interaction with male-specific neurons or circuits (database S7).

Properties of the neural network. The 144 neurons, 64 muscles, and gonad that comprise the mating circuits are joined together by both chemical and gap junction synapses (Fig. 3). To analyze this structural network, we took advantage of the mathematical methods of graph theory. If the connectome is considered as a graph, the neurons and muscles are the nodes or vertices. The links or edges connecting vertices represent the total amount of pairwise connectivity resulting from the often multiple (up to 61) separate synapses connecting pairs of cells (fig. S2). Linked vertices are said to be adjacent or neighbors in the graph. In the graph of the male mating circuits, each vertex has multiple neighbors (Fig. 4A). Edges may be directed, if they represent chemical synapses or rectifying gap junctions, or undirected, if they represent nonrectifying gap junctions.

The graph of the connectome may be considered to contain three main subgraphs: (i) a directed graph encompassing the neurons, muscles, and gonad and the chemical connections between them, (ii) a graph of the neurons and their gap junction connections, and (iii) a graph of the muscles and the gap junction connections between them (28 gap junction edges connect neurons to muscles) (Fig. 3). In addition, there are synapses scattered on the hypodermis. Each of the main subgraphs describes a small-world network (17). Small-world networks are characterized by having a high value of the clustering coefficient, the probability that, if two vertices are each connected to a common third vertex, then they are connected to each other and, at the same time, low values of the characteristic path length, the average minimum number of edges separating any two vertices. High clustering coefficient suggests local computation, and short path length suggests rapid communication across the network. For the male networks, clustering coefficients are greater than 0.3, and minimum path lengths are <3 steps between pairs of neurons and muscles (table S1). For the entire hermaphrodite chemical network, also a small-world network, the clustering coefficient is 0.22, and the mean path length is 3.48 steps (2).

The dynamic properties of a neural network depend on the functional strengths of the synaptic interactions between the cells—in the terms of graph theory, the weights of the edges. To estimate functional strengths from the structure, we judged the physical size of each synapse from the size of the presynaptic density or gap junction

¹Department of Genetics, Albert Einstein College of Medicine, 1300 Morris Park Avenue, Bronx, NY 10461, USA. ²Medical Research Council Laboratory of Molecular Biology, Hills Road, Cambridge CB2 0QH, UK. ³Dominick P. Purpura Department of Neuroscience, Albert Einstein College of Medicine, 1300 Morris Park Avenue, Bronx, NY 10461, USA.

*These authors contributed equally to this work.

†Present address: Department of Statistics, University of California, Berkeley, Berkeley, CA 94720, USA.

‡Present address: Helen Diller Family Comprehensive Cancer Center, University of California, San Francisco, 1450 Third Street, San Francisco, CA 94158, USA.

§To whom correspondence should be addressed. E-mail: scott.emmons@einstein.yu.edu

structure and summed over all the synapses between each pair of cells (16). (The resulting structural weight adjacency matrices for the chemical and gap junction networks are given as databases S8 and S9). Individual presynaptic densities varied in size over a 40-fold range, whereas individual gap junctions varied in size over a 30-fold range (fig. S2). As a result of the variation in both number of synapses between pairs

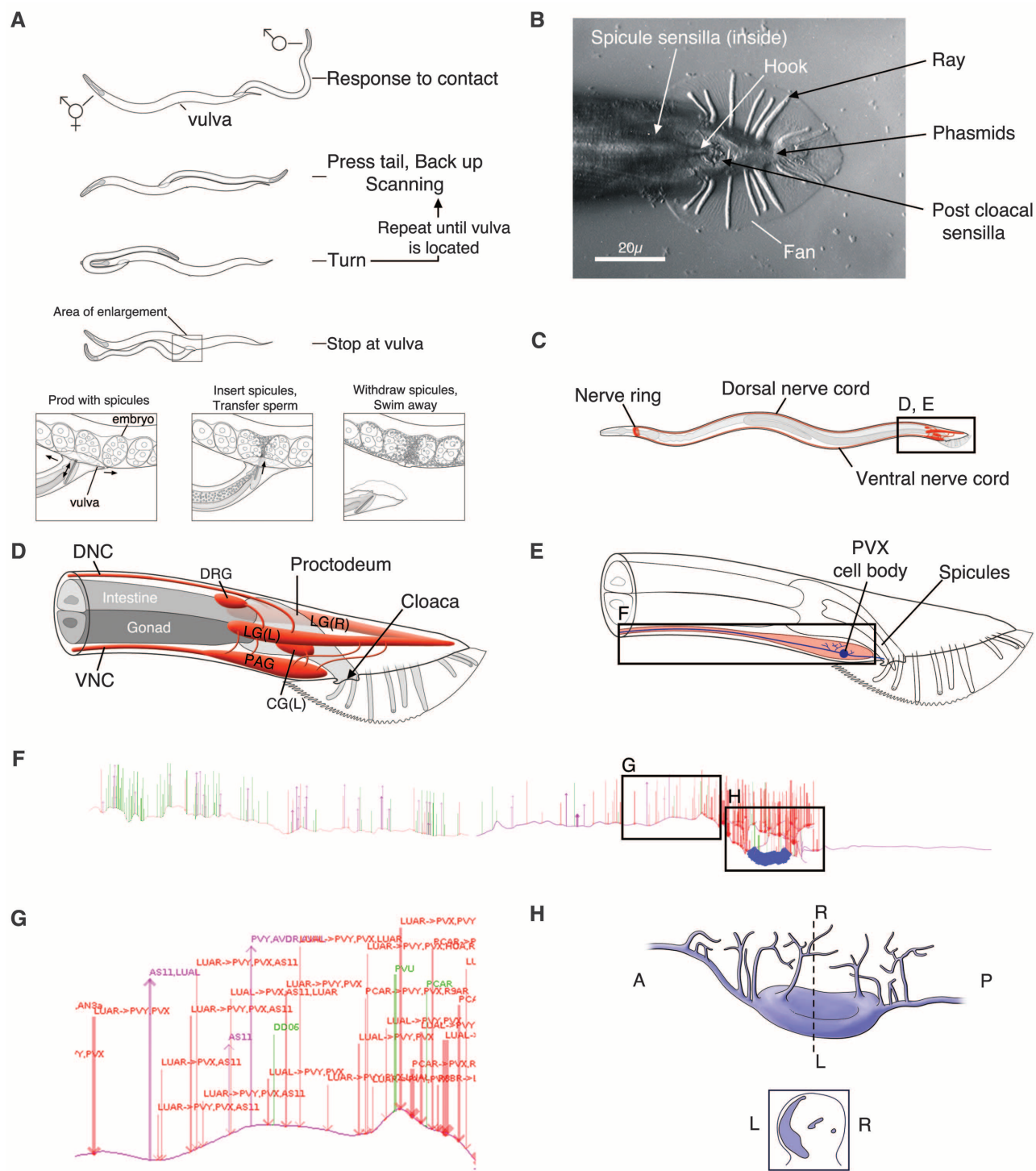


Fig. 1. Specializations of the *C. elegans* adult male tail for mating. (A) The substeps of mating. (B) Ventral view of the adult male tail showing mating structures with five types of sensilla. (C) Overall structure of the male nervous system. (D) Ganglia in the tail containing the neuron cell bodies, connected through commissures. Most synaptic connectivity occurs in the preanal ganglion (PAG). DNC, dorsal nerve cord; VNC, ventral nerve cord; DRG, dorsorectal ganglion; LG, lumbar ganglion (left and right); CG, cloacal ganglion (left and right). (E) An example of a male-specific interneuron, PVX, which has a cell body and extensive sensory input in the PAG, and a

process extending into the VNC, where there is output onto motorneurons and muscles. (F) Overall structure of PVX showing distribution of synapses (dorsal view). Red: chemical input; magenta: chemical output; green: gap junction. (G) Detail of individual synapses showing synaptic partners. Many chemical synapses are dyadic or polyadic. Width of lines indicates synapse size. Intermingling of input and output is consistent with PVX being a graded potential neuron (46). (H) Branching structure around the PVX cell body (dorsal view). The cell body forms a crescent shape lying against the basement membrane surrounding the PAG (transverse section in inset).

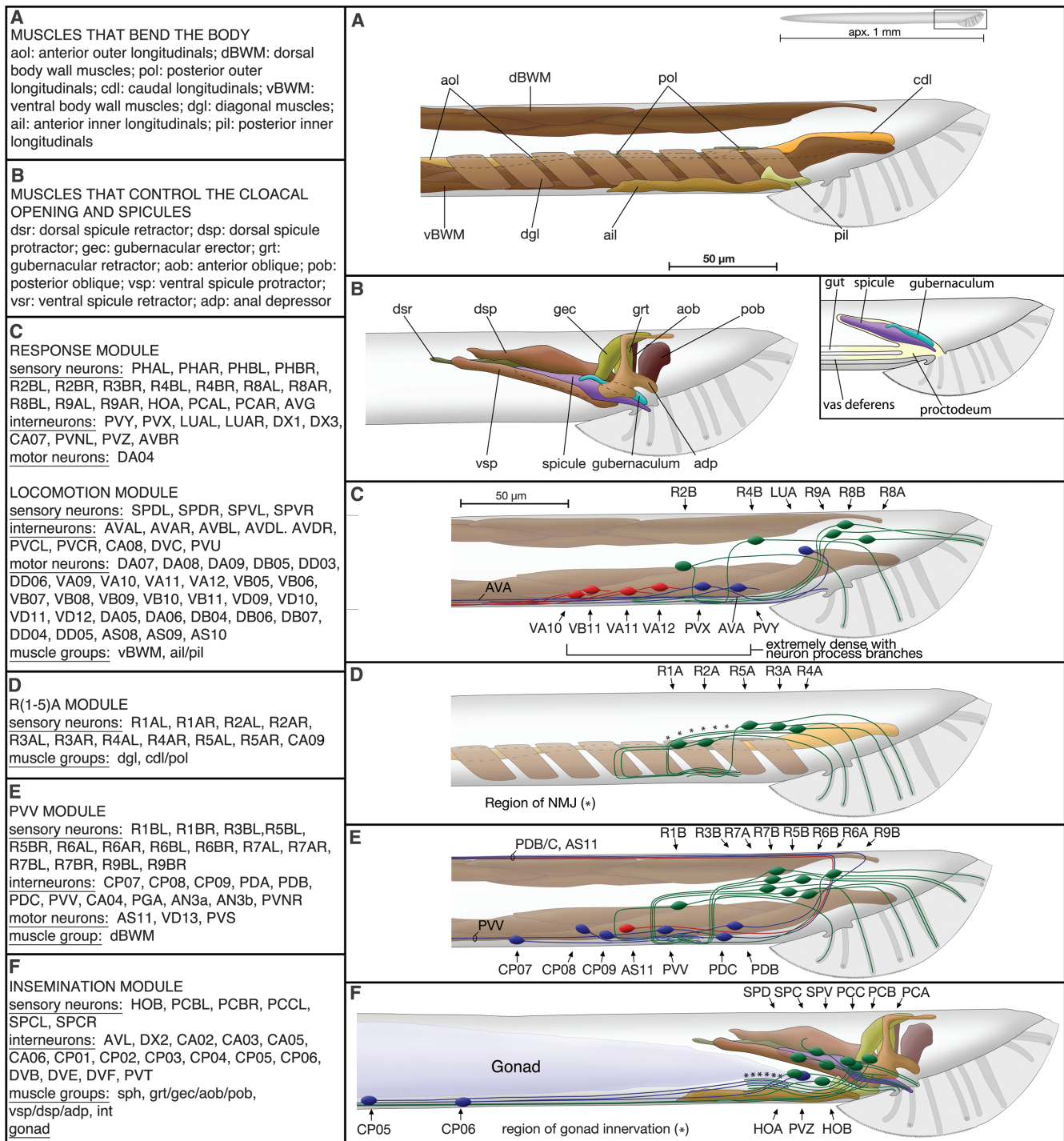


Fig. 2. The neurons and muscles of the mating circuits. (A) and (B) show the muscles. (C to F) The left column lists the neurons and muscles grouped into mathematically defined “modules” on the basis of their connectivity that match elements of mating behavior (Fig. 1A); the right column illustrates the locations of the cell bodies and processes of the key neurons in each module together with the muscles that are targeted (sensory neurons: green; interneurons: blue; motor neurons: red). (C) Response and Locomotion modules. The key sensory input to the Response module is from the B-type neurons of the subset of rays with openings on the ventral side of the fan, rays 2, 4, and 8. The dendritic endings of these neurons will be in contact with the hermaphrodite body when the male is correctly oriented to mate. Experimental evidence indicates that the B-type ray neurons promote the Response step (27, 26). The Response module drives the Locomotion module, containing body-wall motor neurons, via the command interneurons. (D) R(1-5)A module. Neuromuscular junctions of the A-type ray neurons onto the

diagonal and longitudinal muscles are consistent with experimental evidence for a role of these sensory neurons in promoting ventral curling of the tail during mating (25). (E) PVV module. This module, so-named for the large, male-specific PVV interneuron, has output onto the ventral body-wall motor system, via PVV, and onto the dorsal body-wall muscles, via PDA, PDB, PDC, and AS11. The dual innervation of both dorsal and ventral gender-shared body-wall muscles, mostly bypassing the command interneurons, suggests that this module, like the R(1-5)A module, is involved in aspects of male posture during mating (47). (F) Insemination module. This module will take over the male’s behavior once the vulva is sensed. All the neurons involved in insemination are shown here, although PCA, owing to its strong connection to PVX; HOA, owing to its connection to LUA; and PVZ, owing to its connection to HOA are all in the Response module, whereas SPD, because of its muscle output, and SPV, because of its connection to SPD, are in the Locomotion module (see Fig. 6).

of cells and sizes of individual synapses, total morphometric connectivity weights vary more than 100-fold and cover a continuous range of values (Fig. 4B). Each neuron has both strong and weak synaptic partners (Fig. 4C). Structural weights are likely to be related to the functional strengths of the synaptic interactions (18), but the signs of the chemical interactions, that is whether a given synapse is excitatory or inhibitory, cannot be determined from the electron micrographs.

We next asked whether all of the interactions, including the large number of weak interactions, are likely to be significant to network function. Weak connections (chemical connections of less than 20 sections and gap junction connections of less than 16 sections) carried half the load through the respective graphs (Fig. 4D). For both chemical and gap junction networks, left-right homologs—presumptively equivalent cells—had similar sets of synaptic partners, and this was true even when only the connections in their weaker set were compared (fig. S3) (16). Therefore, at least some of the weaker connections are not random. For the purpose of exploring network structure, we have included all synaptic interactions in our analysis.

Information flow through the network. With the morphological sizes of the physical connections serving as proxies for functional synaptic strengths, the weight adjacency matrices allow us to trace a hypothetical overall information flow through the network from sensory input to end-organ output (Fig. 5A). Much of this information flow is through monosynaptic pathways. Fifty-five percent of the input to the motor system (muscles, body-wall motor neurons, and command interneurons) comes directly from sensory neurons, including 45% of the input to the muscles themselves. Similarly, 76% of the input to the gonad comes directly

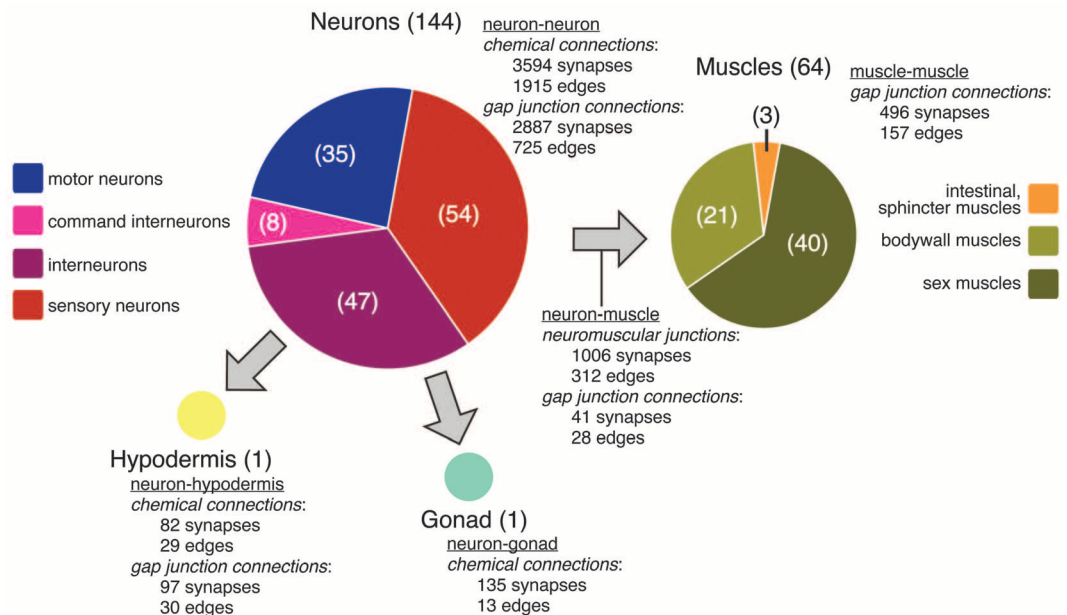
from sensory neurons and is expected to control outflow of sperm during mating. The remaining input to the motor system and gonad comes from a subset of 32 neurons that we classify as interneurons because they have considerable output onto other neurons, including motor neurons, but some of them also form neuromuscular junctions and, hence, have motor neuron character as well (databases S8 and S9). Because these interneurons all receive sensory input, much of the remaining information flow to the end organs is through disynaptic pathways, and the network has an overall feedforward-loop architecture. The virtual absence of neural feedback from the end organs means that it is the physical output of the system—the male's motion with respect to the hermaphrodite and sperm transfer—that feeds back to the sensory inputs to provide control to the network.

In addition to the interneurons that participate locally in the mating circuits, which we term type I interneurons, a second class of 12 interneurons (type II interneurons) interacts with neurons and end organs in the mating circuits and, in addition, they have a process extending through the ventral nerve cord and into the nerve ring, where they presumably interact with the anterior nervous system through connections that are yet to be determined. Type II interneurons are likely to play a role in coordinating mating with other behavioral programs. In support of this conclusion, the mate-searching behavioral state, which is stimulated by the male rays, requires communication to the anterior through three male-specific type II interneurons—EF1, EF2, and EF3—which receive extensive input from sensory neurons, particularly B-type ray sensory neurons (8). In the posterior circuits, type II interneurons interact (both input and output) primarily with sensory neurons and, to a lesser extent, with the type I interneurons.

The locally acting type I interneurons can be further subdivided into three subtypes based on the nature of their primary postsynaptic targets (Fig. 5, B and C). Type Ia, consisting of 14 neurons in six classes, has output primarily onto the end organs—elements of the motor system or the gonad or both. Information flow through the Ia interneurons is strongly feedforward. Type Ib, consisting of 10 neurons in three classes, has output primarily onto type Ia interneurons and also has feedback onto sensory neurons. Type Ic, consisting of seven neurons in two classes, is connected to sensory neurons, type Ia interneurons, and end organs (the spicule muscles) in such a way as to suggest that this class of interneurons mediates ending mating or moving the program to an earlier step (supplementary text and fig. S11).

Network community structure identifies subcircuits for separate functions in mating. To map the behavioral program for mating onto the connectome and to ask whether each substep has a dedicated neural substrate, we examined the network for modular architecture (19). Modules or communities in a graph are subsets of vertices more strongly connected to each other than to vertices in other communities. Using the spectral method (20) for optimal network partitioning, we found that the network could be partitioned with high statistical significance into five meaningful communities (modularity coefficient $Q = 0.451$; $P < 10^{-7}$) (Fig. 2) (16). Other methods for graph partitioning gave similar results (supplementary text). These communities placed the sensory neurons into coherent receptive fields. The neurons and end organs suggest that they contain subcircuits dedicated, respectively, to the search for the vulva [Response step (21)], locomotion, posture (two communities), and insemination. These functional assignments and the cellular composition of

Fig. 3. Total numbers of vertices (numbers in parentheses), synapses, and edges in the subgraphs of the posterior connectome. For comparison, the graph of neuron-to-neuron connections for the entire hermaphrodite nervous system (excluding the 20 neurons of the pharyngeal nervous system) has 279 vertices (neurons), 2194 directed chemical edges, and 514 gap junction edges (2). The numbers of chemical and gap junction edges in the subgraph of neuron-to-neuron connections are, respectively, 11% and 10% of the total number of possible edges among the 144 neurons.



each module correlate well with experimental evidence (21–26).

Sensory neurons are recurrently connected.

Whereas much of the information flow through the network from sensory neurons to end organs—either in monosynaptic pathways or through type Ia interneurons in disynaptic pathways—is feedforward, the 52 sensory neurons are extensively reciprocally and recurrently connected by both chemical and gap junction synapses. Forty-nine percent of the chemical synaptic output of sensory neurons is onto other sensory

neurons, and this constitutes input to the sensory neurons that is seven times the feedback from type Ib and type Ic interneurons. Nineteen out of the 36 ray sensory neurons make autapses, constituting 6.9% of their input from sensory neurons. Fifty-eight percent of the gap junction connectivity of the sensory neurons is with other sensory neurons.

Only on the basis of the recurrent connectivity of the sensory neurons and their connections to the type Ib interneurons, the network of sensory neurons could be partitioned into a set

of modules similar to those of the entire network (supplementary text) (fig. S6). Recurrent and reciprocal connectivity of sensory neurons is expected to amplify input signals through loop gain. Recurrent dynamic networks may exhibit fixed point or attractor behavior characterized by feedback-reinforced stable modes of network activity (27, 28). Modularity at the level of the sensory neurons suggests that sensory input may drive the network into discrete modes of self-reinforcing activity, each associated with one aspect or substep of the mating program (29, 30).

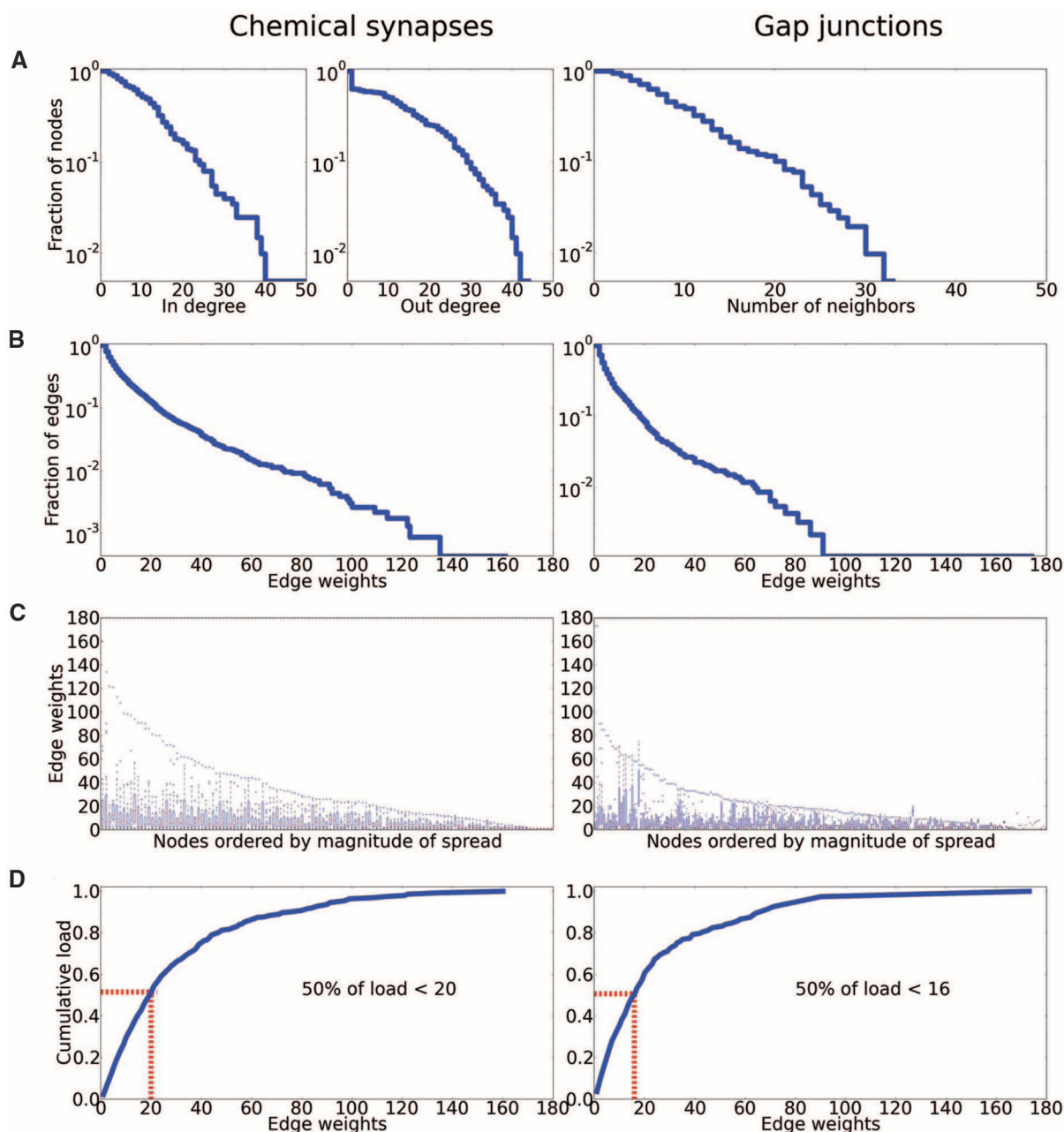


Fig. 4. Network properties of the connectome. **(A)** Degree (neighbor) distributions (number of edges for each vertex) in the chemical and gap junction networks (survival function). **(B)** Distributions of the edge weights (survival function). Edge weights are determined by counting the number of 70- to 90-nm serial sections crossed by individual synapses and sum-

ming over all the synapses between pairs of neurons and muscles. **(C)** Each neuron has a range of stronger and weaker synaptic partners. Points on the abscissa give the strengths of the individual edges of a given vertex. **(D)** Distribution of cumulative load versus edge weight. Weak connections carry a significant fraction of the load through the network.

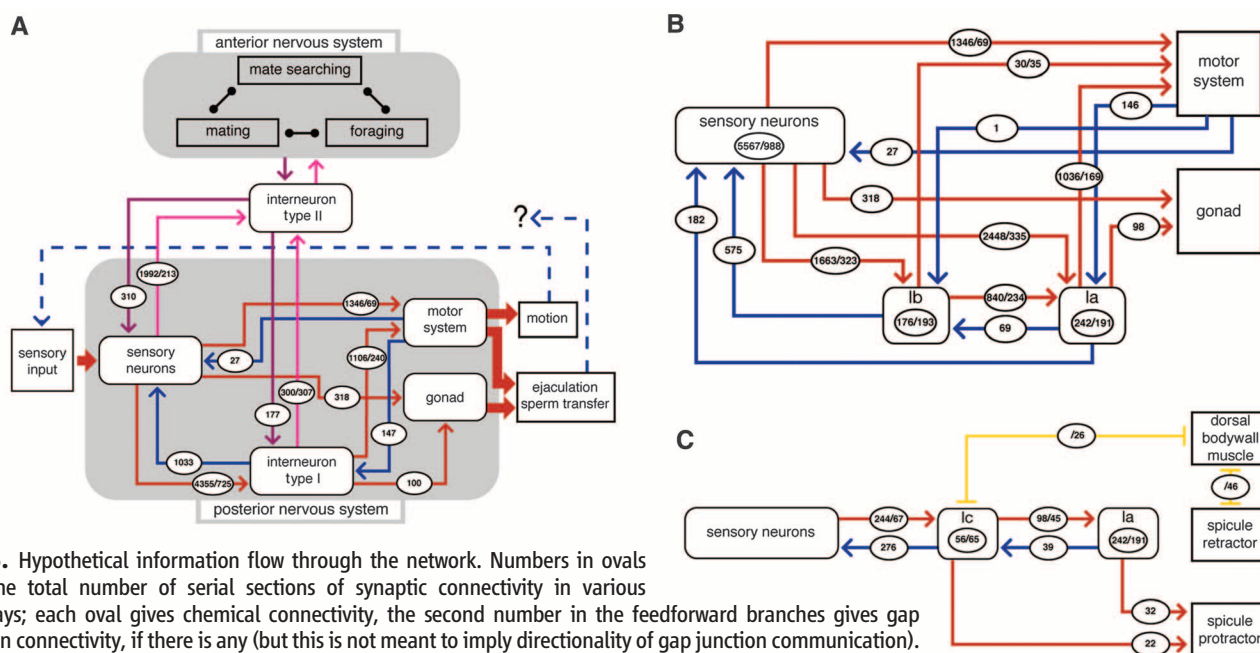


Fig. 5. Hypothetical information flow through the network. Numbers in ovals give the total number of serial sections of synaptic connectivity in various pathways; each oval gives chemical connectivity, the second number in the feedforward branches gives gap junction connectivity, if there is any (but this is not meant to imply directionality of gap junction communication). Ovals placed inside a box in (B) and (C) represent synaptic interactions within a class. **(A)** Global information flow. Information flow between sensory neurons and end organs is both direct in monosynaptic pathways and via interneurons. A second class of interneurons communicates to the head. **(B)** Two layers of interneurons convey information to the end organs. Information flow through the type Ia layer is almost exclusively feedforward. **(C)** A third class of interneurons has feedback onto sensory neurons and output onto elements of the ejaculatory circuits, including the spicule muscles, which suggests that this class is involved in ending mating (see supplementary materials for greater detail of the type Ic circuits).

Information flow through interneurons creates feedforward loops. The male mating circuits have a statistically high frequency of feedforward loops (fig. S10). Examination of the feedforward circuits through the Ia and Ib interneurons reveals that these circuits are loops in which, for each interneuron class, input sources and output targets are themselves connected (Fig. 6A). At a finer level of detail, Fig. 6B illustrates this role of the CP(01-06) class in the Insemination module.

The function of a feedforward loop depends on whether the net signs of the two branches are the same (coherent feedforward loop) or opposite (incoherent feedforward loop) (31, 32). Because the targets receiving input from CP(01-06) would all seem to function together during insemination behavior at the vulva, it appears most likely that the feedforward loops created by the CP(01-06) class are coherent feedforward loops. They pool sensory inputs and may serve to coordinate the actions of end organs that individually receive much of their input from different sets of sensory neurons. Their activity may, in addition, reinforce and sustain the activity within the insemination module. As a similar logic can be applied to the other feedforward loops in the network, each may be a coherent feedforward loop. Coordination and reinforcement of functional pathways that receive multiple sensory inputs and have multiple end-organ targets may be the general function of interneurons and this circuit motif here.

Conclusion. Mating is typically a complex behavior essential for the survival of most spe-

cies. In the *C. elegans* male, enlargement of the posterior nervous system in support of this behavior adds some 30% more neurons and complex connectivity equal to that of the entire hermaphrodite nervous system. Connectomics emphasizes the importance of a complete, synapse-level structural description of the nervous system for understanding nervous system function (33–39). Our structural analysis allowed us to define the neural substrate for mating behavior, to identify classes of neurons and assign functions to them, and to suggest how the topology of the network of connections contributes to the control of behavioral output.

The brain performs certain types of computations far faster, more robustly, and with much less power consumption than digital computers based on semiconductors and Von Neumann architecture (27, 40). Parallel distributed processing and recurrent connectivity are thought to provide part of the explanation for these properties. Both of these structural principles are present in the *C. elegans* male mating neural network. Sensory information is aggregated at three levels through the network—at the level of recurrent connectivity among the sensory neurons; at the end organs, which receive direct sensory input from multiple sensory neurons; and at the interneurons. Information flow to each end organ through many parallel pathways will ensure network robustness. Recurrent connectivity among the sensory neurons and between sensory neurons and the type Ib interneurons suggests that, at these levels, the network could have so-called attractor dynamics. Attractor dynamics are char-

acterized by abrupt transitions between self-reinforcing stable modes of network activity (41–43). Such rapid shifts in behavior are observed in *C. elegans* male mating. If the male mating network exhibits attractor dynamics, then, as a transition in network output occurs as a direct result of a change in sensory input, decision-making and behavioral switching are one and the same event. In this way, the structure could provide economy and efficiency. In contrast to the recurrent connectivity of the sensory neurons, aggregation of sensory information at the level of the type Ia and Ib interneurons in feedforward pathways suggests the architecture of a perceptron (44). Indeed, the system may be considered to solve a pattern recognition or classification problem, where the male attempts to interpret correctly its position with respect to the hermaphrodite.

The set of activity weights in an adjacency matrix of a neural network, upon which the network's input-output function in part depends, may be considered the network's "knowledge" about its environment (45). Because *C. elegans* male mating is an innate behavior, the weights in the mating neural network, both physical, as measured here, and functional, are genetically specified. Genetic specification is evident in the reproducibility of the connectivity of presumptively equivalent neurons, such as left-right homologs, as well as in the sexual dimorphism of certain shared neurons (sexual phenotype is thought to be cell-autonomous in *C. elegans*). Because the network's structure is genetically encoded, the learning algorithm by which this

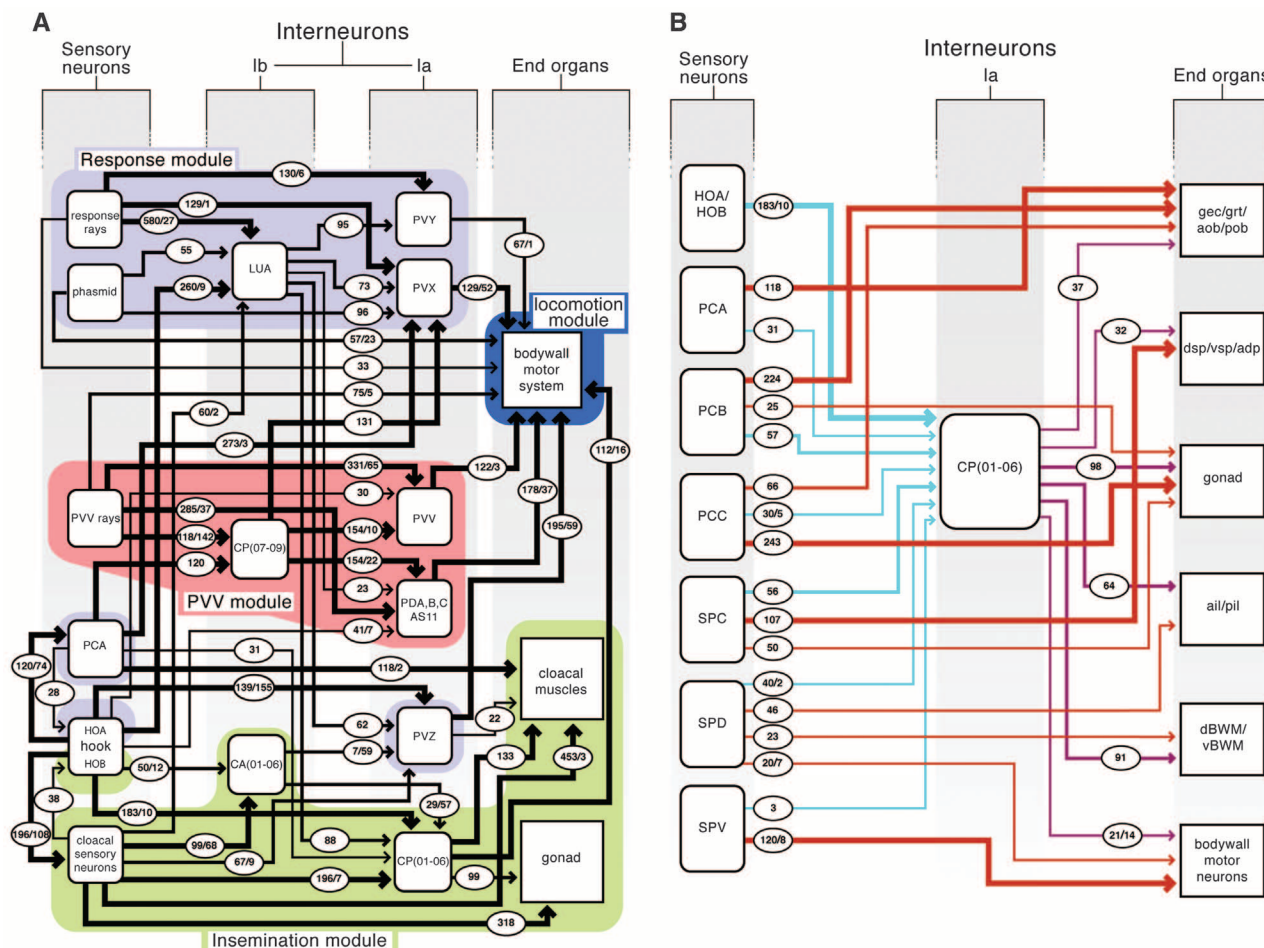


Fig. 6. The feedforward circuits through the modules. Numbers in ovals as for Fig. 5. [The R(1-5)A module is omitted.] **(A)** The Response, PVV, and Insemination modules each contain a subset of type Ia interneurons and one class of type Ib interneuron. All interneuron classes participate in feedforward loops, type Ia targeting end organs, type Ib targeting type Ia. Cross connections between the modules are created at the level of the type Ib interneurons. Among sensory neurons, the hook neurons are distinctive in not having any direct output onto

end organs and in having strong output onto other classes of sensory neurons, namely, the neurons located in the postcloacal sensilla and the spicules. (The many other cross-connections between sensory neurons are not shown.) PCA is separated out from the other cloacal sensory neurons to show its feedforward loop involving CP(07-09) and PVX. LUA(L/R), PDA, PDB, and AS11 are shared neurons that are sexually dimorphic. **(B)** Greater detail of the feedforward loops in the insemination circuits through the CP(01-06) interneuron class.

knowledge has been acquired is natural selection. The structural design must be fault-tolerant in order to allow for developmental error. The continuous distribution of connection strengths in the male posterior connectome suggests a probabilistic mechanism of synapse formation in which each cell pair has a genetically specified probability of forming a synapse. Small evolutionary changes in these probabilities will allow gradual evolution of structural connectivity and hence of network function and behavior.

References and Notes

- J. G. White, E. Southgate, J. N. Thomson, S. Brenner, *Philos. Trans. R. Soc. Lond. B Biol. Sci.* **314**, 1 (1986).
- L. R. Varshney, B. L. Chen, E. Paniagua, D. H. Hall, D. B. Chklovskii, *PLOS Comput. Biol.* **7**, e1001066 (2011).
- M. de Bono, A. V. Maricq, *Annu. Rev. Neurosci.* **28**, 451 (2005).
- M. de Bono, M. B. Sokolowski, in *Invertebrate Neurobiology*, G. North, R. J. Greenspan, Eds. (Cold Spring Harbor Laboratory Press, Cold Spring Harbor, NY, 2007).
- X.-J. Wang, *Neuron* **60**, 215 (2008).
- J. Lipton, G. Kleemann, R. Ghosh, R. Lints, S. W. Emmons, *J. Neurosci.* **24**, 7427 (2004).
- J. M. Simon, P. W. Sternberg, *Proc. Natl. Acad. Sci. U.S.A.* **99**, 1598 (2002).
- A. Barrios, S. Nurish, S. W. Emmons, *Curr. Biol.* **18**, 1865 (2008).
- J. Q. White *et al.*, *Curr. Biol.* **17**, 1847 (2007).
- J. E. Sulston, D. G. Albertson, J. N. Thomson, *Dev. Biol.* **78**, 542 (1980).
- M. M. Barr, L. R. Garcia, in *Neurobiology and behavior section*, E. M. Jorgensen, J. M. Kaplan, Eds., *WormBook* (The C. elegans Research Community, WormBook, 2006); www.wormbook.org/toc_complete.html
- L. R. Garcia, B. LeBoeuf, P. Koo, *Genetics* **175**, 1761 (2007).
- G. A. Kleemann, A. L. Basolo, *Anim. Behav.* **74**, 1339 (2007).
- Neuron maps, synapse lists, and connectivity matrices are available at <http://wormwiring.org>.
- S. Brenner, *Genetics* **77**, 71 (1974).
- Materials and methods are available as supplementary materials on Science Online.
- D. J. Watts, S. H. Strogatz, *Nature* **393**, 440 (1998).
- T. Schikorski, C. F. Stevens, *J. Neurosci.* **17**, 5858 (1997).
- M. E. J. Newman, *Proc. Natl. Acad. Sci. U.S.A.* **103**, 8577 (2006).
- E. A. Leicht, M. E. J. Newman, *Phys. Rev. Lett.* **100**, 118703 (2008).
- K. S. Liu, P. W. Sternberg, *Neuron* **14**, 79 (1995).
- K. Liu, Ph.D. thesis, California Institute of Technology (1995).
- L. R. Garcia, P. Mehta, P. W. Sternberg, *Cell* **107**, 777 (2001).
- Y. Liu *et al.*, *PLoS Genet.* **7**, e1001326 (2011).
- P. K. Koo, X. Bian, A. L. Sherlekar, M. R. Bunkers, R. Lints, *J. Neurosci.* **31**, 7497 (2011).
- M. M. Barr, P. W. Sternberg, *Nature* **401**, 386 (1999).
- J. Hertz, A. Krogh, R. G. Palmer, *Introduction to the Theory of Neural Computation*, Santa Fe Institute Studies in the Sciences of Complexity (Westview Press, Boulder, CO, 1991).
- J. J. Hopfield, *Proc. Natl. Acad. Sci. U.S.A.* **79**, 2554 (1982).
- D. Kleinfeld, *Proc. Natl. Acad. Sci. U.S.A.* **83**, 9469 (1986).
- D. Kleinfeld, H. Sompolinsky, *Biophys. J.* **54**, 1039 (1988).
- S. Mangan, U. Alon, *Proc. Natl. Acad. Sci. U.S.A.* **100**, 11980 (2003).
- U. Alon, *Nat. Rev. Genet.* **8**, 450 (2007).
- H. S. Seung, *Neuron* **62**, 17 (2009).
- O. Sporns, G. Tononi, R. Kötter, *PLOS Comput. Biol.* **1**, e42 (2005).
- J. W. Lichtman, J. R. Sanes, *Curr. Opin. Neurobiol.* **18**, 346 (2008).
- Y. Mishchenko *et al.*, *Neuron* **67**, 1009 (2010).

37. D. D. Bock *et al.*, *Nature* **471**, 177 (2011).
38. K. L. Briggman, M. Helmstaedter, W. Denk, *Nature* **471**, 183 (2011).
39. S. Seung, *Connectome: How the Brain's Wiring Makes Us Who We Are* (Houghton Mifflin Harcourt, Boston, 2012).
40. N. Nagarajan, C. F. Stevens, *Curr. Biol.* **18**, R756 (2008).
41. K. Jezek, E. J. Henriksen, A. Treves, E. I. Moser, M. B. Moser, *Nature* **478**, 246 (2011).
42. T. J. Wills, C. Lever, F. Cacucci, N. Burgess, J. O'Keefe, *Science* **308**, 873 (2005).
43. J. Niessing, R. W. Friedrich, *Nature* **465**, 47 (2010).
44. F. Rosenblatt, *Psychol. Rev.* **65**, 386 (1958).
45. S. Haykin, *Neural Networks and Learning Machines* (Pearson Prentice-Hall, New York, 2009).

46. M. B. Goodman, D. H. Hall, L. Avery, S. R. Lockery, *Neuron* **20**, 763 (1998).
47. A. J. Whittaker, P. W. Sternberg, *BMC Biol.* **7**, 33 (2009).

Acknowledgments: H. Eckholdt played a key role in the early stages of this project. Contributions were also made by Z. Martirosyan, A. Singh, T. Stephney, and M. Zhang. C. Crocker made the figures. We thank J. White for encouragement and interest; A. Bergman, M. Chklovskii, D. Faber, A. Massimi, and S. Seung for helpful discussions; N. Baker, H. Buelow, D. Faber, R. Garcia, Z. Kaprielian, R. Lints, D. Portman, J. Sze, and J. Vijg for comments on the manuscript; and J. White and J. Hodgkin for their help in transferring archival transmission EM data from the U.K. Medical Research Council (MRC)–Laboratory of Molecular Biology to the Hall lab at Einstein for long-term

curation and study. This work was supported by MRC, the U.S. NIH (R21MH63223 to S.W.E. and OD 010943 to D.H.H.), and by the G. Harold and Leila Y. Mathers Charitable Foundation.

Supplementary Materials

www.sciencemag.org/cgi/content/full/337/6093/437/DC1
Materials and Methods
Supplementary Text
Figs. S1 to S11
Table S1
References (48–60)
Movie S1
Databases S1 to S9
10.1126/science.1221762

REPORTS

Binary Interaction Dominates the Evolution of Massive Stars

H. Sana,^{1*} S. E. de Mink,^{2,3} A. de Koter,^{1,4} N. Langer,⁵ C. J. Evans,⁶ M. Gieles,⁷ E. Gosset,⁸ R. G. Izzard,⁵ J.-B. Le Bouquin,⁹ F. R. N. Schneider⁵

The presence of a nearby companion alters the evolution of massive stars in binary systems, leading to phenomena such as stellar mergers, x-ray binaries, and gamma-ray bursts. Unambiguous constraints on the fraction of massive stars affected by binary interaction were lacking. We simultaneously measured all relevant binary characteristics in a sample of Galactic massive O stars and quantified the frequency and nature of binary interactions. More than 70% of all massive stars will exchange mass with a companion, leading to a binary merger in one-third of the cases. These numbers greatly exceed previous estimates and imply that binary interaction dominates the evolution of massive stars, with implications for populations of massive stars and their supernovae.

With masses larger than 15 times that of our Sun (M_{\odot}), stars of spectral type O are rare (2) and short-lived (3). Nevertheless, through their large luminosities, strong stellar winds, and powerful explosions, massive stars heat and enrich surrounding gas clouds in which new generations of stars form (4) and drive the chemical evolution of galaxies (5). Massive stars end their lives in luminous explosions, as core-collapse supernovae (CCSN) or gamma-ray bursts (GRBs), that can be observed throughout most of the universe.

In a binary system, the evolutionary path of a massive star is drastically altered by the presence of a nearby companion (6–8). Because stars expand as they evolve, those in pairs with orbital periods up to ~1500 days exchange mass (6). The more massive star can be stripped of its entire envelope and, thus, loses much of its original mass. The companion star gains mass and angular momentum, which trigger mixing processes in the stellar interior and modify its evolutionary path (3). In very close binaries, the two stars may even merge. The nature of the binary interaction is largely determined by the initial orbital period and mass ratio. The relative roles of interaction scenarios and the overall importance of binary- versus single-star evolution so far remain uncertain because of the paucity of direct measurements of the intrinsic distributions of orbital parameters (9–14).

In this work, we homogeneously analyze the O star population of six nearby Galactic open stellar clusters and simultaneously measure all the relevant intrinsic multiplicity properties (15). Our observational method, spectroscopy, is sensitive to orbital periods as long as 10 years (13), corresponding to the relevant period range for binary interaction (6). In a spectroscopic binary, the periodic Doppler shift of spectral lines allows the determination of the radial velocity and,

hence, of the orbital motion of one (“single-lined” spectroscopic binary) or both (“double-lined” spectroscopic binary) stars. Given sufficient orbital-phase coverage, the orbital period (P), the eccentricity (e), and, for double-lined spectroscopic binaries, the mass-ratio (q) follow from Kepler’s laws.

Our sample contains 71 single and multiple O-type objects (see supplementary text A). With 40 identified spectroscopic binaries, the observed binary fraction in our sample is $f_{\text{obs}} = 40/71 = 0.56$. We combined observations obtained with the Ultraviolet and Visible Echelle Spectrograph at the Very Large Telescope for long-period systems with results from detailed studies of detected systems in the individual clusters (16–21). In total, 85 and 78% of our binary systems have, respectively, constrained orbital periods and mass ratios. This allowed us to build statistically significant observed period and mass-ratio distributions for massive stars (Fig. 1), which are representative of the parameter distributions of the Galactic O star population (13).

The precise fraction of interacting O stars and the relative importance of the different interaction scenarios are determined by the distributions of the orbital parameters. The observed distributions result from the intrinsic distributions and the observational biases (see supplementary text B). To uncover the intrinsic distributions, we simulate observational biases with the use of a Monte Carlo approach that incorporates the observational time series of each object in our sample. We adopt power laws for the probability density functions of orbital periods (in \log_{10} space), mass ratios, and eccentricities with exponents π , κ , and η , respectively (fig. S3 and table S3). These power-law exponents and the intrinsic binary fraction f_{bin} were simultaneously determined by a comparison of simulated populations of stars with our sample allowing for the observational biases. We determined the accuracy of our method by applying it to synthetic data.

Compared with earlier attempts to measure intrinsic orbital properties (9–14): (i) The average number of epochs per object in our sample is larger by up to a factor of 5, making binary detection more complete. (ii) More than

¹Astronomical Institute Anton Pannekoek, Amsterdam University, Science Park 904, 1098 XH, Amsterdam, Netherlands.

²Space Telescope Science Institute, 3700 San Martin Drive, Baltimore, MD 21218, USA. ³Department of Physics and Astronomy, Johns Hopkins University, Baltimore, MD 21218, USA. ⁴Astronomical Institute, Utrecht University, Princetonplein 5, 3584 CC, Utrecht, Netherlands. ⁵Argelander-Institut für Astronomie, Universität Bonn, Auf dem Hügel 71, 53121 Bonn, Germany. ⁶UK Astronomy Technology Centre, Royal Observatory Edinburgh, Blackford Hill, Edinburgh EH9 3HJ, UK. ⁷Institute of Astronomy, University of Cambridge, Madingley Road, Cambridge CB3 0HA, UK. ⁸Fonds de la Recherche Scientifique—FNRS, Institut d’Astrophysique, Liège University, Allée du 6 Août 17, B-4000 Liège, Belgium. ⁹Université Joseph Fourier—Grenoble 1/CNRS—Institut National des Sciences de l’Univers, Institut de Planétologie et d’Astrophysique de Grenoble UMR 5274, Grenoble, France.

*To whom correspondence should be addressed. E-mail: h.sana@uva.nl

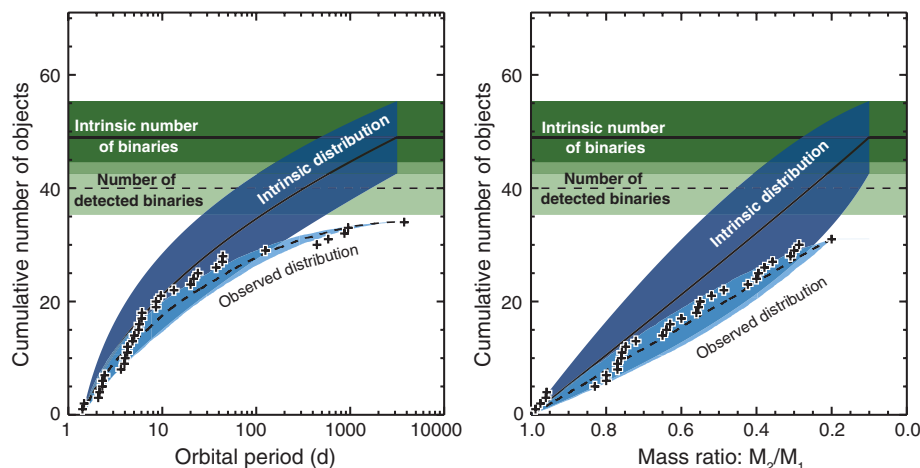
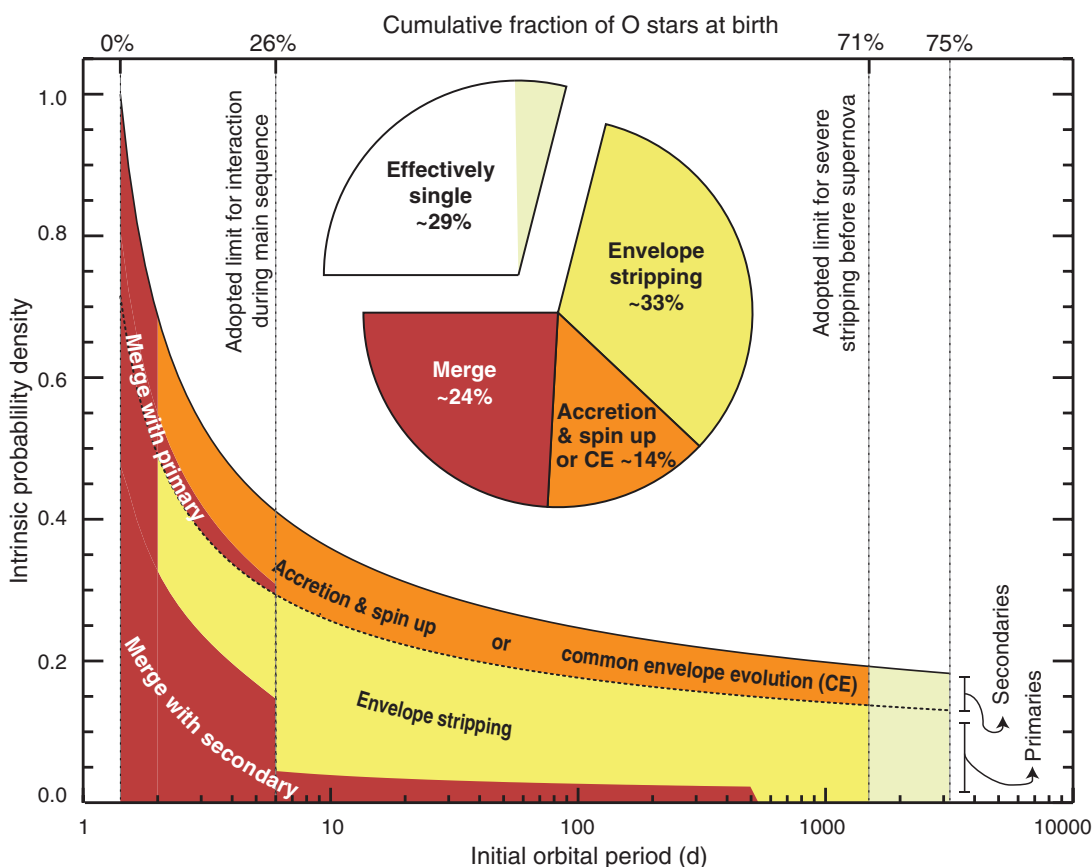


Fig. 1. Cumulative number distributions of logarithmic orbital periods (**left**) and mass ratios (**right**) for our sample of 71 O-type objects, of which 40 are identified binaries. The horizontal solid lines and the associated dark green areas indicate the most probable intrinsic number of binaries (49 in total) and its 1σ uncertainty, corresponding to an intrinsic binary fraction $f_{\text{bin}} = 0.69 \pm 0.09$. The horizontal dashed lines indicate the most probable simulated number of detected binaries (40 ± 4), which agrees very well with the actual observed number of binaries (40 in total). Crosses denote the observed cumulative distributions for systems with known periods (34 in total) and mass ratios (31 in total). The lower dashed lines indicate the best simulated observational distributions and their 1σ uncertainties, corresponding to intrinsic distributions with power-law exponents $\pi = -0.55 \pm 0.22$ and $\kappa = -0.10 \pm 0.58$, respectively. The lower solid lines and associated dark blue areas indicate the most probable intrinsic number distributions and their errors. The latter were obtained from a combination of the uncertainties on the intrinsic binary fraction and on the power-law exponents of the respective probability density functions. d, days.

Fig. 2. Schematic representation of the relative importance of different binary interaction processes given our best-fit binary fraction and intrinsic distribution functions. All percentages are expressed in terms of the fraction of all stars born as O-type stars, including the single O stars and the O stars in binaries, either as the initially more massive component (the primary) or as the less massive one (the secondary). The solid curve gives the best-fit intrinsic distribution of orbital periods (corresponding to $\pi = -0.55$), which we adopted as the initial distribution. For the purpose of comparison, we normalized the ordinate value to unity at the minimum period that we considered. The dotted curve separates the contributions from O-type primary and secondary stars. The colored areas indicate the fractions of systems that are expected to merge (red), experience stripping (yellow), or accretion/common envelope evolution (orange). Assumptions and uncertainties are discussed in the text and in supplementary text C. The pie chart compares the fraction of stars born as O stars that are effectively single [i.e., single (white) or in wide binaries with little or no interaction effects (light green)—29% combined] with those that experience significant binary interaction (71% combined).



three-quarters of our binaries have measured orbital properties, which allowed us to directly model the orbital parameter distributions. (iii) The orbital properties cover the full range of periods and mass ratios relevant for binary interaction. Thus, we are better equipped to draw direct conclusions about the relative importance of various binary interaction scenarios.

We find an intrinsic binary fraction of $f_{\text{bin}} = 0.69 \pm 0.09$, a strong preference for close pairs ($\pi = -0.55 \pm 0.2$), and a uniform distribution of the mass ratio ($\kappa = -0.1 \pm 0.6$) for binaries with periods up to about 9 years. Comparison of the intrinsic, simulated, and observed cumulative distributions of the orbital parameters shows that observational biases are mostly restricted to the longest periods and the most extreme mass ratios (Fig. 1).

Compared with previous works, we find no preference for equal-mass binaries (22). We obtain a steeper period distribution and a larger fraction of short period systems than previously thought (9–14, 23), resulting in a much larger fraction of systems that are affected by binary evolution.

Because star-cluster dynamics and stellar evolution could have affected the multiplicity properties of only very few of the young O stars in our sample (see supplementary text A.2), our derived distributions are a good representation of the binary properties at birth. Thus, it is safe

to conclude that the most common end product of massive-star formation is a rather close binary. This statement challenges current star formation theories (24). However, according to recent simulations (25, 26), accretion disk fragmentation, through gravitational instabilities, seems to naturally result in the formation of binary systems containing two massive stars with similar but not equal masses (i.e., within a factor of a few). Though the companions are initially formed in a wide orbit, dynamical interactions with the remnant accretion disk may substantially harden the system, thus providing a better agreement with the observations.

Intrinsic binary properties are key initial conditions for massive-star evolution; that is, evolutionary paths and final fates. Integration of our intrinsic distribution functions (Fig. 2 and supplementary text C) implies that 71% of all stars born as O-type interact with a companion, over half of which do so before leaving the main sequence. Such binary interactions drastically alter the evolution and final fate of the stars and appear, by far, the most frequent evolutionary channel for massive stars. Based on calculations of binary evolution in short-period systems (6, 27–29), we also find that 20 to 30% of all O stars will merge with their companions and that 40 to 50% will either be stripped of their envelope or will accrete substantial mass (see supplementary text C). In summary, we find that almost three-quarters of all massive stars are strongly affected by binary interaction before they explode as supernovae.

The interaction and merger rates that we computed are, respectively, two and three times larger than previous estimates (6, 11, 23). This results in a corresponding increase in the number of progenitors of key astrophysical objects, such as close double compact objects, hydrogen-deficient CCSN, and GRBs, that are thought to be produced by binary interaction.

We predict that 33% of O stars are stripped of their envelope before they explode as hydrogen-deficient CCSN (types Ib, Ic, and IIb). This fraction is close to the observed fraction of hydrogen-poor supernovae; that is, 37% of all CCSN (30). Extrapolation of our findings from O stars to the 8- to 15-solar mass range to include all CCSN progenitors implies that hydrogen-poor CCSN predominantly result from mass transfer in close binaries. This rate is large enough to explain the discrepancy between the large observational fraction of type Ib/c supernovae and the dearth of single stars stripped by stellar winds. Our results also imply that more than half of the progenitors of hydrogen-rich (type II) supernovae are merged stars or binary mass gainers, which might explain some of the diversity of this supernova class.

Our results further indicate that a large fraction of massive main-sequence stars (~40%) is expected to be spun-up either by accretion or coalescence. In lower-metallicity galaxies, these stars should remain rapidly rotating and, hence, constitute a major channel for the production of long-duration GRBs (31), which are thought to

accompany the death of massive stars in case their iron cores collapse to critically rotating neutron stars or black holes (32, 33).

In sum, we show that only a minority of massive stars evolve undisturbed toward their supernova explosions. Hence, the effects of binarity must be considered to further our understanding of the formation and evolution of massive stars and to help us interpret the integrated properties of distant star-forming galaxies (34, 35).

References and Notes

1. F. Martins, D. Schaerer, D. J. Hillier, *Astron. Astrophys.* **436**, 1049 (2005).
2. P. Kroupa, C. Weidner, *Astrophys. J.* **598**, 1076 (2003).
3. I. Brott *et al.*, *Astron. Astrophys.* **530**, A115 (2011).
4. C. Chiappini *et al.*, *Nature* **472**, 454 (2011).
5. M. E. De Rossi, P. B. Tissera, S. E. Pedrosa, *Astron. Astrophys.* **519**, A89 (2010).
6. P. Podsiadlowski, P. C. Joss, J. J. L. Hsu, *Astrophys. J.* **391**, 246 (1992).
7. S. Wellstein, N. Langer, *Astron. Astrophys.* **350**, 148 (1999).
8. J. S. W. Claeys, S. E. de Mink, O. R. Pols, J. J. Eldridge, M. Baes, *Astron. Astrophys.* **528**, A131 (2011).
9. C. D. Garmany, P. S. Conti, P. Massey, *Astrophys. J.* **242**, 1063 (1980).
10. B. D. Mason, W. I. Hartkopf, D. R. Gies, T. J. Henry, J. W. Helsel, *Astron. J.* **137**, 3358 (2009).
11. H. A. Kobulnicky, C. L. Fryer, *Astrophys. J.* **670**, 747 (2007).
12. D. C. Kiminki, H. A. Kobulnicky, *Astrophys. J.* **751**, 4 (2012).
13. H. Sana, C. J. Evans, in *Active OB Stars: Structure, Evolution, Mass Loss, and Critical Limits*, C. Neiner, G. Wade, G. Meynet, G. Peters, Eds. (Proceedings of the International Astronomical Union Symposium 272, Cambridge Univ. Press, Cambridge, 2011), pp. 474–485.
14. S. Pfalzner, C. Olczak, *Astron. Astrophys.* **475**, 875 (2007).
15. Supplementary materials are available on Science Online.
16. M. De Becker, G. Rauw, J. Manfroid, P. Eenens, *Astron. Astrophys.* **456**, 1121 (2006).
17. T. C. Hillwig *et al.*, *Astrophys. J.* **639**, 1069 (2006).
18. H. Sana, E. Gosset, Y. Nazé, G. Rauw, N. Linder, *Mon. Not. R. Astron. Soc.* **386**, 447 (2008).
19. H. Sana, E. Gosset, C. J. Evans, *Mon. Not. R. Astron. Soc.* **400**, 1479 (2009).
20. G. Rauw *et al.*, *Mon. Not. R. Astron. Soc.* **398**, 1582 (2009).
21. H. Sana, G. James, E. Gosset, *Mon. Not. R. Astron. Soc.* **416**, 817 (2011).

22. M. H. Pinsonneault, K. Z. Stanek, *Astrophys. J.* **639**, L67 (2006).
23. K. Belczynski, V. Kalogera, T. Bulik, *Astrophys. J.* **572**, 407 (2002).
24. H. Zinnecker, H. W. Yorke, *Annu. Rev. Astron. Astrophys.* **45**, 481 (2007).
25. M. R. Krumholz, R. I. Klein, C. F. McKee, S. S. R. Offner, A. J. Cunningham, *Science* **323**, 754 (2009).
26. K. M. Kratter, C. D. Matzner, M. R. Krumholz, R. I. Klein, *Astrophys. J.* **708**, 1585 (2010).
27. O. R. Pols, *Astron. Astrophys.* **290**, 119 (1994).
28. S. Wellstein, N. Langer, H. Braun, *Astron. Astrophys.* **369**, 939 (2001).
29. S. E. de Mink, O. R. Pols, R. W. Hilditch, *Astron. Astrophys.* **467**, 1181 (2007).
30. N. Smith, W. Li, A. V. Filippenko, R. Chornock, *Mon. Not. R. Astron. Soc.* **412**, 1522 (2011).
31. M. Cantiello, S.-C. Yoon, N. Langer, M. Livio, *Astron. Astrophys.* **465**, L29 (2007).
32. S. E. Woosley, J. S. Bloom, *Annu. Rev. Astron. Astrophys.* **44**, 507 (2006).
33. S. E. Woosley, A. Heger, *Astrophys. J.* **637**, 914 (2006).
34. J. J. Eldridge, E. R. Stanway, *Mon. Not. R. Astron. Soc.* **400**, 1019 (2009).
35. N. Bastian, K. R. Covey, M. R. Meyer, *Annu. Rev. Astron. Astrophys.* **48**, 339 (2010).

Acknowledgments: Support for this work was provided by NASA through Hubble Fellowship grant HST-HF-51270.01-A awarded by the Space Telescope Science Institute, which is operated by the Association of Universities for Research in Astronomy for NASA, under contract NAS 5-26555. S.E.d.M. is a Hubble fellow. M.G. acknowledges financial support from The Royal Society. This work is based on European Southern Observatory (ESO) observations, and we acknowledge support from the ESO Paranal Observatory and the User Support Department. H.S. also acknowledges support from SARA Computing and Networking Services. Measurements used in this work have been made available at the Centre de Données astronomiques de Strasbourg (<http://cdsweb.u-strasbg.fr/>).

Supplementary Materials

www.sciencemag.org/cgi/content/full/337/6093/444/DC1
Supplementary Text
Figs. S1 to S4
Tables S1 to S4
References (36–62)

13 April 2012; accepted 19 June 2012
10.1126/science.1223344

Excitation of Orbital Angular Momentum Resonances in Helically Twisted Photonic Crystal Fiber

G. K. L. Wong,^{1*} M. S. Kang,¹ H. W. Lee,¹ F. Biancalana,¹ C. Conti,¹ T. Weiss,¹ P. St. J. Russell^{1,2}

Spiral twisting offers additional opportunities for controlling the loss, dispersion, and polarization state of light in optical fibers with noncircular guiding cores. Here, we report an effect that appears in continuously twisted photonic crystal fiber. Guided by the helical lattice of hollow channels, cladding light is forced to follow a spiral path. This diverts a fraction of the axial momentum flow into the azimuthal direction, leading to the formation of discrete orbital angular momentum states at wavelengths that scale linearly with the twist rate. Core-guided light phase-matches topologically to these leaky states, causing a series of dips in the transmitted spectrum. Twisted photonic crystal fiber has potential applications in, for example, band-rejection filters and dispersion control.

The effect of twisting on the propagation of light in different kinds of optical fibers has been explored for polariza-

tion control (1–3), long-period grating couplers (4–7), and elimination of higher-order modes from fiber lasers (8). We study twisted solid-core

photonic crystal fiber (PCF), a type of microstructured fiber in which a regular hexagonal lattice of hollow channels is disposed symmetrically around a central glass core (9). When continuously twisted, PCF exhibits a series of

dips in its transmission spectrum, an effect that has been previously attributed to some form of grating-diffraction (10, 11). We show that it can be explained by the formation in the cladding of leaky orbital resonances that

couple to the core mode, causing transmission loss.

The helical fibers (Fig. 1) were fabricated by rigidly fixing one end of a length of solid-core PCF while mounting the other end at the center of a motorized rotation stage. The PCF had a hexagonal array of hollow channels of diameter $d \sim 0.9 \mu\text{m}$ and spacing $\Lambda \approx 2.9 \mu\text{m}$, yielding $d/\Lambda < 0.4$, which makes it “endlessly single-mode”; that is, it supports only one transverse mode at all wavelengths (12). A scanning electron micrograph of its microstructure is shown in the Fig. 2A inset. A permanent twist was produced by rotating the stage while scanning a focused CO_2 laser beam along the fiber with a steering mirror fixed to a precision motorized linear translation stage. The laser power was chosen to heat the fiber to the glass-softening temperature.

Linearly polarized light from a supercontinuum source was coupled into the samples, and the transmitted power spectra were measured by using an optical spectrum analyzer. The results for two 6-mm-long pieces of PCF with twist

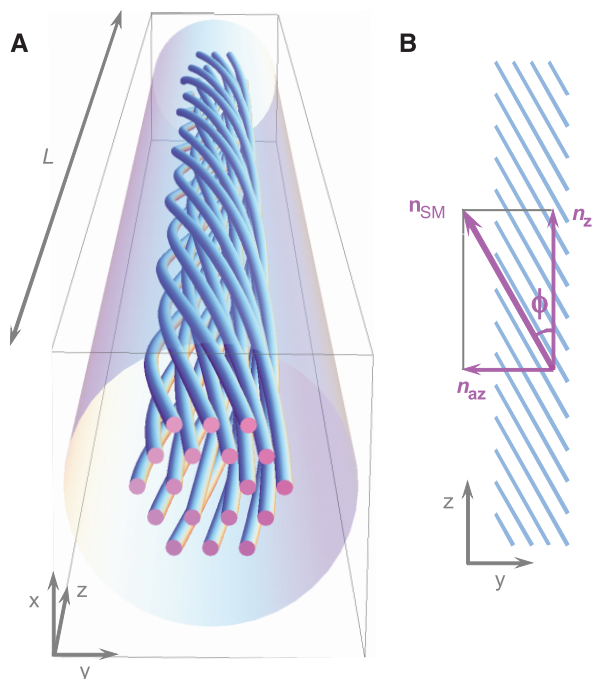
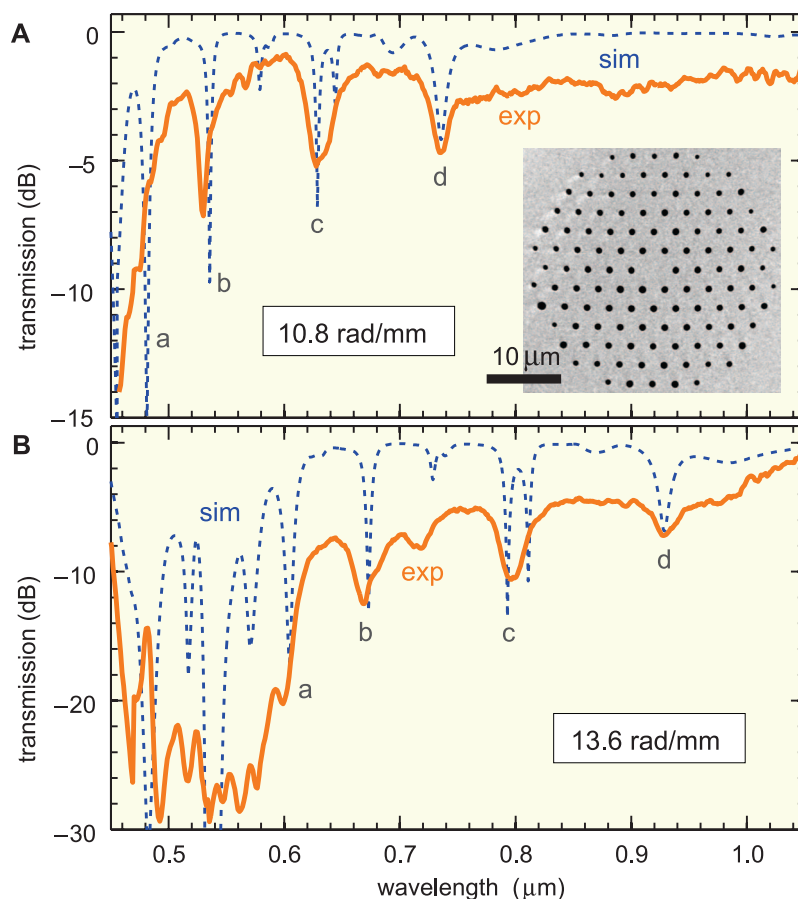


Fig. 1. (A) Perspective view of one period $L (= 2\pi/\alpha)$, where α is the twist rate) of a helical PCF with a negative twist (i.e., anticlockwise looking in the direction of propagation, $+z$). The blue tubes represent the hollow channels passing through the glass, and the solid glass core is formed by a missing channel at the center. For clarity, the twist rate is greatly exaggerated in this sketch (L/Λ is of order 100 in the experiments, where Λ is interhole spacing). (B) Local axial and azimuthal components of the refractive index n_{SM} of the fundamental space-filling Bloch mode in the twisted cladding. The angle ϕ between the fiber axis and the channels increases with radius ρ , following the approximate relationship $\phi \approx \alpha\rho$.

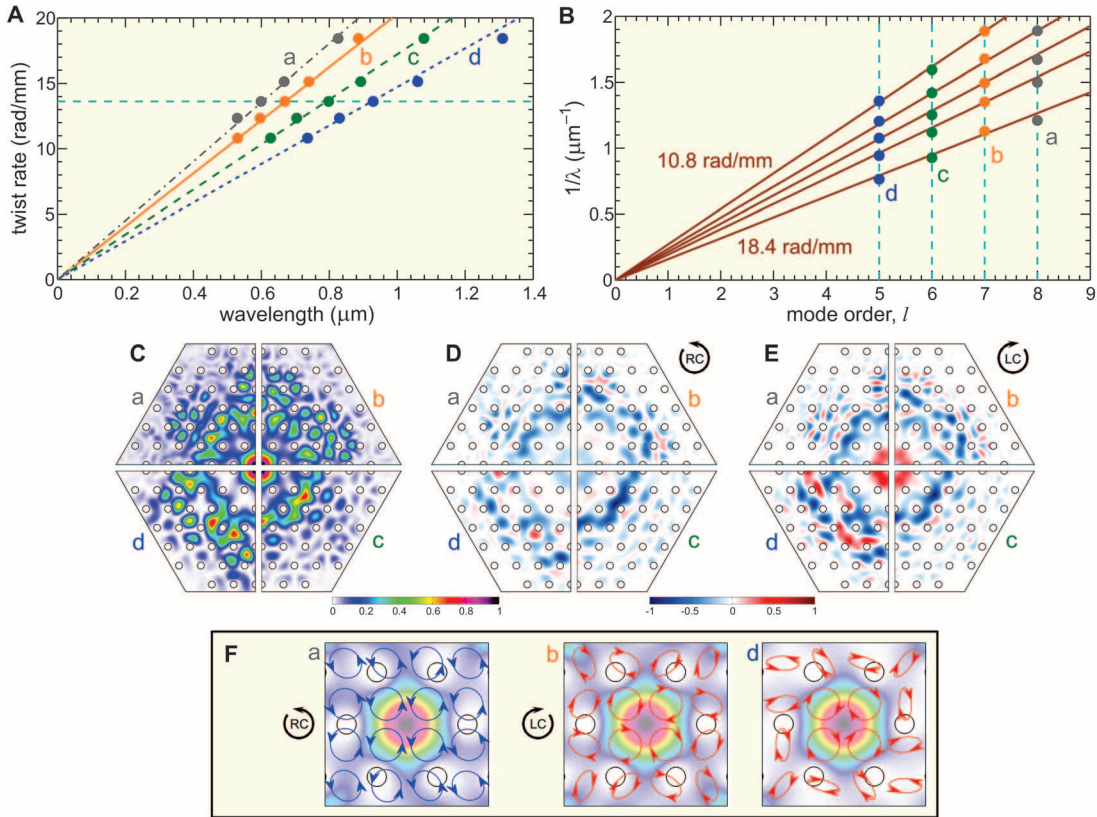
Fig. 2. Measured (solid curve) and calculated (dotted curve) transmission spectra of PCFs with twist rates α of (A) 10.8 rad/mm and (B) 13.6 rad/mm. The letters a, b, c, and d mark the strongest individual cladding resonances, which track linearly to longer wavelength as the twist rate increases (Fig. 3A). [(A) inset] Scanning electron micrograph of the PCF structure.



¹Max Planck Institute for the Science of Light, Günther-Scharowsky Strasse 1, 91058 Erlangen, Germany. ²Department of Physics, University of Erlangen-Nuremberg, Staudtstrasse 7, 91058 Erlangen, Germany.

*To whom correspondence should be addressed. E-mail: gordon.wong@mpl.mpg.de

Fig. 3. (A) Twist rate plotted versus vacuum wavelength for the four resonances a, b, c, and d in Fig. 2. The solid circles are the experimental measurements, and the lines fit both to FE modeling and to a simple theory based on azimuthal resonances. **(B)** Reciprocal optical wavelength at resonance in units of μm^{-1} plotted against mode order for the experimental data (solid points). From top to bottom, the values of L are 581, 509, 461, 415, and 341 μm , yielding twist rates of 10.8, 12.3, 13.6, 15.1, and 18.4 rad/mm. The lines are plotted by using Eq. 2 with $\rho^2 n_{\text{SM}} = 54.6 \mu\text{m}^2$. **(C)** The S_z distributions (very slightly off-resonance to enhance the visibility of the cladding fields) for the four resonances at a twist rate of 13.6 rad/mm [dashed horizontal line in (A)]. For compactness, only one quadrant is shown per mode; the patterns have perfect sixfold symmetry. **(D and E)** The S_{az} distributions for the RC- and LC-polarized versions of the four modes; blue shading indicates clockwise power flow. **(F)** Polarization state of the transverse electric field.



rates of $\alpha = 10.8$ and 13.6 rad/mm (helical pitch $L = 581$ and $461 \mu\text{m}$) show a pattern of distinct transmission dips (Fig. 2) that shifts toward longer wavelength at higher twist rates. The data points from a series of measurements at different twist rates are plotted in Fig. 3A for the four strongest resonances in Fig. 2. Despite such a complex and dispersive system, the dip wavelengths scale linearly with twist rate, each orbital resonance having a different slope, and the lines pass through zero wavelength at zero twist rate.

A comparison of the experimental results with transmission spectra modeled by using a helicoidal coordinate transformation (supplementary text section S1) shows excellent agreement (Fig. 2) considering that no fitting parameters were used. Almost-identical numerical spectra are obtained for right-circular (RC) and left-circular (LC) polarization states (we define LC as spinning in the same direction as the spiral, which is taken to be clockwise looking in the direction of propagation). In Fig. 3, C to E, the axial (S_z) and azimuthal (S_{az}) Poynting vector distributions are plotted for the four modes. They are ring-shaped, S_{az} flowing in the direction of the spiral in each case. S_{az} has the same sign in both core and cladding for the RC-polarized case, whereas the signs are opposite for the LC case. In Fig. 3F, the polarization states in the vicinity of the core are shown for resonance a in the RC case and for resonances b and

d in the LC case ($\alpha = 13.6$ rad/mm); they are almost perfectly circular in both core and cladding in all cases (for more details, see supplementary text section S2).

The hexagonal cladding structure in the untwisted PCF cladding supports a fundamental “space-filling” mode (SM) whose axial Poynting vector, S_{SM} , points precisely along the fiber axis ($l2$). This Bloch mode, which occurs at the Γ point at the center of the Brillouin zone, has an effective axial refractive index that is greater than 1, with the result that field antinodes form in the glass strands, trapped laterally by total internal reflection at the glass-air interfaces. When the fiber is gently twisted ($\alpha L \ll 1$), these field antinodes are forced to follow a helical path around the core. This permits S_{SM} to point partially into the transverse plane of the fiber, the local angle between the fiber axis and the helical path being $\phi = \sin^{-1}[\alpha\rho/(1 + \alpha^2\rho^2)^{0.5}] \approx \alpha\rho$ at radius ρ . This leads to a component of momentum flow in the azimuthal direction (Fig. 1B), creating orbital angular momentum (OAM) and causing orbital resonances to form for certain combinations of radius, twist rate, and wavelength. Taking \vec{n}_{SM} as the refractive index vector of the SM mode along the helical path, the orbital resonance condition can be readily derived by requiring that the azimuthal component of the wave vector (proportional to the refractive index $n_{\text{az}} \approx \alpha\rho n_{\text{SM}}$), multiplied by the circum-

	AM order	cladding mode			
		d	c	b	a
RC	$l + \sigma$	~ 6	~ 7	~ 8	~ 9
	$J2\pi/P\lambda$	4.5	6.0	7.2	8.4
LC	$l + \sigma$	~ 4	~ 5	~ 6	~ 7
	$J2\pi/P\lambda$	2.9	4.0	5.4	6.1

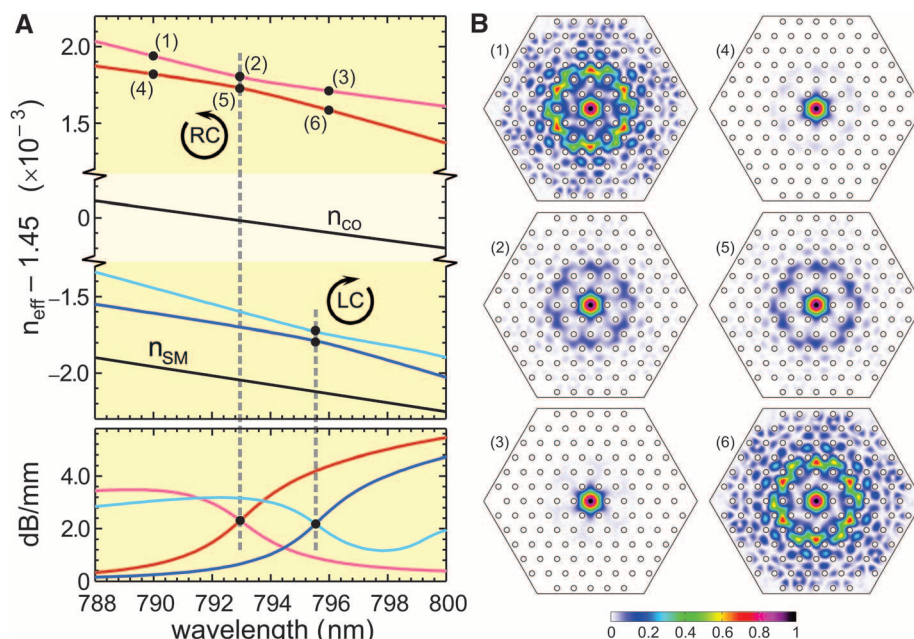
Fig. 4. Angular momentum (AM) orders predicted by the fits in Fig. 2 ($l \pm 1$) at each of the four resonances for $\alpha = 13.6$ rad/mm (almost identical results are obtained at other twist rates), compared with $J2\pi/P\lambda$ evaluated from the FE results.

ference, should equal a multiple of 2π . This leads to the relationship

$$\vec{\rho} \cdot (\vec{n}_{\text{SM}} \times \vec{a}) = n_{\text{SM}} \rho^2 \alpha = l \frac{\lambda}{2\pi} \quad (1)$$

where l is an integer representing the order of the resonance, λ is the vacuum wavelength, and α twists clockwise in the $+z$ direction. Fitting to the experimental results [and the finite-element (FE) modeling] reveals that the product $n_{\text{SM}} \rho^2$ is a constant for the system. The resonant wavelengths in Eq. 1 scale with the reciprocal of L , which distinguishes the effect from grating-related phenomena, when the resonant wavelength would scale with L (apart from slight deviations because of dispersion).

Fig. 5. Numerical modeling of the behavior in the vicinity of anticrossing c at ~ 794 nm ($\alpha = 13.6$ rad/mm, $L = 461$ μ m). **(A)** (Top) Calculated dispersion of the modal refractive indices for LC- and RC-polarized modes. The indices n_{co} (core mode) and n_{SM} (space-filling cladding mode) refer to the untwisted case. The splitting at the center of each anticrossing corresponds to a coupling length of ~ 4 mm. (Bottom) Loss spectra in dB/mm. At the center of both LC and RC anticrossings, the loss of even and odd modes at this wavelength is ~ 2.3 dB/mm. **(B)** Distributions of axial Poynting vector at the six points (1 to 6), illustrating the coupling between orbital cladding resonance and core mode in the vicinity of the anticrossings. These distributions are almost identical for equivalent points in the LC case.



Equation 1 also requires that the orbital mode order should be proportional to the reciprocal wavelength at a fixed twist rate and that $\lambda \rightarrow \infty$ at $l = 0$. Applying this condition to the experimental data in Fig. 3A and selecting values of l so that each line consistently goes through the point $1/\lambda = 0$, $l = 0$ produce the plot in Fig. 3B, which shows that the orders of successive resonances (a, b, c, and d in Fig. 2A) run from $l = 5$ to $l = 8$. To obtain these excellent fits (accurate to within $\pm 2.5\%$), we set n_{SMP}^2 equal to $54.6 \mu\text{m}^2$.

The LC- and RC-polarized cladding modes predicted by FE modeling yield almost identical transmission spectra, but do they carry the same angular momentum? By analogy with Laguerre-Gaussian beams (13, 14), one would expect, in the paraxial approximation,

$$\frac{J}{P} = \frac{\iint_{\text{mode}} \rho S_{az}(\rho, \phi) \cdot \rho d\rho d\phi}{\iint_{\text{mode}} S_z(\rho, \phi) \cdot \rho d\rho d\phi} = (l + \sigma) \frac{\lambda}{2\pi} \quad (2)$$

where J is the total axial flux of angular momentum and P is the axial energy flux. The integrals are evaluated over the entire cladding mode ($\rho > \Lambda$). It turns out that J/P , evaluated from the FE results, takes values that are quite close to integral multiples of $\lambda/2\pi$ as predicted by Eq. 2, being smaller by 2 for the LC case as expected from the opposite spin angular momentum. The results are summarized in Fig. 4. The values of l in Fig. 4 are derived from the fit to Eq. 2 and represent the OAM order, and σ is taken to be ± 1 depending on whether the mode is RC or LC polarized. The total angular momentum order is then $l + \sigma$, which does not yield perfect agreement with the expression in

Eq. 2, although the trend is correct. We attribute this to a breakdown in the paraxial approximation (15).

A further aspect of the helical system is that the effective axial refractive indices of the orbital resonances and the core mode are topologically affected by the helical path (Fig. 5A). In the RC case, the effective axial refractive indices of both cladding and core (denoted by \tilde{n}_{co} and \tilde{n}_{SM}) rise in the twisted structure, the cladding index increasing by a larger factor as expected from the topology, and an anticrossing appearing at ~ 793 nm. In the LC case, however, \tilde{n}_{co} actually falls in the twisted structure while \tilde{n}_{SM} rises, although by a much smaller amount than in the RC case. As a result, an anticrossing forms at a lower value of index, centered at ~ 795.5 nm. At the center of the anticrossings, even and odd modes exist, each with identical loss and a coupling length of $\lambda/(2\delta n) \approx 4$ mm. Moving away from synchronism, the modes split strongly into cladding-ring-like and corelike modes, the interaction becoming weaker as the wavelength detunes from the anticrossing point and the dephasing increases. The axial Poynting vector distributions of the modes illustrate this coupling phenomenon (Fig. 5B).

Figure 5A suggests that the transmission should exhibit some polarization dependence in the vicinity of the resonances, but this is not seen in the experimental results. We attribute this to fabrication-related nonuniformities in pitch, which would need to be kept below 0.05% to observe the small (2.5 nm) splitting between resonances in Fig. 5. In addition to their fundamental scientific interest as guided wave devices in “twisted space,” helical PCF has many potential applications in wavelength filtering and dispersion control. The thermal postprocess-

ing technique also allows structures with axially varying twist rates to be fabricated, providing further flexibility in design.

References and Notes

1. R. Ulrich, A. Simon, *Appl. Opt.* **18**, 2241 (1979).
2. M. Monerie, L. Jeunhomme, *Opt. Quantum Electron.* **12**, 449 (1980).
3. A. J. Barlow, J. J. Ramkov-Hansen, D. N. Payne, *Appl. Opt.* **20**, 2962 (1981).
4. S. T. Oh, K. R. Lee, U. C. Paek, Y. J. Chung, *Opt. Lett.* **29**, 1464 (2004).
5. V. I. Kopp *et al.*, *Science* **305**, 74 (2004).
6. C. J  uregui, J. M. L  pez-Higuera, *Opt. Lett.* **30**, 14 (2005).
7. O. V. Ivanov, *Opt. Lett.* **30**, 3290 (2005).
8. X. Ma, C.-H. Liu, G. Chang, A. Galvanauskas, *Opt. Exp.* **19**, 26515 (2011).
9. P. St. J. Russell, *J. Lightwave Technol.* **24**, 4729 (2006).
10. W. Shin, Y. L. Lee, B. A. Yu, Y. C. Noh, K. Oh, *Opt. Commun.* **282**, 3456 (2009).
11. V. M. Churikov, V. I. Kopp, A. Z. Genack, *Opt. Lett.* **35**, 342 (2010).
12. T. A. Birks, J. C. Knight, P. St. J. Russell, *Opt. Lett.* **22**, 961 (1997).
13. L. Allen, M. W. Beijersbergen, R. J. C. Spreeuw, J. P. Woerdman, *Phys. Rev. A* **45**, 8185 (1992).
14. L. Allen, M. J. Padgett, M. Babiker, *Progr. Opt.* **39**, 291 (1999).
15. S. M. Barnett, *J. Opt. B Quantum Semiclassical Opt.* **4**, 57 (2002).

Acknowledgments: The authors wish to thank M. Padgett and S. Barnett for helpful comments on the analysis in the manuscript and S. Burger from JCMwave GmbH for assistance with the finite element modeling.

Supplementary Materials

www.sciencemag.org/cgi/content/full/337/6093/446/DC1
Materials and Methods
Figs. S1 and S2
References (16–18)

25 April 2012; accepted 19 June 2012
10.1126/science.1223824

Plasmonic Nanolaser Using Epitaxially Grown Silver Film

Yu-Jung Lu,^{1*} Jisun Kim,^{2*} Hung-Ying Chen,¹ Chihhui Wu,² Nima Dabidian,² Charlotte E. Sanders,² Chun-Yuan Wang,¹ Ming-Yen Lu,³ Bo-Hong Li,⁴ Xianggang Qiu,⁴ Wen-Hao Chang,⁵ Lih-Juann Chen,³ Gennady Shvets,² Chih-Kang Shih,^{2†} Shangjr Gwo^{1†}

A nanolaser is a key component for on-chip optical communications and computing systems. Here, we report on the low-threshold, continuous-wave operation of a subdiffraction nanolaser based on surface plasmon amplification by stimulated emission of radiation. The plasmonic nanocavity is formed between an atomically smooth epitaxial silver film and a single optically pumped nanorod consisting of an epitaxial gallium nitride shell and an indium gallium nitride core acting as gain medium. The atomic smoothness of the metallic film is crucial for reducing the modal volume and plasmonic losses. Bimodal lasing with similar pumping thresholds was experimentally observed, and polarization properties of the two modes were used to unambiguously identify them with theoretically predicted modes. The all-epitaxial approach opens a scalable platform for low-loss, active nanoplasmonics.

Miniaturization of semiconductor lasers holds the key to emerging applications in on-chip integration of nanophotonics and nanoelectronics (1–3). Currently, miniaturization of semiconductor lasers based on dielectric optical cavities is impeded by the diffraction limit—that is, $\sim(\lambda/2n)^3$ for three-dimensional (3D) cavities, where λ is the free-space wavelength and n is the refractive index of the dielectric (4–7). The recent advent of nanoplasmonics based on metalodielectric structures has led to the design of optical components and optoelectronic devices in the deep subwavelength regime (8–13). In particular, a new class of lasers based on surface plasmon amplification by stimulated emission of radiation (SPASER) has been proposed (14, 15) and experimentally demonstrated (16–19). Surface plasmon polaritons (SPPs) excited in noble metal structures adjacent to gain media dramatically shrink the optical mode volume and provide the necessary feedback mechanism for a SPASER.

Among the available plasmonic cavity materials in the visible and near-infrared ranges, silver (Ag) is the best choice because of its minimal plasmonic damping (20). However, so far most plasmonic devices have their basis in granular polycrystalline Ag films, where surface roughness and grain boundaries lead to scattering of SPPs. Thus, atomically smooth or single-crystalline plasmonic structures are desirable building blocks for low-loss applications (21, 22).

With use of polycrystalline metallic materials, the lasing threshold for plasmonic nanolasers remains impractically high, and the continuous-wave (CW) operation of a plasmonic laser has yet to be demonstrated (16–19).

Having developed epitaxially grown, atomically smooth Ag films as a scalable plasmonic platform, we report a SPASER under CW operation with an ultralow lasing threshold at liquid nitrogen temperature and a mode volume well below the 3D diffraction limit. The device has its basis in the plasmonic nanocavity formed between epitaxial Ag film and a single nanorod consisting of a gallium nitride (GaN) shell and a green-emitting indium gallium nitride (InGaN) core, which acts as gain medium and which was

chosen, in part, for its relatively large optical gain (23).

Under normal growth conditions, the non-wetting nature of low-loss noble metals on semiconductor or insulator substrates leads to granular film growth. The key to achieving smooth single-crystalline Ag film is to refine a two-step process (low-temperature deposition followed by room-temperature annealing) originally developed for GaAs(110) substrates (24, 25) and to apply it to the silicon surface [Si(111), 7×7 reconstruction] (26). However, dewetting eventually occurs (25). This problem is solved by capping the as-grown Ag film with a thin dielectric layer.

During deposition at low temperature (90 K), Ag forms nanoclusters, as indicated by a spotty reflection high-energy electron diffraction (RHEED) pattern Fig. 1A, top). Upon annealing to room temperature, these nanoclusters smoothen, as indicated by streaky RHEED patterns (Fig. 1A, bottom). In situ scanning tunneling microscopy (STM) reveals that the surface is atomically smooth (Fig. 1B), with a surface step structure similar to that of the underlying Si(111) surface. The large-area film uniformity is confirmed by scanning tunneling spectroscopy (STS) (Fig. 1C), which reveals identical quantum well states at different locations on the sample surface (24, 25). At the end of growth, the sample is capped with about 1.5 nm of amorphous germanium (Ge) grown by molecular beam epitaxy (MBE). Atomic force microscopy (AFM) reveals that the Ge-capped Ag film remains atomically smooth in air (Fig. 1D).

The nanocavity is defined by a GaN nanorod (480 nm in length) partially filled with an InGaN gain medium (170 nm in length) and separated

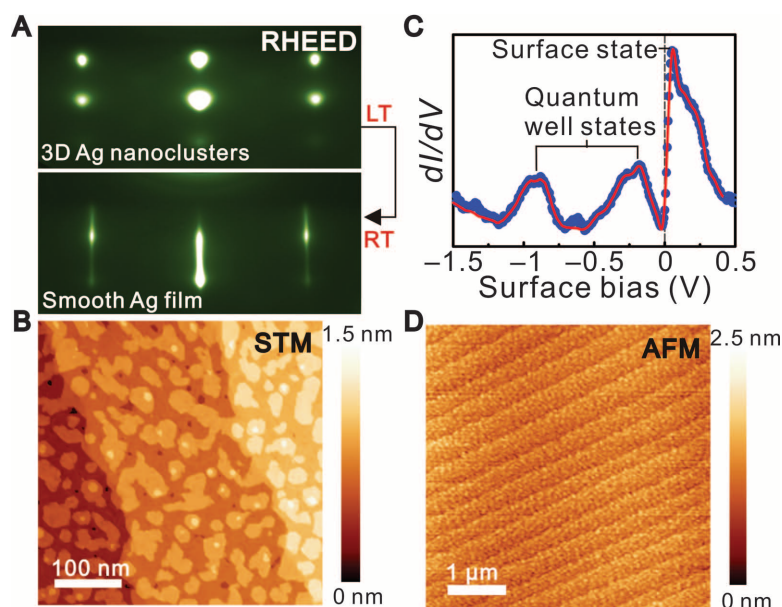


Fig. 1. (A) RHEED patterns taken during the two-step growth process. At low temperature (LT, 90 K), 3D Ag nanoclusters are observed after Ag deposition on Si(111). After room-temperature (RT) annealing, atomically smooth epitaxial Ag film forms. (B) In situ STM image of an atomically smooth epitaxial Ag film (4-nm thickness). (C) STS spectrum showing multiple quantum-well states and a surface state on epitaxial Ag film. Raw data (blue line) are shown with a superimposed smoothed spectrum (red line). (D) AFM image showing that Ge-capped Ag film remains atomically smooth in air (at RT).

¹Department of Physics, National Tsing-Hua University, Hsinchu 30013, Taiwan. ²Department of Physics, The University of Texas at Austin, Austin, Texas 78712, USA. ³Department of Materials Science and Engineering, National Tsing-Hua University, Hsinchu 30013, Taiwan. ⁴Beijing National Laboratory for Condensed Matter Physics and Institute of Physics, Chinese Academy of Sciences, Beijing 100190, China. ⁵Department of Electrophysics, National Chiao-Tung University, Hsinchu 30010, Taiwan.

*These authors contributed equally to this work.

†To whom correspondence should be addressed. E-mail: shih@physics.utexas.edu (C.-K.S.); gwo@phys.nthu.edu.tw (S.G.)

by a 5-nm silicon dioxide (SiO_2) spacer from the epitaxial Ag (Fig. 2A). A nanoscale metal-oxide-semiconductor (MOS) structure is adopted here to confine the electromagnetic field in the low-dielectric-constant oxide nanogap, which greatly reduces plasmonic loss (27). The InGaN@GaN core-shell nanorods were grown on Si(111) by plasma-assisted MBE (26), with the nanorods growing along the wurtzite polar c -axis direction (28). Detailed structural information about the InGaN@GaN core-shell nanorods is given in Fig. 2, B and C.

Because the Ag layer is atomically flat and the core-shell nanorod has well-defined facets and contact geometry, a low-loss plasmonic cavity with atomically smooth interfaces is formed between them. Strong plasmonic confinement enables extraordinary localization of the hybrid optical mode around the nanorod, resulting in excellent spatial overlap between the mode and the gain medium and enabling the ultralow-threshold CW lasing operation in a diffraction-unlimited footprint. Figure 3A shows CW lasing spectra from a single nanorod at 78 K under varying optical power densities excited by a CW semiconductor diode laser at 405 nm. The scanning electron microscope (SEM) image in Fig. 2B depicts the actual core-shell nanorod on the epi-

taxial Ag film that was used for the reported lasing measurements. Two lasing peaks can be observed, at 510 and 522 nm. Investigations carried out with similar InGaN@GaN core-shell nanorods on a 20-nm polycrystalline Ag film (26) covered with a 5-nm SiO_2 spacer layer confirm that no lasing phenomena can be observed even at 8 K [under either continuous or pulsed pumping conditions; see figs. S6 and S7 (26)], which indicates the critical role of atomically smooth epitaxial Ag film for the observation of plasmonic lasing.

A light-light (L - L) plot shows the output power of the lasing mode at 510 nm as a function of pump power for two different temperatures, 8 and 78 K (Fig. 3B). The lasing signature can be seen from the concurrent onset of the linewidth narrowing plateau and the nonlinear kink of the “S”-shaped L - L plot. The lasing thresholds are 2.1 and 3.7 kW/cm^2 for the temperatures 8 and 78 K, respectively. For a single nanorod, these power densities correspond to threshold powers of 56 and 100 nW at the respective temperatures. In comparison with previously reported lasing thresholds for MOS-based plasmonic nanolasers under pulsed mode, our CW thresholds are at least two orders of magnitude smaller (17–19). Moreover, a high spontaneous-emission

coupling factor β is estimated at 0.73, on the basis of fitting the L - L plot at 8 K; this indicates that the plasmonic cavity can effectively restrict undesired spontaneous emission in a single plasmonic mode under lasing conditions. The temperature-dependent emission properties, with lasing occurring for temperatures below 120 K (Fig. 3C), show that at higher temperatures only spontaneous emission occurs; this is because the reduced gain in InGaN cannot overcome the losses for the present device structure. The weak emissions at 532 and 556 nm, according to their L - L plots, are nonlasing peaks. The availability of multiple modes (510 and 522 nm) for such an ultrasmall cavity is due to the strong wavelength compression effects in plasmonic cavities. The second-order photon correlation function, $g^{(2)}(\tau)$, can provide another unambiguous signature for lasing in small cavities (7). As shown in Fig. 3D, below the lasing threshold $g^{(2)}(\tau = 0)$ is greater than one, signifying spontaneous emission. Above the lasing threshold, we confirm that $g^{(2)}(0) = 1$ and remains at unity for all τ , which is an unambiguous signature for the temporal coherence of lasing.

Three-dimensional simulations of the plasmonic nanolaser using COMSOL finite-element code (www.comsol.com) were carried out to clarify the nature of the two lasing modes, to determine their quality factors (Q factors) and lasing thresholds, and to elucidate the role of the atomically smooth Ag film in low-pumping-threshold lasing. The optical response of InGaN was described by an idealized single-resonance frequency-dependent permittivity function $\epsilon_g = \epsilon_\infty^g - \frac{\omega_p^2}{\omega_G^2 - \omega^2 - i2\omega\gamma_G}$.

Here, ω_G is the emission peak; ϵ_∞^g is the high-frequency permittivity of the gain medium; $\gamma_G = \omega_G/2Q_{nr}$ is the nonradiative linewidth of the emitters, with Q_{nr} the emitters' nonradiative Q factor ($Q_{nr} \approx 17$); and ω_p is the effective plasma frequency of photoexcited carriers, as determined by the population inversion and proportional to the pumping power. The eigenvalue simulations reveal the existence of two dominant high- Q modes [labeled $Q^{(n)}$, where n is the integer number of charge density nodes inside the semiconductor rod] spectrally overlapping with the gain region responsible for lowest-threshold lasing. In the absence of optical pumping (i.e., for $\omega_p^2 = 0$), these $n = 5$ and $n = 4$ modes have the highest Q factors— $Q^{(5)} \approx 13$ and $Q^{(4)} \approx 9$ —and Purcell factors— $F_p^{(5)} \approx 1.8$ and $F_p^{(4)} \approx 1.4$, respectively—as well as strongly subdiffraction mode volumes, $V \approx 0.03\lambda^3$ (26). The free-space emission profiles for the two modes are very different and can be easily identified. The $n = 5$ mode possesses a finite electric dipole moment d_x along the rod's length, responsible for highly x -polarized far-field emission, as shown in Fig. 4A (a schematic of the emission geometry is shown in Fig. 4C). On the contrary, $d_x = 0$ for the $n = 4$ mode, and the far-field radiation is dominated by the nonvanishing quadrupolar moments Q_{xx} and Q_{yy} (29) of the total charge distribution inside the hybrid plasmonic/photonic antenna. The emitted light's

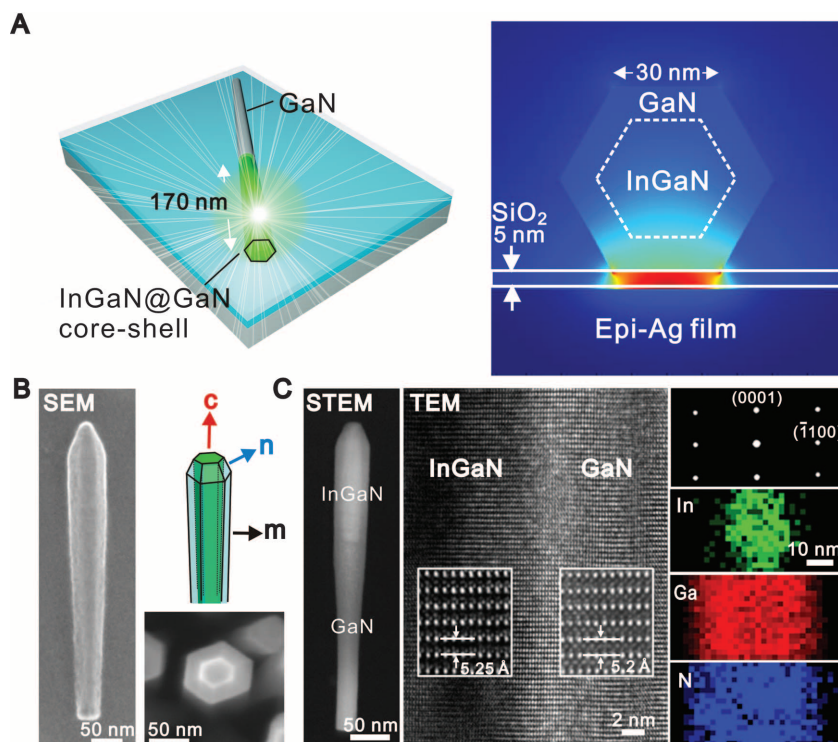


Fig. 2. (A) Schematic of device: a single InGaN@GaN core-shell nanorod on a SiO_2 -covered epitaxial Ag film (28 nm thick). The energy-density distribution (right) is calculated by the eigenmode method. (B) SEM images of InGaN@GaN core-shell nanorods. The left-hand SEM image shows the actual nanorod on epitaxial Ag film that was used for all lasing measurements. (C) Scanning transmission electron microscopy (STEM) and transmission electron microscopy (TEM) structural analyses of a single-crystalline InGaN@GaN core-shell nanorod. The bright area inside the nanorod in the high-angle angular dark field STEM image indicates the presence of the InGaN core. The elemental mapping images obtained by energy dispersive x-ray spectroscopy are used to confirm the core-shell structure and to estimate the In composition in InGaN core ($\sim 14\%$).

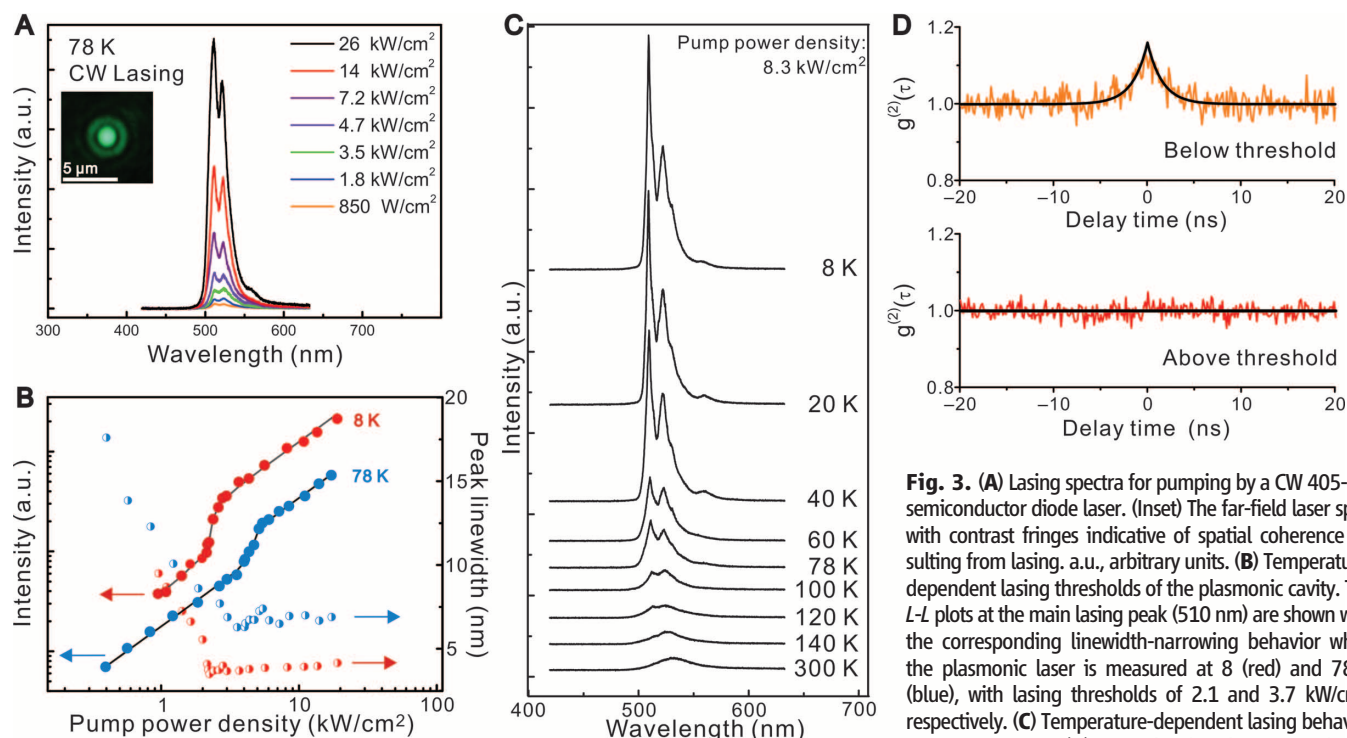


Fig. 3. (A) Lasing spectra for pumping by a CW 405-nm semiconductor diode laser. (Inset) The far-field laser spot, with contrast fringes indicative of spatial coherence resulting from lasing. a.u., arbitrary units. (B) Temperature-dependent lasing thresholds of the plasmonic cavity. The I - L plots at the main lasing peak (510 nm) are shown with the corresponding linewidth-narrowing behavior when the plasmonic laser is measured at 8 K (red) and 78 K (blue), with lasing thresholds of 2.1 and 3.7 kW/cm², respectively. (C) Temperature-dependent lasing behavior from 8 to 300 K. (D) Second-order photon correlation function measurements at 8 K.

polarization is mixed between x and y (Fig. 4B). Indeed, as can be seen from Fig. 4D, the experimentally observed bimodal lasing modes (510 and 522 nm) are highly polarized along the rod axis, with a polarization ratio of 96% for the 510-nm mode and 60% for the 522-nm mode (simulation predicts 100% and 69% polarization, respectively, for a collection geometry with a numerical aperture = 0.55 objective).

Eigenvalue simulations (26) clarify the relative importance of the four physical processes determining the modes' lifetimes: ohmic loss in the metal, emission of SPPs to outside the cavity, radiation leakage into the substrate, and far-field emission. The most important lifetime-limiting factor is SPP emission to outside the cavity; this, for atomically smooth metal, occurs only at the ends of the GaN nanorod. Therefore, the nanolaser is a highly efficient source of coherent SPPs and can be classified as a SPASER (Fig. 4C). The prevalence of SPP generation also explains why atomically smooth metal is crucial for low-threshold CW lasing: Grain boundaries in polycrystalline Ag cause additional SPPs to be scattered out of the cavity. Our 3D simulations indicate a precipitous increase in modal volume for granular Ag (26), which explains the absence of CW lasing for polycrystalline Ag in the present experiment. Simulations also show that, because modes' intrinsic Q factors are comparable with the non-radiative Q factors of the emitters [$Q_{\text{nr}} \approx Q^{(n)}$], considerable hybridization between inhomogeneously broadened emitters and plasmonic modes takes place as ω_p^2 increases with pumping. Considerable blue-shifting (26) and rapid linewidth

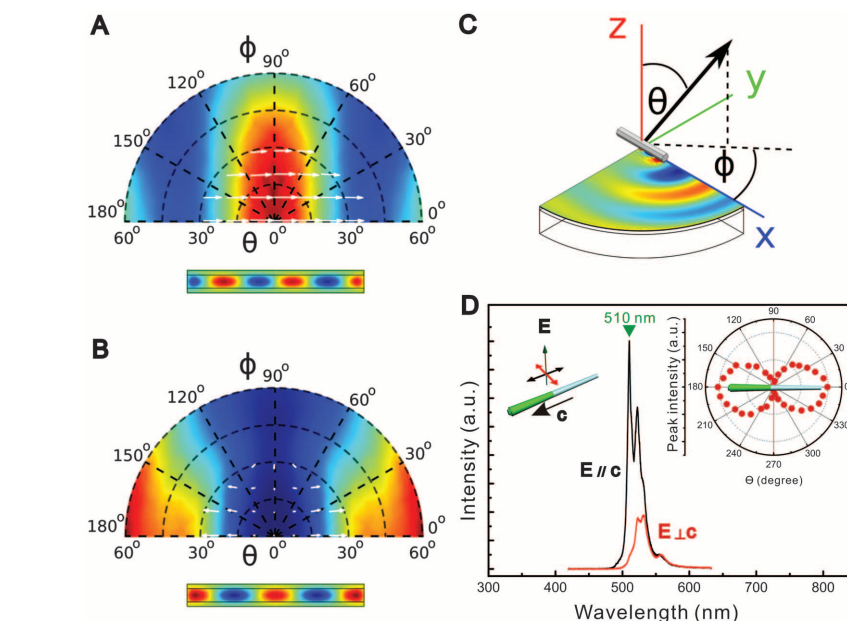


Fig. 4. (A and B) Simulations of the far-field radiation patterns (color-coded far-field radiation intensity) for two experimentally observed lasing modes. Surface charge distribution below the nanorod is color-coded. (C) Simulated emission geometry, showing that in-plane coherent SPPs are generated at the ends of the GaN nanorod. (D) Polarization-sensitive lasing spectra at 8 K, with the emission polarization oriented parallel (black curve) and perpendicular (red curve) to the nanorod axis (the c axis of wurtzite structure). (Inset) The polar plot of the emission intensity at 510 nm.

decrease of the emitter and nanocavity polaritons are the main experimentally observed signatures of such hybridization.

In summary, the development of atomically smooth epitaxial Ag on Si as a new platform

for plasmonics not only allows us to demonstrate a SPASER-enabled nanolaser but also promotes the development of monolithically integrated plasmonics and Si-based electronics on a single platform.

References and Notes

- S. Noda, *Science* **314**, 260 (2006).
- H. Altug, D. Englund, J. Vučković, *Nat. Phys.* **2**, 484 (2006).
- M. T. Hill, *J. Opt. Soc. Am. B* **27**, B36 (2010).
- K. J. Vahala, *Nature* **424**, 839 (2003).
- O. Painter *et al.*, *Science* **284**, 1819 (1999).
- A. Tandraechanurat *et al.*, *Nat. Photonics* **5**, 91 (2011).
- S. Strauf, F. Jahnke, *Laser Photon. Rev.* **5**, 607 (2011).
- W. L. Barnes, A. Dereux, T. W. Ebbesen, *Nature* **424**, 824 (2003).
- S. A. Maier, H. A. Atwater, *J. Appl. Phys.* **98**, 011101 (2005).
- D. K. Gramotnev, S. I. Bozhevolnyi, *Nat. Photonics* **4**, 83 (2010).
- J. A. Schuller *et al.*, *Nat. Mater.* **9**, 193 (2010).
- M. T. Hill *et al.*, *Nat. Photonics* **1**, 589 (2007).
- M. P. Nezhad *et al.*, *Nat. Photonics* **4**, 395 (2010).
- D. J. Bergman, M. I. Stockman, *Phys. Rev. Lett.* **90**, 027402 (2003).
- M. I. Stockman, *J. Opt.* **12**, 024004 (2010).
- M. A. Noginov *et al.*, *Nature* **460**, 1110 (2009).
- R. F. Oulton *et al.*, *Nature* **461**, 629 (2009).
- R.-M. Ma, R. F. Oulton, V. J. Sorger, G. Bartal, X. Zhang, *Nat. Mater.* **10**, 110 (2011).
- C.-Y. Wu *et al.*, *Nano Lett.* **11**, 4256 (2011).
- P. R. West *et al.*, *Laser Photon. Rev.* **4**, 795 (2010).
- P. Nagpal, N. C. Lindquist, S.-H. Oh, D. J. Norris, *Science* **325**, 594 (2009).
- J.-S. Huang *et al.*, *Nat. Commun.* **1**, 150 (2010).
- K. L. Shaklee, R. E. Nahory, R. F. Leheny, *J. Lumin.* **7**, 284 (1973).
- A. R. Smith, K.-J. Chao, Q. Niu, C. K. Shih, *Science* **273**, 226 (1996).
- H. Yu *et al.*, *Phys. Rev. Lett.* **88**, 016102 (2001).
- Information on methods, analyses, and simulations can be found in the supplementary materials available on Science Online.
- R. F. Oulton, V. J. Sorger, D. A. Genov, D. F. P. Pile, X. Zhang, *Nat. Photonics* **2**, 496 (2008).
- Y.-J. Lu, H.-W. Lin, H.-Y. Chen, Y.-C. Yang, S. Gwo, *Appl. Phys. Lett.* **98**, 233101 (2011).
- J. D. Jackson, *Classical Electrodynamics* (Wiley, New York, ed. 3, 1999), chap. 9.

Acknowledgments: We acknowledge support from the National Science Council in Taiwan (NSC-100-2120-M-007-001, NSC-98-2112-M-007-014-MY3, and NSC-98-2221-E-007-104-MY3) and, in the United States, the NSF (DMR-0906025, CMMI-0928664, and DGE-0549417), the Office of Naval Research (N00014-10-1-0929), the Air Force Office of Scientific Research (FA9550-08-1-0394), the Welch Foundation (F-1672), and the MOST of China (2009CB929102, 2012CB921302).

Supplementary Materials

www.sciencemag.org/cgi/content/full/337/6093/450/DC1
Materials and Methods
Supplementary Text
Figs. S1 to S7
References (30–34)

18 April 2012; accepted 14 June 2012
10.1126/science.1223504

Predictive Self-Assembly of Polyhedra into Complex Structures

Pablo F. Damasceno,^{1*} Michael Engel,^{2*} Sharon C. Glotzer^{1,2,3†}

Predicting structure from the attributes of a material's building blocks remains a challenge and central goal for materials science. Isolating the role of building block shape for self-assembly provides insight into the ordering of molecules and the crystallization of colloids, nanoparticles, proteins, and viruses. We investigated 145 convex polyhedra whose assembly arises solely from their anisotropic shape. Our results demonstrate a remarkably high propensity for thermodynamic self-assembly and structural diversity. We show that from simple measures of particle shape and local order in the fluid, the assembly of a given shape into a liquid crystal, plastic crystal, or crystal can be predicted.

The spontaneous organization of individual building blocks into ordered structures is ubiquitous in nature and found at all length scales. Examples include simple and complex crystals in atomic systems, liquid and plastic crystals in molecular materials, and superlattices of nanoparticles and colloids. Understanding the relation between building blocks and their assemblies is essential for materials design because physical properties depend intimately on structure. The formation of atomic materials structures can be rationalized, to first approximation, from geometric considerations (*1*), and with growing length scale, the shape of the building blocks becomes increasingly important. For colloidal particles interacting through the excluded volume arising from their shape (*2–5*), thermodynamic equilibrium structures ("phases") reported were relatively simple (*6–10*). The simulation prediction of a dodecagonal quasicrystal with tetrahedra (*11*) demonstrated the unexpected complexity that could be achieved for particles solely with hard interactions. Since then, ordered

structures have been reported for various polyhedra (*11–16*), which are now routinely synthesized as nanocrystals (*4, 5, 13, 17*). However, the a priori prediction of structure from particle shape has yet to be demonstrated.

The thermodynamic behavior of hard particles can be understood through entropy maximization (*18*). Packing efficiency plays an increasingly important role toward higher density and induces a preferential alignment of flat facets (*13, 19, 20*). Because packing efficiency increases with contact area, the alignment can be interpreted as the result of an effective, many-body directional entropic force (*14*) arising from the increased number of configurations available to the entire system, causing suitably faceted polyhedra to order. This notion of directional entropic forces and their relation to particle faceting suggests that particle shape can be used to predict assembled structures. To establish clear quantitative trends, however, requires data on many different shapes. We present thermodynamic Monte Carlo simulations of the self-assembly of 145 different polyhedra, including all the Platonic, Archimedean, Catalan, and Johnson solids and some zonohedra, prisms, and antiprisms, and we show that we can use particle shape to predict the general category of ordered structure that forms.

The polyhedra simulated, classified according to the structure(s) they assemble into from the dense fluid, are shown in Fig. 1. The names

of each polyhedron simulated and additional details can be found in fig. S1 and table S1 (*21*). We group polyhedra into three assembly categories (*12*): (i) crystals, (ii) plastic crystals, and (iii) liquid crystals. Polyhedra that are not observed to form ordered structures are grouped as (iv) disordered solids (glasses). The categories are further subdivided into classes based on the type of order and crystallographic symmetry. All structures reported form repeatedly from disordered fluid phases at packing fractions between 0.49 and 0.63, depending on particle shape. We first note that 101/145 \approx 70% of the polyhedra simulated assemble on the time scale of our simulations, which demonstrates a strong propensity for order in systems of polyhedra, even in the absence of explicit attractive interactions.

For crystals, we find five different Bravais lattices [hexagonal, cubic, body-centered tetragonal (BCT), rhombohedral, and orthorhombic]. The lattice shear we find with truncated cubes has been observed in experiments (*13, 22, 23*). The A5 lattice, graphite structure, honeycomb lattice, diamond structure (*14*), and "supercube" lattice are periodic and have only a few particles in the unit cell. The quasicrystals have been reported previously with tetrahedra (*11*) and triangular bipyramids (*24*). A new type of hexagonal random tiling forming independent layers is observed for the bilunabirotunda, a two-dimensional version of the random tiling seen in a molecular network (*25*).

Both the diversity and structural complexity possible with polyhedra are demonstrated by 12 representative structures. Four examples of crystals are analyzed in more detail. Dürer's solids form a simple cubic crystal (Fig. 2A), which is unusual because it is a degenerate crystal (*26*). Particles align randomly in four equivalent orientations. The space-filling gyrobifastigium assembles into a crystal isostructural to β -Sn, the metallic form of tin (Fig. 2B). Six square pyramids assemble into cubes ("supercubes") and then into a slightly sheared simple cubic lattice (Fig. 2C). The supercubes demonstrate the possibility of hierarchical

¹Applied Physics Program, University of Michigan, Ann Arbor, MI 48109, USA. ²Department of Chemical Engineering, University of Michigan, Ann Arbor, MI 48109, USA. ³Department of Materials Science and Engineering, University of Michigan, Ann Arbor, MI 48109, USA.

*These authors contributed equally to this work.

†To whom correspondence should be addressed. E-mail: sglotzer@umich.edu

assembly, similarly to a face-centered cubic (FCC) crystal reported for paired hemispheres (27). Pentagonal orthobicupola have a disklike shape and arrange with their five-fold symmetry axes aligned into the β -U crystal with the tiling (3.4.3².4). A periodic approximant to a dodecagonal quasicrystal, this tiling is known as the sigma phase and has been observed in micelles (28, 29) and colloids (30), but with different decoration of the tiles (Fig. 2D).

We find that 66 of the 145 polyhedra crystallize into plastic crystals [rotator phases (31)] in which the particles are free to rotate about their lattice positions. The plastic crystals we find all correspond to the crystallographically dense packings FCC (or hexagonally close-packed, HCP), body-centered cubic (BCC), and three topologically close-packed (TCP) polytetrahedral structures isostructural to β -W, β -Mn, and γ -brass. We do not distinguish between FCC and HCP, because simulations of these structures often contain high densities of stacking faults. In a TCP structure, lattice sites are coordinated by distorted tetrahedra. We always observe plastic crystals for these three types of crystals.

In Fig. 2E, we show that rhombic dodecahedra (the Voronoi cell of FCC) order into an FCC plastic crystal. We observe that the plastic crystal transforms into a nonrotator phase at higher packing fractions. Elongated triangular cupolas assemble a plastic BCC crystal (Fig. 2F). The formation of a high-symmetry phase is counterintuitive given the asymmetric shape of the cupola. The paradigmatic rhombicosidodecahedron has two large parallel faces and forms a plastic TCP phase isostructural to β -W (Fig. 2G). This phase, also known as the A15 structure, is frequently observed with micelles (32). Dodecahedra assemble into the complex β -Mn structure (Fig. 2H). Because the distribution of Bragg peaks in the diffraction pattern resembles eight-fold symmetry, β -Mn can be interpreted as an approximant of an octagonal quasicrystal (33). Indeed, we often observe eight-fold symmetry in the diffraction pattern during intermediate stages of crystallization. Truncated dodecahedra form γ -brass (Fig. 2I). With 52 atoms per unit cell, it is the most complex periodic crystal observed in this study.

A nematic liquid crystal is formed by the pentagonal pyramid, which has a plateletlike shape (Fig. 2J). The up-down orientation of the pyramid relative to the director is random. The elongated square pyramid assembles into smectic layers (Fig. 2K). We confirmed that there is no preferred orientation or long-range translational order within the layers. Like all regular prisms and antiprisms with five-fold or higher symmetry, the pentagonal prism assembles a columnar phase (34). Particles are free to both shift along and rotate around the column axis (Fig. 2L).

Forty-four polyhedra never self-assemble into an ordered structure on the time scale of our simulations, despite run times more than an order of magnitude longer than that needed for the slowest formation of a crystal. Instead, the par-

ticle dynamics becomes gradually slower with increasing packing fraction, which eventually produces a glassy state without discernible rotational or translational order. Because studies of dense packings of these polyhedra (34) yield crystals with higher packing fractions, we expect that the 44 particles have ordered "ground states" in the limit of infinite pressure. As in other examples (11, 24), those ordered states may not be kinetically accessible in experiments. It is interesting to note that 41 of the 44 that form glasses are Johnson solids, and most are not centrally symmetric. Johnson solids are typically less symmetric than Platonic and Archimedean solids, which all order in our simulations. This agrees with the intuition that highly symmetric polyhedra might be more easily assembled than nonsymmetric ones. A complete investigation of assembly kinetics and propensity requires a careful analysis of the equations of state (10, 15, 24, 35). Preliminary data suggest that particles from the same assembly category have a comparable entropy gain ΔS at the transition. For instance, liquid crystals have $\Delta S = (1.8 \pm 0.5)k_B$ and plastic crystals, $\Delta S = (1.0 \pm 0.5)k_B$, where k_B is the Boltzmann constant. No clear trend is observed for shapes that assemble into crystals.

Several parameters have been used in the literature to analyze the shape of polyhedra (12, 19, 34). A parameter that is sufficiently sensitive to large shape changes, but not too sensitive to small deformations, is the isoperimetric quotient, defined as $IQ = 36\pi V^2/S^3$, where V is volume and S is surface area (36, 37). IQ can be calculated easily from the vertex vectors and is closely related to the shape factor used in equations of state of hard convex bodies (38). A second parameter, the coordination number CN_f , accounts for the local arrangement of particles in the fluid phase before crystallization. In the case of glasses, we measure the coordination number at packing fraction 55%, which is the packing fraction where we typically observe crystallization of polyhedra that do not form glasses.

A correlation between the parameters IQ and CN_f and the assembly categories of Fig. 1 can be seen in Fig. 3A. We divide the parameter space into three regions. In the rightmost region ($IQ > 0.7$), 58 of 59 highly spherical polyhedra are observed to form plastic crystals. In the bottom-most region ($CN_f < 2$), 21 of 24 polyhedra with few neighbors form liquid crystals. Finally, 16 of 18 particles in the center region ($IQ \leq 0.7$ and $CN_f \geq 2$) assemble into crystals. Thus, based on

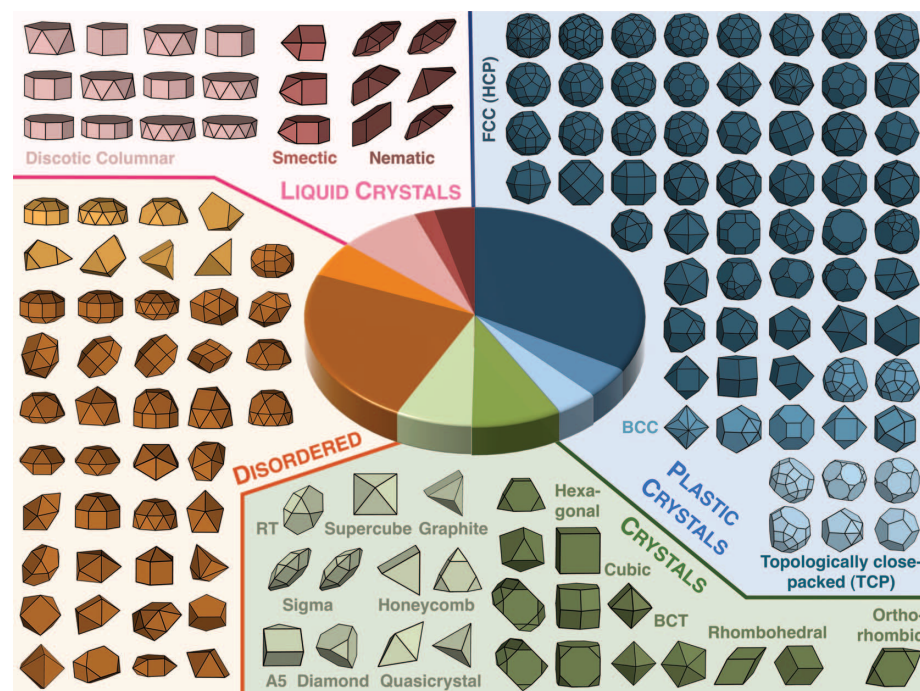


Fig. 1. Polyhedra are separated into four categories of organization as indicated by different colors: liquid crystals, plastic crystals, crystals, and disordered (glassy) phases. Subcategories (classes) are indicated by shades. The assembly category of liquid crystals contains the classes discotic columnar, smectic, and nematic (different shades of pink). Plastic crystal classes are FCC (dark blue), BCC (blue), and TCP (light blue). In the case of crystals, we distinguish Bravais lattices (dark green) and non-Bravais lattices (light green). RT stands for random tiling. For the glasses, no assembly is observed, and we distinguish those that strongly order locally with preferential face-to-face alignment (light orange) from those with only weak local order (dark orange). The pie chart in the center compares the relative frequency of the 10 observed classes. In each of the classes, polyhedra are listed in decreasing order of the isoperimetric quotient. A polyhedron is included multiple times if it was found to assemble into more than one ordered structure.

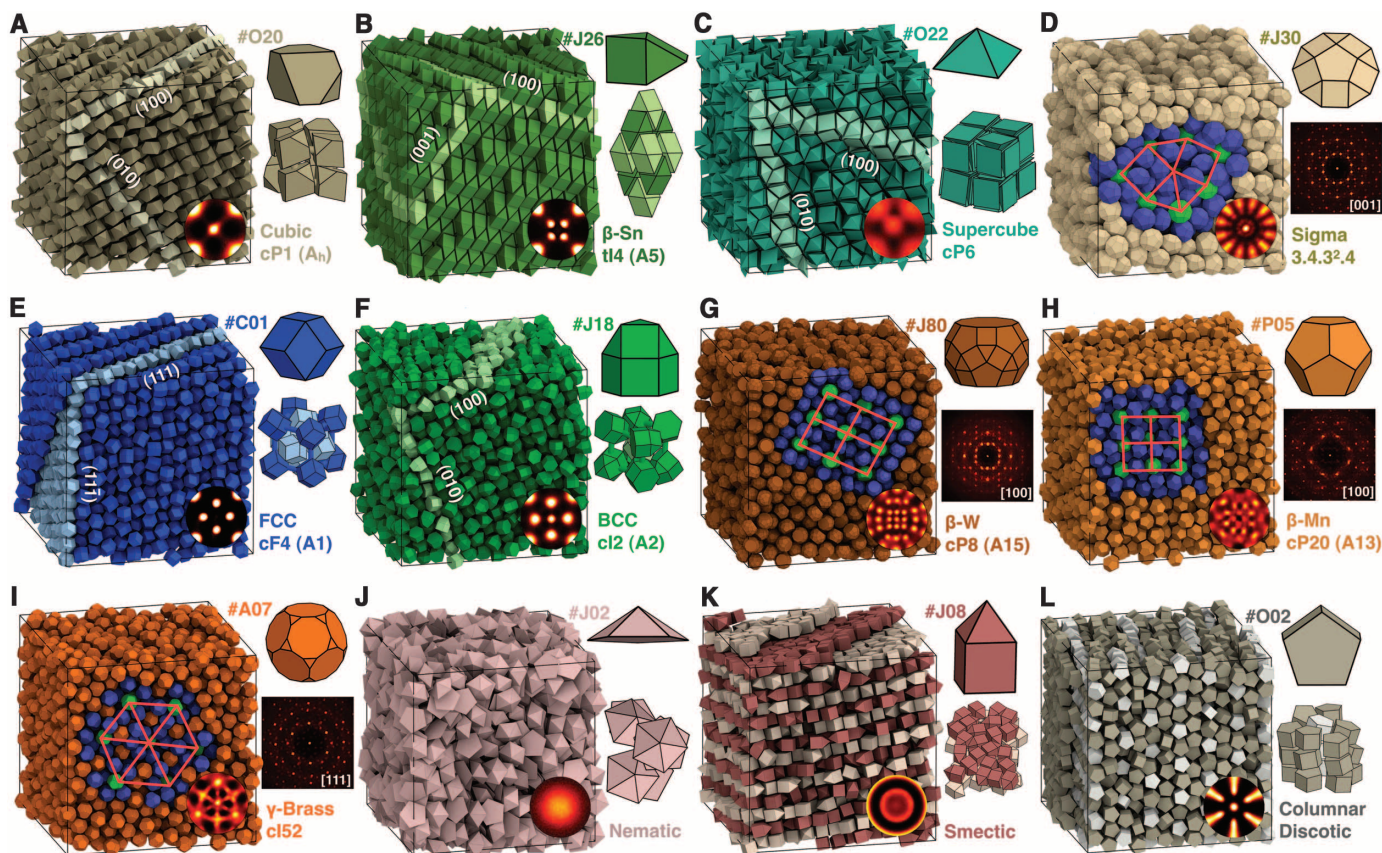


Fig. 2. Systems of 2048 polyhedra were assembled starting from the disordered fluid. In each subfigure, a snapshot of the simulation box (left), the bond-order diagram for nearest neighbors (inset), the polyhedron shape and ID (top right), a small group of particles or the diffraction pattern (middle right), and the crystallographic characterization consisting of name or atomic proto-

type, Pearson symbol, and Strukturbericht designation (bottom right) are shown. The snapshots depict crystals (A to D), plastic crystals (E to I), and liquid crystals (J to L). Some low index planes (A to C, E, and F), tiling descriptions consisting of squares and triangles (D and G to I) and structural features (K and L) are highlighted in the simulation snapshots by different colors.

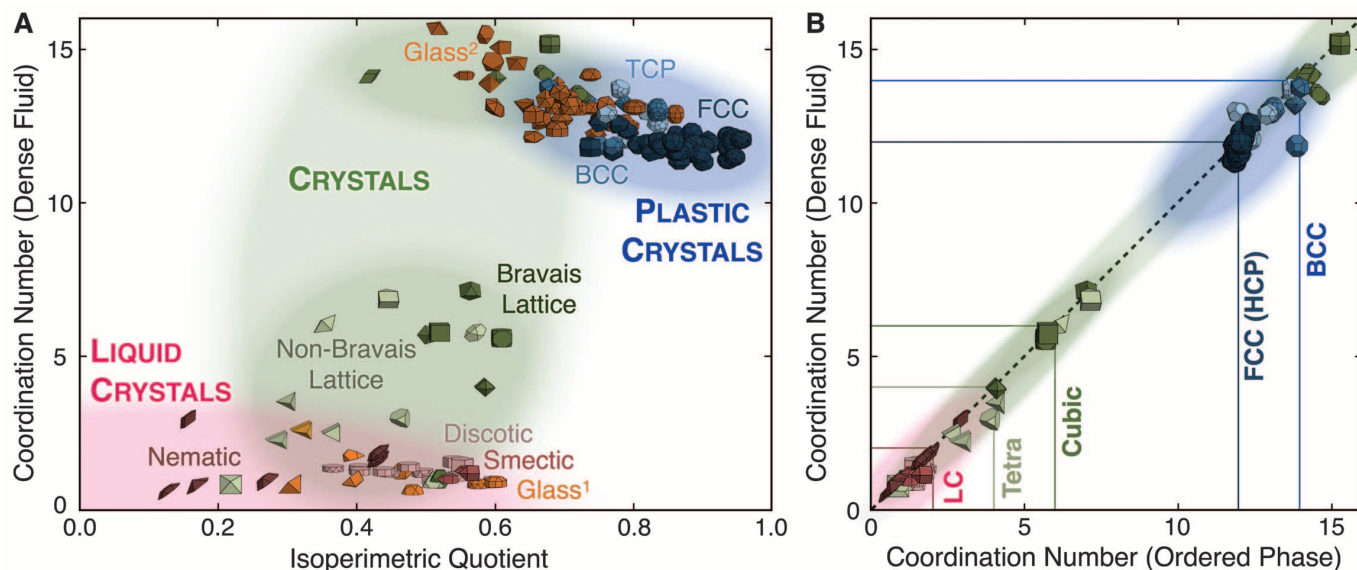


Fig. 3. (A) The coordination number in the fluid phase, CN_f , is correlated to the isoperimetric quotient (IQ) of the polyhedron. Here, IQ is a scalar parameter for the sphericity of the shape and coordination number is a measure for the degree of local order. Data points are drawn as small polyhedra. Polyhedra are colored and grouped according to the assem-

blies they form. (B) Polyhedra have, in most cases, nearly identical coordination number in the ordered phase (CN_o) and the fluid phase (CN_f) close to the ordering transition. Because of this strong correlation, combining CN_f and IQ allows for prediction of the assembly category expected for most cases.

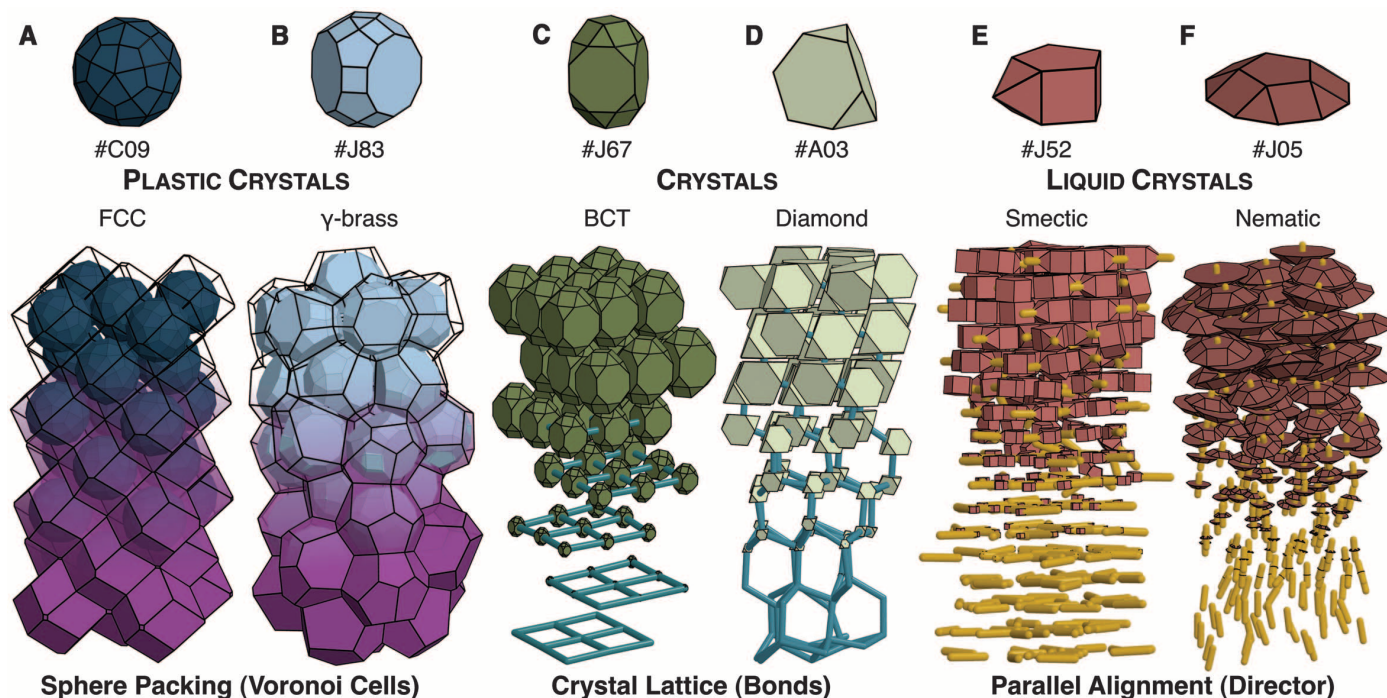


Fig. 4. We analyze six systems of polyhedra that span the three assembly categories observed with hard polyhedra. Polyhedra and their IDs are shown at top and small groups of particles are extracted from simulation snapshots below. (A and B) In plastic crystals, polyhedra rotate inside their Voronoi cells.

(C and D) Entropic “bonds” in the direction of the face normal are important for crystals. (E and F) Parallel alignment dominates in the case of liquid crystals. From top to bottom, the transparency of Voronoi cells is decreased and/or the size of polyhedra is reduced.

IQ and CN_f alone, the assembly of $95/101 = 94\%$ of the polyhedra studied into crystals, liquid crystals, or plastic crystals is predicted. The outliers either lie within boundaries between regions, or they are nearly space-filling, which favors crystals over liquid or plastic crystals. We expect the shaded regions in Fig. 3A to become further refined as additional shapes are investigated. For example, the liquid crystal region is expected to expand upward for prolate particles (not studied here), which have a higher CN_f than oblate particles yet still have a low IQ.

We compare the coordination number measured close to the ordering transition in the fluid (CN_f) and in the ordered structure (CN_o) in Fig. 3B. Both numbers are nearly identical for almost all 101 shapes that assemble. This explains why it is sufficient to determine the coordination number in the dense fluid, which can be obtained from short simulations and experiments by integrating over the first peak of the radial distribution function, to predict with reasonable accuracy the category of structure that will form from the disordered fluid. As an independent test of Fig. 3A, we calculated the IQ and CN_f for the family of truncated tetrahedra studied in (14) and correctly predict that each member should form a crystal (fig. S2).

When comparing our observations with known crystal structures of atoms and molecules, which can be rationalized in terms of a few parameters, like the strength and directionality of bonds between atoms (39) and the molecular geometry (40),

we can interpret our findings as follows. First, FCC (HCP) and BCC crystals form from highly spherical polyhedra that have nondirectional or weakly directional entropic interactions. TCP structures are a compromise between high density and maintaining icosahedral local order present in the dense liquid. The coordination geometry can be visualized with Voronoi cells (Fig. 4, A and B). Voronoi cells of TCP structures often have pentagonal or hexagonal faces. We frequently find TCP structures with particles that resemble the Voronoi cells, such as the (truncated) dodecahedron. The assembly of plastic crystals is dominated by packing, and their atomic analog is metals and metallic bonding. It is interesting to note that all of our plastic crystals except γ -brass are isostructural to crystals found in elementary metals. Second, polyhedra that form crystals are more aspherical, with more pronounced and fewer faces. The crystal lattice is well represented by an ordered network of entropic “bonds” (Fig. 4, C and D). Polyhedra assembling into crystals do not always resemble the Voronoi cells of the crystal, but usually have strong directional entropic bonding, reminiscent of covalent bonds. Third, polyhedra forming liquid crystals typically have an axial shape. Alignment of the most prominent faces is important for these phases and can be analyzed by the alignment of the directors (Fig. 4, E and F). In general, we expect for axial particles to align prominent faces and long particle dimensions first. The behavior of polyhedra forming liquid crystals corresponds most closely to mo-

lecular liquid crystals. In all cases, the degree of directional entropic bonding may be quantified through various shape descriptors and correlation functions (fig. S3).

Our results push the envelope of entropic crystallization and the assembly behavior of hard particle fluids and provide an important step toward a predictive science of nanoparticle and colloidal assembly, which will be necessary to guide experiments with families of polyhedrally shaped particles that are now becoming available. Although we are not yet able to predict a specific structure (e.g., BCC or diamond), the knowledge that obtaining, e.g., the diamond structure requires a shape with intermediate IQ or that a complex, topologically close-packed structure like γ -brass requires a shape with high IQ provides important predictive guidance for building block design and synthesis. With further developments, more refined future structure prediction, with the level of detail now possible for atoms (41), should be attainable.

References and Notes

1. L. Pauling, *J. Am. Chem. Soc.* **51**, 1010 (1929).
2. F. Li, D. P. Josephson, A. Stein, *Angew. Chem. Int. Ed.* **50**, 360 (2011).
3. S. C. Glotzer, M. J. Solomon, *Nat. Mater.* **6**, 557 (2007).
4. Z. Quan, J. Fang, *Nano Today* **5**, 390 (2010).
5. M. H. Huang, P.-H. Lin, *Adv. Funct. Mater.* **22**, 14 (2012).
6. B. J. Alder, T. E. Wainwright, *J. Chem. Phys.* **27**, 1208 (1957).
7. M. D. Eldridge, P. A. Madden, D. Frenkel, *Nature* **365**, 35 (1993).
8. L. Onsager, *Ann. N.Y. Acad. Sci.* **51**, 627 (1949).

9. D. Frenkel, H. N. W. Lekkerkerker, A. Stroobants, *Nature* **332**, 822 (1988).
10. D. Frenkel, B. M. Mulder, *Mol. Phys.* **55**, 1171 (1985).
11. A. Haji-Akbari *et al.*, *Nature* **462**, 773 (2009).
12. U. Agarwal, F. A. Escobedo, *Nat. Mater.* **10**, 230 (2011).
13. J. Henzie, M. Grünwald, A. Widmer-Cooper, P. L. Geissler, P. Yang, *Nat. Mater.* **11**, 131 (2011).
14. P. F. Damasceno, M. Engel, S. C. Glotzer, *ACS Nano* **6**, 609 (2012).
15. R. Ni, A. P. Gantapara, J. de Graaf, R. van Roij, M. Dijkstra, <http://dx.doi.org/10.1039/C2SM25813G>.
16. F. Smalenburg, L. Filion, M. Marechal, M. Dijkstra, <http://arXiv.org/abs/1111.3466>.
17. L. Rossi *et al.*, *Soft Matter* **7**, 4139 (2011).
18. D. Frenkel, *Physica A* **263**, 26 (1999).
19. S. Torquato, Y. Jiao, *Nature* **460**, 876 (2009).
20. K. L. Young *et al.*, *Proc. Natl. Acad. Sci. U.S.A.* **109**, 2240 (2012).
21. Materials and methods are available as supplementary materials on Science Online.
22. K. Zhao, R. Bruinsma, T. G. Mason, *Proc. Natl. Acad. Sci. U.S.A.* **108**, 2684 (2011).
23. Y. Zhang, F. Lu, D. van der Lelie, O. Gang, *Phys. Rev. Lett.* **107**, 135701 (2011).
24. A. Haji-Akbari, M. Engel, S. C. Glotzer, *Phys. Rev. Lett.* **107**, 215702 (2011).
25. M. O. Blunt *et al.*, *Science* **322**, 1077 (2008).
26. S. J. Gerbode, S. H. Lee, C. M. Liddell, I. Cohen, *Phys. Rev. Lett.* **101**, 058302 (2008).
27. M. Marechal, R. J. Kortschot, A. F. Demirörs, A. Imhof, M. Dijkstra, *Nano Lett.* **10**, 1907 (2010).
28. G. Ungar, Y. Liu, X. Zeng, V. Percec, W.-D. Cho, *Science* **299**, 1208 (2003).
29. S. Lee, M. J. Bluemle, F. S. Bates, *Science* **330**, 349 (2010).
30. D. V. Talapin *et al.*, *Nature* **461**, 964 (2009).
31. Although "rotator phases" constitute a subset of "plastic crystals" in molecular materials, the terms are used synonymously for hard particles.
32. P. Zihler, R. D. Kamien, *J. Phys. Chem. B* **105**, 10147 (2001).
33. M. Elenius, F. Zetterling, M. Dzugutov, D. Fredrickson, S. Lidin, *Phys. Rev. B* **79**, 144201 (2009).
34. J. de Graaf, R. van Roij, M. Dijkstra, *Phys. Rev. Lett.* **107**, 155501 (2011).
35. A. Haji-Akbari, M. Engel, S. C. Glotzer, *J. Chem. Phys.* **135**, 194101 (2011).
36. G. Poly, *Induction and Analogy in Mathematics* (Princeton Univ. Press, Princeton, NJ, 1954), pp. 188–189.
37. W. L. Miller, A. Cacciuto, *J. Chem. Phys.* **133**, 234903 (2010).
38. I. Nezbeda, *Chem. Phys. Lett.* **41**, 55 (1976).
39. G. S. Rohrer, *Structure and Bonding in Crystalline Materials* (Cambridge Univ. Press, Cambridge, 2004).
40. J. N. Israelachvili, *Intermolecular and Surface Forces* (Academic Press, Waltham, MA, 2010), pp. 535–576.
41. S. M. Woodley, R. Catlow, *Nat. Mater.* **7**, 937 (2008).

Acknowledgments: This material is based in part upon work supported by the Assistant Secretary of Defense for Research and Engineering, U.S. Department of Defense [DOD/ASD(R&E)] (N00244-09-1-0062). Any opinions, findings, and conclusions or recommendations expressed in this publication are those of the authors and do not necessarily reflect the views of the DOD/ASD(R&E). S.C.G. acknowledges support by the U.S. Army Research Office under Grant Award no. W911NF-10-1-0518. M.E. acknowledges support from the Deutsche Forschungsgemeinschaft (EN 905-1/1). P.F.D. was supported in part by the U.S. Air Force Office of Scientific Research under Multidisciplinary University Research Initiative no. FA9550-06-1-0337, subaward no. 444286-P061716. We thank R. G. Petschek and J. M. Millunchick for comments on the original manuscript.

Supplementary Materials

www.sciencemag.org/cgi/content/full/337/6093/453/DC1
Materials and Methods
Supplementary Text
Figs. S1 to S3
Table S1
References (42, 43)

21 February 2012; accepted 11 June 2012
10.1126/science.1220869

The Tides of Titan

Luciano Iess,^{1*} Robert A. Jacobson,² Marco Ducci,¹ David J. Stevenson,³ Jonathan I. Lunine,⁴ John W. Armstrong,² Sami W. Asmar,² Paolo Racioppa,¹ Nicole J. Rappaport,² Paolo Tortora⁵

We have detected in Cassini spacecraft data the signature of the periodic tidal stresses within Titan, driven by the eccentricity ($e = 0.028$) of its 16-day orbit around Saturn. Precise measurements of the acceleration of Cassini during six close flybys between 2006 and 2011 have revealed that Titan responds to the variable tidal field exerted by Saturn with periodic changes of its quadrupole gravity, at about 4% of the static value. Two independent determinations of the corresponding degree-2 Love number yield $k_2 = 0.589 \pm 0.150$ and $k_2 = 0.637 \pm 0.224$ (2σ). Such a large response to the tidal field requires that Titan's interior be deformable over time scales of the orbital period, in a way that is consistent with a global ocean at depth.

Since its gravitational capture by Saturn on 1 July 2004, the spacecraft Cassini has flown by Titan more than 80 times, carrying out extensive observations of the surface and the atmosphere by means of particle and remote sensing instruments. In contrast, information on the moon's deep interior is scarce. Lacking a detectable internally generated magnetic field, constraints on the interior of Titan come from gravity, topography, and rotation measurements. Titan's main deviations from spherical symmetry are caused by centrifugal and tidal forces, associated respectively with the rotation about its spin axis and the gradient of Saturn's gravity. The moon responds to the centrifugal and tidal potentials

with deformations that (to the lowest order) change its quadrupole field. In a body-fixed frame with the prime meridian pointing to the central planet at pericenter and the z axis along the instantaneous rotation axis (coinciding with the orbit normal), only the J_2 and C_{22} quadrupole coefficients are different from zero for a relaxed, synchronous satellite. They are bound by the constraint $J_2/C_{22} = 10/3$. The satellite's static response to the external fields is usually characterized by a single parameter, the fluid Love number k_F , which reaches its maximum value of $3/2$ for an incompressible fluid body. Previous determinations of Titan's gravity (I) yielded $k_F = 1.0097 \pm 0.0039$, implying a relaxed shape, very close to hydrostatic equilibrium. The value smaller than $3/2$ revealed a significant concentration toward the center, with a moment of inertia factor $\tilde{C} = 0.3414 \pm 0.0005$ (inferred from the Radau-Darwin equation). However, the non-negligible eccentricity of Titan's orbit causes a variation with time of the quadrupole tidal field [proportional to $1/r^3$ (r , distance between Titan and the Saturn barycenter)]. These short-term variations change the satellite's physical shape

and gravity. Titan's linear response to the periodic tidal field entails a corresponding periodic change in its own quadrupole potential. The ratio between the perturbed and the perturbing potentials is known as the k_2 Love number. It is an indication of the mass redistribution inside the body in response to the forcing potential. k_2 , like k_F , reaches its theoretical upper limit of $3/2$ for an incompressible liquid body, whereas for a perfectly rigid body, $k_2 = 0$. If Titan hosts a global subsurface ocean, then k_2 must differ substantially from zero. We have detected the signature of the tidal forcing in Cassini data and derived a value of k_2 .

Our observational strategy entailed gravity determinations near the pericenter and apocenter of Titan's orbit. For $k_2 = 0.4$ (a typical value if an ocean is present), the expected peak-to-peak variations of the quadrupole coefficients are about 4% for J_2 and 7% for C_{22} (2, 3). The corresponding change in the spacecraft acceleration, about 0.2 mgal in the most favorable geometry, is measurable by the Cassini tracking

Table 1. Titan's k_2 Love number, estimated from different data analysis procedures (supplementary materials) and representations of the gravity field: multi-arc analysis and 3×3 gravity field (SOL1a); multi-arc analysis and 4×4 gravity field (SOL1b); and global solution with 3×3 gravity field (SOL2). SOL1 and SOL2 were produced independently by the Cassini Radio Science Team and the Navigation Team.

	k_2 (value $\pm 1\sigma$)		
SOL1a	0.589	\pm	0.075
SOL1b	0.670	\pm	0.090
SOL2	0.637	\pm	0.112

¹Dipartimento di Ingegneria Meccanica e Aerospaziale, Università La Sapienza, via Eudossiana 18, 00184 Rome, Italy. ²Jet Propulsion Laboratory, 4800 Oak Grove Drive, Pasadena, CA 91109, USA. ³Division of Geological and Planetary Sciences, California Institute of Technology, Pasadena, CA 91125, USA. ⁴Department of Astronomy, Cornell University, Ithaca, NY 14850, USA. ⁵DIEM-II Facoltà di Ingegneria, Università di Bologna, I-47121 Forlì, Italy.

*To whom correspondence should be addressed. E-mail: luciano.iess@uniroma1.it

Table 2. Coefficients of the unnormalized spherical harmonics (3×3 gravity field, static component), estimated using two different approaches.

	SOL1a [value $\pm 1\sigma$ ($\times 10^{+06}$)]	SOL2 [value $\pm 1\sigma$ ($\times 10^{+06}$)]
J_2	33.599 ± 0.332	31.911 ± 0.563
C_{21}	0.186 ± 0.101	0.014 ± 0.116
S_{21}	0.664 ± 0.246	-1.291 ± 0.368
C_{22}	10.121 ± 0.029	9.964 ± 0.062
S_{22}	0.194 ± 0.033	0.262 ± 0.061
J_3	-1.097 ± 0.606	-1.236 ± 0.818
C_{31}	0.595 ± 0.174	1.070 ± 0.247
S_{31}	1.062 ± 0.286	0.492 ± 0.327
C_{32}	0.275 ± 0.069	0.410 ± 0.116
S_{32}	0.072 ± 0.048	0.168 ± 0.094
C_{33}	-0.222 ± 0.008	-0.223 ± 0.014
S_{33}	-0.264 ± 0.011	-0.265 ± 0.021

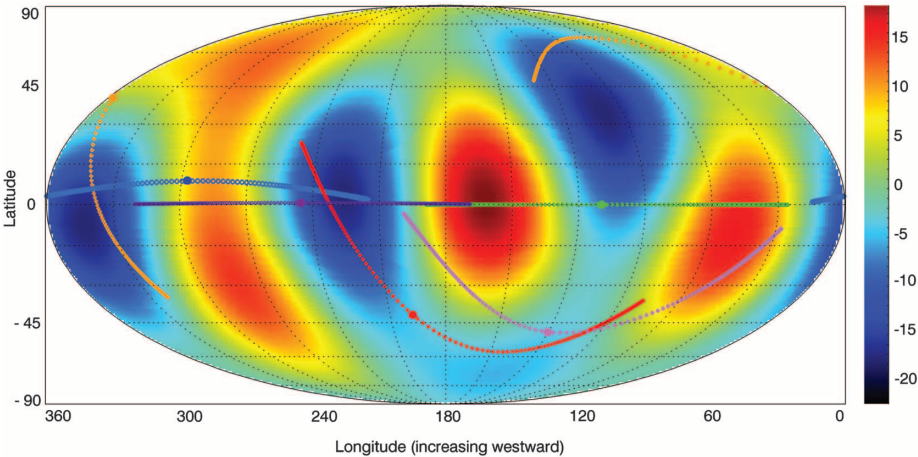


Fig. 1. Geoid heights (in meters) from SOL1a, over the reference ellipsoid defined by the gravitational parameter (GM) of Titan, J_2 , C_{22} , and the rotational velocity ω . The ground tracks of the six gravity flybys [T11 (green), T22 (orange), T33 (blue), T45 (red), T68 (magenta), and T74 (purple)] show the unequal coverage of the satellite: Although the spacecraft repeatedly probed the equatorial regions, no measurements at high latitudes are available. The geoid height uncertainties reach the maximum value of 2.2 m over the poles (fig. S3).

system. We inferred the gravity field of Titan and its tidal variations from precise range-rate measurements of the spacecraft, enabled by microwave radio links with the ground antennas of NASA’s Deep Space Network (4). In order to increase the confidence in the results, and following the same approach adopted in the previous determination of Titan’s gravity (1), we carried out two independent analyses. In the first one (SOL1), all Doppler data from the six gravity flybys (table S1) were processed in a multi-arc fit estimating a full 3×3 static gravity field; the (real) Love number (5); Titan’s state vector (position and velocity) at a reference epoch; and, for each flyby, the state vector of the spacecraft. The second analysis (SOL2) combined all available radiometric tracking and optical navigation data from the Cassini mission, data from the Pioneer and Voyager Saturn encounters, and astronomical observations of Saturn and its satellites, in a global solution for the planet and sat-

ellite ephemerides and the gravitational parameters of the bodies in the saturnian system. Both solutions provide consistent values of k_2 (Table 1) and gravity harmonics (Table 2) at 3σ for quadrupole gravity coefficients and 1σ for k_2 . The large k_2 value (~ 0.6) indicates that Titan is highly deformable over time scales of days. The central value exceeds the range previously expected for a subsurface ocean and a silicate core (6). Although the consistency of the two analyses strengthens the result, we have further tested the robustness of the solutions to perturbations of the dynamical model (3). The estimate of k_2 survived to an increase of the solution rank by using a 4×4 gravity field (SOL1b in Table 1) and to changes of the a priori uncertainties in the state vectors of Titan, Cassini, and the gravity coefficients. Estimating a complex k_2 leaves the real part statistically unchanged (5). The inclusion of a nonzero k_2 and two new flybys in the solution does not modify in any statistically significant way the gravity field previ-

ously determined (1). Titan is confirmed to be in a relaxed shape with a moment of inertia factor (inferred from C_{22} using the Radau-Darwin equation) of 0.3431 ± 0.0004 in SOL1a and 0.3438 ± 0.0005 in SOL2. The updated geoid and associated uncertainties (from SOL1a) are shown in Fig. 1 and fig. S2. The physically likely range of k_2 for Titan is bounded by the purely elastic value of ~ 0.04 (6) and the perfectly hydrostatic (fluid) value of about 1.0 (7) for the measured permanent tide (a higher formal value for k_2 of 1.5 is obtained for a fluid body of uniform density). Our result is closer to the perfectly hydrostatic value and clearly excludes the elastic value. It is physically unrealistic for Titan to be entirely elastic yet have a very much lower rigidity than that of solid ice or rock, given its size; therefore our result strongly suggests that some global layer within Titan is behaving like a fluid on orbital time scales. There are two ways in which this can arise: by the presence of a very low-viscosity layer (an ocean) beneath an outer ice shell or a low-viscosity deep interior (or some combination) (6). In the former model, the outer ice shell must be sufficiently thin that the resulting increase in hoop stress allows for a nearly fluidlike strain for the tidal forcing (a state also postulated for Io and Europa). In that thin-shell limit, the value of the shell elasticity has little effect on the Love number. For example, doubling the rigidity decreases k_2 by $\sim 10\%$. The thickness of the underlying ocean is unimportant. The resulting predicted k_2 is then about 0.42 to 0.48 for a shell thickness ranging from 100 to 0 km, assuming that the portion of the interior below the ocean (the deep interior) is effectively rigid; i.e., contributes negligibly to the external time-dependent tidal gravity. Relaxing the assumption of a rigid deep interior yields k_2 values all the way up to 1.0 for sufficiently low viscosity, even when an ocean is absent. In (6), such a model is formulated as a Maxwell viscoelastic body, but in the low-viscosity limit (where Maxwell time is less than the orbital period) the elastic part of the response is unimportant. For a homogeneous and entirely viscous body, the relevant viscosity is determined by a dimensionless number introduced by Darwin (7)

$$\epsilon = \arctan \left[\frac{19\eta\omega}{2\rho gR} \right]$$

where η is the dynamic viscosity, ω is the orbital angular velocity, ρ is the density, g is gravitational acceleration, and R is radius. Darwin found that the tidal amplitude is reduced by $\cos(\epsilon)$ relative to the hydrostatic tide and that the ratio of the imaginary to real parts of the Love number is $\tan(\epsilon)$. For Titan, ϵ is $\sim 0.6(\eta/10^{14} \text{ Pa} \cdot \text{s})$. This model predicts a small imaginary part of the Love number (<0.1) and satisfies the real part for a viscosity ~ 1 to a few $10^{13} \text{ Pa} \cdot \text{s}$ (8), which is several times less than the value often attributed to ice near its freezing point. The correct value for

water ice depends on grain size, which is not an independent variable but is determined by the stress level. Unlike Europa, the tidal stress in Titan's deep interior is lower than the stress expected for convection; this means that the correct viscosity to use may be the same as that needed to transport the heat out by convection. However, the nature of the rheology at tidal frequencies is still imperfectly understood. A rocky core made weak by active dehydration and hence fracturing and the circulation of water through cracks (9) could also contribute to raising the value of k_2 .

Alternatively, the value of k_2 contributed by the ocean itself would be enhanced if the ocean were more massive; that is, denser than the value of 1 g/cm^3 assumed for an ammonia-doped liquid water composition (10). A model in which the ocean has a large amount of sulfur; for example, in the form of ammonium sulfate $(\text{NH}_4)_2\text{SO}_4$; increases the ocean density by 35% (11), raising the value of k_2 contributed by the ocean alone to 0.57 (2). The value of k_2 owing to the ocean could be even higher were it not for the very thick shell required to accommodate the presence of additional ammonium sulfate (11).

Our results do not distinguish between the various models because of the large range of admissible values of k_2 . Were one to demand that any given model provide a value of k_2 closer to the central value, a model with a low-viscosity deep interior or a sulfur-rich ocean would be re-

quired. However, these models have other problems. A low viscosity for the high-pressure ice phases of Titan's deep interior is difficult to reconcile with the values compatible with reasonable heat flows (10), as well as with a largely or fully differentiated rock core. The sulfur-rich ocean model (11) requires extensive leaching of sulfur from the core to a near-surface ocean, which is yet to be quantitatively demonstrated. A further objection to the high-density ocean model is that there is no evidence for the expected sulfur deposits on the surface (12). A simple water or ammonia-doped water ocean overlain by a thin ($<100 \text{ km}$) shell is favored on various physical grounds quantified in almost all published evolution models (13), indirectly by the Huygens electric-field measurements (14), and consistent with the lowest end of the range of k_2 derived here.

References and Notes

1. L. Iess *et al.*, *Science* **327**, 1367 (2010).
2. N. Rappaport *et al.*, *Icarus* **126**, 313 (1997).
3. See the supplementary materials for additional discussion.
4. Thanks to the use of X- and Ka-band (8.4 and 32.5 GHz) frequencies and state-of-the-art instrumentation, range-rate accuracies were in the range from 2×10^{-5} to $9 \times 10^{-5} \text{ m/s}$ at integration times of 60 s, depending on the solar elongation angle. The dependence is due to interplanetary plasma noise, which dominates the Doppler error budget (15).
5. A determination of the complex Love number yields a value for $\text{Im}(k_2)$ compatible with zero at the 1σ level.

Because the flybys and their geometry were selected to maximize the sensitivity to the real part of k_2 , the estimate of $\text{Im}(k_2)$ is less stable than for the real counterpart.

6. N. Rappaport *et al.*, *Icarus* **194**, 711 (2008).
7. G. H. Darwin, *Philos. Trans. R. Soc. London* **170**, 1 (1879).
8. D. L. Goldsby, D. L. Kohlstedt, *J. Geophys. Res. Solid Earth* **106**, 11017 (2001).
9. J. C. Castillo-Rogez, J. I. Lunine, *Geophys. Res. Lett.* **37**, L20205 (2010).
10. G. Tobie, O. Grasset, J. I. Lunine, A. Mocquet, C. Sotin, *Icarus* **175**, 496 (2005).
11. A. D. Fortes, P. Grindrod, S. Trickett, L. Vocablo, *Icarus* **188**, 139 (2007).
12. F. Paganelli *et al.*, *Planet. Space Sci.* **56**, 100 (2008).
13. F. Sohl, *Science* **327**, 1338 (2010).
14. C. Béghin, C. Sotin, M. Hamelin, C. R. Geosci. **342**, 425 (2010).
15. S. W. Asmar *et al.*, *Radio Sci.* **40**, RS2001 (2005).

Acknowledgments: L.I., M.D., P.R., and P.T. acknowledge support from the Italian Space Agency. The work of R.A.J., J.W.A., S.W.A., and N.J.R. was carried out at the Jet Propulsion Laboratory, California Institute of Technology, under a contract with NASA. The Doppler data used in this analysis are archived in NASA's Planetary Data System.

Supplementary Materials

www.sciencemag.org/cgi/content/full/science.1219631/DC1
Materials and Methods
Supplementary Text
Figs. S1 to S3
Tables S1 to S4
References (16–20)

25 January 2012; accepted 6 June 2012

Published online 28 June 2012;

10.1126/science.1219631

Isotropic Events Observed with a Borehole Array in the Chelungpu Fault Zone, Taiwan

Kuo-Fong Ma,^{1,2*} Yen-Yu Lin,¹ Shiann-Jong Lee,² Jim Mori,³ Emily E. Brodsky⁴

Shear failure is the dominant mode of earthquake-causing rock failure along faults. High fluid pressure can also potentially induce rock failure by opening cavities and cracks, but an active example of this process has not been directly observed in a fault zone. Using borehole array data collected along the low-stress Chelungpu fault zone, Taiwan, we observed several small seismic events (I-type events) in a fluid-rich permeable zone directly below the impermeable slip zone of the 1999 moment magnitude 7.6 Chi-Chi earthquake. Modeling of the events suggests an isotropic, nonshear source mechanism likely associated with natural hydraulic fractures. These seismic events may be associated with the formation of veins and other fluid features often observed in rocks surrounding fault zones and may be similar to artificially induced hydraulic fracturing.

Fluid-driven cracks and fractures are often found in the rocks surrounding fault zones and are thought to play a critical role in determining fault strength (1). However, the pro-

cess by which these fault zone features form has not been seismically observed. Hydraulic fracturing features should be accompanied by small earthquakes with nonshearing faulting mechanisms. Analogous events have been observed seismically in volcanic and geothermal systems, as well as during artificial situations in which fluids are pumped into or out of the ground [e.g., extraction of hydrocarbons, development of enhanced geothermal energy, or storage and capture of carbon (2)]. The events can cluster into a pipe-like zone with dimensions up to a few hundred

meters (3) and may be more common in low-stress environments. Because major earthquakes often result in decreased stress, recently ruptured tectonic faults provide an ideal setting to understand the active role of fluids in a low-stress environment.

In this study, we examined the Chelungpu Fault in central Taiwan (Fig. 1A), which ruptured during the 1999 moment magnitude (M_w) 7.6 Chi-Chi earthquake. We relied on data collected during The Taiwan Chelungpu-fault Drilling Project (TCDP), which produced a 2-km borehole that penetrated the fault at 1111 m (4), where more than 10 m of coseismic displacement (5) occurred. Stress measurements indicate a near zero value of shear stress on the fault after the earthquake (6) and are consistent with the observations from seismic and Global Positioning System modeling (7, 8). We installed a seven-level array of three-component 4.5-Hz seismometers, with sampling rates of 1 kHz at the drill site across the large slip of the fault zone from depths of about 950 to 1300 m in November 2006 (Fig. 1C). The shallowest (BHS1) to deepest (BHS7) seismometers were placed at depth intervals of about 50 to 60 m. Because of the very close proximity to the fault and the low noise level in the borehole, the seismometer array allowed us to observe very-low-magnitude ($>M = -1.5$) events near the fault zone.

The continuous records (Fig. 2A) collected during the first 6 months revealed a variety of

¹Department of Earth Sciences, and Institute of Geophysics, National Central University, Taiwan, Republic of China. ²Institute of Earth Sciences, Academia Sinica, Taiwan, Republic of China. ³Disaster Prevention Research Institute, Kyoto University, Japan. ⁴Department of Earth Sciences, University of California Santa Cruz, Santa Cruz, CA 95060, USA.

*To whom correspondence should be addressed. E-mail: fong@ncu.edu.tw

seismic events. In addition to the regular microearthquakes, which show clear P and S waves [Fig. 2B, (9)], we observed several smaller events, which we call I-type (for isotropic) events, that show only distinct P waves without identifiable S waves [Fig. 2C, (10)]. Using a cross-correlation scheme, we found 88 detectable I-type events (cross-correlation coefficient of >0.6). The spectrum of the I-type event (Fig. 2E) has a dominant frequency of about 10 Hz. There are 30 I-type events that show distinct first motions, which can be used to locate the earthquakes (Fig. 2F). The temporal distribution of both the I-type events and the ordinary earthquakes with $t_S - t_P$ times of less than 2 s shows no time correlation (Fig. 2D).

Using the velocity structure obtained from well logs (Fig. 1C and fig. S3), we determined the locations for microearthquakes (9) and I-type events. These data show several low-velocity layers, including the slip zone for the 1999 Chi-Chi earthquake, within the Chinshui Shale Formation, and the layer of the Kueichulin formation (6, 11–13). The low-velocity layer has a large Poisson ratio of about 0.34 (14), suggesting the

possibility of fluids in these zones. We adopted a location procedure that used both the arrival times on the borehole array and the observed directions of the first motions to estimate the incidence angles (15). First, we used only the ordinary microearthquakes with S minus P times of less than 2 s. We located 242 events of this background seismicity, which occurred mostly in a zone at a depth of about 10 to 13 km [Fig. 1B, (9)], similar to the distribution of most aftershocks of the 1999 Chi-Chi earthquake (16). We then used the same procedure—except only P times were used—to locate 30 I-type events (table S1). The locations of the I-type events are mostly beneath the slip zone of the 1999 Chi-Chi earthquake (Fig. 1C) within a pipelike region that extends horizontally about 500 m northeast from the drill site (Fig. 1D), with depths from about 1300 to 1800 m. The depth range of these events corresponds to the depth of the Kueichulin Formation (Fig. 1C), which has high porosity and permeability, as constrained by laboratory measurements of the TCDP cores (17). From the locations and maximum amplitudes, the magni-

tudes of these I-type events mostly correspond to about $M = -0.5$ to $M = -1.5$ (table S1).

Several studies have shown that the anomalously low amplitudes of S waves in the high-frequency radiation (18, 19) are associated with isotropic mechanisms; therefore, our observations of small S amplitude might be associated with a fault-opening motion or isotropic mechanisms in the fault zone. To further investigate the source mechanism, we carried out a three-dimensional finite-difference simulation [fig. S3, (20)] using six components of the moment tensors. The modeling shows that the distinct direct S wave is observed for each component of the moment tensor (fig. S4). The absence of an S wave could only be found for the case of an isotropic source, where $M_{11} = M_{22} = M_{33}$, in which only the P wave and other fault zone-related phases following the direct P wave (P_{FM}) were seen. However, there is limited azimuthal coverage of the focal sphere, so there may be some uncertainties in the source parameter determinations.

To explain the pulslike P wave in the observation, we used a 10-Hz oscillatory volumetric source

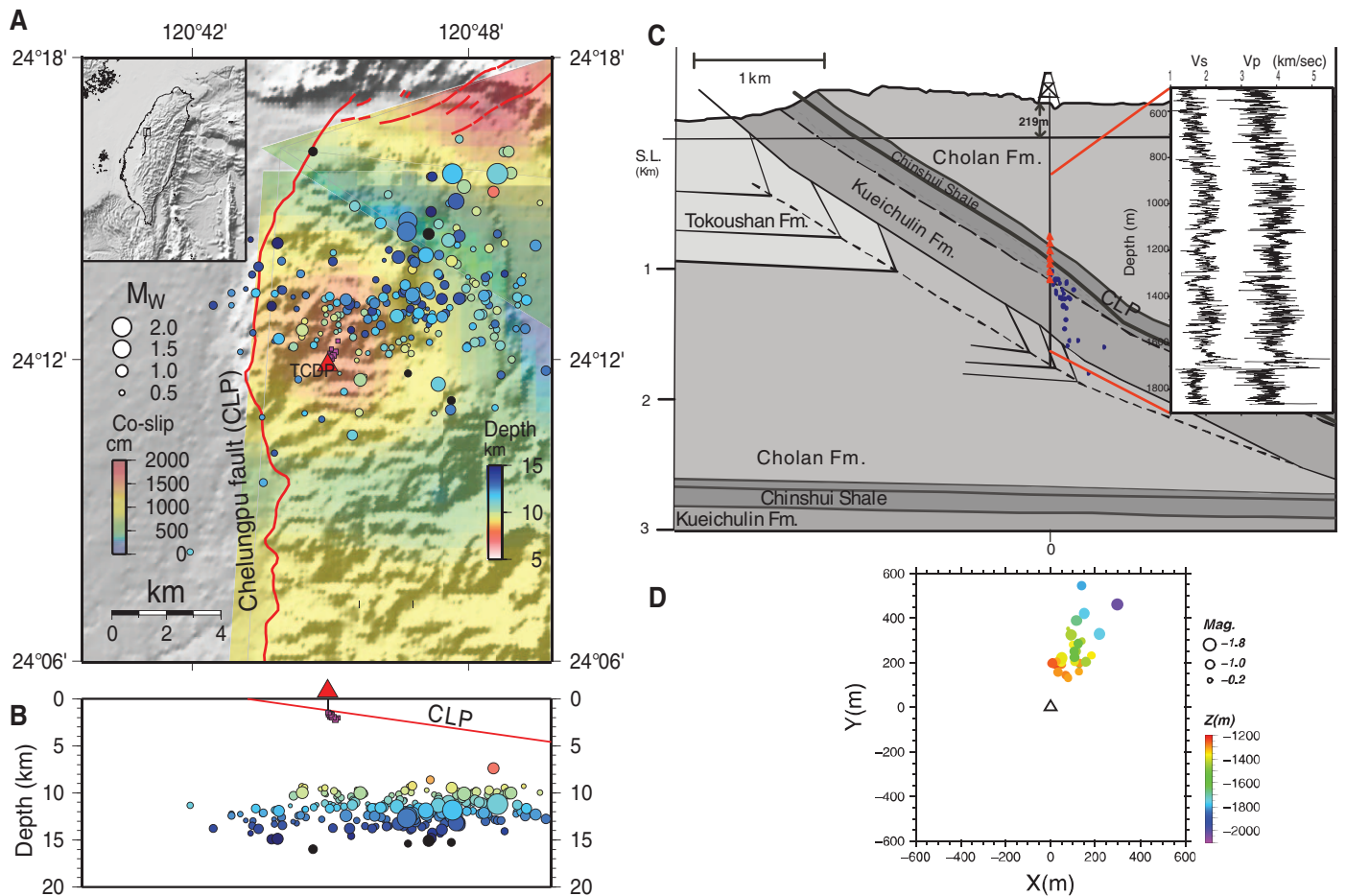


Fig. 1. (A) Site of the Taiwan Chelungpu-fault Drilling Project (TCDP), and borehole seismometers (BHS) on the northern portion of the Chelungpu fault (red line). The coseismic slip (color scale) is about 10 m from the drill site. The distribution of seismicity [color circles, (9)] and the I-type events (purple squares) are shown. (B) The east-west profile of the seismicity (9) and I-type events across

the TCDP site. (C) A geological cross section near the drill site (31) with the projection of the I-type events (blue dots). The vertical borehole array (red triangles) were deployed at depths of 947, 1008, 1059, 1110, 1162, 1213, and 1274 m, respectively. The P -wave and S -wave velocities from logging are shown. (D) Map view of the I-type events relative to the location of the TCDP site (triangle).

in the modeling. The observed (200611201628) vertical records of BHS1 to BHS7 compares well to the seismograms calculated with the assumed velocity model (fig. S3). Using the snapshots (fig. S5) and the synthetic seismograms of the pseudo-station, we identified the arrivals in the synthetic waveforms as the direct P , fault zone multiples (P_{FM}), and a reflected P -to- S phase (PS) from the

depth of 1.8 km. Although the fault zone multiples (P_{FM}) are relatively weak in the synthetic seismograms, the correlation of these multiples to the observations can be still seen (Fig. 3A). The particle motions of the direct P of the synthetic seismograms matches the observations, and the 1.8-km reflected phase shows a P -to- S converted phase as shown by its particle motion (Fig. 3B).

Our modeling suggests that the I-type events involved a nonshearing-type source, such as a volumetric expansion source within a 500-m distance of the TCDP drill site, and within the Kueichulin formation beneath the slip zone. Based on a nonshearing mechanism of an isotropic source of $M_{11} = M_{22} = M_{33}$, the calculated seismograms (Fig. 3C) can explain the polarities,

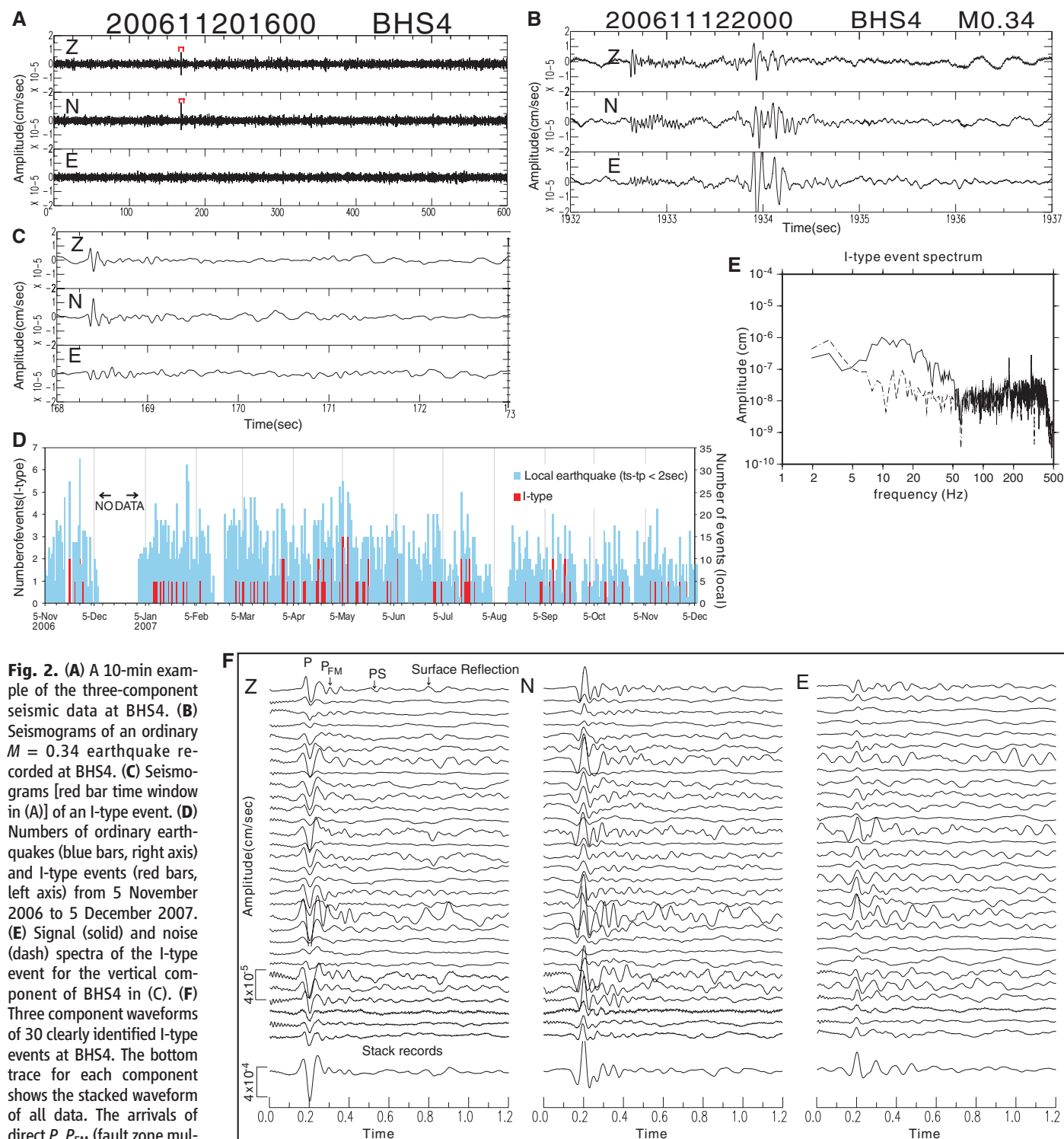


Fig. 2. (A) A 10-min example of the three-component seismic data at BHS4. (B) Seismograms of an ordinary $M = 0.34$ earthquake recorded at BHS4. (C) Seismograms [red bar time window in (A)] of an I-type event. (D) Numbers of ordinary earthquakes (blue bars, right axis) and I-type events (red bars, left axis) from 5 November 2006 to 5 December 2007. (E) Signal (solid) and noise (dash) spectra of the I-type event for the vertical component of BHS4 in (C). (F) Three component waveforms of 30 clearly identified I-type events at BHS4. The bottom trace for each component shows the stacked waveform of all data. The arrivals of direct P , P_{FM} (fault zone multiples) and possible P -to- S converted phase, and the surface reflection phase are marked.

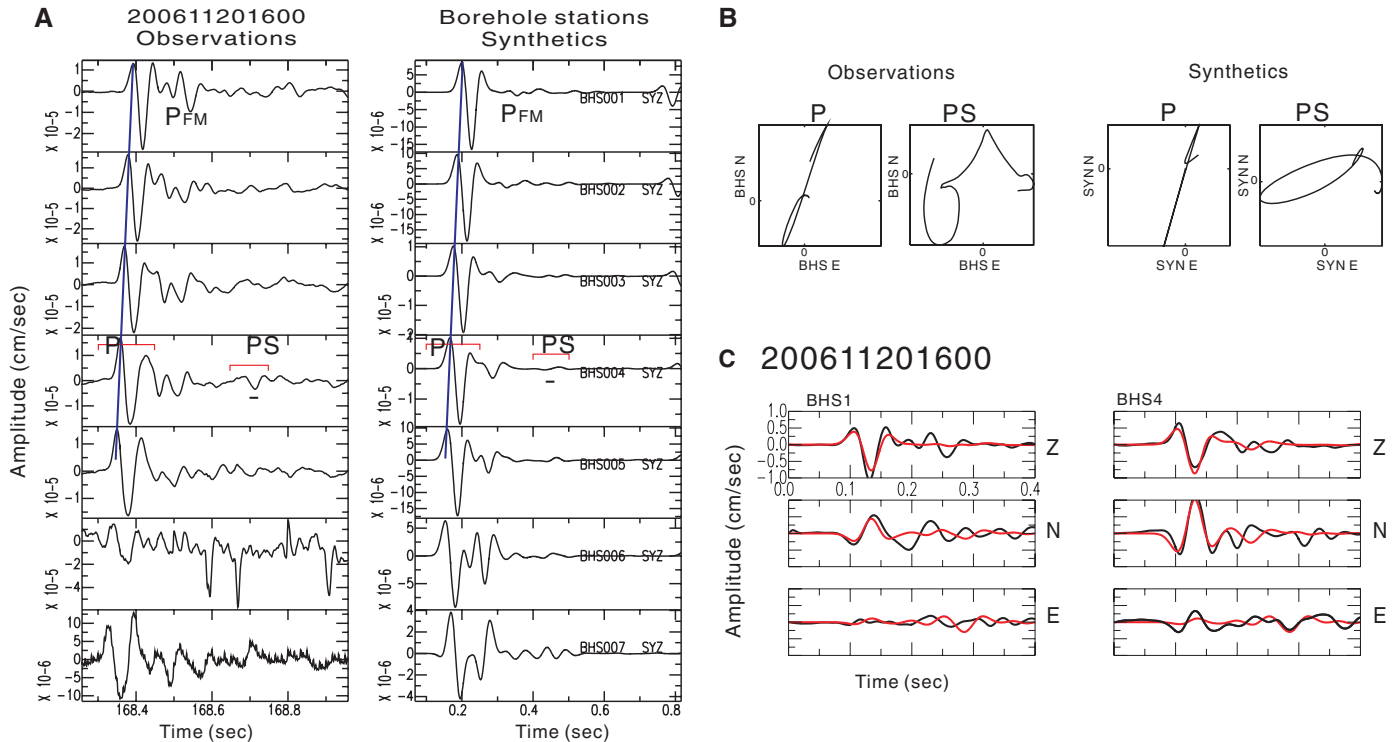


Fig. 3. (A) The observed (left) and calculated (right) vertical component waveforms for the seven-level borehole seismometers of the I-type event shown in Fig. 2. The bottom two borehole seismometers did not function well for the small events. The purple line shows the theoretical arrival times for the I-type event location. The possible fault zone multiples are shown

with small blue and red markers. **(B)** The particle motions of the wave for *P* and *P*-to-*S* converted phase for the time windows marked by the red bars in BHS004 of (A). **(C)** Comparisons for an isotropic source of the three component waveforms of the model waveforms (red) and observations (black) at BHS1 and BHS4.

the relative amplitudes of the first arrivals in the observations, and the absence of *S* waves. We also compared a tensile failure mechanism to the observation, but the synthetics fit the observed waveforms less well than those from the isotropic mechanism (Fig. 3C and fig. S6).

Nonshearing sources are often intimately related to fluid flow. The slip zone of the 1999 earthquake itself forms an impermeable cap with permeabilities of $\sim 10^{-19}$ to 10^{-16} m² (21, 22) overlying the much more permeable Kueichulin formation with permeabilities of 10^{-14} to 10^{-13} m² (17, 23). Despite this hydrogeological structure, fluid from the Kueichulin has been detected at the drill site (24). Therefore, it seems that there may be some transient flow from the capped layer, possibly related to breaching by the fracturing of the earthquake.

The occurrence of the I-type events can be explained by overpressurized fluid flow below the recent slipped zone, which is capped by the impermeable slip zone. A localized breach of the fault would provide a conduit through which fluid could escape to the overlying formations. This fluid flow results in hydraulic fractures, which result in I-type events (fig. S7). The volume change during the opening process of these events is about 30 to 300 cm³ (10). This volume change corresponds to a radius of about 1 to 2.5 cm of opening and closing of cracks or cavities, which in this case, may have been originally formed

by damage during the 1999 Chi-Chi earthquake. The isotropic opening may be due to the relatively isotropic stress field remaining in the nearfield of the fault in the wake of the Chi-Chi earthquake.

Although the I-type events we observed might be a transient episode after a near-complete stress drop of a large earthquake, similar mechanisms may be appropriate for other types of fluid-driven cracks observed in the field at seismogenic depths (25–27). Furthermore, the damaged region of the fault zone (28) could have a strong contribution to these unusual earthquake sources. A recent study from two arrays of borehole seismometers in a carbon capture and storage experiment in the Michigan Basin also detected events with only distinct *P* waves and no *S* waves (29); these events had a single force mechanism associated with degassing of CO₂ due to the leakage from an injection layer. The rapid attenuation with distance of these high-frequency events (40 Hz) explains why no other I-type events at farther distances were observed by the borehole array. Indeed, fluid interaction in fracture zones could nucleate earthquakes due to stress readjustment (30). Regardless, if the driving mechanism of I-type events is related to fractured material and/or interaction of fluid or gas in the fault zone, such events may correspond to cross-cutting veining structures and other fluid features, such as echelon quartz, that are often observed in rocks adjacent to fault zones.

References and Notes

1. R. H. Sibson, *Tectonophysics* **211**, 283 (1992).
2. C. T. Montgomery, M. B. Smith, *J. Pet. Technol.* **62**, 26 (2010).
3. R. J. Davies *et al.*, *Mar. Pet. Geol.* 10.1016/j.marpetgeo.2012.04.001 (2012).
4. K.-F. Ma *et al.*, *Nature* **444**, 473 (2006).
5. Y.-G. Chen *et al.*, *Bull. Seismol. Soc. Am.* **91**, 977 (2001).
6. H.-Y. Wu *et al.*, *Geophys. Res. Lett.* **34**, L01303 (2007).
7. K.-F. Ma *et al.*, *Geophys. Res. Lett.* **30**, 1244 (2003).
8. Y.-J. Hsu, P. Segall, S.-B. Yu, L.-C. Kuo, C. A. Williams, *Geophys. J. Int.* **169**, 367 (2007).
9. Y.-Y. Lin, K.-F. Ma, V. Oye, *Geophys. J. Int.* **190**, 665 (2012).
10. Materials and methods are available as supplementary materials on Science Online.
11. A. T. Lin *et al.*, *Terr. Atmos. Ocean. Sci.* **18**, 22 (2007).
12. E.-C. Yeh *et al.*, *Terr. Atmos. Ocean. Sci.* **18**, 327 (2007).
13. J.-H. Wang, J.-H. Hung, J. J. Dong, *J. Asian Earth Sci.* **36**, 135 (2009).
14. J.-H. Wang, *Terr. Atmos. Ocean. Sci.* **21**, 655 (2010).
15. V. Oye, M. Roth, *Comput. Geosci.* **29**, 851 (2003).
16. S. Carena, J. Suppe, H. Kao, *Geology* **30**, 935 (2002).
17. J.-J. Dong *et al.*, *Int. J. Rock Mech. Mining Sci.* **47**, 1141 (2010).
18. B. R. Julian, G. R. Foulger, *Bull. Seismol. Soc. Am.* **86**, 972 (1996).
19. A. McGarr, *Geophys. Res. Lett.* **19**, 1579 (1992).
20. S. J. Lee, H. W. Chen, K. F. Ma, *J. Geophys. Res.* **112**, B06307 (2007).
21. W. Tanikawa *et al.*, *Geochem. Geophys. Geosyst.* **10**, Q04013 (2009).
22. M. L. Doan, E. E. Brodsky, Y. Kano, K. F. Ma, *Geophys. Res. Lett.* **33**, L16317 (2006).
23. H. Tanaka *et al.*, *Terr. Atmos. Ocean. Sci.* **13**, 227 (2002).
24. C.-Y. Chen, National Taiwan University, thesis (2010).
25. R. H. Sibson, *Am. Assoc. Petrol. Geol. Mem.* **82**, 1 (2004).
26. Y. C. Chan, K. Okamoto, T.-F. Yui, Y. Iizuka, H.-T. Chu, *Terra Nova* **17**, 493 (2005).

27. F. Cappa, Y. Guglielmi, J. Virieux, *Geophys. Res. Lett.* **34**, L05301 (2007).
28. Y. Ben-Zion, J.-P. Ampuero, *Geophys. J. Int.* **178**, 1351 (2009).
29. M. Bohnhoff, M. D. Zoback, *J. Geophys. Res.* **115**, B11305 (2010).
30. F. Cappa, Y. Guglielmi, P. Fénart, V. Merrien-Soukatchoff, A. Thoraval, *Int. J. Rock Mech. Min. Sci.* **42**, 287 (2005).
31. J.-H. Hung *et al.*, *Tectonophysics* **466**, 307 (2009).

Acknowledgments: We thank C. Y. Wang for operational support for the TCDP site. This study benefited from discussions with H. Kanamori, M. Campillo, and T.-R. Alex Song. The TCDP BHS data are available to the public at the Data Center of the Taiwan Earthquake Research Center (TECRC) (<http://tcrcs.earth.sinica.edu.tw/TCDP>). This project is supported by National Science Council of Taiwan, NSC 100-2119-M-008 -031, and Ministry of Education 100G901-26 at National Central University.

Supplementary Materials

www.sciencemag.org/cgi/content/full/337/6093/459/DC1
Materials and Methods
Figs. S1 to S7
Table S1

19 March 2012; accepted 5 June 2012
10.1126/science.1222119

Adenylate Cyclases of *Trypanosoma brucei* Inhibit the Innate Immune Response of the Host

Didier Salmon,^{1,2*} Gilles Vanwalleghem,^{1†} Yannick Morias,^{3,4} Julie Denoeud,⁵ Carsten Krumbholz,⁶ Frédéric Lhomme,⁷ Sabine Bachmaier,⁶ Markus Kador,⁶ Jasmin Gossmann,⁶ Fernando Braga Stehling Dias,^{1,2} Géraldine De Muylder,¹ Pierrick Uzureau,¹ Stefan Magez,^{4,8} Muriel Moser,⁵ Patrick De Baetselier,^{3,4} Jan Van Den Abbeele,⁹ Alain Beschin,^{3,4} Michael Boshart,^{6*} Etienne Pays^{1,10*}

The parasite *Trypanosoma brucei* possesses a large family of transmembrane receptor-like adenylate cyclases. Activation of these enzymes requires the dimerization of the catalytic domain and typically occurs under stress. Using a dominant-negative strategy, we found that reducing adenylate cyclase activity by about 50% allowed trypanosome growth but reduced the parasite's ability to control the early innate immune defense of the host. Specifically, activation of trypanosome adenylate cyclase resulting from parasite phagocytosis by liver myeloid cells inhibited the synthesis of the trypanosome-controlling cytokine tumor necrosis factor- α through activation of protein kinase A in these cells. Thus, adenylate cyclase activity of lysed trypanosomes favors early host colonization by live parasites. The role of adenylate cyclases at the host-parasite interface could explain the expansion and polymorphism of this gene family.

The protozoan flagellate *Trypanosoma brucei* infects a wide range of mammals, including humans, where it causes sleeping

sickness. Bloodstream parasites are coated with a glycosylphosphatidylinositol (GPI)-anchored antigen termed variant surface glycoprotein

(VSG) (1). Upon cellular stress, including cell lysis, activation of a GPI-specific phospholipase C (VSG lipase) triggers release of soluble VSG (2). Massive VSG release at the peak of parasitaemia contributes to interferon- γ (IFN- γ)-dependent tumor necrosis factor- α (TNF- α) synthesis by macrophages and high TNF- α serum levels, but early in infection, myeloid cells recruited

¹Laboratory of Molecular Parasitology, Institute for Molecular Biology and Medicine (IBMM), Université Libre de Bruxelles, 12, rue des Professeurs Jeener et Brachet, B6041 Gosselies, Belgium. ²Institute of Medical Biochemistry, Centro de Ciências e da Saúde, Federal University of Rio de Janeiro, Avenida General Trompowsky, Rio de Janeiro 21941-590, Brazil. ³Myeloid Cell Immunology Laboratory, Vlaams Instituut voor Biotechnologie, Brussels, Belgium. ⁴Cellular and Molecular Immunology Unit, Vrije Universiteit Brussel, Brussels, Belgium. ⁵Laboratory of Immunobiology, IBMM, Université Libre de Bruxelles, Gosselies, Belgium. ⁶Biocenter, Section Genetics, Ludwig-Maximilians-Universität München, Martinsried, Germany. ⁷Center for Microscopy and Molecular Imaging, Gosselies, Belgium. ⁸Department of Structural Biology, VIB, Brussels, Belgium. ⁹Department of Biomedical Sciences, Unit of Veterinary Protozoology, Institute of Tropical Medicine Antwerp, Antwerp, Belgium. ¹⁰Walloon Excellence in Life Sciences and Biotechnology (WELBIO), Wavre, Belgium.

*To whom correspondence should be addressed. E-mail: salmon@bioqmed.ufrj.br (D.S.); boshart@lmu.de (M.B.); epays@ulb.ac.be (E.P.)

†These authors contributed equally to this work.

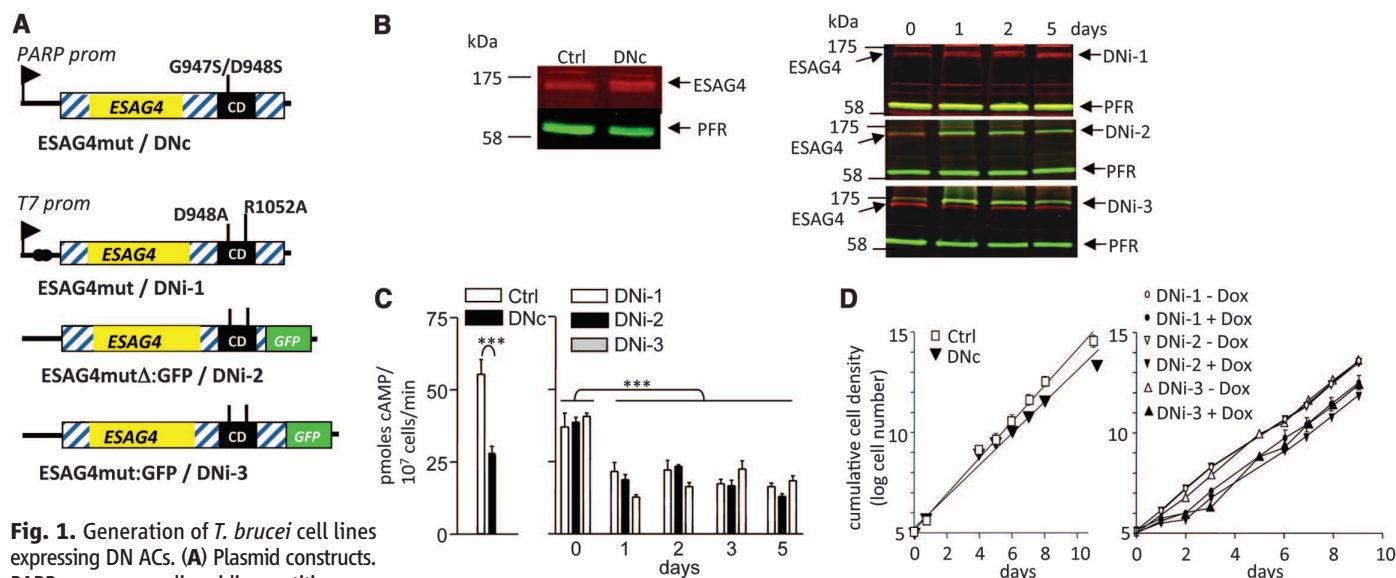


Fig. 1. Generation of *T. brucei* cell lines expressing DN ACs. (A) Plasmid constructs. PARP prom, procyclic acidic repetitive protein promoter; CD, catalytic domain. In DNi-2, the ESAG4 C terminus is truncated by 112 amino acids. (B) Immunoblot evidence for ESAG4 expression in pleomorphic DNc and monomorphic DNi parasites. Loading control: PFR, paraflagellar rod protein; d, day after doxycycline (Dox) induction. (C) AC activity (cAMP synthesis), measured by swell dialysis after pH 5.5 treatment (2). AC activity of uninduced DNi parasites remained

constant during the entire incubation period. (D) In vitro growth rate of the different cell lines. In this and the following figures, control (Ctrl) trypanosomes are transgenic pleomorphic trypanosomes containing an ESAG4-free plasmid (pTSARib0), and the values are means of at least three independent experiments (error bars, mean \pm SEM). * P < 0.05, ** P < 0.01, *** P < 0.001 (Student-Newman-Keuls post hoc analysis of variance).

in liver and spleen already synthesize $\text{TNF-}\alpha$ independently from $\text{IFN-}\gamma$ (3, 4). Although involved in early trypanosome growth control, $\text{TNF-}\alpha$ also contributes to tissue pathogenicity during chronic infection (5–7).

Unlike related kinetoplastids developing intracellularly (*T. cruzi* and *Leishmania*), extracellular African trypanosomes (*T. brucei*, *T. congolense*, and *T. vivax*) show a remarkable expansion of receptor-like adenylate cyclases (ACs) without evidence for isoform orthologs between species (fig. S1). The *T. brucei* genome encodes more than 80 ACs, many of

which were detected at the cell surface (8–10). The prototype gene of this family, termed *ESAG4* (expression site-associated gene 4), is included in polycistronic *VSG* transcription units, in contrast to the other genes termed *GRESAG4s* (genes related to *ESAG4*) (10, 11). All ACs share a similar structure, with a large extracellular domain and a conserved intracellular catalytic domain, the dimerization of which is required for activity (8, 12, 13). Although the basal cellular cyclic adenosine monophosphate (cAMP) concentration is extremely low ($\sim 0.67 \mu\text{M}$) (table S1), stress, such as acid treat-

ment or osmotic lysis, activates ACs to produce ~ 250 times the basal cellular content per minute (2, 14, 15). AC and VSG lipase activities are triggered simultaneously but independently (2). Apart from *ESAG4* involvement in cytokinesis (10), the function of *T. brucei* ACs is unknown.

To develop a dominant-negative (DN) approach, the catalytic domain of *ESAG4* was inactivated by mutagenesis of key residues (16). A pleomorphic *T. brucei* clone was transformed for constitutive expression of the G947S/D948S mutant (DNc cell line), and three monomorphic

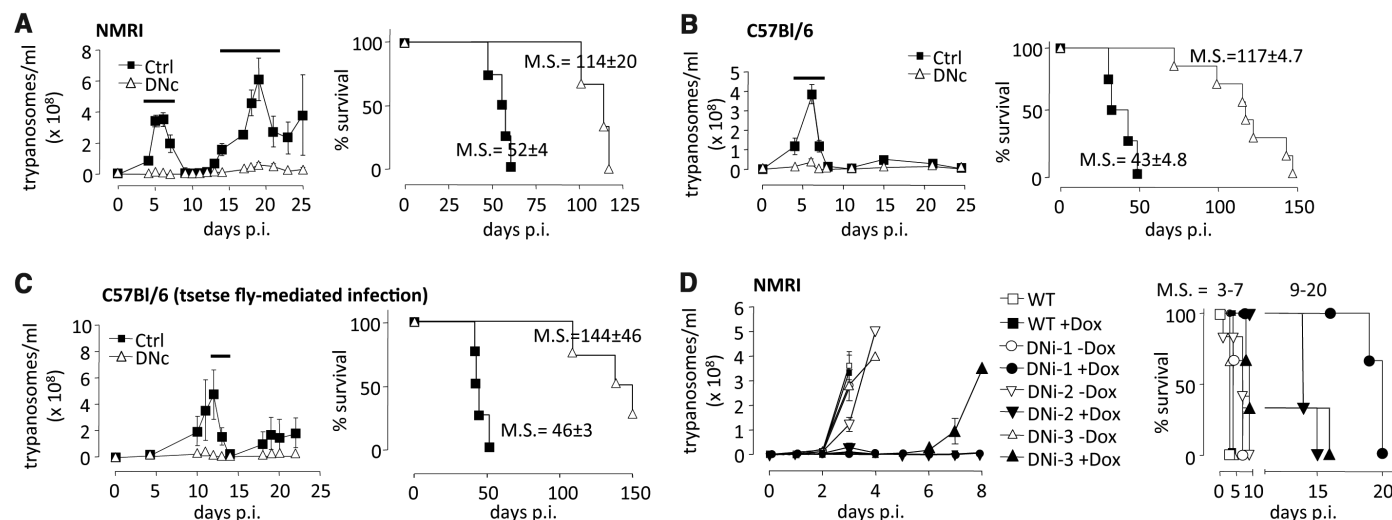


Fig. 2. Increased host capacity to control DN AC parasites. (A to C) Parasitaemia and survival time of different mice inoculated with pleomorphic control or DNc parasites by syringe [(A) and (B)] or infected tsetse flies (C). (D) Parasitaemia and survival time of NMRI mice inoculated by syringe with

monomorphic WT or DN1 parasites. M.S., median survival time. In this and the following figures, the bars above the parasitaemia graphs highlight significant differences between Ctrl and DNc or the respective comparison ($P < 0.05$).

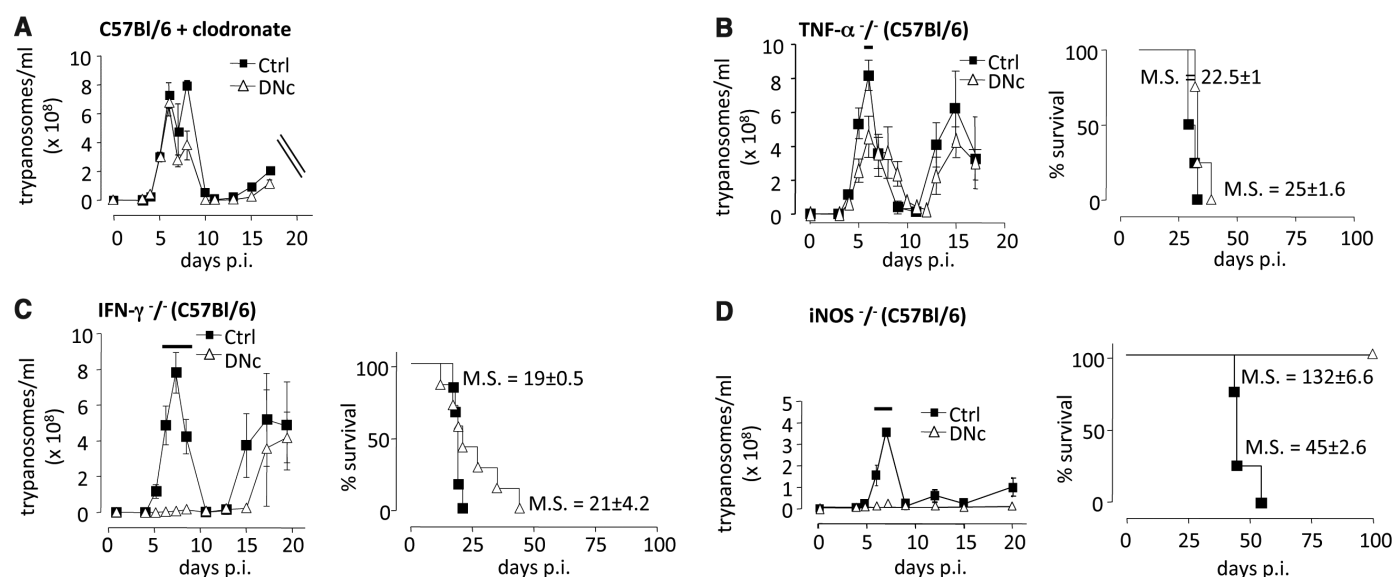


Fig. 3. Involvement of phagocytes and $\text{TNF-}\alpha$ in host capacity to control trypanosomes. (A to D) Parasitaemia and survival time of C57Bl/6 mice treated with clodronate-containing liposomes or deficient in $\text{TNF-}\alpha$,

$\text{IFN-}\gamma$, or iNOS, after inoculation with pleomorphic control or DNc parasites. The survival time of infected clodronate-treated mice was not determined.

trypanosome lines were generated for doxycycline-inducible expression of the D948A/R1052A mutant, with or without a C-terminal green fluorescent protein (GFP) tag (DNi-1, -2, and -3) (Fig. 1, A and B). The GFP-tagged DNi proteins showed the expected surface localization (17) (fig. S2). In DNa and induced DNi parasites, total AC activity, measured under stress conditions, was reduced by ~50% (Fig. 1C).

In culture, DNa growth was slightly reduced compared with control cells (Fig. 1D). Upon induction, the three DNi cell lines showed transient (~2 days) growth retardation and cytokinesis abnormalities (Fig. 1D and fig. S3A). Reversion correlated with up-regulation

of *GRESAG4.1* expression, which was also seen in DNa (fig. S3B) and *ESAG4* knock-out parasites (10). In mice, DNa AC expression strongly affected the infection pattern. After parasite inoculation by either intraperitoneal syringe-mediated injection or the bite of infected tsetse flies, DNa parasitaemia was considerably lower than control parasitaemia, and the host survival time was longer (Fig. 2, A to C). Serial DNa passaging in mice led to reversion of parasitaemia to control levels, linked to the loss of the DNa AC transgene and recovery of AC activity (fig. S4). The DNa infection phenotype was mimicked by DNi parasites. Without induction, the three DNi lines killed

mice after 3 to 4 days, as expected for monomorphic parasites (Fig. 2D). In contrast, doxycycline induction led to drastic reduction of parasitaemia and prolongation of host survival time, whereas doxycycline itself had no effect on wild-type (WT) parasite infection (18) (Fig. 2D).

The DNa infection pattern was largely conserved in mice deficient in either T lymphocytes (nude), T + B lymphocytes (severe combined immunodeficiency), or B lymphocytes (immunoglobulin μ -chain defective) (fig. S5). In contrast, DNa parasitaemia strongly increased in WT mice injected with clodronate-containing liposomes, indicating a crucial role for phagocytic

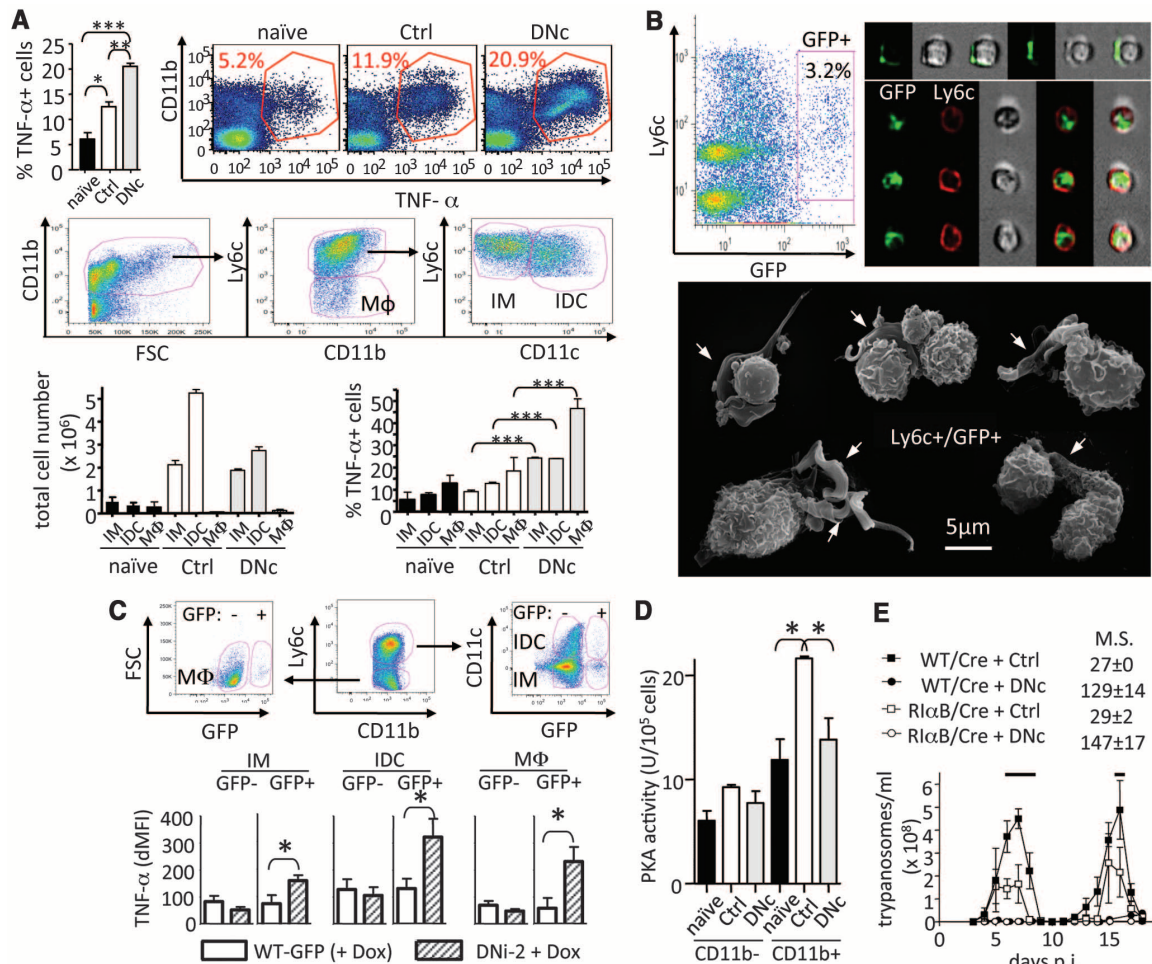


Fig. 4. Modulation of TNF- α synthesis after trypanosome infection. **(A)** Measurement of TNF- α cells in total live nonparenchymal liver cells (top, mean values from three experiments and representative flow cytometry profiles) and in liver IMs (CD11b⁺/Ly6c⁺/CD11c⁻), IDCs (CD11b⁺/Ly6c⁺/CD11c⁺), and macrophages (M Φ) (CD11b⁺/Ly6c⁺/CD11c⁻) (middle, gating strategy illustrated for DNa-infected mice; bottom, mean number of IM, IDC, and M Φ , and percentage of TNF- α cells thereof, from three experiments) of C57BL/6 mice at day 4 p.i. with pleomorphic control or DNa parasites. **(B)** Imaging of liver Ly6c⁺/GFP⁺ myeloid cells from C57BL/6 mice at day 3 p.i. with GFP-expressing monomorphic WT trypanosomes. (Left) The gating of Ly6c⁺/GFP⁺ cells by Imagestream analysis. (Right and Bottom) Representative examples of Ly6c⁺/GFP⁺ cells with surface-bound or internalized parasites, seen by Imagestream and scan-

ning electron microscopy, respectively (arrows point to myeloid cell-associated trypanosomes). **(C)** TNF- α levels in liver myeloid cells of C57BL/6 mice at day 3 p.i. with GFP-expressing monomorphic WT trypanosomes or induced DNi-2 parasites, determined as mean fluorescence intensity difference (dMFI) between antibodies to TNF- α and isotype control antibodies. The gating strategy is illustrated for WT-infected mice. **(D)** PKA activity (pmol of phosphate transferred to substrate per 10⁵ cells per min at 30°C) in myeloid cells from WT mice at day 4 p.i. with control or DNa parasites. **(E)** Parasitaemia and survival time after inoculation of control or DNa parasites in C57BL/6 mice issued from a cross between heterozygous Rl α B mice and homozygous CD11b/Cre expressor mice; the Cre recombinase activates Rl α B expression through removal of an intervening neomycin cassette.

cells (19) (Fig. 3A). Key immune modulators affecting trypanosome infection are TNF- α , IFN- γ , and NO (4, 5). In TNF- $\alpha^{-/-}$ mice, the DNe infection pattern reverted to that of control parasites, whereas in IFN- $\gamma^{-/-}$ mice, DNe parasitaemia reverted to control levels after the first peak, and in inducible nitric oxide synthase-negative (iNOS $^{-/-}$) mice, no reversion occurred (Fig. 3, B to D). Infection phenotype reversion in TNF- $\alpha^{-/-}$ mice was specific to DNe parasites because it was not observed with other subvirulent transgenic *T. brucei* lines (fig. S6). Infection phenotype reversion also occurred for induced DNI trypanosomes upon clonate treatment or growth in TNF- $\alpha^{-/-}$ mice, but not in nude mice (fig. S7). Thus, TNF- α was involved in the effects of trypanosome ACs on infection.

Splenectomy did not affect the DNe infection phenotype (fig. S5), presumably because in mice, the major site of trypanosome interaction with myeloid cells is the liver (20). At day 4 post-injection (p.i.), the number of liver TNF- α -synthesizing CD11b $^{+}$ cells was higher with DNe than with control parasites (Fig. 4A). Specifically, with both parasites, the number of inflammatory monocytes (IMs) (CD11b $^{+}$ /Ly6c $^{+}$ /CD11c $^{-}$) and inflammatory dendritic cells (IDCs) (CD11b $^{+}$ /Ly6c $^{+}$ /CD11c $^{+}$) significantly increased while the number of macrophages (CD11b $^{+}$ /Ly6c $^{-}$ /CD11c $^{-}$) decreased, but in all subpopulations, the percentage of TNF- α -synthesizing cells was ~2.5 times as high with DNe than with control parasites (Fig. 4A). Thus, parasite AC inactivation was linked to early expansion of liver TNF- α^{+} myeloid cells.

To evaluate whether the effects of ACs required direct parasite interaction with myeloid cells, monomorphic trypanosomes expressing GFP (WT-GFP) or AC-GFP fusion protein (induced DNI-2) were used. To ensure proper comparison, all mice were treated with doxycycline. In myeloid cells associated with GFP-labeled trypanosomes at day 3 p.i. (3% of the population) (Fig. 4B), the intracellular level of TNF- α was 2 to 4 times as high with induced DNI than with WT parasites (Fig. 4C and fig. S8). Thus, myeloid cell-associated parasite AC activity was linked to reduction of TNF- α synthesis.

Because cAMP-mediated activation of protein kinase A (PKA) can inhibit TNF- α synthesis (21), we measured the PKA activity in CD11b $^{+}$ and CD11b $^{-}$ cells from WT mice 4 days p.i. with control or DNe parasites. Increased PKA activity was only observed in CD11b $^{+}$ cells after control parasite infection (Fig. 4D). Reciprocally, the influence of myeloid cell PKA on infection was addressed. PKA was down-regulated in CD11b $^{+}$ cells by Cre-mediated activation of a dominant negative regulatory PKA subunit (RI α B) (22). Compared with control mice, in RI α B/Cre mice parasitaemia was reduced by a factor of 2.5 (Fig. 4E). Thus, myeloid cell PKA affected trypanosome infection and could be targeted by parasite ACs.

The increased host survival time observed with DNe parasites was associated with reduced liver damage and drastically reduced serum levels of pathogenic TNF- α (fig. S9). This presumably resulted from lower IFN- γ -dependent myeloid cell activation linked to the very low parasitaemia and subsequent low release of VSG (3, 4). In IFN- $\gamma^{-/-}$ mice, the reduction of systemic TNF- α (fig. S9B) could account for increased parasitaemia after the first peak and consecutive reduction of host survival time (compare Figs. 3C and 2B).

Our results indicate that ~50% of total *T. brucei* AC activity is not essential for parasite growth but is crucial to regulate processes involved in parasitaemia control. Specifically, AC activity of trypanosomes, whether triggered upon phagocytosis by the acidic phagosome environment or by trypanolysis, appeared to reduce the early innate defense against live parasites before the massive release of immunomodulatory factors such as VSG GPI anchor fragments at the first parasitaemia peak. Even a few trypanosomes or dead trypanosomes are able to durably affect host innate immunity (23). *T. brucei* ACs inhibited TNF- α synthesis in liver myeloid cells, linked to activation of myeloid cell PKA. This evokes the effects of AC toxins from extracellular pathogenic bacteria (*Bordetella pertussis* and *Bacillus anthracis*) (24), but contrasts with TNF- α induction by AC from intracellular *Mycobacterium tuberculosis* (25).

TNF- α was found to be crucially involved in controlling trypanosome parasitaemia. However, systemic TNF- α did not seem to affect late infection. Thus, the trypanosome-controlling activity of TNF- α would occur early and be restricted to the environment of TNF- α -producing cells. Myeloid cell-proximal TNF- α is thought to facilitate parasite phagocytosis in niches such as the liver, the major organ for trypanosome clearance (5, 20, 23). Therefore, at the beginning of infection, liver myeloid cells could target most invading parasites, and without efficient parasite AC response, only low parasitaemia could develop in the blood.

The AC function at the host-parasite interface would explain the specific expansion and diversification of ACs in extracellular trypanosomes continuously exposed to the immune system. This conclusion could also apply to other extracellular parasites such as *Trichomonas vaginalis* (26). The sequence diversity of the AC extracellular domain might help to prevent efficient recognition by antibodies. Examples of polymorphism associated with parasite enzymes exposed to the immune system include the *T. cruzi* transglutaminases (27) or the *Toxoplasma gondii* protein kinases (28).

References and Notes

1. E. Pays, L. Vanhamme, D. Pérez-Morga, *Curr. Opin. Microbiol.* **7**, 369 (2004).
2. S. Rolin et al., *J. Biol. Chem.* **271**, 10844 (1996).
3. S. Magez et al., *J. Immunol.* **160**, 1949 (1998).

4. J. M. Mansfield, D. M. Paulnock, *Parasite Immunol.* **27**, 361 (2005).
5. S. Magez, M. Radwanska, A. Beschin, K. Sekikawa, P. De Baetselier, *Infect. Immun.* **67**, 3128 (1999).
6. M. Williams et al., *J. Immunol.* **182**, 1107 (2009).
7. S. Magez, B. Stijlemans, T. Baral, P. De Baetselier, *Microbes Infect.* **4**, 999 (2002).
8. S. Alexandre et al., *Mol. Biochem. Parasitol.* **77**, 173 (1996).
9. D. J. Bridges et al., *Proteomics* **8**, 83 (2008).
10. D. Salmon et al., *Mol. Microbiol.* **84**, 225 (2012).
11. E. Pays et al., *Cell* **57**, 835 (1989).
12. S. Alexandre et al., *Mol. Biochem. Parasitol.* **43**, 279 (1990).
13. C. Naula, R. Schaub, V. Leech, S. Melville, T. Seebeck, *Mol. Biochem. Parasitol.* **112**, 19 (2001).
14. T. Seebeck, R. Schaub, A. Johnner, *Curr. Mol. Med.* **4**, 585 (2004).
15. H. P. Voorheis, B. R. Martin, *Eur. J. Biochem.* **113**, 223 (1980).
16. B. Bieger, L. O. Essen, *EMBO J.* **20**, 433 (2001).
17. P. Paindavoine et al., *Mol. Cell. Biol.* **12**, 1218 (1992).
18. L. Lecordier et al., *Mol. Biochem. Parasitol.* **140**, 127 (2005).
19. N. Van Rooijen, A. Sanders, *J. Immunol. Methods* **174**, 83 (1994).
20. W. L. Dempsey, J. M. Mansfield, *J. Immunol.* **130**, 405 (1983).
21. E. A. Wall et al., *Sci. Signal.* **2**, ra28 (2009).
22. B. S. Willis, C. M. Niswender, T. Su, P. S. Amieux, G. S. McKnight, *PLoS ONE* **6**, e18772 (2011).
23. G. Wei, H. Bull, X. Zhou, H. Tabel, *J. Infect. Dis.* **203**, 418 (2011).
24. K. A. McDonough, A. Rodriguez, *Nat. Rev. Microbiol.* **10**, 27 (2012).
25. N. Agarwal, G. Lamichhane, R. Gupta, S. Nolan, W. R. Bishai, *Nature* **460**, 98 (2009).
26. J. Cui, S. Das, T. F. Smith, J. Samuelson, *PLoS Negl. Trop. Dis.* **4**, e782 (2010).
27. L. Ratier et al., *PLoS ONE* **3**, e3524 (2008).
28. J. P. J. Saeij et al., *Science* **314**, 1780 (2006).

Acknowledgments: We thank S. McKnight and P. Amieux (University of Washington) for the RI α B mice and helpful suggestions; O. Leo (IBMM, Gosselies) for excellent advice; and D. Monteyne, P. Poelvoorde, M. A. Laute, E. Omasta, and P. Tebabi for technical assistance. This work was supported by the Belgian Fund for Scientific Research (FRSM), the Wallonie-Bruxelles International/Fundação Coordenação de Aperfeiçoamento de Pessoal de Nível Superior (CAPES) bilateral cooperation agreement, the Jean Brachet Fund, the Interuniversity Attraction Poles Programme—Belgian Science Policy, German Research Foundation (DFG) grant 1100/7-1, and the University of Munich. The trypanosome DNA sequences can be retrieved from release 4.0 of the TriTrypDB (www.tritrypdb.org) and NCBI GenBank. The kinetoplastid AC sequence alignments and accession nos. have been deposited at TreeBase (<http://purl.org/phylo/treebase/phylo/study/TB2:S12552>). Author contributions: D.S., G.V., M.B., A.B., and E.P. conceived the work; D.S., G.V., Y.M., J.D., C.K., F.L., S.B., J.G., M.K., F.B.S.D., G.D.M., P.U., S.M., and J.V.D.A. performed experiments; D.S., M.M., P.D.B., M.B., A.B., and E.P. supervised different aspects of the experimental plan; and E.P. wrote the paper. The authors declare that they have no competing financial interests.

Supplementary Materials

www.sciencemag.org/cgi/content/full/science.1222753/DC1
Materials and Methods
Figs. S1 to S9
Table S1
References (29–41)

2 April 2012; accepted 1 June 2012
Published online 14 June 2012;
10.1126/science.1222753

GFAJ-1 Is an Arsenate-Resistant, Phosphate-Dependent Organism

Tobias J. Erb,^{1,*†} Patrick Kiefer,^{1,*} Bodo Hattendorf,² Detlef Günther,² Julia A. Vorholt^{1,†}

The bacterial isolate GFAJ-1 has been proposed to substitute arsenic for phosphorus to sustain growth. We have shown that GFAJ-1 is able to grow at low phosphate concentrations (1.7 μM), even in the presence of high concentrations of arsenate (40 mM), but lacks the ability to grow in phosphorus-depleted (<0.3 μM), arsenate-containing medium. High-resolution mass spectrometry analyses revealed that phosphorylated central metabolites and phosphorylated nucleic acids predominated. A few arsenylated compounds, including C6 sugar arsenates, were detected in extracts of GFAJ-1, when GFAJ-1 was incubated with arsenate, but further experiments showed they formed abiotically. Inductively coupled plasma mass spectrometry confirmed the presence of phosphorus in nucleic acid extracts, while arsenic could not be detected and was below 1 per mil relative to phosphorus. Taken together, we conclude that GFAJ-1 is an arsenate-resistant, but still a phosphate-dependent, bacterium.

The discovery of GFAJ-1, a Gammaproteobacterium that was claimed to use arsenic instead of phosphorus, has challenged the universal role of phosphorus in biology (*1*), although the arguments used in the study were doubted (*2–9*). Here, we combine classical physiological experiments with high-resolution mass spectrometry, as well as inductively coupled plasma optical emission spectrometry and mass spectrometry (ICP-OES/ICP-MS), to provide evidence that GFAJ-1 is highly resistant to arsenate, yet still requires phosphate for growth.

To understand the physiological properties of GFAJ-1, we studied the organism's phosphate dependency in greater detail. Using reagents of the highest purity available for medium preparation, we reduced the phosphorus background in the minimal medium below the detection limit (<0.3 μM phosphorus), which is an order of magnitude less than that detected by Wolfe-Simon *et al.*, that is, 2.7 to 3.2 μM phosphorus impurity (*1*). In the phosphorus-depleted medium (<0.3 μM) we made, no growth of GFAJ-1 was observed; however, the amount of growth of GFAJ-1 correlated with the amount of external phosphorus added in the form of phosphate up to a concentration of 20 μM , beyond which other nutrients might become limiting (*10*) (Fig. 1, A and B). Notably, 1.7 μM phosphate was sufficient to sustain the growth of GFAJ-1 similar to that remaining as impurity in the arsenate-grown culture media published by Wolfe-Simon *et al.* (*1*). From this observation, we conclude that cultures in the previous study might have grown on trace amounts of phosphate rather than on the arsenate provided. Indeed, when GFAJ-1 was tested for growth, by optical density measurements and direct cell counts, on arsenate (40 mM) using phosphorus-depleted medium (<0.3 μM), no growth was

observed unless trace amounts of phosphate were added (Fig. 1C). ICP-MS was used to follow the fate of trace phosphate during the growth of GFAJ-1 in arsenate-containing medium. The concentration of phosphorus in the medium supernatant decreased with time and became enriched in the cellular fraction, in parallel with the growth of GFAJ-1, as shown by optical density and cell-number counting (Fig. 1D). The accumulation of phosphorus in the cellular fraction during the growth of GFAJ-1 in these experiments provided additional evidence that GFAJ-1 is a phosphate-dependent organism, even when cultivated in the presence of high arsenate concentrations.

Next, we addressed the question of whether arsenate enters intermediates of the central carbon metabolism of GFAJ-1 and how this might affect the organism's metabolome. For that purpose, cells of GFAJ-1 were grown on the minimal medium described by Wolfe-Simon *et al.* with 10 mM glucose (*1*) in the absence or presence of 40 mM arsenate and trace amounts of phosphate. Cells were collected in mid-log phase through fast filtration and washed rapidly at 24°C on the filter to remove inorganic salts of the medium before metabolites were extracted and analyzed by a high-resolution mass spectrometry platform that allows detection of compounds in the femto/attomole range (*11*). Metabolite peaks were searched against a modified EcoCyc-metabolite database (*12*) that had been systematically extended by all the arsenylated and arsinylated phospho-metabolite analogs theoretically possible (e.g., glucose-arsenate, glucose-arsenite), as well as permutations of mixed phosphorylated, arsinylated, or arsenylated species to detect modified bis- or trisphosphate metabolites [e.g., different adenosine diphosphate (ADP) or adenosine triphosphate (ATP) species]. Features that matched a database entry with an accuracy $<1 \times 10^{-3}$ atomic mass units were assigned as potential metabolites, and their retention time was compared to the known retention times of corresponding phospho-metabolite standards for further characterization. With the caveat that the metabolome

of GFAJ-1 might have been perturbed to some extent by the short washing step, we found that when GFAJ-1 was grown in the presence of arsenate, most core metabolites (e.g., nucleotides and sugar phosphates) were only detected in their phosphorylated, but not arsenylated, form (Table 1 and tables S1 to S4). Moreover, the absolute concentrations of most phospho-metabolites did not differ between GFAJ-1 cells grown in the presence or absence of arsenate (Table 1). Notably, the levels of nucleotide trisphosphates [ATP, cytidine trisphosphate (CTP), guanosine trisphosphate (GTP), and uridine trisphosphate (UTP)], as a measure for cellular energy status, were similar between both growth conditions, although some nucleotide bisphosphates [ADP, cytidine diphosphate (CDP), and guanosine diphosphate (GDP)], but not their corresponding monophosphates, appeared elevated in GFAJ-1 cells grown in the presence of arsenate. The elevated nucleotide bisphosphate levels might result from a higher energy demand of GFAJ-1 cells when grown in the presence of arsenate (e.g., due to ATP-dependent detoxification mechanisms, such as active export of arsenate) or might point to the formation of transient, instable nucleotide-bisphosphate-arsenate species, as proposed before (*13*). Nevertheless, our results indicated that the core metabolism of GFAJ-1 is based on phospho-metabolites, independent of its growth condition without major perturbation of most core metabolite levels (except the above-discussed nucleotide-bisphosphates), as a consequence of arsenate addition to the medium, which strongly argues against the use of arsenate to replace phosphate in GFAJ-1.

Yet, we observed hexose-arsenate in metabolome extracts of arsenate-grown cells of GFAJ-1 that co-eluted with the glucose-phosphate standard, as well as a potentially bisarsenylated hexose species (Table 1). However, the retention time of the latter deviated from that of fructose-1,6-bisphosphate, which makes it questionable that it represented an arsenate analog of the glycolytic intermediate. The origin of arsenylated hexoses in metabolome extracts of arsenate-grown GFAJ-1 cells was subsequently addressed in more detail. Notably, hexose-arsenate and bisarsenylated hexose were also detected in control extracts of filters that had been mock-treated with arsenate-amended, glucose-containing growth medium, indicating abiotic formation of these arsenylated hexoses (Table 1). This finding is in line with thermodynamic considerations and previous reports indicating spontaneous formation of glucose-arsenate from arsenate and glucose in solutions of alkaline pH (*14*). Consequently, the bisarsenylated hexose species that we detected is likely to be abiotically formed glucose-bisarsenate or an unspecific glucose-arsenate adduct, rather than an arsenate analog of fructose-1,6-bisphosphate.

Although our experiments indicated that hexose-arsenate is preformed abiotically in the growth medium, we could not exclude the possibility that some might be produced biotically, for ex-

¹Institute of Microbiology, Eidgenössische Technische Hochschule (ETH) Zurich, Wolfgang-Pauli-Strasse 10, 8093 Zurich, Switzerland.

²Laboratory of Inorganic Chemistry, ETH Zurich, Wolfgang-Pauli-Strasse 10, 8093 Zurich, Switzerland.

*These authors contributed equally to this work.

†To whom correspondence should be addressed. E-mail: toerb@ethz.ch (T.J.E.); vorholt@micro.biol.ethz.ch (J.A.V.)

ample, through transient ADP-arsenate as suggested before (13). Hence, to reduce the background levels of abiotically formed hexose-arsenates in metabolome preparations, a more stringent washing step with water was included during cell collection. The modified protocol changed the metabolite pool sizes, particularly of hexose-phosphate, which decreased by a factor of about 10 (table S5). However, when GFAJ-1 cells, grown in the presence of arsenate, were extracted with this stringent protocol, we were not able to detect any arsenylated hexoses (table S5). Similarly, when 10 mM glucose was added to the washing solution to minimize depletion effects, we did not observe the formation of hexose-arsenates beyond small abiotic background levels in extracts of GFAJ-1 cells grown in the presence of arsenate (table S5). Although we did not find evidence for the biotic formation of hexose-arsenates, GFAJ-1 cells remained metabolically active in these experiments, as demonstrated by the addition of 10 mM ^{13}C -labeled glucose to the wash solution: About 80% of the hexose-phosphate pool and 60% of the fructose-1,6-bisphosphate pool were exchanged with the ^{13}C -label, even during stringent washing, indicating active glycolysis (table S6). These results suggest that the biotic formation of glucose-arsenate is most likely negligible in GFAJ-1.

To probe the metabolic plasticity of GFAJ-1, we analyzed its metabolome in response to perturbation with arsenate in the absence of phosphate and without preadaptation of the organism to high arsenate concentrations. Cultures of phosphate pregrown GFAJ-1 cells were exchanged with medium that contained 40 mM arsenate, but no (i.e., $<0.3\ \mu\text{M}$) phosphate, and incubated for 6 and 360 s, respectively. To avoid depletion of glycolysis metabolite pool sizes that occurred during stringent washing (see above), the standard washing protocol was applied, resulting in the detection of abiotically formed arsenylated hexoses, as expected (Table 1). However, all other central metabolites were only detected in their phosphorylated form, and their pool sizes remained virtually unchanged upon arsenate incubation (Table 1). Most notably, there was no change in either the levels of triphosphate nucleotides (e.g., ATP) or the levels of glycolysis-derived phosphorylated metabolites (e.g., glucose-phosphate and fructose-1,6-bisphosphate) indicating energy status as well as metabolic activity of the cell (15). This suggested that, independent of its preadaptation to arsenate, the pool sizes of core metabolites in GFAJ-1 are not affected by perturbation through arsenate or hexose-arsenate. At the same time, our experiments also did not indicate that GFAJ-1 possesses a detectable downstream metabolism of these abiotically formed arseno-hexoses.

When our search for arseno-metabolites was extended beyond core metabolism, a total of six potentially arsenylated compounds were detected in extracts of GFAJ-1, although most of them only at low abundance and not in every

experiment or replicate (table S7). Two of the corresponding phosphate analogs are also not known to be of biotic origin, according to the EcoCyc-metabolite database (12). To understand whether formation of these compounds was a feature specific to GFAJ-1 or might be a more general phenomenon, we examined the metabolome of *Escherichia coli* in response to arsenate perturbation. In contrast to GFAJ-1, *E. coli* is able to cope only with low arsenate concentrations, when phosphate limited (16, 17), and has not

been reported to incorporate arsenate into its biomass. However, similarly to GFAJ-1, some putatively arsenylated compounds were detected at low abundance in metabolome extracts of arsenate-incubated *E. coli* (table S7), indicating that the presence of such low-abundance, putatively arsenylated compounds is not specific to GFAJ-1 and thus might not be of physiological relevance. Because these compounds are apparently unlinked to central carbon metabolism, they might also have formed abiotically.

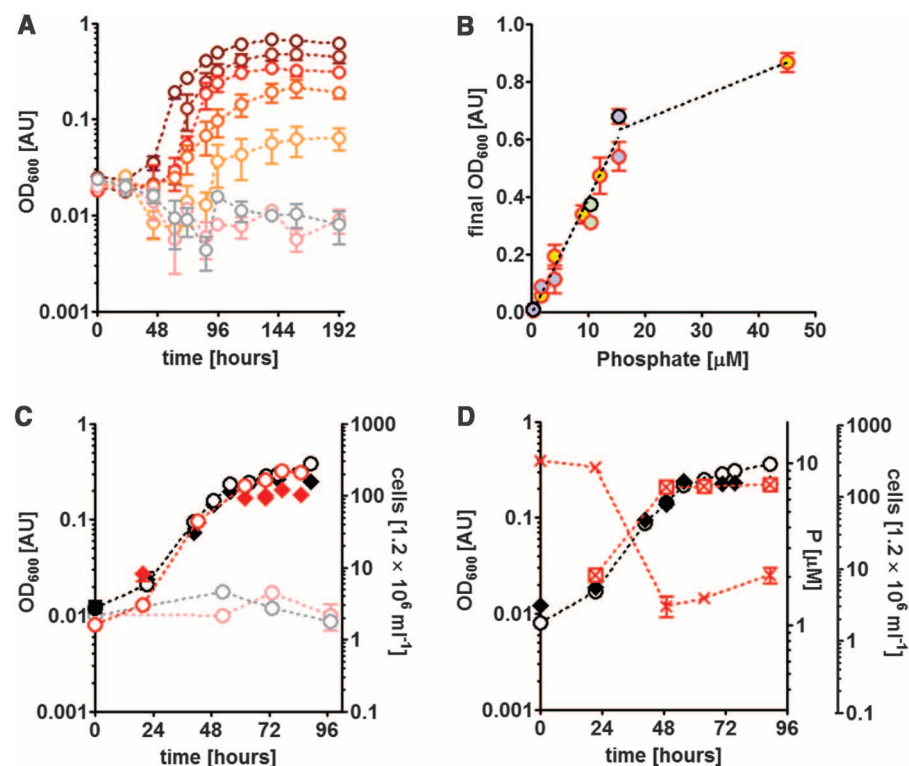


Fig. 1. Growth behavior of GFAJ-1 on minimal medium containing 10 mM glucose amended with different concentrations of phosphate and arsenate. Cell growth was followed by an increase in optical density at 600 nm (OD_{600} , open circles), or direct cell counting (closed diamonds). (A) Phosphate-dependent growth of GFAJ-1, as determined by OD_{600} . Shown are triplicate growth curves of GFAJ-1 in the presence of 15.4 μM phosphate, as determined by elemental analysis (brown open circles); 12 μM phosphate, mixed from 15.4 μM phosphate medium and $<0.3\ \mu\text{M}$ phosphate medium (dark red open circles); 9 μM phosphate, mixed from 15.4 μM phosphate medium and $<0.3\ \mu\text{M}$ phosphate medium (red open circles); 4 μM phosphate, as determined by elemental analysis (light red open circles); 1.7 μM phosphate, as determined by elemental analysis (orange open circles); $<0.3\ \mu\text{M}$ phosphate, as determined by elemental analysis (pale red-violet open circles); 40 mM arsenate, $<0.3\ \mu\text{M}$ phosphate, as determined by elemental analysis (gray open circle). (B) Correlation of stationary phase OD_{600} and phosphate concentration in the medium. Shown are the results from three independently prepared batches of growth media and precultures. Red circles indicate the absence of arsenate in the growth medium. Black circles indicate the presence of 40 mM arsenate in the growth medium. Medium batch 1 (yellow filled circles); medium batch 2 (light blue filled circles); medium batch 3 (light green filled circles). (C) Phosphate-dependent growth of GFAJ-1 in the presence and absence of arsenate, as determined by OD_{600} and direct cell counting. Open circles indicate OD_{600} measurements; diamonds indicate direct cell counts. Shown are representative growth curves of GFAJ-1 cultures in the presence of 40 mM arsenate, 10 μM phosphate (black open circles, black closed diamonds); 10 μM phosphate, no arsenate (red open circles, red closed diamonds); 40 mM arsenate, $<0.3\ \mu\text{M}$ phosphate (pale red-violet open circles); and $<0.3\ \mu\text{M}$ phosphate, no arsenate (gray open circles). (D) Dynamics of phosphorus during growth of GFAJ-1 in the presence of arsenate and limited amounts of phosphate. Shown are OD_{600} measurements (black open circles) and direct cell counts (black closed diamonds) of a GFAJ-1 culture in the presence of 40 mM arsenate and 10.4 μM phosphate, as well as the distribution of elemental phosphorus in the supernatant fraction (red crosses) or the cellular fraction (boxed red crosses). Phosphorus concentrations were determined by ICP-MS.

The apparent absence of arsenylated nucleotides and desoxynucleotides in GFAJ-1 under all conditions tested raises the question of how and whether arsenate would find its way into larger biomolecules (e.g., RNA and DNA). To answer this question, total nucleic acids were extracted from GFAJ-1 cells grown in the presence of 10 μ M phosphate with or without 40 mM arsenate (fig.

S1) and analyzed for their arsenic and phosphorus content, respectively, by ICP-MS. In line with the metabolome results in general and the lack of evidence for (alpha)-arsenylated nucleotides in particular, we did not find evidence for significant incorporation of arsenic into nucleic acids. The amount of arsenic in nucleic acid preparations was found to be below detection limit (Table 2), result-

ing in an arsenic-to-phosphorus ratio of less than 1 per mil, confirming that metabolism of GFAJ-1 is essentially based on phosphorylated compounds.

In conclusion, our experiments indicate that GFAJ-1 requires phosphorus for growth. We did not find evidence that arsenate can replace phosphate; however, in line with previous results, we confirm that GFAJ-1 is able to grow in the presence of high arsenate and limiting phosphate concentrations (phosphate:arsenate \approx 1:10,000), in contrast to other arsenate-resistant strains that require much higher phosphate concentrations (typically phosphate:arsenate \approx 1:10 to 1:100; *Aspergillus* sp. P37 \approx 1:1,000) (16–18). Phosphorus incorporation studies and metabolome analysis indicated that the core metabolism of GFAJ-1 is based on phosphorylated metabolites, even when cells are grown at high concentrations of arsenate (40 mM) and low concentrations of phosphate (below 10 μ M). Feeding of arsenate to GFAJ-1 leads to the abiotic formation of some arsenylated compounds (hexose-arsenates), yet most of the phosphorylated metabolite pools do not change upon arsenate feeding. We note that the abiotic formation of hexose-arsenates observed by us might explain the results of Wolfe-Simon *et al.* in which the intracellular accumulation of arsenate organoesters by GFAJ-1 was indicated by secondary ion mass spectrometry and x-ray analysis (1). However, the facts that these abiotically formed arseno-compounds apparently were not metabolized by GFAJ-1 and that virtually no arsenic was detected in nucleic acid preparations of GFAJ-1 are in line with our conclusions that GFAJ-1 is an arsenate-resistant, yet phosphate-dependent, organism. The molecular basis for arsenate resistance in GFAJ-1 might be the subject of further investigations, in particular given the finding that the concentrations of arsenic and phosphorus were found within the same order of magnitude in the cellular fraction of growing GFAJ-1 cultures, despite the ratio of phosphate and arsenate in the medium differing by four orders of magnitude (fig. S3).

References and Notes

1. F. Wolfe-Simon *et al.*, *Science* **332**, 1163 (2011).
2. S. A. Benner, *Science* **332**, 1149-c (2011).
3. D. W. Borhani, *Science* **332**, 1149-e (2011).
4. J. B. Cotner, E. K. Hall, *Science* **332**, 1149-f (2011).
5. I. Csabai, E. Szathmáry, *Science* **332**, 1149-b (2011).
6. P. L. Foster, *Science* **332**, 1149-i (2011).
7. S. Oehler, *Science* **332**, 1149-g (2011).
8. R. J. Redfield, *Science* **332**, 1149-h (2011).
9. B. Schoepp-Cothenet *et al.*, *Science* **332**, 1149-d (2011).
10. J. Liebig, in *Die Grundsätze der Agrikultur-Chemie mit Rücksicht auf die in England angestellten Untersuchungen*. (Friedrich Vieweg und Sohn Publ. Co., Braunschweig, Germany, 1855).
11. P. Kiefer, N. Delmotte, J. A. Vorholt, *Anal. Chem.* **83**, 850 (2011).
12. I. M. Keseler *et al.*, *Nucleic Acids Res.* **39** (Database issue), D583 (2011).
13. S. A. Moore, D. M. Moennich, M. J. Gresser, *J. Biol. Chem.* **258**, 6266 (1983).
14. R. Lagunas, *Arch. Biochem. Biophys.* **205**, 67 (1980).
15. D. E. Atkinson, G. M. Walton, *J. Biol. Chem.* **242**, 3239 (1967).
16. G. R. Willsky, M. H. Malmay, *J. Bacteriol.* **144**, 366 (1980).

Table 1. Selected core metabolites of GFAJ-1 cells actively growing on limiting amounts of phosphate in the absence or presence of 40 mM arsenate, and metabolic response of phosphate-grown cells upon incubation with 40 mM arsenate in the absence of phosphate. AMP, adenosine monophosphate; CMP, cytidine monophosphate; GMP, guanosine monophosphate; TDP, thymidine diphosphate; TTP, thymidine triphosphate; UDP, uridine diphosphate; UMP, uridine monophosphate.

Metabolites (fmol/ μ l extract)	Cells grown with 9 μ M P	Cells grown with 9 μ M P 40 mM As	Medium-treated filter	Cells grown with 10 μ M P 6 s As incubation	Cells grown with 10 μ M P 360 s As incubation
<i>Nucleotide monophosphates</i>					
AMP/dGMP	4.5 \pm 1.2	5.2 \pm 0.6	<0.3*	2.9 \pm <0.1	3.9 \pm 0.8
CMP	1.3 \pm 0.1	1.4 \pm 0.3	<0.3*	1.0 \pm 0.1	1.1 \pm 0.2
UMP	0.7 \pm 0.3	0.5 \pm 0.1	<0.3*	0.2 \pm 0.1	0.2 \pm 0.2
<i>Nucleotide bisphosphates</i>					
ADP	58 \pm 16	141 \pm 27	<0.8*	33 \pm 5	58 \pm 31
CDP	15 \pm 1	27 \pm 5	<0.5*	13 \pm 2	16 \pm 3
GDP	14 \pm 2.4	31 \pm 0.9	<0.4*	11 \pm 3	14 \pm 4
UDP	2.1 \pm 0.2	4.5 \pm 1.1	<0.2*	1.7 \pm 0.2	2.2 \pm 0.3
<i>Nucleotide triphosphates</i>					
ATP	145 \pm 13	153 \pm 27	<1.2*	166 \pm 15	128 \pm 29
CTP	21 \pm 3	31 \pm 4	<0.2*	25 \pm 2	21 \pm 2
GTP	22 \pm 2	30 \pm 4	<0.7*	25 \pm 2	20 \pm 4
UTP	18 \pm 1	23 \pm 7	<0.3*	18 \pm 1	15 \pm 2
<i>Deoxynucleotide phosphates</i>					
dADP	1.2 \pm 0.1	3.7 \pm 1.2	<0.2*	0.7 \pm 0.1	1.3 \pm 0.8
dTDP	2.4 \pm 0.2	6.1 \pm 2.1	<1.1*	2.2 \pm 0.5	4.0 \pm 0.6
dTTP	32 \pm 3	30 \pm 10	<1.7*	28 \pm 5	19 \pm 3
<i>Sugar phosphates</i>					
Hexose-phosphate	13 \pm 3	13 \pm 3	<0.9*	7.6 \pm 0.1	10 \pm 4
Hexose-bisphosphate	18 \pm 3	18 \pm 4	<0.9*	21 \pm 3	29 \pm 6
Phospho-gluconate	3.6 \pm 0.1	2.9 \pm 1.6	<0.2*	2.7 \pm 0.2	4.0 \pm 1.0
<i>Nucleotide sugar phosphates</i>					
UDP-hexose	42 \pm 2	55 \pm 11	<1.3*	36 \pm 3	28 \pm 2
UDP-N-acetyl-hexosamine	29 \pm 2	37 \pm 4	<1.1*	24 \pm 2	22 \pm 2
<i>Other phospho-metabolites</i>					
Methylerythritol-cyclo-P-P	5.2 \pm 3.0	7.2 \pm 0.7	<1.6*	5.7 \pm 0.3	17 \pm 3
Arsenylated analogs (relative levels)					
Hexose-arsenate	<0.1	159 \pm 18	215 \pm 120	155 \pm 81	74 \pm 75
Hexose-bisarsenate	<0.1	4 \pm 5	4 \pm 2	18 \pm 8	9 \pm 9

*Below detection limit.

Table 2. Elemental analysis of nucleic acid preparations from GFAJ-1 grown on 10 μ M phosphate in the absence or presence of 40 mM arsenate.

Sample	GFAJ-1 grown with 9 μ M P	GFAJ-1 grown with 9 μ M P 40 mM As
Nucleic acids (ng)	15,700 \pm 1800	17,400 \pm 1900
Phosphorus in nucleic acids (ng)	934 \pm 13	1043 \pm 8
Arsenic in nucleic acids (ng)	<1*	<1*
As/P molar ratio	<0.001	<0.001

*Below detection limit.

17. G. R. Willsky, M. H. Marmy, *J. Bacteriol.* **144**, 356 (1980).
 18. D. Cánovas, C. Durán, N. Rodríguez, R. Amils, V. de Lorenzo, *Environ. Microbiol.* **5**, 133 (2003).

Acknowledgments: We thank R. Oremland and J. S. Blum for providing strain GFAJ-1, P. Christen and F. Ryffel for technical and experimental assistance, as well as an anonymous

reviewer for valuable suggestions and comments on our manuscript. T.J.E. was supported through an ETH Fellowship.

Supplementary Materials

www.sciencemag.org/cgi/content/full/science.1218455/DC1
 Materials and Methods

Figs. S1 to S3
 Tables S1 to S8
 References

27 December 2011; accepted 1 June 2012
 Published online 8 July 2012;
 10.1126/science.1218455

Absence of Detectable Arsenate in DNA from Arsenate-Grown GFAJ-1 Cells

Marshall Louis Reaves,^{1,2} Sunita Sinha,³ Joshua D. Rabinowitz,^{1,4}
 Leonid Kruglyak,^{1,5,6} Rosemary J. Redfield^{3*}

A strain of *Halomonas* bacteria, GFAJ-1, has been claimed to be able to use arsenate as a nutrient when phosphate is limiting and to specifically incorporate arsenic into its DNA in place of phosphorus. However, we have found that arsenate does not contribute to growth of GFAJ-1 when phosphate is limiting and that DNA purified from cells grown with limiting phosphate and abundant arsenate does not exhibit the spontaneous hydrolysis expected of arsenate ester bonds. Furthermore, mass spectrometry showed that this DNA contains only trace amounts of free arsenate and no detectable covalently bound arsenate.

Wolfe-Simon *et al.* isolated strain GFAJ-1 from the arsenic-rich sediments of California's Mono Lake by its ability to grow through multiple subculturing in artificial Mono Lake medium AML60 that lacked added phosphate but had high concentrations of arsenate (+As/-P condition) (1). Because GFAJ-1 grew in -P medium only when arsenate was provided, and because substantial amounts of arsenate were detected in subcellular fractions, growth was attributed to the use of arsenate in place of phosphate. However, the basal level of phosphate contaminating the -P medium was reported to be 3 to 4 μM (1), which previous studies of low-phosphate microbial communities suggest is sufficient to support moderate growth (2). GFAJ-1 grew well on medium supplemented with ample phosphate but no arsenate (1500 μM PO_4 , +P/-As condition), indicating that GFAJ-1 is not obligately arsenate-dependent.

Wolfe-Simon *et al.* (1) further inferred that arsenic was incorporated into the DNA backbone of GFAJ-1 in place of phosphorus, with an estimated 4% replacement of P by As based on the As:P ratio measured in agarose gel slices containing DNA samples. This finding was surprising because arsenate is predicted to reduce rapidly

to arsenite in physiological conditions (3, 4) and because arsenate esters in aqueous solution are known to be rapidly hydrolyzed (5). We have now tested this report by culturing GFAJ-1 cells supplied by the authors (1) and by analyzing highly purified DNA from phosphate-limited cells grown with and without arsenate.

Wolfe-Simon *et al.* reported that GFAJ-1 cells grew very slowly in AML60 medium (doubling time ~12 hours) and that, when phosphate was not added to the medium, cells failed to grow unless arsenate (40 mM) was provided (1). How-

ever, although we obtained strain GFAJ-1 from these authors, in our hands GFAJ-1 was unable to grow at all in AML60 medium containing the specified trace elements and vitamins, even with 1500 μM sodium phosphate added as specified in (1). We confirmed the strain's identity using reverse transcription-polymerase chain reaction and sequencing of 16S ribosomal RNA, with primers specified by Wolfe-Simon *et al.* (1); this gave a sequence identical to that reported for strain GFAJ-1. We then found that addition of small amounts of yeast extract, tryptone, or individual amino acids to basal AML60 medium allowed growth, with doubling times of 90 to 180 min. Medium with 1 mM glutamate added was therefore used for subsequent experiments (6).

With 1500 μM phosphate but no added arsenate (Wolfe-Simon *et al.*'s -As/+P condition), this medium produced $\sim 2 \times 10^8$ cells/ml, similar to the -As/+P yield obtained by Wolfe-Simon *et al.* (1). As expected, the growth yield depended on the level of phosphate supplementation (Fig. 1), with even unsupplemented medium allowing growth to $\sim 2 \times 10^6$ cells/ml. Because analysis by inductively coupled plasma-mass spectrometry (ICP-MS) showed that this medium contained only 0.5 μM contaminating phosphate, our supplementation with an additional 3.0 μM phosphate replicates Wolfe-Simon *et al.*'s "-P" culture condition. The growth analyses shown in Fig. 1 were performed in the absence of arsenate and showed

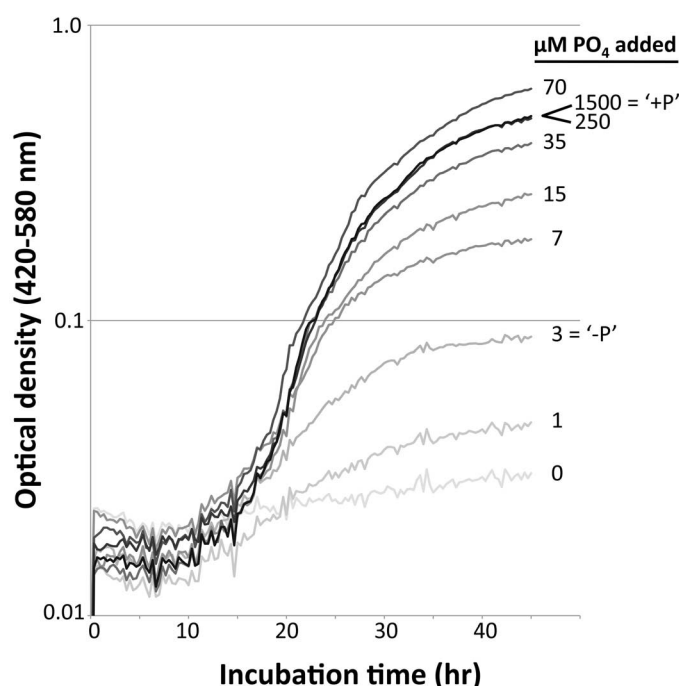


Fig. 1. Growth curves of GFAJ-1 in AML60 medium supplemented with different concentrations of phosphate. Each line is the mean of 10 replicate 300- μl cultures in wells of a Bioscreen C Growth Analyzer. The phosphate additions used to replicate the "-P" and "+P" conditions of (1) are indicated.

¹Lewis Sigler Institute for Integrative Genomics, Princeton University, Princeton, NJ 08544, USA. ²Department of Molecular Biology, Princeton University, Princeton, NJ 08544, USA. ³Department of Zoology, University of British Columbia, Vancouver, BC, Canada. ⁴Department of Chemistry, Princeton University, Princeton, NJ 08544, USA. ⁵Howard Hughes Medical Institute, Lewis-Sigler Institute for Integrative Genomics, Princeton University, Princeton, NJ 08544, USA. ⁶Department of Ecology and Evolutionary Biology, Princeton University, Princeton, NJ 08544, USA.

*To whom correspondence should be addressed. E-mail: redfield@zoology.ubc.ca

that GFAJ-1 does not require arsenate for growth in media with any level of phosphate.

The cause of the discrepancies between our growth results and those of Wolfe-Simon *et al.* is not clear. The arsenate dependence they observed may reflect the presence in their arsenate (purity and supplier unknown) of a contaminant that filled the same metabolic role as our glutamate supplement. Our +As and –As cultures grew to similar densities, and we did not observe any

cases in which +As cultures grew but –As cultures did not. The phosphate dependence we observed is also consistent with that expected from work on other species (2).

To investigate the possible incorporation of arsenate into the GFAJ-1 DNA backbone, we purified and analyzed DNA from GFAJ-1 cells grown in four differently supplemented versions of AML60 medium, matching those analyzed by Wolfe-Simon *et al.*—i.e., –As/–P: no arsenate,

3.5 μM phosphate; +As/–P: 40 mM arsenate, 3.5 μM phosphate; –As/+P: no arsenate, 1500 μM phosphate; +As/+P: 40 mM arsenate, 1500 μM phosphate. Initial purification of DNA consisted of two preliminary organic extractions, precipitation from 70% ethanol, digestion with ribonuclease and proteinase, two additional organic extractions, and a final ethanol precipitation (6). DNA was collected from 70% ethanol by spooling rather than centrifugation, because this reduces contamination with other substances insoluble in ethanol (7).

Wolfe-Simon *et al.* suggested that arsenate ester bonds in GFAJ-1 DNA might be protected from hydrolysis by intracellular proteins or compartmentalization of the DNA (8). We therefore tested whether purification exposed GFAJ-1 DNA to spontaneous hydrolysis. Gel analysis of DNA immediately after purification revealed fragments of >30 kb, whether cells were grown with limiting or abundant phosphate and with or without 40 mM arsenate (Fig. 2A). We also reexamined this DNA after 2 months of storage at 4°C. All preparations showed very similar-sized fragments of double-stranded DNA and of single-stranded DNA (Fig. 2, B and C), with no evidence of hydrolysis. *Haemophilus influenzae* DNA served as a control for gel migration, indicating that GFAJ-1 DNA is not associated with hydrolysis-protecting proteins or other macromolecules that might have persisted through the purification. Unless arsenate-ester bonds are intrinsically stable in DNA, our analysis estimates a minimum separation between arsenates in the DNA backbone of at least 25 kb, three orders of magnitude below that estimated by Wolfe-Simon *et al.*

Arsenate in bonds that were stable to spontaneous hydrolysis should be detectable as free arsenate, arsenate-containing mononucleotides, or arsenate-containing dinucleotides after enzymatic digestion of purified DNA. We therefore used liquid chromatography–mass spectrometry (LC-MS) to analyze GFAJ-1 DNA for arsenate after digestion with P1 and snake venom nucleases (6). Relevant molecular species were identified by negative-mode, full-scan, high-mass resolution LC-MS analysis (6). This method was used to analyze two independent replicate DNA preparations from cells grown in either +As/–P or –As/+P medium and fractions from CsCl gradient analyses of these DNAs.

The initial DNA preparations of +As/–P DNAs contained some free arsenate anion (H₂AsO₄[–]) (Table 1), at levels similar to those reported by Wolfe-Simon *et al.* (1). This arsenate was largely removed by three serial washes with distilled water; digested washed DNA contained arsenate at a level slightly higher than in the water blank (Fig. 3 and Table 1). Thus, we concluded that most of the arsenate we detected after preliminary DNA purification arose by contamination from the arsenate-rich (40 mM) growth medium.

Further analyses compared the nuclease-digested and washed fractions obtained from

Fig. 2. Integrity of GFAJ-1 chromosomal DNA after long-term storage. Lanes: 1 and 7, Hind III digest of lambda DNA; 2, *Haemophilus influenzae* chromosomal DNA; 3 to 6, GFAJ-1 chromosomal DNA grown in the specified combinations of As and P (–As: no arsenate; +As, 40 mM arsenate; –P, 3 μM added phosphate; +P, 1500 μM added phosphate). (A) About 100 ng of GFAJ-1 DNA immediately after purification. (B) The same DNAs (200 ng/lane) after 2 months of storage in tris-EDTA at 4°C. (C) The same DNAs as in (B), but 800 ng/lane and after 10 min at 95°C.

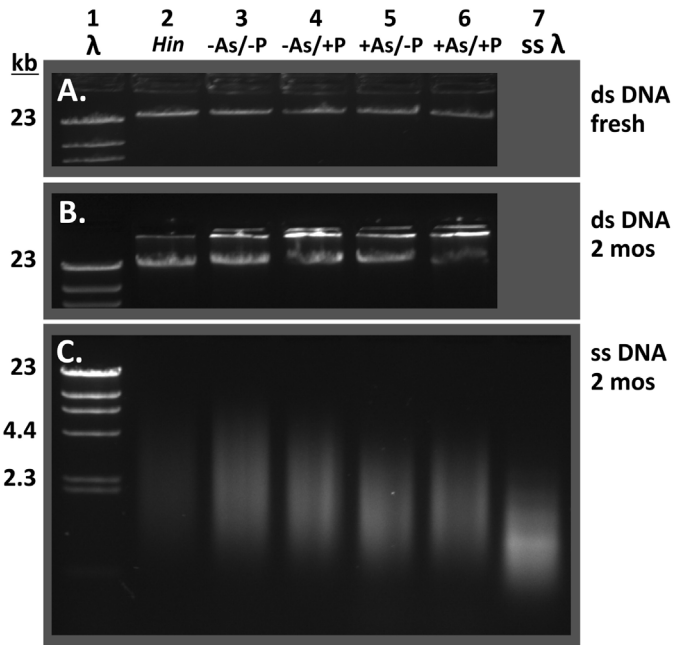


Table 1. DNA, arsenate, and nucleotide content of samples measured by absorbance at 260 nm and LC-MS. AU, absorbance units.

Sample	A ₂₆₀ (DNA)	Compound				
	AU (μg)	Arsenate	dAMP	dAMA	dAMP-dAMP	dAMA-dAMP
		Peak area, ion counts				
Digested CsCl fractions: (increasing density)						
#1 (top)	0.03 (0)	0	0	154	0	0
#2	0.01 (0)	0	0	0	0	0
#3	0.02 (0)	226	0	0	0	0
#4	0.01 (0)	0	160	0	0	0
#5	0.01 (0)	0	0	0	0	0
#6	0.82 (4.5)	157	39,000	0	0	0
#7	1.12 (6.7)	373	52,000	0	0	0
#8 (bottom)	0.44 (1.9)	300	3,700	0	0	197
Water blank	0 (0)	329	0	0	0	0
–As/+P partial digest	(3.3)	515	0	0	21,000	210
+As/–P washed, digested DNA	(1.7)	2625	186,457	0	241	202
+As/–P whole DNA (1:10 dil.)	(1.7)	2794	562	0	781	0
+As/–P wash of gDNA (300 μl)	0 (0)	9545	182	207	0	221
Arsenate standards (molar)						
1.66 × 10 ^{–8}		329				
1.66 × 10 ^{–7}		1959				
1.66 × 10 ^{–5}		59,925				
Expected if DNA As:P = 0.04	(6.7)	~122,000		>0		>0

CsCl isopycnic density gradient centrifugation of the DNAs (Fig. 3) (6). The arsenate detection limit for these measurements was $\sim 5 \times 10^{-8}$ M (table S1), a level that if present in the fractions with the most DNA would correspond to an As:P ratio of $<0.1\%$, 50-fold lower than the 4% ratio estimated by Wolfe-Simon *et al.* Although traces of arsenate (or a contaminant of mass similar to that of arsenate) were found in several fractions of the CsCl gradient, the arsenate peak did not exceed the limit of detection, and a similar-intensity signal at a mass-to-charge ratio (m/z) of arsenate was observed in the water blank. There was no evidence that the arsenate trace comigrated with the DNA. In contrast, normal phosphate-containing deoxynucleotides were observed in rough proportion to the abundance of DNA throughout the gradient for both the +As/-P and -As/+P cells (Fig. 4A and table S2).

Likewise, no arsenate-conjugated mono- or dinucleotides were detected by exact mass (Fig.

4, B and D). Although retention time and ionization efficiency could not be validated with standards for these molecules, their behavior, if the molecules were stable, would be expected to resemble that of their phosphorylated analogs sufficiently to allow detection. Finally, an enrichment of deoxynucleosides per nanogram of DNA obtained from GFAJ-1 grown in the +As/-P condition, relative to either -As/+P or -As/-P conditions, could indicate nicked DNA resulting from arsenate-ester hydrolysis. However, we did not detect any enrichment despite detecting deoxyadenosine, deoxyguanosine, deoxycytidine, and thymidine (fig. S1 and table S2). Thus, although we detected arsenate associated with GFAJ-1 DNA, we found no evidence for arsenate bound sufficiently tightly to resist washing with water or able to comigrate with the DNA in a CsCl gradient. Differences in DNA purity can readily explain the conflict of these results with Wolfe-Simon *et al.*'s claim that GFAJ-1 uses arsenate to replace scarce phosphate in its DNA.

Our LC-MS analyses rule out incorporation of arsenic in DNA at the $\sim 0.1\%$ level, and a much lower limit is suggested by our gel analysis of DNA integrity. Given the chemical similarity of arsenate to phosphate, it is likely that GFAJ-1 may sometimes assimilate arsenate into some small molecules in place of phosphate, such as sugar phosphates or nucleotides. Although the ability to tolerate or correct very-low-level incorporation of arsenic into DNA could contribute to the arsenate resistance of GFAJ-1, such low-level incorporation would not be a biologically functional substitute for phosphate, and thus would have no appreciable effect on the organism's requirements for phosphate.

From a broader perspective, GFAJ-1 cells growing in Mono Lake face the challenge of discriminating an essential salt (PO_4 , 400 μM) from a highly abundant but toxic chemical mimic (AsO_4 , 200 μM). Similar salt management challenges are encountered by many other microorganisms, such as those growing in environments

Fig. 3. LC-MS analysis of arsenate in purified and CsCl-fractionated DNA from arsenate-grown GFAJ-1 cells. Representative extracted ion chromatograms for arsenate [$m/z = 140.9174 \pm 3$ parts per million (ppm)] are shown as the chromatographic retention time (in minutes) plotted against intensity (in ion counts). Sample identity is indicated to the right, along the axis extending into the page. DNA from arsenate-grown GFAJ-1 cells (+As/-P undigested gDNA) was analyzed by LC-MS at a 1:10 dilution, as were the water wash (+As/-P wash of gDNA), the same DNA after washing and enzymatic digestion (+As/-P washed, digested DNA), and finally, fractions of the same DNA after a CsCl gradient purification and digestion (+As/-P CsCl fractions #1 to #8, with DNA concentrating in fractions #6, #7, and #8). Potassium arsenate standards (Std 1.7e-6 to 1.7e-8 [M]) and a water blank were also analyzed. One of four representative experiments is shown.

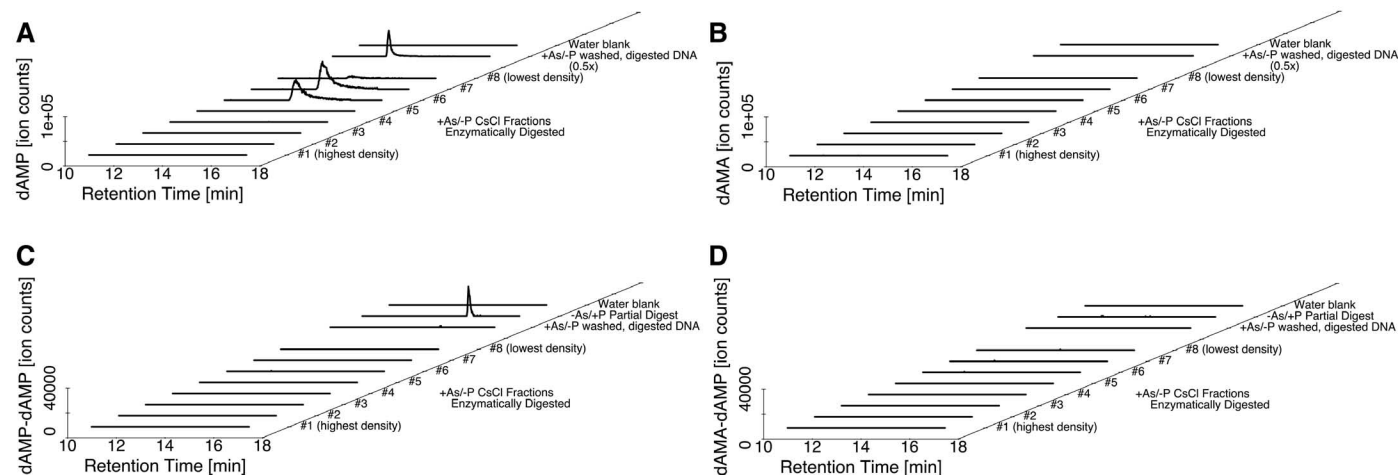
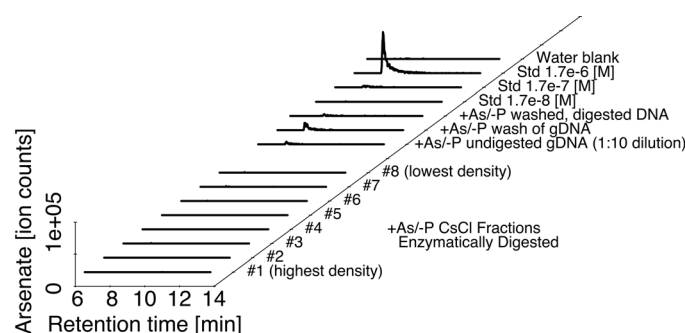


Fig. 4. LC-MS analysis of deoxynucleotides from purified and CsCl-fractionated DNA from arsenate-grown GFAJ-1 cells. Representative extracted ion chromatograms are shown as the chromatographic retention time (in minutes) plotted against intensity (in ion counts). One of four representative experiments is shown. (A and B) Extracted ion chromatograms for (A) deoxyadenosine-phosphate (dAMP; $m/z = 330.0609 \pm 5$ ppm) and (B) its arsenate analog deoxyadenosine-arsenate (dAMA; $m/z = 374.0087 \pm 5$ ppm). DNA from arsenate-grown GFAJ-1 cells (+As/-P washed, digested DNA) was washed, digested, and analyzed by LC-MS, as was the same DNA after a CsCl gradient purification and digestion (+As/-P CsCl fractions #1 to #8). To keep the peak

on scale, the signal for +As/-P washed, digested DNA has been multiplied by 0.5. This observed large peak matches the known retention time of dAMP. (C and D) Extracted ion chromatograms for (C) the dideoxynucleotide deoxyadenosine-phosphate (dAMP-dAMP; $m/z = 643.1185 \pm 5$ ppm) and (D) its mono-arsenate analog deoxyadenosine-arsenate-deoxyadenosine-phosphate (dAMA-dAMP; $m/z = 687.0663 \pm 5$ ppm). DNA from arsenate-grown GFAJ-1 cells (+As/-P washed, digested DNA) was washed, digested, and analyzed by LC-MS, as was the same DNA after a CsCl gradient purification and digestion (+As/-P CsCl fractions #1 to #8). Partially digested -As/+P DNA shows a large peak at the exact mass of dAMP-dAMP.

with scarce potassium and plentiful ammonia (9). Organisms typically adapt to such conditions not by incorporating the mimic in place of the essential salt but by enriching for the salt at multiple stages, from preferential membrane transport to the selectivity of metabolic enzymes. The end result is that the fundamental biopolymers conserved across all forms of life remain, in terms of chemical backbone, invariant (10–12).

References and Notes

1. F. Wolfe-Simon *et al.*, *Science* **332**, 1163 (2011).
2. J. B. Cotner, E. K. Hall, J. T. Scott, M. Haldal, *Front Microbiol.* **1**, 132 (2010).
3. B. Schoepp-Cothenet *et al.*, *Science* **332**, 1149–d (2011).
4. E. Lebrun *et al.*, *Mol. Biol. Evol.* **20**, 686 (2003).

5. C. Baer, J. O. Edwards, P. H. Rieger, *Inorg. Chem.* **20**, 905 (1981).
6. Materials and methods are available as supplementary materials on *Science* Online.
7. O. T. Avery, C. M. Macleod, M. McCarty, *J. Exp. Med.* **79**, 137 (1944).
8. F. Wolfe-Simon *et al.*, *Science* **332**, 1149–j (2011).
9. D. C. Hess, W. Lu, J. D. Rabinowitz, D. Botstein, *PLoS Biol.* **4**, e351 (2006).
10. L. Wang *et al.*, *Proc. Natl. Acad. Sci. U.S.A.* **108**, 2963 (2011).
11. W. Lu *et al.*, *Anal. Chem.* **82**, 3212 (2010).
12. M. T. Zimmermann, A. Kloczkowski, R. L. Jernigan, *BMC Bioinformatics* **12**, 264 (2011).

Acknowledgments: M.L.R. is supported by a Graduate Research Fellowship from the National Science Foundation. J.D.R. is supported by the CAREER Award from the National Science Foundation. L.K. is an Investigator of the Howard

Hughes Medical Institute and a James S. McDonnell Foundation Centennial Fellow. R.J.R. thanks the Canadian Institutes of Health Research for funding and J. Blum and R. Oremland for providing strain GFAJ-1; M. Khoshnoodi for the trace-element mix; the Charles Thompson lab for use of their BioScreen Analyzer; and S. Silver and C. Rensing for helpful discussions. We also thank the ICP Laboratory in the Department of Geosciences at Princeton University for assistance with ICP-MS analysis.

Supplementary Materials

www.sciencemag.org/cgi/content/full/science.1219861/DC1
Materials and Methods
Fig. S1
Tables S1 and S2
References

31 January 2012; accepted 1 June 2012
Published online 8 July 2012;
10.1126/science.1219861

The Structure and Catalytic Cycle of a Sodium-Pumping Pyrophosphatase

Juho Kellosoalo,^{1,2*} Tommi Kajander,^{1*} Konstantin Kogan,¹ Kisun Pokharel,^{1,3} Adrian Goldman^{1†}

Membrane-integral pyrophosphatases (M-PPases) are crucial for the survival of plants, bacteria, and protozoan parasites. They couple pyrophosphate hydrolysis or synthesis to Na⁺ or H⁺ pumping. The 2.6-angstrom structure of *Thermotoga maritima* M-PPase in the resting state reveals a previously unknown solution for ion pumping. The hydrolytic center, 20 angstroms above the membrane, is coupled to the gate formed by the conserved Asp²⁴³, Glu²⁴⁶, and Lys⁷⁰⁷ by an unusual “coupling funnel” of six α helices. Comparison with our 4.0-angstrom resolution structure of the product complex suggests that helix 12 slides down upon substrate binding to open the gate by a simple binding-change mechanism. Below the gate, four helices form the exit channel. Superimposing helices 3 to 6, 9 to 12, and 13 to 16 suggests that M-PPases arose through gene triplication.

Found in plants, protozoans, bacteria, and archaea, membrane-integral pyrophosphatases (M-PPases) contain 14 to 17 transmembrane (TM) helices (1) and link pyrophosphate (PP_i) hydrolysis or synthesis to sodium or proton pumping (2). PPases are essential to drive anabolic reactions such as DNA synthesis to completion. In contrast to the soluble PPases, M-PPases recycle part of the free energy of PP_i hydrolysis to generate electrochemical potential across biological membranes. In plants, they are vital for maturation and enhance survival under abiotic stress conditions (drought, anoxia, cold) (3). They also are important for proliferation of disease causing protozoa (4).

Unlike the rotary F-type adenosine triphosphatases (F-ATPases), M-PPases are dimeric (5), and, unlike the P-type ATPases, there is no phosphorylated enzyme intermediate (6). M-PPases

can be divided into three functional classes: K⁺-independent proton pumps and K⁺-dependent sodium and proton pumps, both of which require potassium for maximal activity (2). The resting enzyme state is EMg₂, and two more metal ions bind with substrate, Mg₂PP_i (7).

We have solved the structure of the Na⁺-pumping M-PPase of *Thermotoga maritima* (TmPPase) in the resting state (TmPPase:Ca:Mg) at 2.6 Å resolution ($R_{\text{work}}/R_{\text{free}} = 20.5/24.5\%$) and with product bound (TmPPase:P_i:Mg₄) at 4.0 Å ($R_{\text{work}}/R_{\text{free}} = 29.5/36.5\%$) (tables S1 and S2, Fig. 1, and fig. S1). In addition, the tungstate derivative used to solve the structure corresponds to the TmPPase:M₂:P_i state (8), thus mapping out the catalytic cycle. TmPPase is a dimer of two very similar (rmsd/Ca 0.58 Å) monomers, each with 16 TM helices (Fig. 1). The helices extend up to 25 Å from the membrane bilayer on the cytoplasmic side but end near the bilayer on the periplasmic side (Fig. 1 and fig. S2). The dimer interface comprises helices 10, 13, and 15 (fig. S2) and a short antiparallel β sheet in the sixth periplasmic loop between TM12 and 13. Although the protein is an obligate dimer, residue conservation (fig. S3) shows that the pump is located entirely within a single monomer. It had been suggested that TmPPase

was structurally similar to the F-ATPases (9), but a DALI search (10) shows that the only homologous structure is the recently published mung bean H⁺-pumping K⁺-dependent PPase (VrPPase) (11).

The unusual active site has four distinct regions: the hydrolytic center, some 20 Å above the membrane surface; a “coupling funnel”; the gate (closed in our structure) just below the membrane surface; and an exit channel for Na⁺ ions (Fig. 2A). The distance from the hydrolytic center to the gate is thus about 20 Å. Six helices, 5–6, 11–12, and 15–16 form the hydrolytic center and coupling funnel, whereas only helices 5, 6, 12, and 16 form the gate and channel, creating an internal “symmetry mismatch” (12) between the two regions. Conserved charged residues, many of which have been extensively mutated in M-PPases (fig. S4 and table S3) line the hydrolytic center, coupling funnel, and gate. Their positioning confirms that M-PPases arose by gene triplication (13). Helices 3 to 6, 9 to 12, and 13 to 16 of TmPPase, which carry all of the functional residues (Fig. 2), share a similar structural motif (Fig. 1) not found in other proteins except the VrPPase. The structural alignments align key conserved residues (fig. S2C) that cluster in the active site.

Our native 2.6 Å structure has one Ca²⁺ and one Mg²⁺ ion bound. The Ca²⁺ ion is coordinated by the conserved Asp⁶⁸⁸, Asp⁶⁹², and Asp⁶⁶⁰, which are positioned by Lys⁶⁶³, Lys⁶⁶⁴, and Lys⁶⁹⁵ (Fig. 2C and fig. S1), whereas the Mg²⁺ ion is coordinated by Asp²³² and Asp⁴⁶⁵ (fig. S1). The VrPPase structure, crystallized in the presence of Mg²⁺ and the competitive inhibitor imidodiphosphate (PNP) (11), contains two ions with about the same protein coordination (VrPPase M3 and M2) that are coordinated to the PNP inhibitor. We thus assign our Ca²⁺ as M1 (their M3) and our Mg²⁺ as M2 (their M2) because these are the two metal ions bound in the resting enzyme and because the Ca²⁺ is multivalently coordinated in both structures (11), unlike M2, which only binds Asp⁴⁶⁵⁽⁵⁰⁷⁾ in VrPPase (VrPPase numbers in parentheses). In addition, Gd³⁺, which inhibits TmPPase, binds at these two sites (fig. S5). The

¹Structural Biology and Biophysics Program, Institute of Biotechnology, Post Office Box 65, University of Helsinki, FIN-00014, Finland. ²Graduate School of Informational and Structural Biology, Finland. ³Department of Biochemistry and Food Chemistry, FIN-20014 University of Turku, Finland.

*These authors contributed equally to this work.

†To whom correspondence should be addressed. E-mail: adrian.goldman@helsinki.fi

other two metal ions in the VrPPase structure (labeled M1 and M4) must be the two that bind with PNP or substrate. Comparing the VrPPase and TmPPase structures, our M1 and M2 both move toward the PNP by about 2.8 Å from their resting position (fig. S4). A similar cluster of Mg_4P_i can be fit into the difference electron density in our product complex (fig. S1).

The Na_2WO_4 derivative contained one tungstate ion per monomer, and, because this was used for MIRAS phasing, the protein structure must be similar to that of the resting TmPPase:Ca:Mg enzyme (table S1). The tungstate, loosely coordinated by Lys⁶⁶³⁽⁶⁹⁴⁾ and Lys⁶⁶⁴⁽⁶⁹⁵⁾ (3.7 and 4.1 Å away) and within 5 Å of M1, is visible in the anomalous difference Fourier map (Fig. 2F). This is similar to the coordination of the leaving group phosphate in the VrPPase:PNP structure (11), and the lysines are essential for activity (table S3).

Below the PNP/phosphates is an unusual coupling funnel (Fig. 3) containing eight absolutely conserved charged residues (Arg¹⁹¹, Lys¹⁹⁹, Asp²³⁶, Asp²⁴³, Asp⁴⁵⁸, Lys⁴⁹⁹, Lys⁶⁹⁵, and Asp⁶⁹⁶). All show large effects upon mutation (table S3) and couple hydrolysis to ion pumping, as can be seen especially for Arg¹⁹¹. The long-range ionic interactions in the resting structure (Lys⁴⁹⁹-Asp²³⁶, 4.0 Å; Arg¹⁹¹-Asp²³⁶, 4.8 Å; and Asp²⁴³-Arg¹⁹¹, 3.8 Å) suggest that it is poised to switch into an alternate conformation to pump the sodium ion.

Conserved charged and hydrophilic residues from TMs 5, 6, and 16 [Ser¹⁸⁴, Asp²⁴³, Glu²⁴⁶, Ser²⁴⁷, Asp⁷⁰³, and Lys⁷⁰⁷ (table S3)] form the gate, which consists of an ion triplet (Asp²⁴³-Lys⁷⁰⁷-Glu²⁴⁶) buttressed by hydrogen bonds from Ser¹⁸⁴, Ser²⁴⁷, and Asp⁷⁰³. They abut onto a flat, conserved hydrophobic surface (Ala⁵⁰², Ile⁵⁰³, Ala⁵⁰⁶, Ile⁵⁰⁷) on TM12 (Fig. 3A). Intriguingly, Glu²⁴⁶ is only conserved in the sodium-pumping M-PPases. In the plant, proton-pumping M-PPases, the equivalent negative charge [Gly²⁵⁰ (Glu³⁰¹)] is one turn lower in TM6, so the TmPPase ion triplet becomes an ion pair in VrPPase (Asp²⁹⁴-Lys⁷⁴²). The E250(301)Q (14) mutation uncouples proton-pumping from pyrophosphate hydrolysis (15), suggesting that this residue may be responsible for the proton/sodium selectivity, but making the mutation in a Na^+ -pumping PPase produces an inactive enzyme (15). Below the gate, an exit channel lined by nonconserved polar residues from TM 5, 6, 12, and 16 leads out to the periplasm (Fig. 3B).

How are gate and channel motions coupled to PP_i hydrolysis? In all the structures, the gate is closed. Because the structures map all four intermediates in the catalytic cycle (Fig. 4), we suggest that PP_i binding induces a conformational change that allows Na^+ release, analogous to F_0F_1 -ATP synthase (16). On the basis of the isomorphous tungstate derivative, there appear to be no large changes between the resting en-

zyme and the TmPPase: P_i state (Fig. 4). The conformational changes in the VrPPase:PNP and TmPPase: Mg_4P_i active sites are confined to two major regions: the closing and ordering of the 5-6 loop over the active site (Fig. 3D and fig. S6) and the motions of TM11-12, which bend in toward the active-site cavity (Figs. 1 and 2). Consistent with this, binding substrate makes M-PPases more resistant to proteolysis and *N*-ethyl maleimide modification (fig. S6 and table S4). The largest motions, of about 5 Å, occur at the top of helix 8, which bends in, supporting helix 11 and causing TM12 to slide “down” by about 2 Å (Fig. 3). This breaks the Asp⁶⁹⁶⁽⁷³¹⁾-Lys⁴⁹⁹⁽⁵⁴¹⁾-Asp²³⁶⁽²⁸⁷⁾ salt bridge that links the hydrolytic center to the coupling funnel (Figs. 2 and 3). In the VrPPase structure, Arg¹⁹¹⁽²⁴²⁾ has moved so that it only forms an ion pair with the gate Asp²⁴³⁽²⁹⁴⁾ rather than being placed between that and the hydrolytic center Asp²³⁶⁽²⁸⁷⁾.

Because the changes in the inhibited and product-bound states are similar, with the exit channel closed in both, we suggest that the full conformational change that opens the gate involves a larger downward motion of TM12. The unusual break in TM11 (Fig. 3B and fig. S4) could act as a hinge, so that motion of TM11 would open the gate and the periplasmic channel (Fig. 3C), somewhat analogous to the paddles in potassium channels (17). The coupling funnel thus appears to be poised as a switch that flips

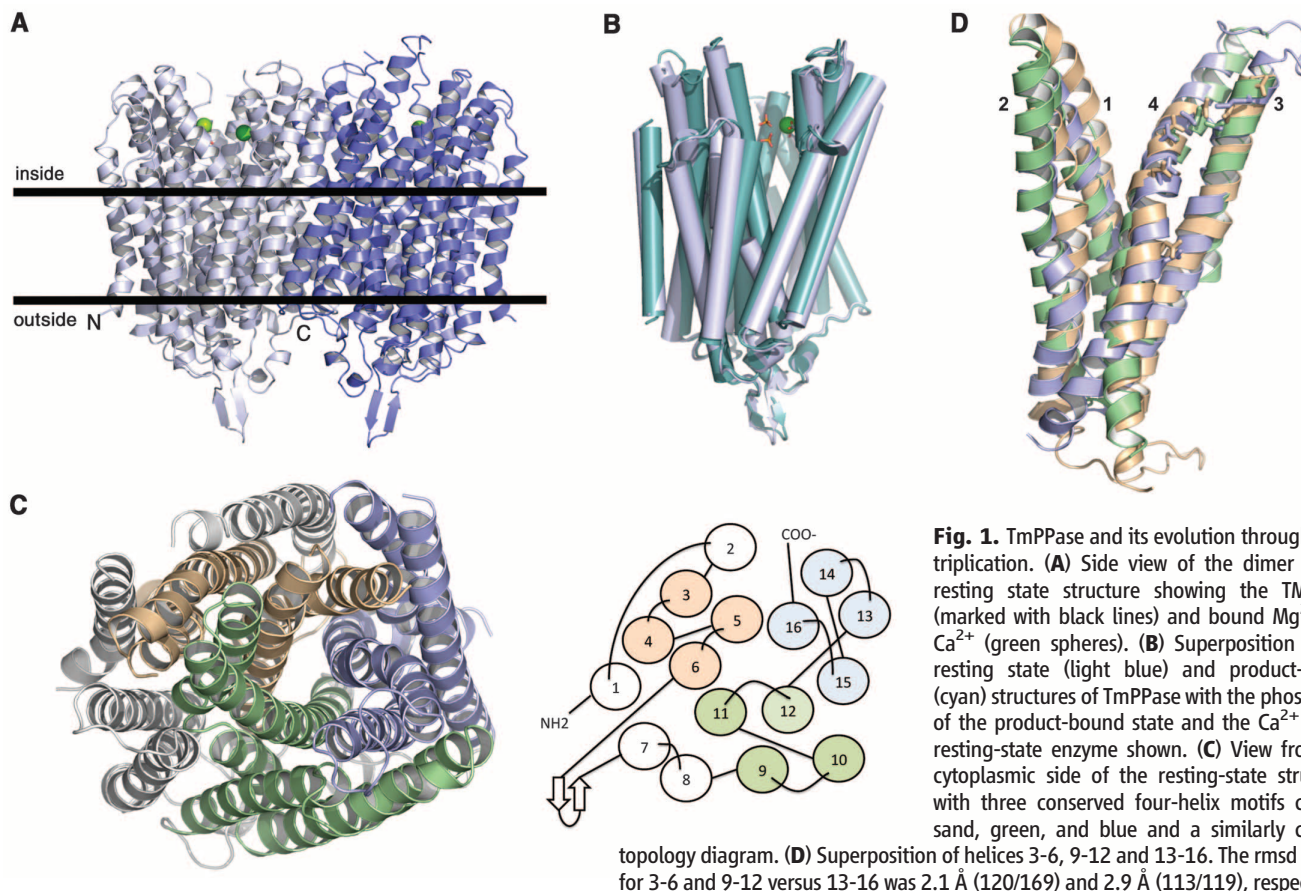


Fig. 1. TmPPase and its evolution through gene triplication. (A) Side view of the dimer of the resting state structure showing the TM area (marked with black lines) and bound Mg^{2+} and Ca^{2+} (green spheres). (B) Superposition of the resting state (light blue) and product-bound (cyan) structures of TmPPase with the phosphates of the product-bound state and the Ca^{2+} of the resting-state enzyme shown. (C) View from the cytoplasmic side of the resting-state structure, with three conserved four-helix motifs colored sand, green, and blue and a similarly colored topology diagram. (D) Superposition of helices 3-6, 9-12 and 13-16. The rmsd per $\text{C}\alpha$ for 3-6 and 9-12 versus 13-16 was 2.1 Å (120/169) and 2.9 Å (113/119), respectively.

between cytoplasmic-open and periplasmic-open states (Fig. 4). Lin and co-workers (11) favor a direct model analogous to bacteriorhodopsin (18). That model, however, does not as easily explain the reversibility of M-PPases (3).

In both models, the conformational change (table S4 and Fig. 3) (19) generates a state with the gate and the periplasmic channel open and the active site closed (Fig. 4). The conformational change presumably eliminates a high-affinity Na^+ -binding site at the top of the gate, leading to transport of the sodium ion to a low-affinity binding site in the exit channel, followed by diffusion into the periplasm. Consistent with this model, there is little conservation of residues below the gate (fig. S3), suggesting that there are no tight ion binding sites. The closed active site would prevent back transfer. Release of the so-

dium ion would allow the gate to close, product to leave, and the protein to revert to its resting state.

Two open questions are the bases of potassium dependence and of sodium selection. Potassium-independent M-PPases contain a Lys at 495 (537) and a Thr at 498 (540) (20), whereas potassium-dependent enzymes like TmPPase have an Ala and a Gly. In the VrPPase:PNP and TmPPase: Mg_4P_i structures, K^+ coordinates the lower phosphate. Modeling the A495(537)K mutation into the TmPPase: P_i structure indicates that Lys⁴⁹⁵⁽⁵³⁷⁾ can easily replace K^+ binding to the lower phosphate (fig. S7). The potassium or lysine thus positions and increases the electrophilicity of the phosphate.

The only difference in residues facing into the active site between TmPPase and VrPPases are Asp⁷⁰³ (Asn⁷³⁷) (not conserved) and Leu²⁴⁰

(Met²⁹¹), and it is unclear how the Leu-Met change could affect cation specificity (fig. S3). We therefore suggest that both Na^+ and H^+ pumps use the same mechanism and binding sites. One possible explanation, consistent with mutation data (15), is that the change from an ion triplet to an ion pair at the gate and the corresponding E250(301)Q change convert a specific Na^+ site at the gate to a proton in an ion pair that can be released to the exit channel by a Grothuss-type mechanism (21).

Overall, our data suggest that pumping is due to a concerted contraction during substrate binding, leading to the movement of TM12 (Fig. 4). This and the VrPPase structure (11) provide the necessary basis for understanding ion specificity and the conformational changes (Figs. 3 and 4) during catalysis and pumping.

Fig. 2. Comparison of the hydrolytic centers of TmPPase and VrPPase. (A) Cutaway view of the active site of the resting-state TmPPase structure showing (top to bottom) hydrolytic center, coupling funnel (light blue), gate, and exit channel (light green). (B) Superposition of the product-bound (cyan) TmPPase structure and inhibitor-bound VrPPase structure (brown) on the resting-state TmPPase structure (light blue) (14). The rmsd/C α are 0.94/542 out of 655 (product:resting) and 1.75/540 out of 695 (VrPPase:resting TmPPase). The lines mark the place of (B) in the (A) structure, and the arrow points to the closure of the active site by the TM5-TM6 loop in the VrPPase structure. Hydrolytic centers of the (C) resting-state TmPPase, (D) substrate-bound VrPPase, (E) product-bound TmPPase, and (F) resting-state TmPPase with the electron density of the tungstate shown.

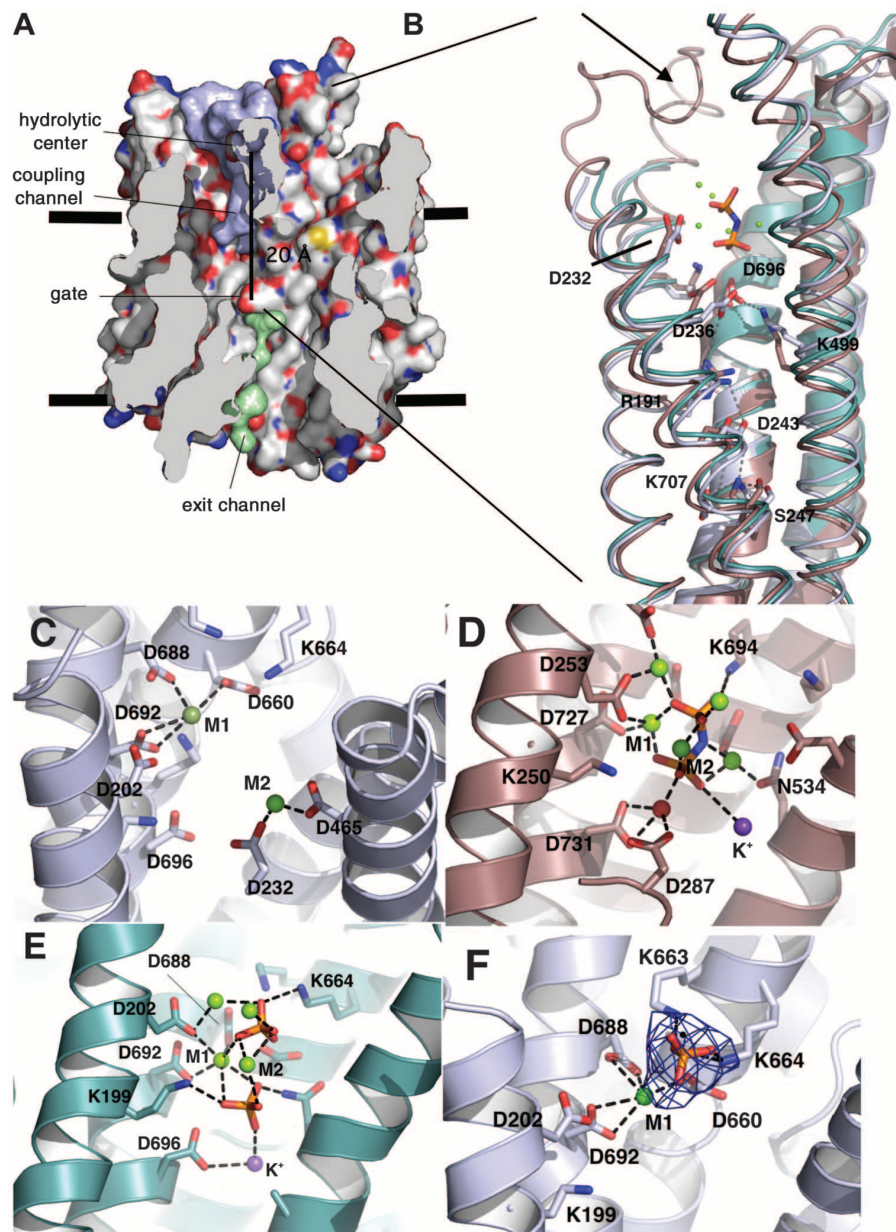


Fig. 3. Structural differences between the catalytic states of M-PPases. Comparison of the coupling funnel and the gate of TmPPase and VrPPase, showing (A) polar residues of the closed exit channel (shown in green) of the resting-state TmPPase and (B) side view of the coupling funnel that connects the hydrolytic center and the gate in TmPPase in the resting state. The Ca^{2+} in M1 is in light green, and the conserved charged coupling residues are shown. Arrow marks the bend in helix 11. (C) Superposition of the coupling funnel and gate of resting-state (light blue) and product-bound (cyan) structures of TmPPase and substrate-bound VrPPase structure (brown). The movement of the helix 12 in the product-bound TmPPase and substrate-bound VrPPase in relation to the resting-state TmPPase is shown with an arrow. Comparison of (D) a cutaway view of the resting state TmPPase structure with the (E) PNP inhibitor complex of VrPPase showing closure of the active site cleft. Movement of helix 12 (labeled h12) is shown for the aligned structures of TmPPase resting-state structure, product complex, and the VrPPase inhibitor complex. Colors are as follows: TmPPase resting state, light blue; TmPPase product complex, cyan; VrPPase inhibitor complex, brown. Key residues are labeled (14).

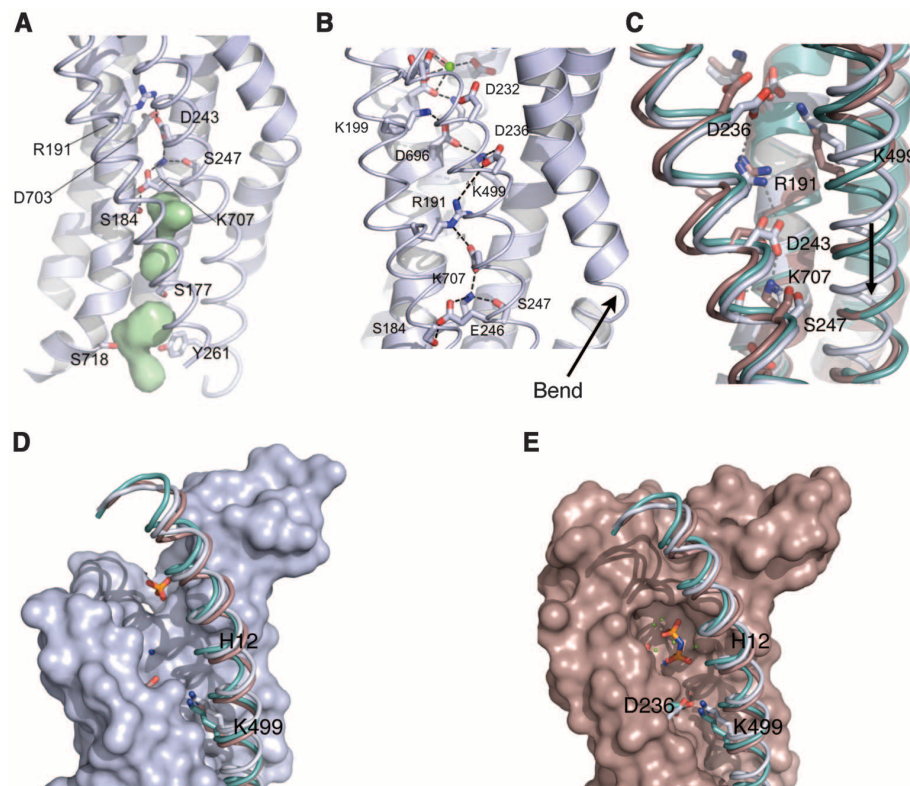
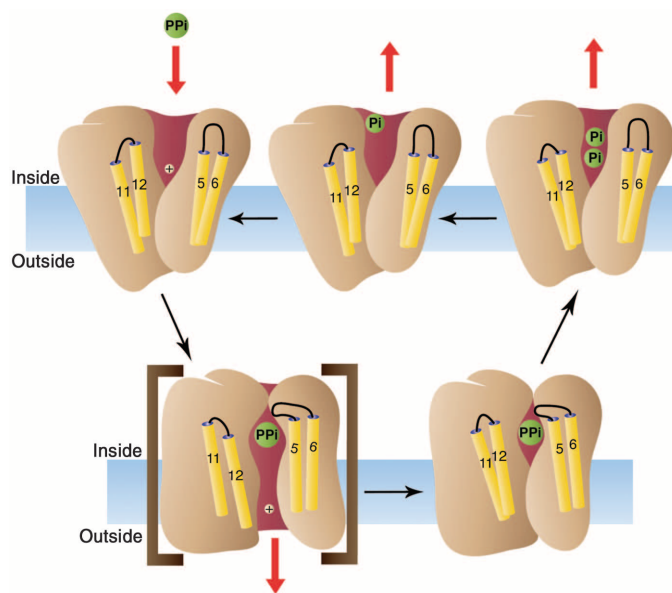


Fig. 4. Proposed binding-change mechanism of M-PPases. Binding of substrate causes the loop between helices 5 and 6 to close the active site. The binding also causes the formation of a transient state where movement of helices 11 and 12 opens the gate and the exit channel, allowing the transport of a cation to the extracellular medium. The active site stays closed until the hydrolysis of the pyrophosphate. After hydrolysis, first the electrophilic and then the leaving-group phosphate dissociate from the enzyme. A similar order for dissociation of phosphate occurs in yeast pyrophosphatase (22).



- G, Gly; H, His; I, Ile; K, Lys; L, Leu; M, Met; N, Asn; P, Pro; Q, Gln; R, Arg; S, Ser; T, Thr; V, Val; W, Trp; and Y, Tyr.
15. H. H. Luoto, G. A. Belogurov, A. A. Baykov, R. Lahti, A. M. Malinen, *J. Biol. Chem.* **286**, 21633 (2011).
 16. D. Stock, C. Gibbons, I. Arechaga, A. G. W. Leslie, J. E. Walker, *Curr. Opin. Struct. Biol.* **10**, 672 (2000).
 17. Y. Jiang, V. Ruta, J. Chen, A. Lee, R. MacKinnon, *Nature* **423**, 42 (2003).
 18. J. K. Lanyi, *Biochim. Biophys. Acta* **1757**, 1012 (2006).
 19. A. M. Malinen, A. A. Baykov, R. Lahti, *Biochemistry* **47**, 13447 (2008).
 20. G. A. Belogurov, R. Lahti, *J. Biol. Chem.* **277**, 49651 (2002).
 21. N. Agmon, *Chem. Phys. Lett.* **244**, 456 (1995).
 22. P. Heikinheimo *et al.*, *Structure* **4**, 1491 (1996).

Acknowledgments: We thank D. Bansfield, K. Rosti, and R. Honkanen for technical assistance; S. Mäki and the Biocenter Finland crystallization unit; A. Serrano (University of Seville) for the generous gift of plasmid pRS1024; I. Braakman (Utrecht University) for the generous gift of *S. cerevisiae* BJ1991; and R. Kolodziejczyk, M. Wikström (University of Helsinki), E. Oksanen (European Spallation Source), and R. Lahti (University of Turku) for fruitful discussions. This work was supported by the European Union Seventh Framework Program EDICT (A.G.), the Sigrid Juselius Foundation (A.G.), the Academy of Finland (A.G. and T.K.), Biocenter Finland (K.K.), and the National Graduate School of Informational and Structural Biology (J.K.). We thank the beamline scientists at ID14-4, ID29, ID23-1 at the European Synchrotron Radiation Facility and at beamline 911-3, Max-Lab. Coordinates and structure factors for the resting state (TmPPase:Ca:Mg) and product complex (TmPPase:P_i:Mg₄) structures have been deposited in the Protein Data Bank with codes 4AV3 and 4AV6, respectively. The authors declare no competing financial interests.

Supplementary Materials
www.sciencemag.org/cgi/content/full/337/6093/473/DC1
 Materials and Methods
 Figs. S1 to S7
 Tables S1 to S4
 References (23–47)

27 March 2012; accepted 7 June 2012
 10.1126/science.1222505

References and Notes

1. H. Mimura, Y. Nakanishi, M. Hirono, M. Maeshima, *J. Biol. Chem.* **279**, 35106 (2004).
2. A. M. Malinen, G. A. Belogurov, A. A. Baykov, R. Lahti, *Biochemistry* **46**, 8872 (2007).
3. M. Maeshima, *Biochim. Biophys. Acta* **1465**, 37 (2000).
4. G. Lemerrier *et al.*, *J. Biol. Chem.* **277**, 37369 (2002).
5. J. Kellösalo, T. Kajander, M. G. Palmgren, R. L. López-Marqués, A. Goldman, *Protein Expr. Purif.* **79**, 25 (2011).
6. A. A. Baykov, V. N. Kasho, N. P. Bakuleva, P. A. Rea, *FEBS Lett.* **350**, 323 (1994).
7. A. A. Baykov, N. P. Bakuleva, P. A. Rea, *Eur. J. Biochem.* **217**, 755 (1993).
8. Materials and methods are available as supplementary materials on Science Online.
9. M. Baltscheffsky, A. Schultz, H. Baltscheffsky, *FEBS Lett.* **457**, 527 (1999).
10. L. Holm, C. Sander, *Trends Biochem. Sci.* **20**, 478 (1995).
11. S. M. Lin *et al.*, *Nature* **484**, 399 (2012).
12. T. Murata, I. Yamato, Y. Kakinuma, A. G. W. Leslie, J. E. Walker, *Science* **308**, 654 (2005); 10.1126/science.1110064.
13. J. Hedlund, R. Cantoni, M. Baltscheffsky, H. Baltscheffsky, B. Persson, *FEBS J.* **273**, 5183 (2006).
14. Single-letter abbreviations for the amino acid residues are as follows: A, Ala; C, Cys; D, Asp; E, Glu; F, Phe;

Human α -Defensin 6 Promotes Mucosal Innate Immunity Through Self-Assembled Peptide Nanonets

Hiutung Chu,¹ Marzena Pazgier,² Grace Jung,³ Sean-Paul Nuccio,¹ Patricia A. Castillo,¹ Maarten F. de Jong,¹ Maria G. Winter,¹ Sebastian E. Winter,¹ Jan Wehkamp,^{1*} Bo Shen,⁴ Nita H. Salzman,⁵ Mark A. Underwood,⁶ Renee M. Tsois,¹ Glenn M. Young,⁷ Wuyuan Lu,^{2†} Robert I. Lehrer,^{3†} Andreas J. Bäuml,^{1†} Charles L. Bevins^{1††}

Defensins are antimicrobial peptides that contribute broadly to innate immunity, including protection of mucosal tissues. Human α -defensin (HD) 6 is highly expressed by secretory Paneth cells of the small intestine. However, in contrast to the other defensins, it lacks appreciable bactericidal activity. Nevertheless, we report here that HD6 affords protection against invasion by enteric bacterial pathogens in vitro and in vivo. After stochastic binding to bacterial surface proteins, HD6 undergoes ordered self-assembly to form fibrils and nanonets that surround and entangle bacteria. This self-assembly mechanism occurs in vivo, requires histidine-27, and is consistent with x-ray crystallography data. These findings support a key role for HD6 in protecting the small intestine against invasion by diverse enteric pathogens and may explain the conservation of HD6 throughout Hominidae evolution.

Paneth cells are specialized small intestinal epithelial cells that maintain intestinal homeostasis, in part by expressing and secreting antimicrobial peptides and proteins (1–3). Human Paneth cells express two peptides, α -defensins HD5 and HD6, deficiencies of which are associated with Crohn's disease, a chronic inflammatory bowel disease (3–5). HD5 is broadly antimicrobial (6–8) and can shape the

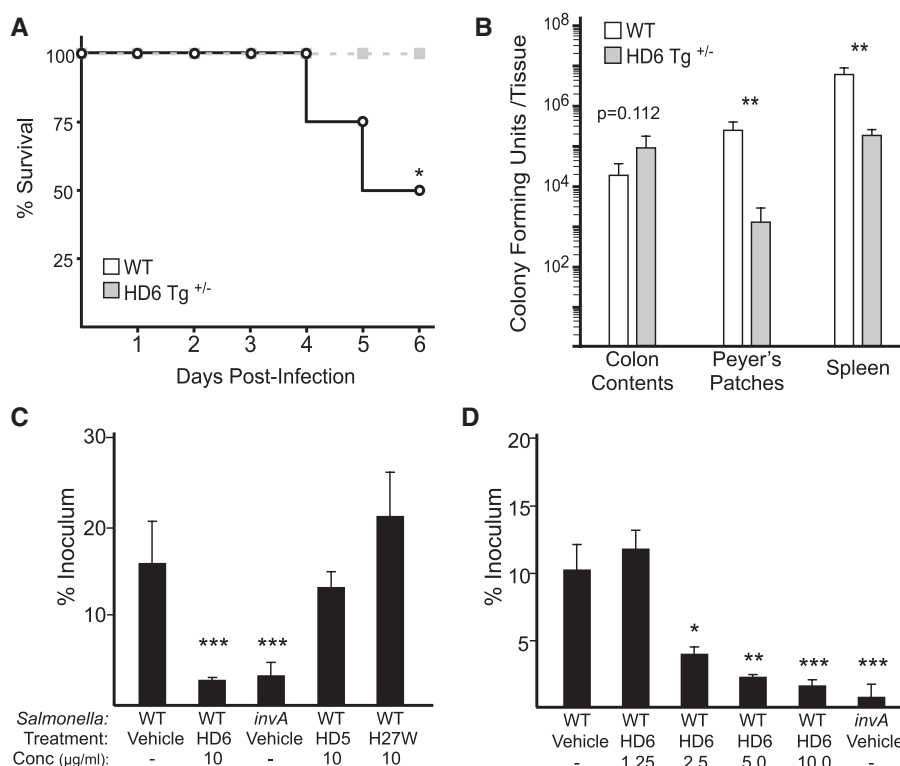
gut microbiota in vivo (9). In contrast, HD6 exerts little antibacterial activity (fig. S1) (8, 10), and its function is unknown.

To investigate HD6, we developed a transgenic mouse model wherein HD6 gene (*DEFA6*) expression was controlled by its endogenous promoter and restricted to Paneth cells (fig. S2, A and B). Transgenic HD6 expression occurred at levels commensurate with endogenous human

and murine Paneth cell α -defensin production and did not alter expression of other murine Paneth cell-derived antimicrobial (poly)peptides (fig. S2, C and D).

When HD6 transgenic mice and littermate controls were challenged intragastrically with 2×10^8 colony forming units (CFU) of *Salmonella* Typhimurium (STM), 50% of wild-type animals but no transgenic mice had died 6 days after infection ($P < 0.05$) (Fig. 1A). Consistent with HD6's lack of direct antibacterial activity, the intestinal lumen of transgenic and wild-type mice contained similar bacterial numbers 4 days after infection. However, STM counts were lower by a factor of 100 in Peyer's patches ($P < 0.001$) and lower by a factor of 10 in spleens ($P < 0.001$) of

Fig. 1. Analysis of in vivo and in vitro invasion by *S. Typhimurium*. (A and B) In vivo challenge of mice with an intragastric inoculum of *S. Typhimurium* (2×10^8 CFU). (A) Kaplan-Meier survival curve of 6-week-old female wild-type ($n = 15$ mice) and HD6^{+/-} transgenic littermates ($n = 9$ mice), with a scheduled experimental endpoint of 6 days. Log-rank test, $*P < 0.05$. The data are representative of three independent experiments. (B) *S. Typhimurium* bacterial load from colon fecal pellets, Peyer's patches (3 per mouse), and spleen tissue of 6-week-old female wild-type ($n = 4$ mice) and HD6^{+/-} transgenic female littermate mice ($n = 6$ mice) 4 days after infection. Error bars, mean \pm SEM. $**P < 0.001$, t test. The data are representative of three independent experiments. (C and D) In vitro invasion assays. (C) *S. Typhimurium* (WT) were pretreated for 1 hour with either 10 μ g/ml of HD5, HD6, or H27W-HD6, or with vehicle alone. Invasion-deficient *S. Typhimurium* (*invA* mutant) were treated with vehicle alone. Bacteria were then allowed to invade the epithelial cells (multiplicity of infection of 10) for 1 hour. Cells were then washed, treated with gentamicin, and then lysed to quantitate intracellular bacteria (expressed as percentage of initial inoculum). Data represent the average of more than nine independent experiments. (D) Concentration dependence of the HD6 activity in assays as described in (C). Error bars, mean \pm SEM. $*P < 0.01$, $**P < 0.001$, $***P < 0.0001$ compared with wild-type vehicle, t test. Data represent the average of three experiments and are representative of more than nine independent experiments.



¹Department of Microbiology and Immunology, School of Medicine, University of California, Davis, CA 95616, USA. ²Institute of Human Virology and Department of Biochemistry and Molecular Biology, University of Maryland School of Medicine, Baltimore, MD 21201, USA. ³Department of Medicine, David Geffen School of Medicine, University of California Los Angeles, Los Angeles, CA 90095, USA. ⁴Department of Gastroenterology and Hepatology, The Cleveland Clinic Foundation, 9500 Euclid Avenue, Cleveland, OH 44195, USA. ⁵Department of Pediatrics, Division of Gastroenterology, Medical College of Wisconsin, Milwaukee, WI 53226, USA. ⁶Department of Pediatrics, School of Medicine, University of California, Davis, CA 95616, USA. ⁷Department of Food Science and Technology, University of California, Davis, CA 95616, USA.

*Present address: Dr. Margarete Fischer-Bosch-Institute of Clinical Pharmacology, 70376 Stuttgart, Germany.

†These authors contributed equally to this work.

††To whom correspondence should be addressed. E-mail: clbevins@ucdavis.edu

HD6 transgenic mice than those found in their wild-type littermates (Fig. 1B). The decreased bacterial burden in these tissues resembled findings in wild-type mice infected with an invasion-deficient STM *invA* mutant (11).

To determine whether HD6 inhibited invasion, intestinal epithelial cells were challenged with α -defensin-treated or untreated STM. The ability of HD6-treated bacteria to invade T84 epithelial cells was impaired in a dose-dependent manner (Fig. 1, C and D). HD6 could reduce invasion by wild-type STM to levels of the minimally invasive *invA* mutant, which lacks a functional invasion-associated type III secretion system (T3SS) (Fig. 1C). Another human intestinal cell line, INT-407, and a mouse small intestinal cell line, MODE-K, exhibited the same pattern of HD6-mediated inhibition of STM invasion (fig. S3). The same concentrations of HD5, the other human

Paneth cell α -defensin (Fig. 1C), or the mouse Paneth cell α -defensins, cryptdins 2 and 3 (fig. S4A), did not inhibit STM invasion. Immunofluorescence microscopy confirmed that HD6 treatment blocked bacterial invasion into intestinal epithelial cells (fig. S5).

No significant difference in STM invasion was observed between untreated and HD6-treated intestinal epithelial cells, suggesting that HD6 does not protect by altering host cells (fig. S4B). The hypothesis that HD6 blocked invasion by interfering with synthesis of T3SS proteins was rejected by findings that STM treated with protective concentrations of HD6 showed normal expression of *flhD* and *fliC* and even induced expression of *hilA* (a key SPI-1 activator) and *invG*, a structural protein of the T3SS-1 system (fig. S6). Also excluded were the possibilities that HD6 reduced invasion by inhibiting bacterial adhesion (fig. S7)

or by altering the intestinal microbiota of the transgenic mice (fig. S8).

To investigate the specificity of HD6, we performed invasion assays with *Yersinia enterocolitica*. This enteropathogenic bacterium invades cells by a different mechanism, involving attachment of its invasin protein (Inv) to host β -integrins (12). Because HD6 reduced *Yersinia* invasion to levels similar to the invasion-deficient Δinv mutant (fig. S9), its ability to prevent bacterial invasion was not pathogen-specific.

Recent studies identified the Trp residue of human neutrophil α -defensin peptide (HNP)-1 as a key functional amino acid (13). Whereas most Hominid α -defensins, including HD5, have a non-polar aromatic residue, Trp, Tyr, or Phe, at the corresponding position, HD6 and its Hominid orthologs contain His (fig. S10). When we replaced His²⁷ of HD6 with Trp, the resulting H27W-HD6

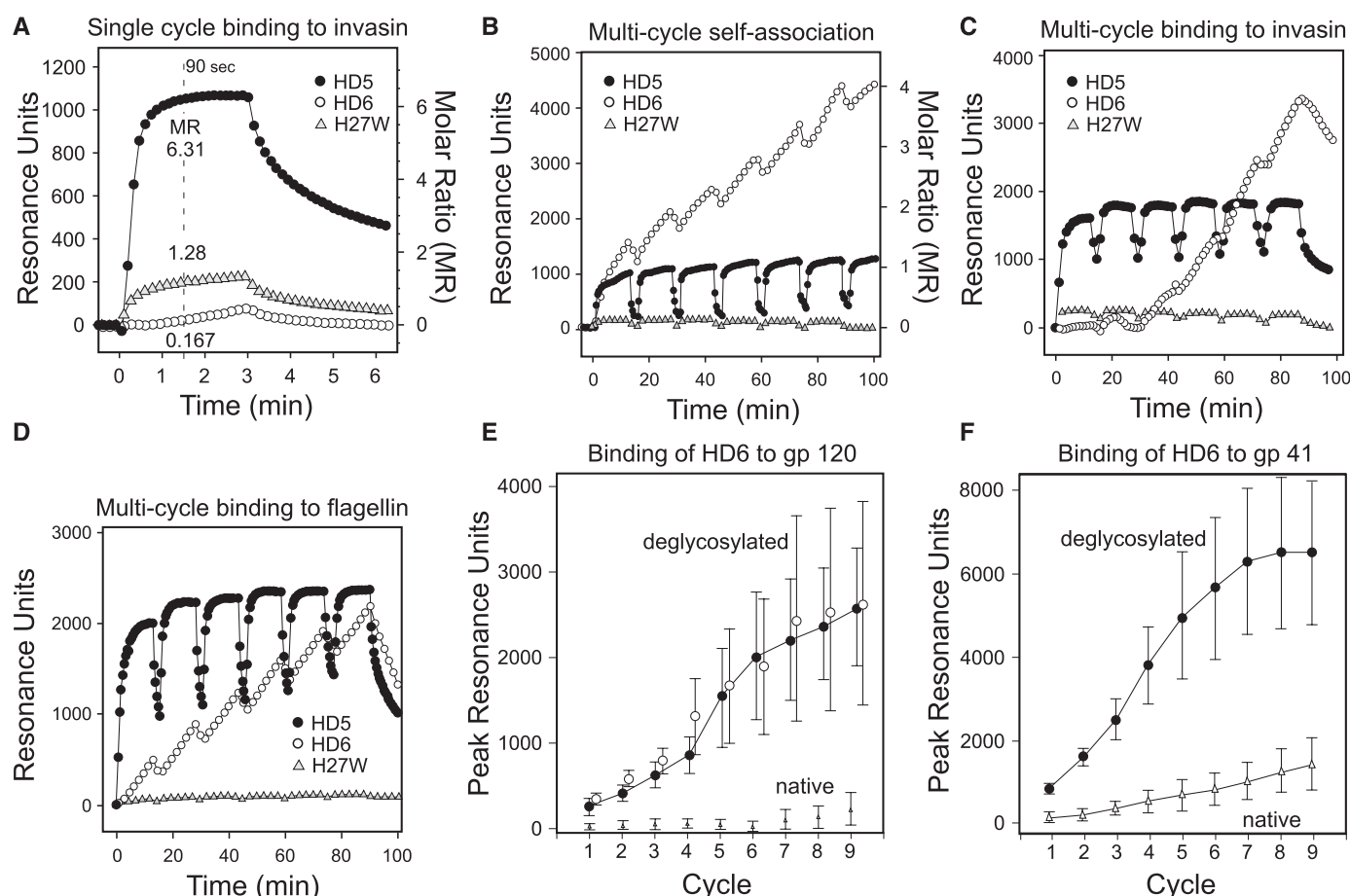


Fig. 2. SPR analysis of binding and self-association. The SPR biosensors presented the following amounts of immobilized ligands (molecule covalently ligated to the biosensor surface), in resonance units (RU): invasin, 2338 RU; HD5, 1158 RU; HD6, 1100 RU; H27W-HD6, 2204 RU; flagellin, 2206 RU; gp120, 8200 RU; gp41, 5600 RU. The defensin peptides were prepared in HEPES-buffered saline buffer [see supplementary materials (10)] and traversed the biosensors at either 50 μ l/min (A) or 25 μ l/min (B to F). Each 15-min cycle in (B) to (F) included a binding period of 12.5 min, followed by a wash period of \sim 2.5 min. Molar ratio (MR) calculations, which took into account the relative masses of the analytes and ligands and the number of RU presented by each biosensor, are described in the supplementary materials.

Shown are representative data from at least three separate experiments. (E) Binding of HD6 to gp120-LAV before (triangles) and after (closed circles) enzymatic deglycosylation of the same biosensor chip. Shown are averaged data from six experiments, with error bars representing mean \pm SEM. $P < 0.002$, Mann-Whitney rank-sum test. Also shown are data from a second set of biosensor chips ($n = 6$ experiments) presenting the same quantity of deglycosylated gp120 (open circles). (F) Binding of HD6 to gp41-LAV before and after enzymatic deglycosylation of the same biosensor chip. Six experiments were done before enzymatic deglycosylation, and six more were done afterwards. Error bars, mean \pm SEM. The differences in each cycle were statistically significant, $P < 0.01$, Mann-Whitney rank-sum test.

failed to block invasion (Fig. 1C and figs. S4 and S9), indicating that His²⁷ was critical for this activity.

Seeking insight into the protective properties of HD6 and the role of His²⁷, we used surface plasmon resonance (SPR) to examine binding to bacterial proteins. HD5 bound rapidly to immobilized *Y. enterocolitica* invasin and reached an equilibrium plateau by 3 min (Fig. 2A). In marked contrast, HD6 binding was less extensive and much slower. Binding of H27W-HD6 was enhanced relative to that of HD6 and, like HD5, the H27W-HD6 binding curve rapidly reached a plateau denoting equal rates of association and dissociation. Because binding of HD6 to invasin was continuing to increase when the conventional 3-min binding period ended, we tested longer binding intervals, eventually adopting a multicycle approach to monitor binding over much longer periods (Fig. 2, B and C). Because other α -defensin molecules self-associate (13–16), we measured the ability of solution-phase HD6 to bind HD6 immobilized on a biosensor. HD6 self-association rose progressively during a six-cycle experiment (Fig. 2B). In contrast, HD5 binding to HD5 reached a molar

ratio close to 1 in each cycle, signifying dimer formation, and then declined to baseline during each intervening “washout” period. Unlike HD6, H27W-HD6 showed minimal ability to self-associate, indicating that His²⁷ was critical to this property. Similarly, H27A-HD6, containing a less bulky Ala substitution, showed kinetics like H27W-HD6 (fig. S11). Therefore, HD6 forms higher-order assemblages with slower kinetics of association and dissociation, whereas HD5 and other α -defensins rapidly (and reversibly) form dimeric complexes.

In a six-cycle binding experiment using immobilized invasin as the target, HD5 oscillated in each binding cycle, rapidly reaching a plateau and then falling by about half during each wash period (Fig. 2C). The oscillations likely represented reversible association and dissociation of solution-phase HD5 to molecules of HD5 that bound the immobilized invasin. H27W-HD6 binding to invasin showed similar cyclic oscillations, reflecting the same phenomenon. In contrast, HD6 binding to invasin rose progressively, with an increase by a factor of 100 from cycle one to cycle six (Fig. 2C). Similar results were observed when *Salmonella* flagellin served to anchor progressive HD6 self-

assembly (Fig. 2D). These data suggested that HD6 molecules bound directly to immobilized proteins, which served as points of origin for progressive assembly of an extended structure composed of HD6 molecules. Importantly, even a low-level binding of HD6 to a target protein created anchoring sites for progressive HD6 self-assembly.

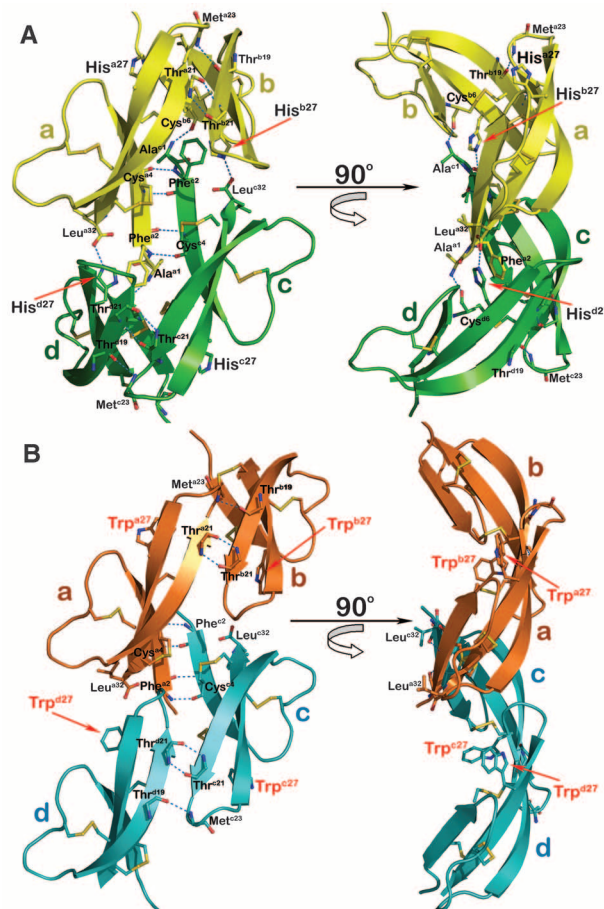
The SPR experiments indicated that HD6 binding to target proteins lacked the specificity typical of high-affinity interactions. To explore this further, we tested HD6 binding to HIV glycoproteins gp41 and gp120. HD6 bound both proteins poorly until they were enzymatically deglycosylated (Fig. 2, E and F). Thus, whereas primary binding of HD6 appears nonspecific with respect to the target protein's sequence, glycosylation can greatly reduce its binding.

Previous crystallographic studies suggested that HD6 can assemble into an elongated, highly ordered helical structure (15), conspicuously different from the dimeric structures formed by HD5 and HNPs (13–16). HD6 monomers associate into dimers (Fig. 3A), but the respective monomers slide apart and form fewer backbone H-bonds between β strands than that for HD5 or the HNPs. This atypical dimer is critically stabilized by dimer-dimer association (Fig. 3A), resulting in a stable tetramer, the repeating unit of the elongated HD6 structure (fig. S12). HD6 tetramerization is mediated by extensive reciprocal interdimer interactions that include electrostatic interactions of the His²⁷ imidazole side chain with the C-terminal carboxyl group of Leu³² (17). The molecular surface buried within the HD6 tetramer (an average value of 760 Å²/monomer) is quite large given the peptide's small size. Comparative structural analyses of HD6 with H27W-HD6 revealed that His²⁷-mediated electrostatic interactions are critical for HD6 tetramer formation (Fig. 3) and higher-order oligomerization (figs. S12 to S14). The H27W substitution eliminates His²⁷-Leu³² interactions important for HD6 dimer-dimer association (Fig. 3B and fig. S14), as further discussed (18).

By scanning electron microscopy (SEM), HD6-treated STM were aggregated (Fig. 4, A to C), and higher magnification revealed a net-like meshwork of fibrils emanating from the bacterial surface that entangled the bacteria and their flagella. These nanonets were again observed in experiments using cleared human small intestinal aspirates (fig. S15). Latex beads coated with a bacterial protein supported formation of similar nanofibrils with wild-type HD6, but not with H27W-HD6, indicating that the structures seen in SEM were not of bacterial origin (Fig. 4D and fig. S16).

HD6 nanonets formed in vivo in a murine ileal loop model (19) wherein HD6 transgenic and littermate wild-type controls received pilocarpine to induce Paneth cell secretion, and ileal loops were inoculated with STM. Abundant nanonet structures that entangled and aggregated STM were observed (Fig. 4, G and H, and fig.

Fig. 3. X-ray crystallography analysis of HD6 and H27W-HD6. (A) The previously described HD6 tetramer formed by four crystallographically independent monomers in the asymmetric unit of crystal (PDB code 1ZMQ) (15). “Canonical” dimers are colored yellow (monomers a and b) and green (monomers c and d); hydrogen bonds are shown as blue dashes. HD6 dimerization is mediated primarily through the hydrogen bonds formed by the backbone atoms of the β 2 strands, involving two reciprocal hydrogen bonds between a pair of Thr²¹ and a single hydrogen bond between Met²³ N and Thr¹⁹ O. Dimer-dimer association is mediated by the backbone atoms of the β 1 strands, forming four H-bonds between Phe² and Cys⁴ of monomers a and c and two between Ala¹ N of monomers a and c and Cys⁶ O of monomers d and b. In addition, the HD6 tetramer is stabilized by electrostatic interactions involving the side chains of two His²⁷ residues (red arrow) and the C-terminal carboxyl groups of two Leu³² residues, among others (fig. S12). The orientation of the imidazole ring of His²⁷ is supported by side-chain stacking interactions with Phe². (B) Equivalent putative tetrameric assembly of four H27W-HD6 monomers from two symmetry-related “canonical” dimers in orange and cyan. The H27W mutation has little impact on the tertiary structure of the mutant defensin (fig. S13) and does not change the interchain backbone H-bonding pattern seen in wild-type HD6. However, what does change is the quaternary structure (fig. S14), where the mutation effectively debilitates HD6 molecules to assemble into high-order oligomers.



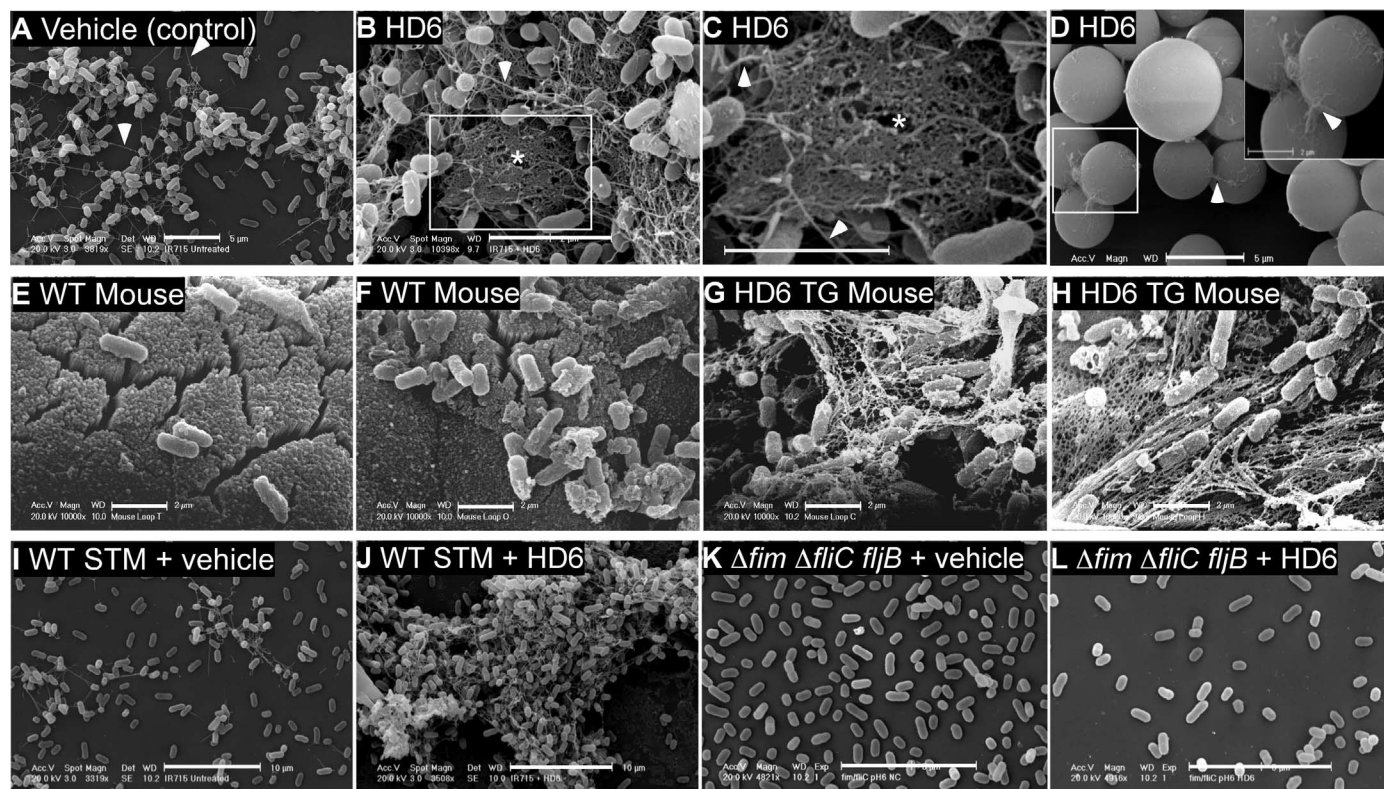


Fig. 4. HD6 nanonets entrap *S. Typhimurium* in vitro and in vivo. (A to D) SEM of in vitro nanonet formation. Wild-type *S. Typhimurium* incubated with vehicle (A) or HD6 (10 $\mu\text{g}/\text{ml}$) [(B) and (C)] in Tris-maleate buffer, as described in the supplementary materials. Scale bar, 5 μm . Magnification 5000X (B) and 10,000X (C). The white rectangle (B) and the asterisks [(B) and (C)] highlight a prominent nanonet. The longer and wider structures are flagellae (white arrowheads), many of which are entangled with other cobweb-like nanonets, but are not evident with $\Delta\text{fliC fljB}$ (fig. S16). SEM of protein A-coated polystyrene beads (D) incubated with HD6 (1 $\mu\text{g}/\text{ml}$) for 5 min at room temperature in 50 mM Tris-maleate buffer. The beads were then washed, fixed, and processed

for SEM. Data are representative of six independent experiments. (E to H) SEM of wild-type [(E) and (F)] and HD6 transgenic [(G) and (H)] mouse ileal loop directly inoculated with *S. Typhimurium*. Scale bar, 2 μm . In a double-blind data acquisition and scoring evaluation, three individuals scored 12 of 12 such images correctly for mouse genotype. $P < 0.001$, Fisher's exact test. See supplementary materials for details. Data are representative of two independent experiments. (I to L) SEM of wild-type *S. Typhimurium* [(I) and (J)] and $\Delta\text{fim } \Delta\text{fliC fljB}$ [(K) and (L)] treated with vehicle alone [(I) and (K)] or 10 $\mu\text{g}/\text{ml}$ HD6 [(J) and (L)]. Scale bar, 10 μm . See supplementary materials for details. Data are representative of three independent experiments.

S17). In contrast, no nanonets were observed in wild-type mouse ileal loops (Fig. 4, E and F, and fig. S17). Thus, HD6 can form small intestinal nanonets that entangled STM in vivo.

Because HD6 lacks lectin-like activity (20), it seemed unlikely to target carbohydrates on the bacterial surface. We therefore directed our attention to the predominant proteinaceous surface appendages of STM, their flagella and type I fimbriae (21). Compared with intact wild-type bacteria, we observed a decreased aggregation by HD6 of STM mutants lacking type I fimbriae or flagella (fig. S18). Neither nanofibrils nor nanonets nor aggregation were evident in an HD6-treated *Salmonella* mutant lacking both fimbriae and flagella (Fig. 4, I to L), suggesting that appendages can function as HD6 anchoring points that trigger HD6 nanonet formation.

Together, these data support a model wherein secreted HD6 molecules bind stochastically (i.e., randomly and at low levels) to any of the various proteinaceous bacterial surface molecules they encounter. These initially bound HD6 molecules provide a nidus that triggers a dynamic and deterministic process of self-assembly, build-

ing nanonets that can aggregate bacteria and/or impede the close physical contact with epithelial cells required for attachment or invasion. Highly expressed in Paneth cells at the base of small intestinal crypts, secreted HD6 will accumulate in the crypt and pericellular space beneath the mucus layer. Host proteins in this location are heavily glycosylated, leaving microbial intruders as the prime targets for HD6 binding.

Any microbial intruder that enters the small intestinal crypt, be it bacterial, fungal or protozoan, is a potential threat, especially because the stem cells that continually renew the intestinal epithelium reside at the crypt base (3). An intruder in this location would encounter HD6 and provide anchorage for the initial, low-level binding of this peptide. Because this binding is not target-sequence specific, HD6 can be effective against diverse threats. Because HD6 concentrations in the crypt are orders of magnitude higher than the highest concentrations (10 $\mu\text{g}/\text{ml}$) used in our experiments (22, 23), fibril and nanonet formation around such intruding microbes should be faster and in greater abundance than those described above. Because mouse Paneth cells lack an

ortholog of HD6 (24), the transgenic mice benefit from expression of this human peptide. On the other hand, it is noteworthy that individuals with Crohn's disease characteristically have an accumulation of invasive bacteria at the epithelial surface of their small intestine (5). A predisposition to this inflammatory bowel disease may, in part, be a result of a deficiency of HD6, as supported by the decreased expression of both HD5 and HD6 observed in Crohn's disease of the ileum (4). Although the present experiments dealt primarily with two model Gram-negative bacteria, the general mechanism that emerged could also apply to many other bacteria, as well as to fungi and some protozoan parasites.

References and Notes

1. R. I. Lehrer, C. L. Bevins, T. Ganz, in *Mucosal Immunology*, J. Mestecky et al., Eds. (Academic Press, New York, ed. 3, 2004), vol. 1, pp. 95–110.
2. A. J. Ouellette, *Curr. Opin. Gastroenterol.* **26**, 547 (2010).
3. C. L. Bevins, N. H. Salzman, *Nat. Rev. Microbiol.* **9**, 356 (2011).
4. J. Wehkamp et al., *Proc. Natl. Acad. Sci. U.S.A.* **102**, 18129 (2005).
5. J. Wehkamp, E. F. Stange, *J. Crohns Colitis* **4**, 523 (2010).

6. E. M. Porter, E. van Dam, E. V. Valore, T. Ganz, *Infect. Immun.* **65**, 2396 (1997).
7. N. H. Salzman, D. Ghosh, K. M. Huttner, Y. Paterson, C. L. Bevins, *Nature* **422**, 522 (2003).
8. B. Ericksen, Z. Wu, W. Lu, R. I. Lehrer, *Antimicrob. Agents Chemother.* **49**, 269 (2005).
9. N. H. Salzman et al., *Nat. Immunol.* **11**, 76 (2010).
10. See supplementary materials on Science Online.
11. A. J. Bäuml, R. M. Tsois, P. J. Valentine, T. A. Ficht, F. Heffron, *Infect. Immun.* **65**, 2254 (1997).
12. P. Cossart, P. J. Sansonetti, *Science* **304**, 242 (2004).
13. G. Wei et al., *J. Biol. Chem.* **285**, 16275 (2010).
14. C. P. Hill, J. Yee, M. E. Selsted, D. Eisenberg, *Science* **251**, 1481 (1991).
15. A. Szyk et al., *Protein Sci.* **15**, 2749 (2006).
16. G. Wei et al., *J. Biol. Chem.* **284**, 29180 (2009).
17. More precisely, the imidazole side chain of His²⁷ of both monomer b and d interacts with the C-terminal carboxyl group of Leu³² in monomers c and a, respectively, and two backbone-backbone H-bonds form between Ala¹ N of monomers a and c and Cys⁶ O of monomers d and b (Fig. 3A and fig. S12).
18. Furthermore, H27W-HD6 does not form the two reciprocal main-chain H-bonds donated by Ala¹ of one dimer to Cys⁶ of the other. Consequently, monomers b and d of H27W-HD6 "spring loose" from monomers a and c, and the resultant mutant tetramer becomes vertically more extended and laterally more flattened than that of wild-type HD6 (Fig. 3B). The extended and flattened H27W tetramer is less stable than its "twisted" wild-type counterpart because of reduced hydrophobic packing and the lost interdimer interactions (fig. S14). Overall, the crystal structures of both defensins suggest that His²⁷ plays an important role in stabilizing HD6 tetramer stabilization and likely contributes to an elongated high-order assembly of HD6 molecules by accentuating a propagating twist within and beyond the tetramer structure. The assembled HD6 structure shown is bowed when viewed from one perspective and linear when rotated by 90° (fig. S12). This bowing, along with coalescence of fibrils extending from different anchoring points on the bacterial surface, might account for the branching and netlike formation evident in the scanning electron micrographs that appear in the figures.
19. K. Brandl, G. Plitas, B. Schnabl, R. P. DeMatteo, E. G. Pamer, *J. Exp. Med.* **204**, 1891 (2007).
20. R. I. Lehrer et al., *J. Immunol.* **183**, 480 (2009).
21. H. L. Andrews-Polymeris, A. J. Bäuml, B. A. McCormick, F. C. Fang, *Infect. Immun.* **78**, 2356 (2010).
22. T. Ayabe et al., *Nat. Immunol.* **1**, 113 (2000).
23. D. Ghosh et al., *Nat. Immunol.* **3**, 583 (2002).
24. M. T. Shanahan, H. Tanabe, A. J. Ouellette, *Infect. Immun.* **79**, 459 (2011).

Acknowledgments: The authors thank W. Yuan for expert assistance in synthesizing the defensin peptides and R. W. Feathers and H. K. Rho for technical help related to transgenic mice. We thank G. Adamson, P. E. Kysar, and E. Lee from Electron Microscopy Laboratory, Department of Pathology and Laboratory Medicine, School of Medicine,

University of California at Davis. We gratefully acknowledge A. J. Ouellette for help with HD6 antibody production. We are indebted to A. C. Gelli and S. C. Dawson for expert guidance in exploring possible biological activities of HD6 and to S. J. Howell for initial investigations of this peptide. Finally, we appreciate the many suggestions from colleagues and members of our laboratories that helped us unravel the properties of HD6 described here. This work was supported by grants from the National Institutes of Health: AI032738 (C.L.B.), AI050843 (C.L.B.), HD059127 (M.A.U. and C.L.B.), AI076246 (A.J.B. and C.L.B.), AI040124 (A.J.B.), AI044170 (A.J.B.), AI073120 (A.J.B.), AI088122 (A.J.B.), AI072732 (W.L.), AI070726 (R.I.L.), AI082320 (R.M.T.), AI057757 (N.H.S.), and T32AI060555 (H.C. and S.P.N.) and a fellowship from the Robert Bosch Foundation (J.W.). The authors declare no competing interests. The data described in this manuscript are tabulated in the main paper and in the supplementary materials. The structure factor files and coordinates for H27W-HD6 are deposited in the Protein Data Bank under accession code 3QTE.

Supplementary Materials

www.sciencemag.org/cgi/content/full/science.1218831/DC1
Materials and Methods
Figs. S1 to S18
Tables S1 and S2
References (25–34)

6 January 2012; accepted 7 June 2012
Published online 21 June 2012;
10.1126/science.1218831

dSarm/Sarm1 Is Required for Activation of an Injury-Induced Axon Death Pathway

Jeannette M. Osterloh,¹ Jing Yang,² Timothy M. Rooney,¹ A. Nicole Fox,¹ Robert Adalbert,⁴ Eric H. Powell,³ Amy E. Sheehan,¹ Michelle A. Avery,¹ Rachel Hackett,^{1*} Mary A. Logan,^{1†} Jennifer M. MacDonald,¹ Jennifer S. Ziegenfuss,¹ Stefan Milde,⁴ Ying-Ju Hou,⁵ Carl Nathan,⁵ Aihao Ding,⁵ Robert H. Brown Jr.,⁶ Laura Conforti,⁷ Michael Coleman,⁴ Marc Tessier-Lavigne,² Stephan Züchner,³ Marc R. Freeman^{1*‡}

Axonal and synaptic degeneration is a hallmark of peripheral neuropathy, brain injury, and neurodegenerative disease. Axonal degeneration has been proposed to be mediated by an active autodestruction program, akin to apoptotic cell death; however, loss-of-function mutations capable of potentially blocking axon self-destruction have not been described. Here, we show that loss of the *Drosophila* Toll receptor adaptor dSarm (sterile α /Armadillo/Toll-interleukin receptor homology domain protein) cell-autonomously suppresses Wallerian degeneration for weeks after axotomy. Severed mouse *Sarm1* null axons exhibit remarkable long-term survival both in vivo and in vitro, indicating that *Sarm1* prodegenerative signaling is conserved in mammals. Our results provide direct evidence that axons actively promote their own destruction after injury and identify dSarm/Sarm1 as a member of an ancient axon death signaling pathway.

When axons are severed, the portion of the axon distal to the injury site undergoes extensive fragmentation. This process, termed Wallerian degeneration, was traditionally thought to result from passive wasting away of axons due to a lack of cell body-derived nutrients (*1*). However, this notion was challenged by the *slow Wallerian degeneration* (*Wld^S*) mutant mouse in which the distal portion of severed axons remained morphologically intact for weeks after axotomy (*2, 3*). The long-term survival of severed *Wld^S* axons raised the intriguing possibility that Wallerian degeneration might be driven by an active molecular program akin to apoptotic cell death (*4, 5*). However, the *Wld^S*

phenotype results from a gain of function, likely neomorphic mutation that leads to neuronal overexpression of a chimeric fusion protein containing the nicotinamide adenine dinucleotide (NAD⁺) biosynthetic enzyme Nmnat1 (*6, 7*). Despite its ability to inhibit axonal degeneration, the gain-of-function nature of the *Wld^S* phenotype does not provide direct evidence supporting the existence of an axon death signaling pathway and may be unrelated to normal Nmnat1 function. Importantly, mutants reported to suppress Wallerian degeneration, such as *wnd/DLK*, delay the clearance of degenerating axons in *Drosophila* for only ~1 to 2 days, and mouse axons for several hours (*8*). This is quite weak sup-

pression when compared with *Wld^S*. Thus, the existence of axon death pathways in Wallerian degeneration has remained largely speculative.

Wallerian degeneration appears to be molecularly distinct from apoptosis, because potent genetic or chemical inhibitors of cell death do not block axonal disintegration (*9–11*). We revisited this question and performed a comprehensive screen of existing mutants and dominant negative constructs for *Drosophila* genes affecting apoptosis, autophagy, or other defined cell degradative pathways, but these failed to suppress Wallerian degeneration (table S1).

If Wallerian degeneration is indeed an active process, then loss-of-function mutants that exhibit *Wld^S*-like protection of severed axons should exist. We therefore performed an F₂ forward genetic screen in *Drosophila* for mutants that exhibited long-term survival of severed axons (fig. S1). Because genes required for Wallerian degeneration may be lethal when mutated, we

¹Department of Neurobiology, University of Massachusetts Medical School, Worcester, MA 01605, USA. ²Laboratory of Brain Development and Repair, The Rockefeller University, New York, NY 10065, USA. ³John P. Hussman Institute for Human Genomics, Dr. John T. Macdonald Foundation Department of Human Genetics, University of Miami Miller School of Medicine, Miami, FL 33136, USA. ⁴Babraham Institute, Cambridge CB22 3AT, UK. ⁵Department of Microbiology and Immunology, Weill Medical College of Cornell University, New York, NY 10021, USA. ⁶Department of Neurology, University of Massachusetts Medical School, Worcester, MA 01605, USA. ⁷School of Biomedical Sciences, University of Nottingham Medical School Queen's Medical Centre, Nottingham, NG7 2UH, UK.

*Howard Hughes Medical Institute, Chevy Chase, MD 20815–6789, USA.

†Present address: Jungers Center for Neurosciences Research, Department of Neurology, Oregon Health & Science University, Portland, OR 97239, USA.

‡To whom correspondence should be addressed. E-mail: marc.freeman@umassmed.edu

designed our screen to allow for characterization of both viable and lethal mutants through mosaic analysis with a repressible cell marker (MARCM) clonal analysis (12). In control animals, severed olfactory receptor neuron (ORN) axons degenerated and were completely cleared from the antennal lobe 7 days after axotomy. We identified three lines, *l(3)896*, *l(3)4621*, and *l(3)4705*, in which severed homozygous mutant axons generated by MARCM remained intact 1 week after axotomy (Fig. 1A). Although the number of uninjured axons is slightly reduced in each mutant, 100% of green fluorescent protein (GFP)-labeled axons exhibited long-term preservation after injury (table S2). Mutant axons remained fully intact 30 days after injury (Fig. 1B), and a significant but reduced number remained even 50 days after injury (Fig. 1C). *l(3)896*, *l(3)4621*, and *l(3)4705* therefore provide axonal preservation that rivals that of *Wld^S* in *Drosophila*, and lasts throughout the life span of the fly. Neuroprotection in these mutants extended to synapses: Synaptobrevin punctae localized to synaptic terminals even 30 days after axotomy (fig. S2, D and E). Neuronal morphology appeared normal in mutant animals (Fig. 1 and fig. S2B), indicating that these mutations do not grossly affect neuronal development.

We next asked whether *l(3)896* was broadly required for neuron pruning or apoptotic cell death. We examined dendritic and axonal pruning in MARCM clones in *Drosophila* mushroom

body γ neurons during metamorphosis (13). In both control and *l(3)896* animals, mushroom body γ neuron axons and dendrites were pruned normally (Fig. 1D). During early embryogenesis, dMP2 neurons are present in each segment, but by late embryogenesis, all but the posterior three pairs undergo developmentally programmed apoptosis (14). We found that dMP2 neurons were generated normally in *l(3)4621* animals, and the appropriate subset of neurons underwent apoptosis (Fig. 1E). Finally, we expressed the proapoptotic gene *hid* in the *Drosophila* visual system (15) to induce widespread apoptotic death in cells of the developing eye disc. We found that *l(3)896* mutant clones failed to suppress activation of cell death (Fig. 1F).

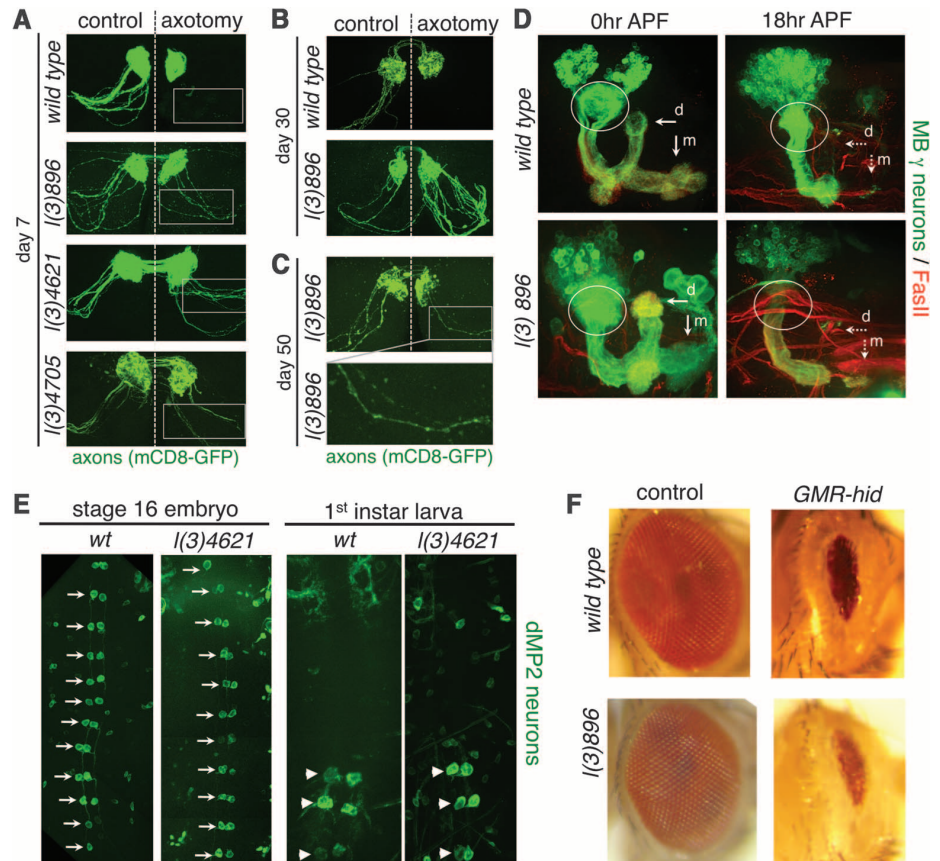
These mutants were all recessive (fig. S2A) in axon degenerative phenotypes and fell into a single lethal complementation group; therefore, each line represented an independently isolated lethal mutation in the same gene. To identify the gene mutated in *l(3)896*, *l(3)4621*, and *l(3)4705*, we took two complementary approaches. First, we mapped the lethality of each mutant using small chromosome deficiencies and identified a single gene at cytogenetic region 66B (Fig. 2A). We also used next-generation sequencing technology to resequence mutant genomes to a read depth of 70x (table S3). We identified a single gene affected in all three mutants, which resided in cytogenetic region 66B: *ect4*, which we refer to as *dsarm* (*Drosophila* sterile alpha and

Armadillo motif). The *dsarm* gene encodes a protein with an Armadillo/HEAT (ARM) domain, two sterile alpha motifs (SAM), and a Toll/interleukin-1 receptor homology (TIR) domain. Each identified *dsarm* allele contained a unique premature stop codon in *dsarm* open reading frame (Fig. 2B and table S4). From these data we conclude that *l(3)896*, *l(3)4621*, and *l(3)4705* are loss-of-function alleles of *dsarm*. Consistent with this interpretation, expression of full-length *dsarm* cDNA using the postmitotic *OR22a-Gal4* driver in *l(3)896* mutant clones was sufficient to fully revert the suppression of axonal degeneration observed in *dsarm* mutants (Fig. 2C). In addition, we rescued both the lethality and suppression of Wallerian degeneration phenotypes of *l(3)896/l(3)4621* and *l(3)896/Df(3L)BSC795* trans-heterozygous animals with a BAC clone containing the *dsarm* gene (fig. S2C). Together, these data indicate that dSarm function is necessary in postmitotic neurons to drive axonal destruction after axotomy.

Based on RNA in situ hybridizations to embryos, larval brains, and adult brains, reverse transcription polymerase chain reaction from dissected neural tissues, and analysis of a *dsarm-Gal4* driver line, *dsarm* is widely expressed in the *Drosophila* nervous system (fig. S3, A to E). These data raise the possibility that dSarm may be broadly required to promote Wallerian degeneration in the nervous system.

We next assayed Wallerian degeneration in null mutants for the mouse ortholog of *dsarm*,

Fig. 1. Identification of mutations that suppress Wallerian degeneration. (A) ORN MARCM clones in control, *l(3)896*, *l(3)4621*, and *l(3)4705*. Right, axotomy; left, uninjured control. $n \geq 15$ brains. (B) Control and *l(3)896* brains 30 days after injury. $n \geq 10$ brains. (C) *l(3)896* clones 50 days after injury. $n = 11$ brains. (D) MARCM clones in mushroom body (MB) γ neurons in control and *l(3)896* backgrounds at the indicated developmental stages. dorsal (d) and medial (m) axonal branches (arrows), and dendrites (circled). $n \geq 15$ brains for all. (E) dMP2 neurons with GFP. Ventral views (anterior up) of stage 16 embryos (left) and first-instar larvae. dMP2 neurons before (arrows) and after (arrowheads) segment-specific apoptosis. $n \geq 20$ flies at each time point. (F) Wild-type and *l(3)896* mutant clones with (right) or without (left) ectopic expression of *hid*. $n \geq 20$ flies.



Sarm1. We grew 5-day cultures of superior cervical ganglia (SCG) from wild-type, *Sarm1*^{-/-} (16) and *Wld^S* mice, severed axons, and scored axonal integrity over the next week. *Sarm1*^{-/-} SCG explants exhibited robust protection from degeneration up to 72 hours after axotomy, similar to what is observed with *Wld^S* SCG neurons, whereas wild-type axons degenerated within 8 hours (Fig. 3, A and B). This robust protection was also seen in cultured *Sarm1*^{-/-} cortical neuron axons (Fig. 3, C and D, and fig. S5C) and dorsal root ganglia (DRG) (Fig. 3, E and F, and fig. S5D). Notably, *Sarm1*^{-/-} DRG explants were not protected from nerve growth factor (NGF)

deprivation (fig. S5, A and B), a model for developmental axon pruning (4, 13, 17, 18), suggesting that *Sarm1* protection is specific to injury-induced axon degeneration.

To determine whether *Sarm1* is required for Wallerian degeneration in vivo, we performed sciatic nerve lesions of the right hind limb of *Sarm1*^{-/-} mice and controls. Whereas *Sarm1*^{+/-} controls exhibited a dramatic breakdown of the axon and myelin sheath within 3 days of injury, 61.2% of lesioned *Sarm1*^{-/-} axons were protected from degeneration at least 14 days after injury ($P = 0.002$) (Fig. 4A). Ultrastructural analysis revealed a remarkable preservation of the

Schwann cell and myelin sheath, axonal neurofilaments, and axonal mitochondria at this time point (Fig. 4B and fig. S4). Western blots of sciatic nerve with antibodies to neurofilament-M (NF-M), α -Internexin, and β -tubulin class III (TUJI) confirmed that the axonal cytoskeleton was robustly preserved in severed *Sarm1*^{-/-} axons (Fig. 4D). We further note preservation of the NF-M signal by immunofluorescent staining nerves in *Sarm1*^{-/-} mutants (fig. S6, A and E).

Synaptic integrity was scored by colocalization of presynaptic marker (NF-M/synaptophysin) with the postsynaptic acetylcholine receptor (AChR) in tibialis anterior muscles after sciatic

Fig. 2. Mutations in *dsarm* block Wallerian degeneration. (A) The lethality of *l(3)896*, *l(3)4621*, and *l(3)4705* was mapped to region 66B using Exel or Bloomington Stock Center deficiencies. (B) *Dsarm* protein domains, positions, and effect of predicted point mutations. (C) *UAS-dsarm* in *l(3)896* mutant clones or *dsarm*⁺ bacterial artificial chromosome rescue axonal degeneration defects in *l(3)896/l(3)4621* flies. $n = 12$ flies.

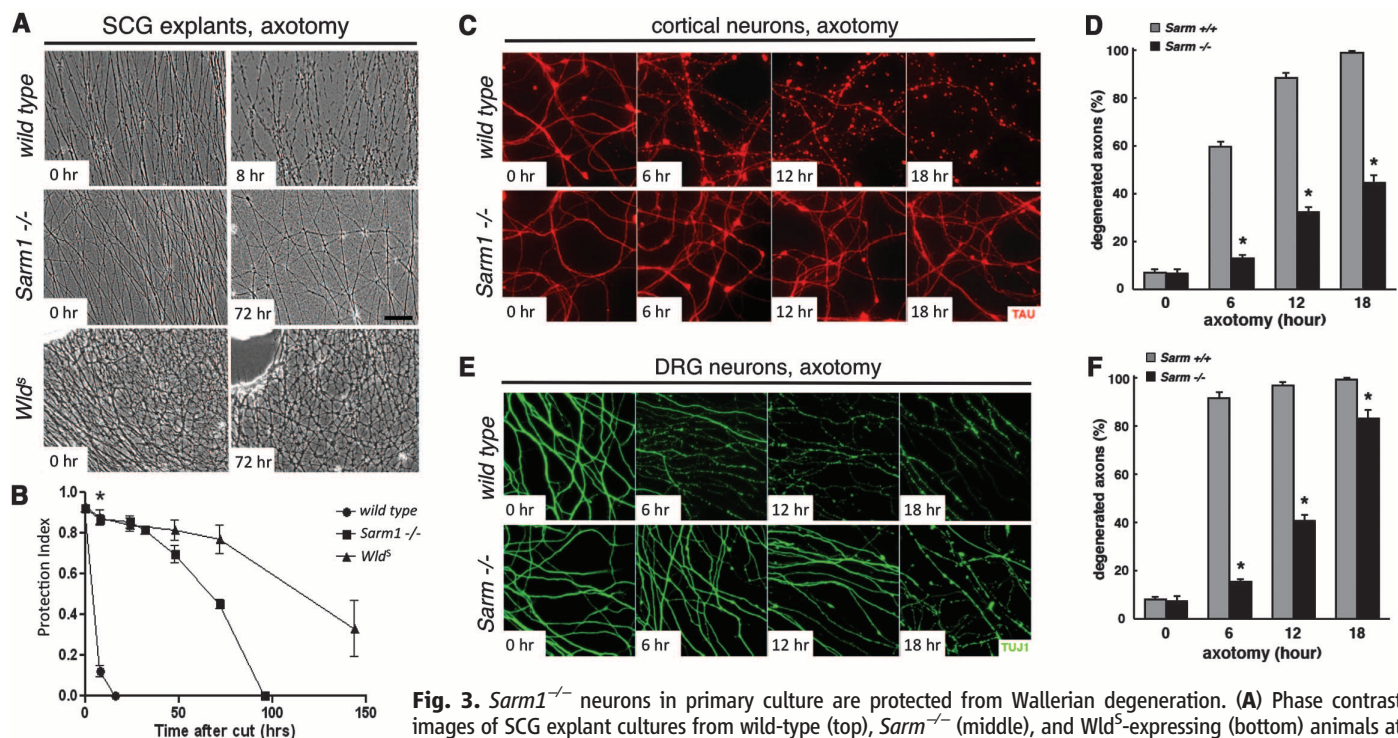
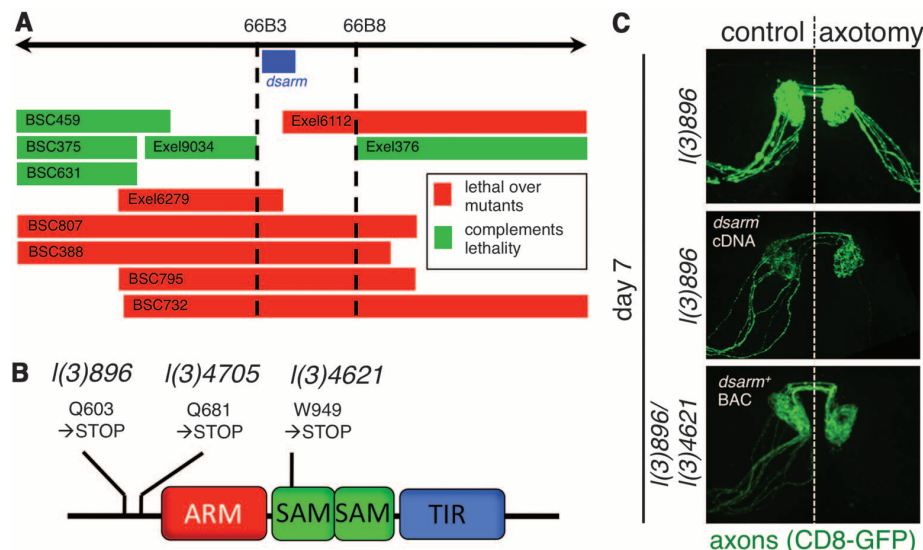


Fig. 3. *Sarm1*^{-/-} neurons in primary culture are protected from Wallerian degeneration. (A) Phase contrast images of SCG explant cultures from wild-type (top), *Sarm1*^{-/-} (middle), and *Wld^S*-expressing (bottom) animals at the indicated time after axotomy. (B) Quantification from (A). Mean \pm SEM, $*P < 0.01$. (C) Axon preservation at the indicated time points in cortical neuron cultures from E16.5 mouse embryos. α -Tau, red. (D) Quantification from (C). Mean \pm SEM, $*P < 0.01$. (E) Axon preservation at the indicated time points in DRG cultures from E13.5 mouse embryos. α -TUJI, green. (F) Quantification from (E). Mean \pm SEM, $*P < 0.01$.

the indicated time points in cortical neuron cultures from E16.5 mouse embryos. α -Tau, red. (D) Quantification from (C). Mean \pm SEM, $*P < 0.01$. (E) Axon preservation at the indicated time points in DRG cultures from E13.5 mouse embryos. α -TUJI, green. (F) Quantification from (E). Mean \pm SEM, $*P < 0.01$.

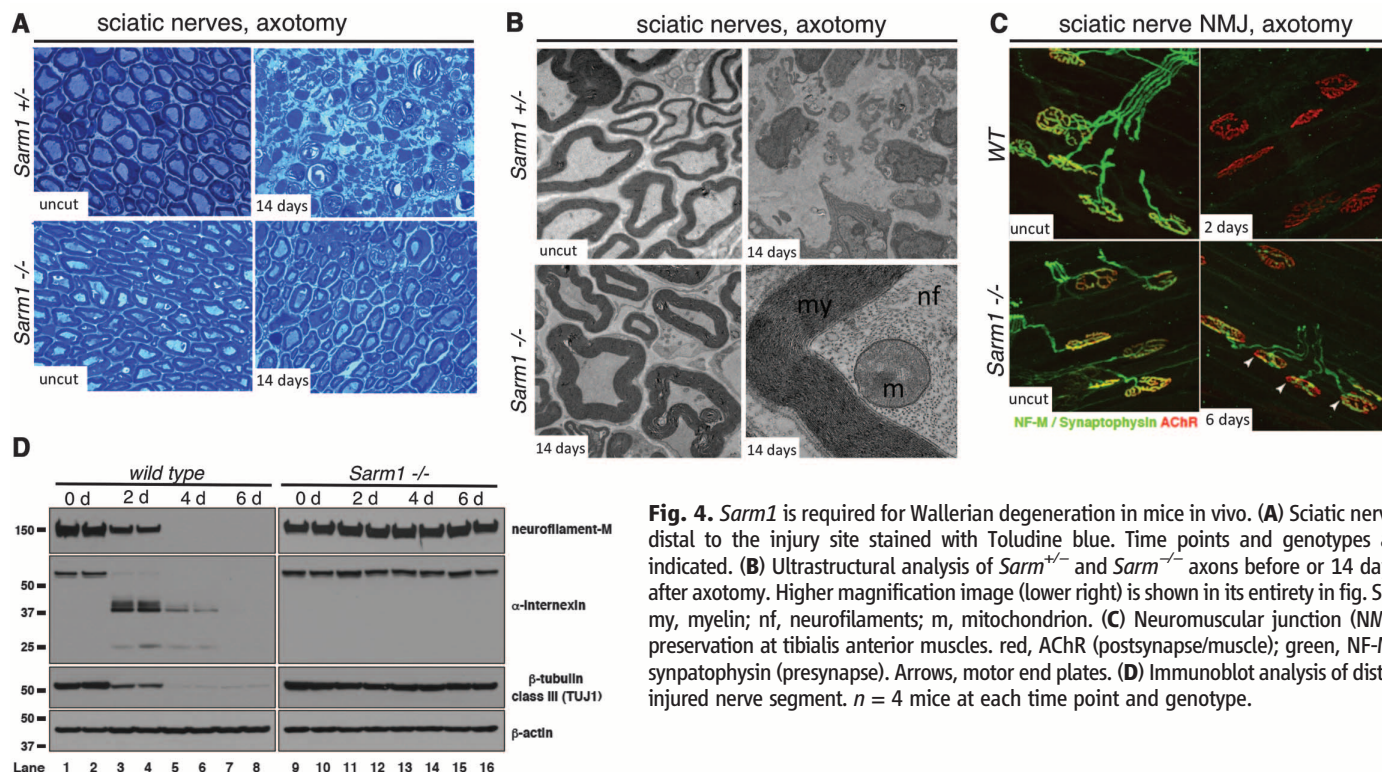


Fig. 4. *Sarm1* is required for Wallerian degeneration in mice in vivo. **(A)** Sciatic nerve distal to the injury site stained with Toluidine blue. Time points and genotypes as indicated. **(B)** Ultrastructural analysis of *Sarm1*^{+/-} and *Sarm1*^{-/-} axons before or 14 days after axotomy. Higher magnification image (lower right) is shown in its entirety in fig. S4. my, myelin; nf, neurofilaments; m, mitochondrion. **(C)** Neuromuscular junction (NMJ) preservation at tibialis anterior muscles. red, AChR (postsynapse/muscle); green, NF-M/synaptophysin (presynapse). Arrows, motor end plates. **(D)** Immunoblot analysis of distal injured nerve segment. *n* = 4 mice at each time point and genotype.

nerve transection. In wild-type animals, motor end plate denervation was complete by 2 days after axotomy. However, in *Sarm1*^{-/-} animals, most synaptic terminals were partially innervated even at 6 days after injury (Fig. 4C and fig. S5D). Consistent with a strong preservation of nerve integrity, macrophage/monocyte infiltration of lesioned nerves was suppressed in *Sarm1* knock-out animals (fig. S6, B, C, and F). Taken together, our results indicate that *Sarm1*^{-/-} mutations strongly preserve sciatic nerves in vivo from initial axonal cytoskeletal breakdown to recruitment of macrophages for myelin clearance.

To help define potential sites of action, we assayed localization of dSarm and Sarm1 in neurons. Expression of dSarm::GFP in *Drosophila* larval neurons resulted in punctate localization in neuronal cell bodies and broad localization to neurites in vivo (fig. S7, A and B). Immunostaining with antibodies to Sarm1 of in vitro cultured mouse neurons showed a similar pattern, and we note that endogenous Sarm1 did not show preferential localization with a mitochondrial marker (fig. S7, C and D), although mitochondrial localization has been reported for overexpressed Sarm1::GFP (16). Thus, dSarm/Sarm1 appears to be broadly localized in the axonal compartment.

Our analysis of dSarm/Sarm1 provides evidence that Wallerian degeneration is driven by an ancient, conserved axonal death program. Intriguingly, its *Caenorhabditis elegans* homolog, Tir-1, was recently implicated in nonapoptotic cell death (19), suggesting mechanistic links between these nonapoptotic degenerative mechanisms. Influx of extracellular calcium is known to be necessary and sufficient to trigger Wallerian

degeneration (20). Tir-1 functions downstream of the Ca^{2+} -CaM kinase signaling pathway in *C. elegans* (21, 22); therefore, dSarm/Sarm1 may respond directly to axonal calcium increases after axotomy. *Sarm1*^{-/-} neurons in slice cultures exhibit reduced cell death in response to oxygen/glucose deprivation (18); whether this is an indirect result or reflects axonal preservation remains untested. Pharmacological inhibition of Sarm1 may represent a promising therapeutic avenue for patients with axonal loss, particularly if Sarm1 deletion is shown to benefit animal models of neurodegenerative disease.

References and Notes

1. A. Waller, *Philos. Trans. R. Soc. London Ser. B Biol. Sci.* **140**, 423 (1850).
2. E. R. Lunn, V. H. Perry, M. C. Brown, H. Rosen, S. Gordon, *Eur. J. Neurosci.* **1**, 27 (1989).
3. J. D. Glass, T. M. Brushart, E. B. George, J. W. Griffin, *J. Neurocytol.* **22**, 311 (1993).
4. M. C. Raff, A. V. Whitmore, J. T. Finn, *Science* **296**, 868 (2002).
5. M. P. Coleman, V. H. Perry, *Trends Neurosci.* **25**, 532 (2002).
6. T. G. Mack et al., *Nat. Neurosci.* **4**, 1199 (2001).
7. M. P. Coleman, M. R. Freeman, *Annu. Rev. Neurosci.* **33**, 245 (2010).
8. B. Miller et al., *Nat. Neurosci.* **12**, 387 (2009).
9. T. L. Deckwerth, E. M. Johnson Jr., *Dev. Biol.* **165**, 63 (1994).
10. J. T. Finn et al., *J. Neurosci.* **20**, 1333 (2000).
11. A. V. Whitmore, T. Lindsten, M. C. Raff, C. B. Thompson, *Cell Death Differ.* **10**, 260 (2003).
12. T. Lee, L. Luo, *Trends Neurosci.* **24**, 251 (2001).
13. L. Luo, D. D. O'Leary, *Annu. Rev. Neurosci.* **28**, 127 (2005).
14. I. Miguel-Alíaga, S. Thor, *Development* **131**, 6093 (2004).
15. M. E. Grether, J. M. Abrams, J. Agapite, K. White, H. Steller, *Genes Dev.* **9**, 1694 (1995).
16. Y. Kim et al., *J. Exp. Med.* **204**, 2063 (2007).
17. B. L. MacInnis, R. B. Campenot, *Mol. Cell. Neurosci.* **28**, 430 (2005).

18. R. R. Buss, W. Sun, R. W. Oppenheim, *Annu. Rev. Neurosci.* **29**, 1 (2006).
19. E. S. Blum, M. C. Abraham, S. Yoshimura, Y. Lu, S. Shaham, *Science* **335**, 970 (2012).
20. E. B. George, J. D. Glass, J. W. Griffin, *J. Neurosci.* **15**, 6445 (1995).
21. C. F. Chuang, C. I. Bargmann, *Genes Dev.* **19**, 270 (2005).
22. C. Chang, Y. W. Hsieh, B. J. Lesch, C. I. Bargmann, C. F. Chuang, *Development* **138**, 3509 (2011).

Acknowledgments: We thank J. Gilley for preliminary work with Sarm1 primary cultures and Y. Hsueh for the Sarm1 antibody. We thank J. Patrick, D. Cameron, and D. Weaver for assistance with mouse work. This work was supported by the U.S. Department of Defense grant BC093796 (to T.M.R.); National Institute for Neurological Diseases and Stroke (NINDS) grants R01NS072248 and U54NS065712 (to S.Z.); an Alzheimer's Research UK Grant ART/PG2009/2, a Biotechnology and Biological Sciences Research Council Institute Strategic Programme Grant (to M.C.); NIH grant AI030165 to A.D.; support from Rockefeller University (J.Y. and M.T.-L.); and NINDS grant R01NS059991 and the ALS Therapy Alliance (to M.R.F.). M.R.F. is an Early Career Scientist with the Howard Hughes Medical Institute. M.R.F. and S.Z. are inventors on a patent applied for by University of Massachusetts Medical School, University of Miami, and the Howard Hughes Medical Institute covering therapeutic applications that target Sarm1 to block axonal and synaptic degeneration. R.H.B. was supported by NINDS5R01-NS050557-05, NINDS ARRA Award RC2-NS070-342, the Angel Fund, the ALS Association, P2ALS, Project ALS, Pierre L. de Bourgknecht ALS Research Foundation, and the ALS Therapy Alliance. R.H.B. is cofounder of Avitx, an ALS research company, and serves as a consultant to BiogenIdec and Iperion, is President of the ALS Therapy Alliance, and serves on the advisory boards of Project ALS, P2ALS, and the Angel Fund for ALS research.

Supplementary Materials

www.sciencemag.org/cgi/content/full/science.1223899/DC1
Materials and Methods
Figs. S1 to S7
Tables S1 to S4
References (23–31)

26 April 2012; accepted 24 May 2012
Published online 7 June 2012;
10.1126/science.1223899

Memory's Penumbra: Episodic Memory Decisions Induce Lingering Mnemonic Biases

Katherine Duncan,¹ Arhanti Sadanand,² Lila Davachi^{2,3*}

How do we decide if the people we meet and the things we see are familiar or new? If something is new, we need to encode it as a memory distinct from already stored episodes, using a process known as pattern separation. If familiar, it can be used to reactivate a previously stored memory, by a process known as pattern completion. To orchestrate these conflicting processes, current models propose that the episodic memory system uses environmental cues to establish processing biases that favor either pattern separation during encoding or pattern completion during retrieval. To assess this theory, we measured how people's memory formation and decisions are influenced by their recent engagement in episodic encoding and retrieval. We found that the recent encoding of novel objects improved subsequent identification of subtle changes, a task thought to rely on pattern separation. Conversely, recent retrieval of old objects increased the subsequent integration of stored information into new memories, a process thought to rely on pattern completion. These experiments provide behavioral evidence that episodic encoding and retrieval evoke lingering biases that influence subsequent mnemonic processing.

When you walk into a café for the first time, your memory system can both encode the details of this new environment and allow you to remember a similar one where you recently dined with a friend. The often effortless way in which we can encode the present and remember the past belies the complexity of the underlying processes, however. Though decades of theoretical and empirical research (1–5) have improved our understanding of both the neural systems and the computations that underlie episodic memory, the convergence of these lines of research reveals a paradox: Neuroscience research shows that both encoding new memories and retrieving old ones depend on the same specific brain region, the hippocampus (6–8), but computational models propose that encoding and retrieval are differentially supported by computationally incompatible network processes (9). Specifically, episodic encoding is thought to rely on pattern separation, a process that makes overlapping representations more distinct, whereas retrieval is thought to depend on pattern completion, a process that increases overlap by reactivating related memory traces. Because a process that emphasizes overlap cannot simultaneously operate on the same representation as one that deemphasizes it, a potential resolution to the paradox is that the hippocampus can establish processing biases that favor either pattern separation or completion, depending on the current context. This suggests that your likelihood of remembering your earlier lunch with a friend may be biased by the specific hippocampal processing

you were engaged in, even before walking into the café. In fact, neurocomputational models have long hypothesized that neuromodulatory systems may dynamically bias hippocampal processing toward either pattern completion or separation (10–13). Here, we test a prediction derived from these models and provide empirical support for these biases in human behavior.

The crux of our approach lies in the relatively slow action of neuromodulators in the hippo-

campus (14). If switching between pattern completion and separation biases is, in fact, mediated by hippocampal neuromodulatory input, it follows that a processing bias should linger in time and, thus, influence subsequent mnemonic processing. To test this, we presented participants with pictures of novel and familiar objects and asked them to make old/new recognition decisions (see supplementary materials and methods). According to models (10–13), detecting novelty should bias the memory system toward pattern separation to support distinctive encoding of the new information, whereas recognizing that a stimulus was previously experienced should induce a pattern completion bias that supports retrieval of stored representations. We measured lingering biases by presenting participants with critical test trials immediately after unrelated old and new memory decisions. We designed test trials across three different experiments to measure biases both at the time of retrieval decisions and during periods of encoding.

In the first two experiments, we measured biases in retrieval decisions with the use of a modified continuous recognition paradigm that has previously been applied to study pattern separation in the human hippocampus (15, 16). Participants were presented with a series of objects that fell into three categories: novel objects, repeated objects, or objects that were similar but not identical to previously presented ones. Participants were then asked to identify each as new (first presentation), old (exact repetition), or similar (not exact repetition) (Fig. 1A, see

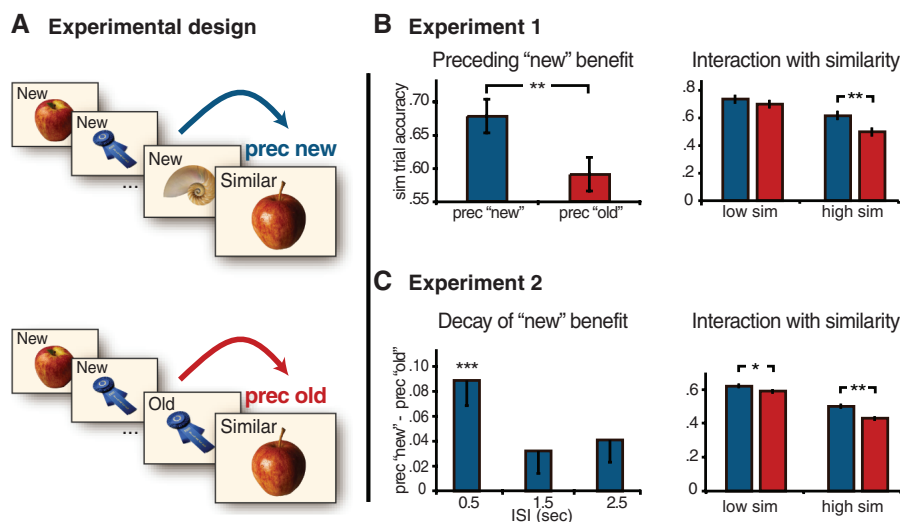


Fig. 1. (A) Participants were presented with a series of objects and asked to identify whether each item is new (first presentation), old (exact repetition), or similar (a modified object). The top sequence provides a preceding new example: The similar object follows a new object. The bottom sequence provides a preceding old example: The similar object follows an old object. (B) Results from experiment 1. (Left) Plot of accuracy on similar trials as a function of the preceding response (new in blue and old in red) ($n = 15$ participants). (Right) The bars on this graph are further divided according to perceptual similarity ratings. (C) Results from experiment 2. (Left) Graph displaying the preceding new benefit (preceding new – preceding old) for similar trial accuracy at an ISI of 0.5, 1.5, and 2.5 s ($N = 52$). (Right) Plot of similarity rating interaction for experiment 2 in the same way as presented above. Error bars mark the standard error of the difference between preceding new and old conditions. * $P < 0.05$, ** $P < 0.005$, *** $P < 0.001$.

¹Department of Psychology, Columbia University, New York, NY 10027, USA. ²Department of Psychology, New York University, New York, NY 10003, USA. ³Center for Neural Science, New York University, New York, NY 10003, USA.

*To whom correspondence should be addressed. E-mail: lila.davachi@nyu.edu

supplementary materials for more task details). Similar trials served as our critical test trials to measure pattern separation/completion biases. Specifically, although participants ($n = 15$) were instructed to respond “similar” to similar objects, the differences were often quite subtle, so similar objects were sometimes mistakenly identified as “old.” Thus, we reasoned that if the memory system was already biased toward pattern completion, these similar stimuli would more often be incorrectly identified as old, whereas if the system was biased toward pattern separation, the likelihood of noticing the small differences would be increased. Hence, we looked for evidence for lingering biases in memory decisions by examining whether participants were more likely to correctly identify similar trials as similar if they followed new trials rather than if they were presented after old trials.

Consistent with our hypotheses, we found that similar trials were more accurately identified as being similar when they were preceded by new trials than when they were preceded by old ones [prec. new = 67.7%, prec. old = 61.7%, $t(14) = 3.41$, $P < 0.005$]. This performance benefit (6%) was even larger (9%) when we binned similar trials based on the preceding response (for example, when participants reported a stimulus as new) rather than the preceding trial type (when a stimulus was actually new) [prec. new = 68.0%, prec. old = 59.4%, $t(14) = 3.32$, $P < 0.005$] (Fig. 1B), suggesting that the critical factor is the subjective memory decision rather than the stimulus type. Moreover, the preceding response still explained a significant portion of the variance in similar trial accuracy after adjusting for several covariates, including preceding trial type, preceding accuracy, and preceding response times (RTs) (Wald $\chi^2 = 8.9$, $P < 0.005$; see supplementary materials for full details and additional control analyses). There was also a similar but nonsignificant trend for the preceding response’s influence on RTs, with similar trials being correctly identified faster when they were preceded by new as compared with old responses [prec. new = 967 ms, prec. old = 988 ms, $t(14) = 2.01$, $P = 0.06$]. Finally, we predicted that similar trials that were difficult, with mnemonic evidence lying close to the decision boundary, would be more influenced by mnemonic biases than similar trials that were easier. We tested this hypothesis by dividing similar trials based on perceptual similarity ratings (see experiment 1a in the supplementary materials). A repeated-measures analysis of variance revealed a significant interaction between the preceding response (old versus new) and similarity rating (high versus low) ($F_{1,28} = 5.27$, $P < 0.05$) (Fig. 1B, also see fig. S4 for a parametric analysis). Consistent with our hypothesis, this interaction was driven by the fact that the preceding response’s influence was largest for the more difficult similar trials, those that were rated as being more similar [high similarity: $t(14) = 3.65$, $P < 0.005$; low similarity: $t(14) = 1.08$, $P = 0.30$].

Experiment 1 demonstrated that memory decisions can influence subsequent ones in a manner consistent with computational models of the hippocampus (10–13). If this bias is, in fact, mediated by neuromodulator action, we reasoned that it should also be temporally limited on the scale of seconds (12, 14). In experiment 2, we measured the time window over which these carry-over effects exert themselves by varying the interstimulus time interval (ISI) that elapsed between trials (0.5, 1.5, and 2.5 s) with a new set of participants ($n = 52$). We replicated the main effect of the preceding response (old versus new) ($F_{1,50} = 21.1$, $P < 0.001$) and the interaction between similarity rating and preceding response ($F_{1,50} = 4.41$, $P < 0.05$). Critically, we also found that the preceding new benefit was time-dependent. Specifically, there was a significant interaction between ISI and preceding response ($F_{2,100} = 3.2$, $P < 0.05$), with the largest preceding-response effect on trial accuracy found for similar trials that were preceded by the shortest ISI [prec. new = 58.3%, prec. old = 49.4%, $t(51) = 4.3$, $P < 0.001$; preceding old versus new differences at longer ISIs were not sig-

nificant] (Fig. 1C). A similar interaction was also found in RTs ($F_{2,100} = 4.2$, $P < 0.05$) (fig. S5B).

In experiment 3, we tested whether old and new memory decisions can also influence subsequent memory formation (Fig. 2, see fig. S6 for example trials). To this end, we modified a paradigm that was designed to assess whether related associations are integrated into newly formed memory traces (17, 18), a process that should be influenced by pattern completion/separation biases. We reasoned that the memory system would be more likely to reactivate previously encountered, but related information after old recognition decisions compared with new decisions and that this reactivation should, in turn, lead to greater integration of the reactivated representations into newly formed memories. To test this hypothesis, we had a new group of participants ($n = 22$) alternate between making old/new object-recognition decisions and encoding overlapping face-scene associations. Critically, these face-scene pairs (A-Y pairs) were associatively related to other face-scene pairs (A-X and B-X pairs) that were learned in an earlier phase of the experiment. Previous research has

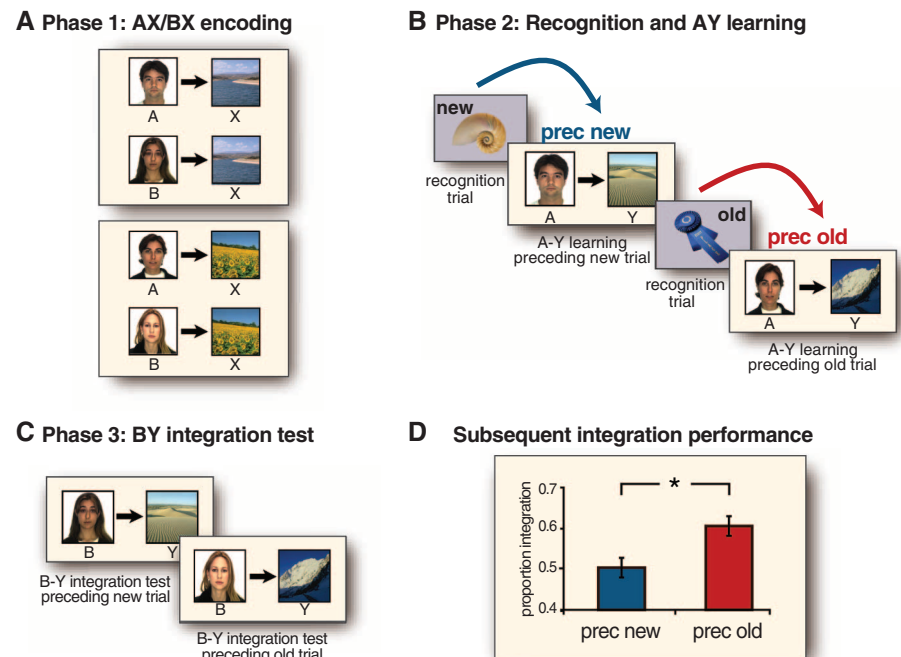


Fig. 2. We used a multiphase design to test integrative encoding. **(A)** Participants first learned face-scene associations in which pairs of faces were associated with the same scene (A-X and B-X associations). **(B)** Participants then learned a new scene association for one face from each pair (A-Y association). These A-Y learning trials were interleaved with object-recognition trials. Each A-Y association was preceded by either a novel object (preceding new condition) or one that had been studied at the beginning of the session (preceding old condition). Participants indicated whether each object was old or new. **(C)** The final phase evaluated whether participants integrated the overlapping associations from the earlier two phases by testing whether they chose to pair the indirectly related faces and scenes (B-Y association). **(D)** Influence of preceding memory decisions on integration in experiment 3. The graph compares how often participants paired indirectly associated faces and scenes (B-Y associations) during the final test phase. Trials are divided according to whether their learned counterpart (A-Y) was encoded after new (blue) or old (red) objects during the earlier phase. Error bars mark the standard error of the difference between preceding new and old conditions. * $P < 0.05$.

demonstrated that participants tend to integrate these related A-X and B-X pairs into their learning of new A-Y pairs, forming a link between the indirectly associated B and Y stimuli (17–19). To assess the strength of this integration, we subsequently tested how often participants chose to pair faces and scenes that were only indirectly related across the two sets (B-Y pairs). Consistent with our hypothesis, participants were 10% more likely to subsequently show this kind of integration when they encoded the A-Y pairs following old objects as compared with new ones [prec. new = 60.1%, prec. old = 50.1%, $t(21) = 2.1$, $P < 0.05$] (Fig. 2D). Moreover, when participants chose to pair indirectly related stimuli, they did so 71 ms faster if the stimuli had previously been learned after old objects as compared with new ones [prec. new = 1487 ms, prec. old = 1558 ms, $t(21) = 2.2$, $P < 0.05$], again consistent with the interpretation that retrieval improves subsequent integrative encoding.

Together, these results provide behavioral evidence that episodic encoding and retrieval can evoke biases that influence subsequent mnemonic processing, a phenomenon that computational models predict to be the consequence of a tension between episodic encoding and retrieval operations. Importantly, the evidence presented here goes beyond simply demonstrating competition between concurrent encoding and retrieval (20, 21), an effect that could be explained by a bottleneck at various cognitive stages (22); rather, we provide evidence that memory decisions can exert a temporally extended bias on subsequent computational processes thought to support encoding and retrieval—namely pattern separation and completion. Specifically, we found that memory decisions on the current trial influenced memory decisions (experiments 1 and 2) and memory formation (experiment 3) made on the subsequent trial.

Although there is agreement across several hippocampal memory models that encoding

and retrieval should be temporally segregated (13, 23–25), the time required to switch between these processing biases varies widely across models from a few hundred milliseconds (24) to 10 s (12). The current results presented in experiment 2 suggest that the influence of an earlier memory decision decays after a few seconds, consistent with the theoretical time scale of acetylcholine modulation in the hippocampus (12, 14). This result dovetails with the finding that acetylcholine antagonists increase proactive interference (26, 27), a potential consequence of pattern separation failure.

An intriguing open question is whether the lingering nature of the observed memory bias could be an adaptive mechanism to dynamically adjust the criterion for memory reactivation based on the nature of the environment. Rarely do our experiences rapidly switch between the familiar and the novel. Instead, we tend to navigate through situations that generally contain more novel or more familiar components. It could be advantageous for our memory system to be more sensitive to change in new environments and less sensitive to irregularities in familiar environments (25, 28–30). Regardless of the adaptive consequences, the current results shed light on fundamental computational issues of memory encoding and retrieval and highlight that our ongoing processing of the world is influenced by other preceding cognitive operations.

References and Notes

1. D. Marr, *Philos. Trans. R. Soc. London Ser. B* **262**, 23 (1971).
2. W. B. Scoville, B. Milner, *J. Neurol. Neurosurg. Psychiatry* **20**, 11 (1957).
3. K. A. Norman, R. C. O'Reilly, *Psychol. Rev.* **110**, 611 (2003).
4. L. R. Squire, *Psychol. Rev.* **99**, 195 (1992).
5. R. J. McDonald, N. M. White, *Behav. Neurosci.* **107**, 3 (1993).
6. L. Davachi, *Curr. Opin. Neurobiol.* **16**, 693 (2006).
7. H. Eichenbaum, A. P. Yonelinas, C. Ranganath, *Annu. Rev. Neurosci.* **30**, 123 (2007).
8. L. R. Squire, J. T. Wixted, R. E. Clark, *Nat. Rev. Neurosci.* **8**, 872 (2007).

9. R. C. O'Reilly, J. L. McClelland, *Hippocampus* **4**, 661 (1994).
10. M. E. Hasselmo, E. Schnell, *J. Neurosci.* **14**, 3898 (1994).
11. M. E. Hasselmo, E. Schnell, E. Barkai, *J. Neurosci.* **15**, 5249 (1995).
12. M. Meeter, J. M. J. Murre, L. M. Talamini, *Hippocampus* **14**, 722 (2004).
13. M. E. Hasselmo, B. P. Wyble, G. V. Wallenstein, *Hippocampus* **6**, 693 (1996).
14. M. E. Hasselmo, B. P. Fehla, *J. Neurophysiol.* **86**, 1792 (2001).
15. C. B. Kirwan, C. E. Stark, *Learn. Mem.* **14**, 625 (2007).
16. A. Bakker, C. B. Kirwan, M. Miller, C. E. L. Stark, *Science* **319**, 1640 (2008).
17. D. Shohamy, A. D. Wagner, *Neuron* **60**, 378 (2008).
18. C. E. Myers *et al.*, *J. Cogn. Neurosci.* **15**, 185 (2003).
19. G. Hall, C. Mitchell, S. Graham, Y. Lavis, *J. Exp. Psychol. Gen.* **132**, 266 (2003).
20. K. Allan, J. Allen, *J. Neurosci.* **25**, 8122 (2005).
21. W. Huijbers, C. M. Pennartz, R. Cabeza, S. M. Daselaar, *PLoS Biol.* **7**, e11 (2009).
22. H. Pashler, *Psychol. Bull.* **116**, 220 (1994).
23. O. S. Vinogradova, *Hippocampus* **11**, 578 (2001).
24. S. Kunec, M. E. Hasselmo, N. Kopell, *J. Neurophysiol.* **94**, 70 (2005).
25. J. E. Lisman, A. A. Grace, *Neuron* **46**, 703 (2005).
26. A. Atri *et al.*, *Behav. Neurosci.* **118**, 223 (2004).
27. E. De Rosa, M. E. Hasselmo, *Behav. Neurosci.* **114**, 32 (2000).
28. D. Kumaran, E. A. Maguire, *Hippocampus* **17**, 735 (2007).
29. J. Lisman, A. A. Grace, E. Duzel, *Trends Neurosci.* **34**, 536 (2011).
30. K. Duncan, N. Ketz, S. J. Inati, L. Davachi, *Hippocampus* **22**, 389 (2012).

Acknowledgments: This work was funded by NIH grant RO1 MH074692 to L.D. We thank V. Skvortsova, A. Berners-Lee, and M. Inhoff for data collection assistance; K. Ochsner and E. Phelps for their helpful comments on an earlier draft of the manuscript; G. Chin for his useful editorial comments; and C. Stark and W. Suzuki for the use of stimuli developed by their labs.

Supplementary Materials

www.sciencemag.org/cgi/content/full/337/6093/485/DC1
Materials and Methods
Figs. S1 to S8
Tables S1 and S2

14 March 2012; accepted 30 May 2012
10.1126/science.1221936

New Products



LOW-TEMPERATURE COOLERS

A line of low temperature coolers provide rapid, low-cost cooling of liquids to temperatures as low as -100°C . Available in both immersion probe and flow through styles, these compact systems are ideal for cooling exothermic reactions, freeze point determinations, freeze drying, impact testing, lyophilization, and vapor and solvent trapping. Excellent for trapping, Dewar-type applications, and the rapid cool down of small volumes of liquids, PolyScience Immersion Probe Style Coolers reduce the expense of using dry ice or liquid nitrogen and are capable of reaching temperatures as low as -100°C . A flexible hose allows convenient placement of the cooling probe. Seven different models as well as a variety of probe types are available. Capable of reaching temperatures as low as -25°C , PolyScience Flow-Through Style Coolers are ideal for extending the temperature range of nonrefrigerated circulators to below ambient as well as boosting the cooling capacity of refrigerated circulators.

PolyScience

For info: 800-229-7569 | www.polyscience.com

IN VITRO TRANSLATION SYSTEM

1-Step Human High Yield In Vitro Translation (IVT) Kits have a continuous-feed device and can produce 10- to 100-times more functional protein per milliliter than other eukaryotic IVT systems. The protein obtained with the 1-Step Human High Yield IVT Kit can be used for structural analysis, antibody production, and kinetic or enzymatic assays. The kit uses modified HeLa cell extracts to provide the protein expression machinery. Protein expression is performed using a proprietary mini-dialysis device that allows the continuous supply of nucleotides, amino acids, and energy-generating substrates to extend the protein translation reaction. The device also allows the removal of protein synthesis inhibitors. With the kit, protein expression can continue for up to 24 hours, providing protein yields ranging from 250 to 750 μg per milliliter. The complete 1-Step High Yield IVT Kits supply all components necessary for the transcription and translation of protein, including an optimized expression vector, pT7CFE1-CGST-HA-His.

Thermo Fisher Scientific

For info: 800-874-3723 | www.thermoscientific.com/pierce

IMAGE CYTOMETRY SYSTEM

The Cytell Image Cytometer is a benchtop-sized image cytometer for rapid cell characterization that introduces researchers to a new, simpler, faster, and more productive way to conduct their cell analysis. The new Cytell Image Cytometer enables researchers to capture detailed data about their cells quickly while using minimal sample volumes. Data can be acquired for up to eight samples at a time and results are delivered through an intuitive graphical interface in less than two-and-a-half minutes. The system simplifies researchers' working practices and increases productivity by removing the need to use specialized cell analysis instruments. Large cell analysis instruments are often in a shared facility, which can be difficult to access at the right time and time-consuming to use.

GE Healthcare

For info: 800-526-3593 | www.gelifesciences.com/cytell

TISSUE-SPECIFIC CONDITIONAL KNOCKOUT

CompoZr Zinc Finger Nuclease (ZFN) technology has been extended to achieve the first tissue-specific conditional knockout of an endogenous gene in rats. Rats engineered to contain tissue-specific conditional gene knockouts are available exclusively through the SAGESpeed Custom Model Development Service. Conventional gene knockout eliminates a gene throughout an entire animal. In contrast, conditional gene knockout can eliminate a gene solely in the relevant tissue or organ, leading to a more accurate understanding of the gene's function. Conditional gene knockout can also knockout genes at certain points in development, enabling studies of genes whose absence in embryos is lethal, but whose loss of function in adulthood is critical to investigate for many human diseases. CompoZr ZFN technology is the first to enable highly efficient, targeted editing of the genome of any species.

Sigma-Aldrich

For info: 800-325-3010 | www.sageresearchmodels.com

DIGITAL HOLOGRAPHIC PHOTOMANIPULATION

The first commercial implementation of a phase-only spatial light modulator (SLM) designed specifically for patterned and 3-D point photomanipulation in optical microscopy. It is a compact, modular device that couples to a microscope documentation port and the 3i LaserStack laser launch. Phasor can be used for optogenetic stimulation, uncaging, and other types of photomanipulation. One major advantage of its technology over older methods is that a significant portion of laser intensity can be simultaneously redirected to just those regions where photomanipulation is desired, rather than being either sequentially scanned or mostly blocked. In optical stimulation of brain slices, for instance, action potentials can be elicited at multiple locations in parallel with less than one millisecond of laser illumination. Region specification, hologram generation, and experimentally synchronized optical path switching and laser illumination gating are managed within 3i's SlideBook software.

Intelligent Imaging Innovations

For info: 303-607-9429 | www.intelligent-imaging.com

Electronically submit your new product description or product literature information! Go to www.sciencemag.org/products/newproducts.dtl for more information.

Newly offered instrumentation, apparatus, and laboratory materials of interest to researchers in all disciplines in academic, industrial, and governmental organizations are featured in this space. Emphasis is given to purpose, chief characteristics, and availability of products and materials. Endorsement by *Science* or AAAS of any products or materials mentioned is not implied. Additional information may be obtained from the manufacturer or supplier.

For more information, including our
FREE SAMPLE special offer, visit
www.Q5PCR.com

Fidelity at its finest.

Q5[™] High-Fidelity DNA Polymerase

Q5 High-Fidelity DNA Polymerase sets a new standard for both fidelity and performance. With the highest fidelity amplification available (>50X higher than *Taq*), Q5 DNA Polymerase results in ultra-low error rates. Its unique buffer system provides superior performance for a broad range of amplicons, regardless of GC content. Available in master mix and hot start formulations, Q5 DNA Polymerase represents the finest in fidelity.

ALSO AVAILABLE: Optimized NEBNext[®] formulation
for next generation sequencing library amplification

Mandarin Ducks (*Aix galericulata*) are frequently featured
in Chinese art and are regarded as a symbol of fidelity.

Robust amplification even with high GC amplicons



Amplification of two human genomic amplicons of mid to high GC content. All reactions were conducted using 30 cycles of amplification and visualized by microfluidic LabChip[®] analysis. All polymerases were cycled according to manufacturer's recommendations. For the 78% GC amplicon, GC Buffers or enhancers were used when supplied with the polymerase.

A = Q5[™] High-Fidelity DNA Polymerase (NEB)

B = Phusion[®] High-Fidelity DNA Polymerase (NEB)

C = KOD DNA Polymerase (EMD)

D = PfuUltra[™] High-Fidelity DNA Polymerase (Agilent)

PHUSION[®] is a registered trademark and property of Thermo Fisher Scientific.
Phusion[®] DNA Polymerase was developed by Finnzymes Oy, now a part of Thermo Fisher Scientific.
PFUULTRA[™] is a trademark of Agilent Technologies, Inc.
LABCHIP[®] is a registered trademark of Caliper Life Sciences, part of Perkin Elmer, Inc.
Q5[™] is a trademark of New England Biolabs, Inc.

Orbitrap mass spec
is better, but it's too
expensive. I may have
to settle for Q-TOF.

think again.



Exactive Plus
LC-MS



Q Exactive
LC-MS/MS



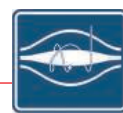
LTQ Orbitrap XL
Hybrid FTMS



Orbitrap Velos Pro
Hybrid MS



Orbitrap Elite
Hybrid MS



Thermo Scientific Orbitrap mass spec is better! The amazing resolution, accuracy, speed and precision of Orbitrap™ technology is the best solution for complex sample analysis. The good news is that it's more affordable than ever. The Orbitrap mass spec portfolio provides a range of solutions from routine screening to ultra-high performance research instruments that will help virtually any lab achieve more. In doubt? Check out the line of researchers waiting to use an Orbitrap mass spec. Then see if there's a line to use the other mass spectrometers in your lab.

• [learn why Orbitrap is better at thermoscientific.com/thinkagain](http://thermoscientific.com/thinkagain)

Thermo
SCIENTIFIC

Purification was never easier!

QIAcube and iPad

Information, update alerts,
and much more at the
touch of the screen



For a limited time only, we are offering the award-winning spin-column instrument, QIAcube®, together with the new, dedicated QIAcube app and a third generation Apple® iPad®, further facilitating sample preparation by adding:

- Easy access to more than 90 protocols for DNA, RNA, and protein purification
- Automatic checks for new protocols and software updates
- All the user support documents you need

Contact QIAGEN today or visit www.qiagen.com/qiacube-tablet.

Trademarks: QIAGEN®, QIAcube® (QIAGEN Group); Apple®, iPad® (Apple Computer, Inc.). Export regulations may apply. QIAGEN and Apple Computer, Inc. are not affiliated companies. For up-to-date licensing information and product-specific disclaimers, see the respective QIAGEN kit handbook or user manual (available at www.qiagen.com, from QIAGEN Technical Services at 00800-22-44-6000, or your local distributor).



Sample & Assay Technologies

MPC-200 Multi-manipulator system

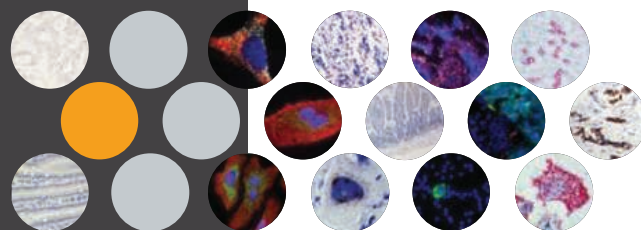
- Versatile:** User friendly interface controls up to two manipulators with one controller. Select components to tailor a system to fit your needs.
- Expandable:** Daisy chain a second controller and operate up to four manipulators with one input device.
- Stable:** Stepper motors and cross-rolled bearings guarantee reliable, drift-free stability.
- Doubly Quiet:** Linear stepper-motor drive reduces electrical noise. Thermostatically-controlled cooling fans barely whisper.

*Make the
right move!*



SUTTER INSTRUMENT

PHONE: 415.883.0128 | FAX: 415.883.0572
EMAIL: INFO@SUTTER.COM | WWW.SUTTER.COM



RNAscope®

in situ hybridization.
easy. powerful.

visualize
single-copy RNA expression

- Biomarker Analysis
- Target ID & Validation
- Molecular Pathology
- Companion Dx
- Validate IHC Results
- Non-coding RNA
- Stem Cell Research
- Tumor Heterogeneity
- Rare-cell Analysis
- Exquisite sensitivity & specificity
- Optimized for archival FFPE tissue
- Easy 7-hour IHC-like workflow
- Quantifiable and automatable
- New assays in < 3 weeks
- Guaranteed assay performance



ADVANCED CELL DIAGNOSTICS, INC.

1-877-576-3636 | www.acdbio.com | order@acdbio.com



AAAS is here – connecting government to the scientific community.

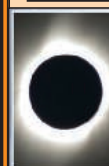
As a part of its efforts to introduce fully open government, the White House is reaching out to the scientific community for a conversation on America's national scientific and technological priorities. To enable this dialogue, AAAS launched Expert Labs, directed by blogger and tech guru Anil Dash. Expert Labs is building online tools that allow government agencies to ask questions of the scientific community and then sort and rank the answers.

As a AAAS member, your dues support our efforts to help government base policy on direct feedback from the scientific community. If you are not already a member, join us. Together we can make a difference.

To learn more, visit
aaas.org/plusyou/expertlabs



AAAS Travels



**Atlantic Crossing
Oct 18–Nov 10, 2013**



On board the Tall Ship Star Flyer

Travel in the path of Columbus across the Atlantic for a journey of a lifetime! See the **Total Solar Eclipse** in the mid-Atlantic on **November 3, 2013!** From \$5,495 + air

**For a detailed brochure,
please call (800) 252-4910**

All prices are per person twin share + air



BETCHART EXPEDITIONS INC.
17050 Montebello Rd, Cupertino, CA 95014
Email: AAASInfo@betchartexpeditions.com
www.betchartexpeditions.com

SCIENCE & DIPLOMACY

A quarterly publication from the AAAS Center for Science Diplomacy

Launched in March 2012, **SCIENCE & DIPLOMACY** provides an open access forum for rigorous thought, analysis, and insight to serve stakeholders who develop, implement, and teach all aspects of science and diplomacy. **SCIENCE & DIPLOMACY** features a mix of original perspectives and research articles by leading science and diplomacy practitioners and thinkers. Learn more about the latest ideas in science diplomacy and receive regular updates by following @SciDip on Twitter and registering for free at www.sciencediplomacy.org/user/register.



WWW.SCIENCEDIPLOMACY.ORG

Senior Advisory Board

Norman P. Neureiter (Chair), AAAS
Peter C. Agre, Johns Hopkins
Nicholas Burns, Harvard
David C. Clary, Oxford and UK FCO
Paula J. Dobriansky, Harvard

Nina V. Fedoroff, Penn State and KAUST
Richard N. Foster, Yale
David A. Hamburg, AAAS
Mohamed Hassan, IAP
Neal F. Lane, Rice

Science & Diplomacy is published by the Center for Science Diplomacy of the American Association for the Advancement of Science (AAAS), the world's largest general scientific society.

New Products



LOW-TEMPERATURE COOLERS

A line of low temperature coolers provide rapid, low-cost cooling of liquids to temperatures as low as -100°C . Available in both immersion probe and flow through styles, these compact systems are ideal for cooling exothermic reactions, freeze point determinations, freeze drying, impact testing, lyophilization, and vapor and solvent trapping. Excellent for trapping, Dewar-type applications, and the rapid cool down of small volumes of liquids, PolyScience Immersion Probe Style Coolers reduce the expense of using dry ice or liquid nitrogen and are capable of reaching temperatures as low as -100°C . A flexible hose allows convenient placement of the cooling probe. Seven different models as well as a variety of probe types are available. Capable of reaching temperatures as low as -25°C , PolyScience Flow-Through Style Coolers are ideal for extending the temperature range of nonrefrigerated circulators to below ambient as well as boosting the cooling capacity of refrigerated circulators.

PolyScience

For info: 800-229-7569 | www.polyscience.com

IN VITRO TRANSLATION SYSTEM

1-Step Human High Yield In Vitro Translation (IVT) Kits have a continuous-feed device and can produce 10- to 100-times more functional protein per milliliter than other eukaryotic IVT systems. The protein obtained with the 1-Step Human High Yield IVT Kit can be used for structural analysis, antibody production, and kinetic or enzymatic assays. The kit uses modified HeLa cell extracts to provide the protein expression machinery. Protein expression is performed using a proprietary mini-dialysis device that allows the continuous supply of nucleotides, amino acids, and energy-generating substrates to extend the protein translation reaction. The device also allows the removal of protein synthesis inhibitors. With the kit, protein expression can continue for up to 24 hours, providing protein yields ranging from 250 to 750 μg per milliliter. The complete 1-Step High Yield IVT Kits supply all components necessary for the transcription and translation of protein, including an optimized expression vector, pT7CFE1-CGST-HA-His.

Thermo Fisher Scientific

For info: 800-874-3723 | www.thermoscientific.com/pierce

IMAGE CYTOMETRY SYSTEM

The Cytell Image Cytometer is a benchtop-sized image cytometer for rapid cell characterization that introduces researchers to a new, simpler, faster, and more productive way to conduct their cell analysis. The new Cytell Image Cytometer enables researchers to capture detailed data about their cells quickly while using minimal sample volumes. Data can be acquired for up to eight samples at a time and results are delivered through an intuitive graphical interface in less than two-and-a-half minutes. The system simplifies researchers' working practices and increases productivity by removing the need to use specialized cell analysis instruments. Large cell analysis instruments are often in a shared facility, which can be difficult to access at the right time and time-consuming to use.

GE Healthcare

For info: 800-526-3593 | www.gelifesciences.com/cytell

TISSUE-SPECIFIC CONDITIONAL KNOCKOUT

CompoZr Zinc Finger Nuclease (ZFN) technology has been extended to achieve the first tissue-specific conditional knockout of an endogenous gene in rats. Rats engineered to contain tissue-specific conditional gene knockouts are available exclusively through the SAGESpeed Custom Model Development Service. Conventional gene knockout eliminates a gene throughout an entire animal. In contrast, conditional gene knockout can eliminate a gene solely in the relevant tissue or organ, leading to a more accurate understanding of the gene's function. Conditional gene knockout can also knockout genes at certain points in development, enabling studies of genes whose absence in embryos is lethal, but whose loss of function in adulthood is critical to investigate for many human diseases. CompoZr ZFN technology is the first to enable highly efficient, targeted editing of the genome of any species.

Sigma-Aldrich

For info: 800-325-3010 | www.sageresearchmodels.com

DIGITAL HOLOGRAPHIC PHOTOMANIPULATION

The first commercial implementation of a phase-only spatial light modulator (SLM) designed specifically for patterned and 3-D point photomanipulation in optical microscopy. It is a compact, modular device that couples to a microscope documentation port and the 3i LaserStack laser launch. Phasor can be used for optogenetic stimulation, uncaging, and other types of photomanipulation. One major advantage of its technology over older methods is that a significant portion of laser intensity can be simultaneously redirected to just those regions where photomanipulation is desired, rather than being either sequentially scanned or mostly blocked. In optical stimulation of brain slices, for instance, action potentials can be elicited at multiple locations in parallel with less than one millisecond of laser illumination. Region specification, hologram generation, and experimentally synchronized optical path switching and laser illumination gating are managed within 3i's SlideBook software.

Intelligent Imaging Innovations

For info: 303-607-9429 | www.intelligent-imaging.com

Electronically submit your new product description or product literature information! Go to www.sciencemag.org/products/newproducts.dtl for more information.

Newly offered instrumentation, apparatus, and laboratory materials of interest to researchers in all disciplines in academic, industrial, and governmental organizations are featured in this space. Emphasis is given to purpose, chief characteristics, and availability of products and materials. Endorsement by *Science* or AAAS of any products or materials mentioned is not implied. Additional information may be obtained from the manufacturer or supplier.

A large, detailed portrait of Sir Isaac Newton, showing him with long, curly hair and a serious expression, wearing a white shirt with a high collar.

Science

There's only one
SIR ISAAC NEWTON

Sir Isaac Newton's contribution to science can only be described as unique. Over his lifetime, Newton offered insights into physics, mathematics, natural philosophy, and even alchemy, and is now considered by many to be one of the greatest scientists who ever lived. In 1687, the publication of his *Philosophiæ Naturalis Principia Mathematica* was an influential landmark in scientific thinking that defined the principles of universal gravitation and the laws of motion—setting the foundation that scientists would turn to for over 300 years.

Today, scientists from around the world turn to *Science*. With 700,000 print readers every week and 3.6 million unique visitors to the online site each month, *Science* reaches more people than any other scientific print publication or website. What's more, as part of the non-profit AAAS, the revenue generated by *Science* supports programs around the world that help inform science policymakers, enhance science diplomacy, strengthen the scientific workforce, and improve science education.

So if you want to reach physicists, mathematicians, life scientists, or even the occasional alchemist, there's only one *Science*. Visit *Science* today at sciencemag.org.



AAAS

For your advertising needs, there's only one **Science**

sciencemag.org

ER

applied
biosystems®
by *life* technologies™

The next
BIG THING
from the inventors of
SYBR®

high**ER** specificity
bett**ER** performance
low**ER** price
bright**ER** dye

Introducing SYBR® Select
Master Mix with GreenER™ dye



Add ER to your SYBR® at lifetechnologies.com/sybr

life
technologies™

For research use only. Not intended for any animal or human therapeutic or diagnostic use. ©2012 Life Technologies Corporation. All rights reserved.
The trademarks mentioned herein are the property of Life Technologies Corporation or their respective owners. C002904 0612

There's only one

Science



Science Careers Advertising

For full advertising details, go to ScienceCareers.org and click For Employers, or call one of our representatives.

Tracy Holmes

Worldwide Associate Director
Science Careers
Phone: +44 (0) 1223 326525

UNITED STATES & CANADA

E-mail: advertise@sciencecareers.org
Fax: 202-289-6742

Tina Burks

United States/Canada/
South America
Phone: 202-326-6577

Marci Gallun

Sales Administrator
Phone: 202-326-6582

Online Job Posting Questions

Phone: 202-312-6375

EUROPE & REST OF WORLD

E-mail: ads@science-int.co.uk
Fax: +44 (0) 1223 326532

Simone Jux

Phone: +44 (0)1223 326529

Lucy Nelson

Phone: +44 (0)1223 326527

Kelly Grace

Phone: +44 (0) 1223 326528

JAPAN

Yuri Kobayashi

Phone: +81-50-3696-5100
E-mail: ykobayas@aaas.org

CHINA & TAIWAN

Ruolei Wu

Phone: +86-1367-1015-294
E-mail: rwu@aaas.org

All ads submitted for publication must comply with applicable U.S. and non-U.S. laws. *Science* reserves the right to refuse any advertisement at its sole discretion for any reason, including without limitation for offensive language or inappropriate content, and all advertising is subject to publisher approval. *Science* encourages our readers to alert us to any ads that they feel may be discriminatory or offensive.

Science Careers

From the journal *Science*



AAAS is here – helping scientists achieve career success.

Every month, over 400,000 students and scientists visit ScienceCareers.org in search of the information, advice, and opportunities they need to take the next step in their careers.

A complete career resource, free to the public, *Science* Careers offers a suite of tools and services developed specifically for scientists. With hundreds of career development articles, webinars and downloadable booklets filled with practical advice, a community forum providing answers to career questions, and thousands of job listings in academia, government, and industry, *Science* Careers has helped countless individuals prepare themselves for successful careers.

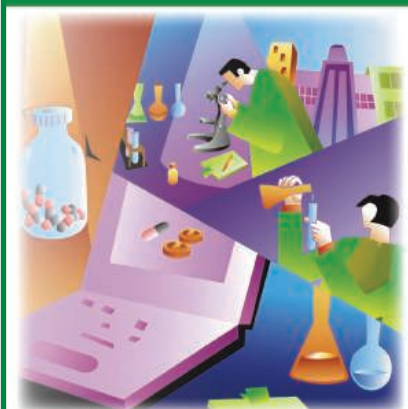
As a AAAS member, your dues help AAAS make this service freely available to the scientific community. If you're not a member, join us. Together we can make a difference.

To learn more, visit

aaas.org/plusyou/sciencecareers



CAREER TRENDS Running Your Lab



Download your free copy today at
ScienceCareers.org/booklets

Science Careers

From the journal *Science*



Brought to you by the
AAAS/Science Business Office

Maharashtra Association for the Cultivation of Science AGHARKAR RESEARCH INSTITUTE

(An Autonomous Institute of Dept. of Science & Technology, Govt. of India) G.G.AGARKAR ROAD, PUNE - 411004, India
E-mail: directorari@vsnl.com

Advt./Rec/13/2012

VACANCIES FOR SCIENTISTS AT VARIOUS LEVELS

The Institute is inviting applications for the positions of Scientists specialized in Agronomy, Anaerobic bacteria and anaerobic archaea, Animal Handling and Experimentation, Bioenergy, Community Nutrition, Developmental Biology, Microbial Taxonomy, Nanomedicine, Natural Product Chemistry, Palaeontology, Plant Molecular Biology, Plant Taxonomy, Virology. Last date for receipt of applications in prescribed application format is 31.08.2012. For full details visit our website <http://www.aripune.org>.

Science

Annual Postdoc Survey

Special Career Feature: August 24

Reserve your ad by August 7 to guarantee space.*

*Ads accepted until August 20 if space is still available.



Looking for postdocs? Here's how *Science* can help:

Content: Ph.D. scientists ready to make their next career move rely on *Science* for sound analysis and career advice. In this feature, *Science* examines what postdocs can do in the current economic climate to advance their career opportunities. Tell these scientists what exciting postdoc experiences await them at your university or organization.

Reach: With a worldwide readership of over 700,000 readers, your ad reaches scientists around the globe with varied backgrounds. Your ad sits on a special bannered page drawing attention to your postdoc opportunities

Results: When it comes to finding the right postdoc, *Science* offers a simple formula: relevant content that spotlights your ad + a large, qualified audience = your hiring success.

Customized
packages
to correspond with
this special feature
are available

To Book Your Ad:

E-mail:
advertise@sciencecareers.org

Or telephone us:
US: 202-326-6582
Europe/RoW: +44 (0) 1223 326500
Japan: +81-50-3696-5100
China/Korea/Singapore/Taiwan/Thailand: +86-1367-1015-294

ScienceCareers.org

Find your next postdoc by advertising in this special feature.

For recruitment in science, there's only one **Science**





JOB POSTING **EXECUTIVE DIRECTOR,** AARHUS INSTITUTE OF ADVANCED STUDIES

The university is seeking an internationally accomplished academic and administrative executive director of Aarhus Institute of Advanced Studies (AIAS) at Aarhus University (AU). Aarhus is a thriving Scandinavian city known for its culture, knowledge-based industries, vibrant student environment, and exceptional natural surroundings, within a country marked by a high quality of life, flexible and secure social structure, and a tradition of research and innovation.

During the last decade, AU has consolidated its position as one of the world's top-ranked universities with a high research impact, state-of-the-art research infrastructures, and several research groups belonging to the absolute world elite. AU is widely acknowledged for its outstanding pioneering work within basic research, as illustrated by research awards such as the 1997 Nobel Prize in Chemistry and the 2010 Nobel Prize in Economic Sciences. Since 2007, 20 European Research Council (ERC) grants have been awarded to researchers at AU, representing more than a third of ERC grants in Denmark. In addition, AU is committed to providing opportunities for highly qualified early career researchers through a dedicated focus on talent development.

The mission of AIAS is to support highest caliber research at AU by attracting talented, highly qualified fellows worldwide and within all research disciplines, providing ideal opportunities to further develop their research, and ensuring fellows' participation in collaboration and exchange with researchers and research groups at AU. AIAS provides a physical home and programmatic framework for excellent researchers who come to AU from outside Denmark for shorter or longer periods.

Competencies

The university is seeking an accomplished academic and administrative leader who will take the Aarhus Institute of Advanced Studies through its inaugural phase and build it into an established and globally visible intellectual landmark for research excellence and talent development. The executive director must have a commitment to talent development and a passion for the research enterprise that constitutes the core of AU.

Area of responsibility

The executive director creates a strategy for the institute, and develops programs to promote joint development and exchange of ideas and research results. The executive director maintains connections to AU's research environments, oversees recruitment processes, manages a significant operating budget, and supervises a team of administrators. Fundraising and board development are also part of the responsibilities of the executive director. The executive director represents AIAS to a variety of constituencies internal and external to the university.

Employment conditions

The executive director will be hired in accordance with the agreement for academics in Denmark between the Danish Ministry of Finance and the Danish Confederation of Professional Associations (AC).

The executive director will be hired on a fixed term contract for a period of up to 6 years with an option of extension by up to 3 years.

The total salary including allowances and pension is expected to be around 165,000 USD a year before taxes (current level).

Appointment procedure

Applications must be received no later than **12 p.m. CET on September 3, 2012** and should be submitted online via Aarhus University's website, www.au.dk/om/stillinger/adm/tap/, where more details are available regarding job and person profile.

For further information, please see www.aias.au.dk, or contact Professor Jørgen Frøkiær, Vice-chair of the Board of Aarhus Institute of Advanced Studies, by email at jf@ki.au.dk.

Aarhus University has signed the charter for more women in management, and encourages both men and women to apply for the position.



Aarhus University offers an inspiring education and research environment for 40,000 students and 11,000 members of staff, ensuring results of a high international standard. The budgeted turnover for 2012 amounts to DKK 6.2 billion. The university's strategy and development contract are available at www.au.dk/en.

Science

Faculty Careers

Special Career Feature: September 14

Reserve your ad by August 28 to guarantee space.*

*Ads accepted until September 10 if space is still available.



Hiring Faculty? Here's why you should advertise in this issue:

Content: This special focus on balancing faculty duties with entrepreneurship will be a must-read for those pursuing faculty positions—or anyone working in the academic sector.

Reach: With over 57% of our weekly readers working in academia and 67% with Ph.D.s, *Science* connects you with more scientists in academia than any other publication.

Results: If you are looking to hire faculty, *Science* offers a simple formula: relevant content that spotlights your ad + a large qualified audience = hiring success.

Customized
packages
to correspond with
this special feature
are available

To Book Your Ad:

E-mail:
advertise@sciencecareers.org

Or telephone us:
US: 202-326-6582
Europe/RoW: +44 (0) 1223 326500
Japan: +81-50-3696-5100
China/Korea/Singapore/Taiwan/Thailand: +86-1367-1015-294

Find your next faculty member by advertising in this special feature.

ScienceCareers.org

For recruitment in science, there's only one **Science**

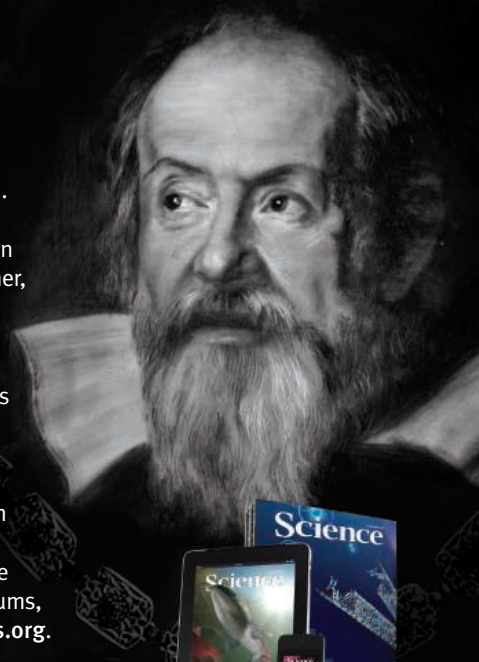


There's only one GALILEO GALILEI

Born in 1564, Galileo Galilei once contemplated a career in the priesthood. It's perhaps fortunate for science that upon the urging of his father, he instead decided to enroll at the University of Pisa. His career in science began with medicine and from there he subsequently went on to become a philosopher, physicist, mathematician, and astronomer, for which he is perhaps best known. His astronomical observations and subsequent improvements to telescopes built his reputation as a leading scientist of his time, but also led him to probe subject matter counter to prevailing dogma. His expressed views on the Earth's movement around the sun caused him to be declared suspect of heresy, which for some time led to a ban on the reprinting of his works.

Galileo's career changed science for all of us and he was without doubt a leading light in the scientific revolution, which is perhaps why Albert Einstein called him the father of modern science.

Want to challenge the status quo and make the Earth move? At *Science* we are here to help you in your own scientific career with expert career advice, forums, job postings, and more — all for free. Visit *Science* today at **ScienceCareers.org**.



For your career in science, there's only one **Science**

ScienceCareers.org



Career advice | Job postings | Job Alerts | Career Forum | Crafting resumes/CVs | Preparing for interviews



Research Position at ICYS, NIMS, Japan



The International Center for Young Scientists (ICYS) of the National Institute for Materials Science (NIMS) is now seeking a few researchers. Successful applicants are expected to pursue innovative research on broad aspects of materials science using most advanced facilities in NIMS (<http://www.nims.go.jp/eng/index.html>).

In the ICYS, we offer a special environment that enables young scientists to work independently based on their own idea and initiatives. All management and scientific discussions will be conducted in English. An annual salary between 5.03 and 5.35 million yen (level of 2011) will be offered depending on qualification and experience. The basic contract term is two years and may be renewed to one additional year depending on the person's performance. A research grant of 2 million yen per year will be supplied to the ICYS researcher.

All applicants must have obtained a PhD degree within the last ten years. Applicants should submit an application form, which can be downloaded from our website, together with a resume (CV) and a list of publications. A research proposal on an interdisciplinary or integrated area related to the materials science should also be submitted. The application letter should reach the following address via e-mail or air mail by September 30, 2012. Visit our website for more details (<http://www.nims.go.jp/icys/>).

ICYS Administrative Office,
National Institute for Materials Science
Sengen 1-2-1, Tsukuba, Ibaraki 305-0047, Japan
e-mail: icys-recruit@nims.go.jp

PRIZES



18th MARCH OF DIMES PRIZE IN DEVELOPMENTAL BIOLOGY (2013)

The March of Dimes Prize in Developmental Biology is bestowed upon investigators whose research has profoundly advanced the science that underlies our understanding of birth defects.

The award of \$250,000 includes a silver medal in the design of the Roosevelt dime.

Nominations are solicited prior to **September 17, 2012**.

Nomination forms and a list of prior recipients are available from:

Joe Leigh Simpson, M.D., FACOG, FACMG
Senior Vice President for Research and
Global Programs March of Dimes
1275 Mamaroneck Avenue
White Plains, NY 10605
Telephone: (914) 997-4555
Facsimile: (914) 997-4560
jsimpson@marchofdimes.com



Nontraditional Careers: Opportunities Away From the Bench Webinar

Want to learn more about exciting and rewarding careers outside of academic/industrial research? View a roundtable discussion that looks at the various career options open to scientists and strategies you can use to pursue a nonresearch career.

Now Available On Demand
www.sciencecareers.org/webinar

Produced by the
 Science/AAAS Business Office.

Science Careers
 From the journal *Science* AAAS

POSITIONS OPEN

TENURE-TRACK FACULTY POSITION Georgia Institute of Technology School of Chemistry and Biochemistry

The Georgia Institute of Technology, School of Chemistry and Biochemistry seeks to fill one or more tenure-track faculty positions in the area of Biochemistry. Exceptional candidates at all levels are encouraged to apply. Candidates with interdisciplinary research programs may be considered for joint appointments with other campus units. Candidates for appointment at the **ASSISTANT PROFESSOR** level should submit an application letter, curriculum vitae, a summary of research plans, and arrange for submission of three letters of reference. Candidates for advanced levels should submit an application letter, curriculum vitae, and the names of three references. All materials and requests for information should be submitted electronically, as per the instructions found at [website: https://academicjobsonline.org/ajob/jobs/1552](https://academicjobsonline.org/ajob/jobs/1552).

The application deadline is September 14, 2012, with application review continuing until the positions are filled. *Georgia Tech is an Equal Education/Employment Opportunity Institution.*

POSTDOCTORAL FELLOW

We are seeking a full-time Postdoctoral Fellow to work in the **David Schwartz and Ivana Yang Lab** in the Pulmonary Division at the University of Colorado, Denver. The research in the Schwartz/Yang Lab focuses on understanding the genetic and biological determinants of diseases that are influenced by the environment. Specific areas of interest include genetic and epigenetic mechanisms that underlie the development of asthma, pulmonary fibrosis, and innate immunity. State-of-the-art techniques, including next generation sequencing, genome-wide association studies (GWAS), and genome-wide epigenetic analysis in animal models and human cohorts are used to accomplish these goals. Those interested in the position should apply through [website: http://www.jobsatcu.com](http://www.jobsatcu.com). The posting number for this position is **818601**.

Find
 your future
 here.

Science Careers

From the journal *Science* AAAS

www.ScienceCareers.org

We deliver
 customized job alerts.

www.ScienceCareers.org

POSITIONS OPEN

**UT SOUTHWESTERN
 MEDICAL CENTER**

FACULTY POSITIONS IN PATHOLOGY Assistant Professor, Associate Professor, or Professor

University of Texas Southwestern Medical Center

The University of Texas Southwestern (UTSW) Medical Center, Department of Pathology, invites applications for two faculty positions from highly qualified scientists (M.D., M.D.-Ph.D., or Ph.D.) with a demonstrated ability to lead an independent, funded research program in cancer, immunology, or neuroscience. Appointments can be at the Assistant, Associate, or full Professor level. Generous salary, startup packages, and laboratory space will be provided. UTSW offers a highly collaborative environment, outstanding research infrastructure, and dynamic translational opportunities.

Applicants should submit a cover letter, curriculum vitae, a statement of research interest, and three letters of reference to:

Diego Castrillon M.D., Ph.D.

Department of Pathology

UT Southwestern Medical Center

5323 Harry Hines Boulevard

Dallas, TX 75390-9072

E-mail: kim.deimling@utsouthwestern.edu

UT Southwestern Medical Center is an Equal Opportunity/Affirmative Action Employer.



PHILOMATHIA POSTDOCTORAL FELLOWSHIP

in Energy and Climate Research University of
 California, Berkeley

The newly established Philomathia Center at the University of California, Berkeley is accepting applications from outstanding research scientists for a two-year postdoctoral fellowship in the field of energy and climate research. Applicants from a wide range of disciplines—from architecture to biology, from engineering to public policy—are encouraged to apply. Research undertaken by the Philomathia Fellow will transcend traditional disciplinary boundaries, with Fellows expected to work with faculty in various disciplines.

Competitive salary commensurate with experience; each Fellow will receive an annual research allowance of up to \$25,000. The application deadline is September 17, 2012. Start date is flexible, but no later than January 2013.

For information about the Philomathia Center, application guidelines, and to submit the required application materials, please visit [website: http://vcresearch.berkeley.edu/philomathia](http://vcresearch.berkeley.edu/philomathia). Please direct any questions to e-mail: energy@berkeley.edu.

The University of California is an Equal Opportunity/Affirmative Action Employer and encourages women and minority candidates to apply.

MARKETPLACE

Widely
 Recognized
 Original &
 Guaranteed

KlenTaq1

8¢/u
 Truncated
 Taq DNA
 Polymerase
 Withstand 99°C

US Pat #5,436,149

Call: **Ab Peptides**

Fax: 314•968•8988

e-mail: abpeps@msn.com

1•800•383•3362

www.abpeps.com